

UCLA

UCLA Electronic Theses and Dissertations

Title

Understanding the Stability and Reactivity of Highly Dispersed Metal Catalysts Supported on Titania for the Decomposition of Chemical Warfare Agents

Permalink

<https://escholarship.org/uc/item/6zc6w2wh>

Author

Tesvara, Celine

Publication Date

2024

Peer reviewed|Thesis/dissertation

UNIVERSITY OF CALIFORNIA

Los Angeles

Understanding the Stability and Reactivity
of Highly Dispersed Metal Catalysts Supported on Titania for the Decomposition
of Chemical Warfare Agents

A dissertation submitted in partial satisfaction of the
requirements for the degree Doctor of Philosophy
in Chemical Engineering

by

Celine Tesvara

2024

© Copyright by

Celine Tesvara

2024

ABSTRACT OF THE DISSERTATION

Understanding the Stability and Reactivity
of Highly Dispersed Metal Catalysts Supported on Titania for the Decomposition
of Chemical Warfare Agents

by

Celine Tesvara

Doctor of Philosophy in Chemical Engineering

University of California, Los Angeles, 2024

Professor Philippe Sautet, Chair

Chemical warfare agents (CWAs), in particular sarin pose a severe threat to both military personnel and civilians, necessitating the development of effective and efficient methods for their decontamination. The use of small, highly dispersed metal catalysts and single atom catalysts (SACs) supported on metal oxides has been a growingly appealing solution due to their superior reactivity and efficiency for the decomposition of CWAs. However, their dynamic stability and reactivity in reaction conditions are still subject of debate and insufficiently understood due to experimental limitation. This thesis aims to reconcile these shortcomings using Density Functional Theory, ab-initio thermodynamics theorem, and microkinetic modeling to help understand: (1) the

dynamic stability of these highly dispersed metal single atom and nanoparticles, and (2) understand its implication towards the catalytic activity of CWA decomposition.

Firstly, DFT calculations were performed to understand sarin's base reactivity on plain, undoped rutile titanium dioxide, r-TiO₂(110). We found that DMMP is a sufficient simulant to describe the chemistry of sarin as both molecules have strong binding on titania, with low reactivity and similar barrier to decompose. We then incorporate ab atomistic thermodynamics to explore the stability of Pt single atom (SA) on anatase TiO₂(101). In reducing pretreatment, we show that Pt prefers adsorbed structure, occupying the surface oxygen vacancy. Using CO as probe molecule, we showcase the dynamic behavior of the Pt single atom and its intricacies in determining the rate determining intermediates during steady state reactions that is elusive to be determined by experiments alone. We then study the reactivity of GB and DMMP on Pt SA in oxidative conditions. Pt provides the thermodynamic drive to cleave P-X bond, while lowering the barrier to do so via a unique PtO₄ planar-like structure.

We then briefly study the role of highly dispersed Cu₄ cluster with and without co-deposition of potassium to facilitate the decomposition of dimethyl methyl phosphonate, a simulant for sarin in controlled environments. We studied the role of highly dispersed Cu₄ clusters, with and without potassium, in decomposing dimethyl methyl phosphonate (DMMP), a sarin simulant. Using NAP-XPS and DFT, we found that DMMP decomposes into highly reduced P-species at room temperature. Co-deposition of K and Cu₄ clusters further improved reactivity, leaving no intact DMMP. The Cu₄ clusters' fluxional nature enhances the exothermic cleavage of DMMP bonds, with reaction products binding preferentially to TiO₂. Calculations of P 2p chemical shifts from various decomposition products align well with observed XPS spectra.

Finally, we explored the stability of Pt_6O_x supported on anatase $\text{TiO}_2(101)$ using the grand canonical basin hopping algorithm. Methanol reactivity studies showed that Pt single atoms facilitate methoxy formation, leading to $\text{CO}_2 + 2\text{H}_2\text{O}$ and dioxomethylene pathways. Pt clusters oxidize to Pt_6O_{10} in oxidative conditions, forming a stable bilayer structure with planar PtO_4 -subunits. This structure provides active O adatoms for oxidation reactions, crucial in methanol dehydrogenation. We found that reactivity of methanol translates well to the thermodynamic analysis of CWA decomposition, providing additional insights on potential catalyst performance for CWA degradation.

The dissertation of Celine Tesvara is approved.

Panagiotis D. Christofides

Kendall N. Houk

Dante A. Simonetti

Philippe Sautet, Committee Chair

University of California, Los Angeles

2024

I dedicate this work to my family and friends.

Table of Contents

ABSTRACT OF THE DISSERTATION	ii
Table of Contents	vii
List of Tables.....	xi
List of Figures.....	xiv
Acknowledgements.....	xxvi
Curriculum Vitae.....	xxxii
Chapter 1	1
Introduction.....	1
1.1. Motivation.....	1
1.2. Review on experimental (thermal) catalytic reactivity of sarin and DMMP on titania. .	4
1.3. Highly dispersed catalysts: Structure, Stability, and its relation to reactivity	7
1.3.1. Single atom catalyst	7
1.3.2. Nanoparticles	9
1.4. Modeling highly dispersed metal catalysts in realistic conditions.....	11
1.4.1. Ab initio Thermodynamics	11
1.4.2. Grand Canonical Basin Hopping	12
1.5. Thesis Objectives	15
Chapter 2 Decomposition of the Toxic Nerve Agent Sarin on Oxygen Vacancy Sites of Rutile TiO ₂ (110)	16
2.1. Introduction.....	16
2.2. Methods.....	20
2.2.1. Computational Set-up	20
2.2.2. Computational Model	20

2.3.	Results.....	22
2.3.1.	Pristine surface.....	22
2.3.2.	The effect of O vacancy	25
2.3.3.	Vibrational analysis.....	28
2.3.4.	Discussion.....	32
2.3.5.	Conclusion	37
Chapter 3 Unraveling the CO Oxidation Mechanism over Highly Dispersed Pt Single Atom on Anatase TiO ₂ (101)		39
3.1.	Introduction.....	39
3.2.	Computational Methods	42
3.3.	Results and Discussion	44
3.3.1.	Synthesis, Structure, and Stability of Pt _{SA} /a-TiO ₂ (101).....	44
3.3.2.	Elucidation of CO Oxidation Pathway and Active Species	47
3.3.3.	Kinetics of CO oxidation: Microkinetic Analysis.....	52
3.3.4.	Origin of Partial Orders and Apparent Activation Energy	59
3.3.5.	Conclusions.....	62
Chapter 4 Chemical Warfare Agent decomposition on Pt SA/a-TiO ₂ (101): reactivity & establishing descriptors		64
4.1.	Introduction.....	64
4.1.1.	Computational Set-up	65
4.2.	Results & Discussions.....	67
4.2.1.	Thermodynamic analysis	69
4.2.2.	Kinetic analysis.....	72
4.2.3.	Descriptor screening across transition metal	74
4.2.4.	Relating the activity with the d-state center of active SAC	81

4.2.5. Conclusion	82
Chapter 5	85
Decomposition of Dimethyl Methyl Phosphonate on Surface Modified TiO ₂ (110): Cu Clusters and Alkali Atoms	85
5.1. Introduction.....	85
5.2. Computational methods	87
5.3. Results.....	88
5.3.1. Experimental Characterization of Cu ₄ /TiO ₂ (110) and K/Cu ₄ /TiO ₂ (110).....	88
5.3.2. Theoretical description of Cu ₄ /TiO ₂ (110) and K/Cu ₄ /TiO ₂ (110) surfaces and adsorption of molecular DMMP	90
5.3.3. NAP-XPS results for DMMP exposure at room temperature.....	94
5.3.4. Temperature dependence	100
5.4. Discussion.....	104
5.5. Conclusions.....	112
Chapter 6.....	115
Methanol as a probe for CWA decomposition on highly dispersed Pt nanocluster on Anatase TiO ₂ (101)	115
6.1. Introduction.....	115
6.2. Computational Methods.....	118
6.2.1. VASP set-up	118
6.2.2. Cell size for reaction pathway optimization	119
6.2.3. Global optimization using GCBH.....	120
6.3. Results & Discussion	122
6.3.1. Pt ₆ O _x stability and its electronic effect	122
6.3.2. Methanol reactivity on Pt SA.....	124

6.3.3.	Methanol adsorption on Pt ₆ O ₁₀ NP	129
6.3.4.	Methanol reactivity on Pt ₆ O ₁₀ NP: Proton Coupled Electron Transfer (PCET)	130
6.3.5.	CWA thermodynamics on Pt ₆ O ₁₀ NP	133
6.4.	Conclusions.....	137
Chapter 7	140
Conclusion	140
Appendix A	147
Appendix B	150
Appendix C	169
Bibliography	178

List of Tables

Table 2. 1 Experimental and calculated vibrational frequencies for gas phase sarin. Experimental data is from ref ¹³	29
Table 2. 2 IR band assignment comparison between sarin adsorption experiments at room temperature (ref 13) and theoretical frequencies for molecularly adsorbed sarin. Corrected frequencies are shown in parentheses. *Data unavailable in reference.	30
Table 2. 3 IR band assignment comparison of decomposed sarin after heating to 500 K between the experiment and theory. A negative sign (-) indicates disappearing bands and a positive sign (+) indicates increasing bands.....	32
Table 2. 4 Barrier comparison of the first step of sarin decomposition via P-O, P-F, and O-C bond cleavage on pristine and defective surface.....	35
Table 3. 1 Turnover Frequency (TOF), CO and O ₂ reaction orders, and apparent activation energy (E _{app}) obtained from microkinetic modeling under experimental conditions. TOF, CO order, and O ₂ order values are at 160 °C and apparent activation energy was measured between 150 and 170 °C.	56
Table 3. 2 Computed Degree of Rate Control obtained from the Microkinetic Modeling (MKM) at reaction conditions (T = 160 °C, P _{CO} = 1 kPa, P _{O2} = 10 kPa, conversion = 5%) for the TOF-determining transition states (TDTS).....	58
Table 3. 3 Results from the decomposed microkinetic analysis of the three simpler reactive cycles within the complete reaction cycle	59

Table 5. 1 Summary of P 2p and C 1s binding energies for DMMP on TiO ₂ (110) surfaces with and without Cu ₄ clusters and K atoms, along with data from previous studies on related surfaces ...	95
Table A. 1 Reaction rate constants [1/s] at 300 K of Sarin on the pristine surface starting from intermediate C.....	148
Table A. 2 Reaction rate constants [1/s] at 300 K of Sarin on the pristine surface starting from intermediate C.....	149
Table A. 3 Reaction rate constants [1/s] at 300 K of Sarin on the defective surface starting from intermediate E.....	149
Table B. 1 Average crystallite size of TiO ₂ in the fresh TiO ₂ , calcined TiO ₂ , and the spent PtSA/TiO ₂ (after CO oxidation kinetics experiment on the reduced PtSA/TiO ₂) samples calculated using the Scherrer equation and the line broadening of TiO ₂ (101) and TiO ₂ (200) diffraction peaks.	152
Table B. 2 Elementary reaction steps used for the microkinetic modeling (MKM).....	160
Table B. 3 Vibrational Stretch of CO on various intermediates during CO oxidation obtained from DFT calculation.	161
Table B. 4 The Bader charge analysis of various Pt states of the Pt _{SA} /TiO ₂ . The most stable Pt states (supported and dopant) adopts +4 oxidation state.	161
Table B. 5 Binding energy (heat of adsorption) of the chemisorbed CO on the Pt SA/a-TiO ₂ catalysts during steady-state CO oxidation reaction estimated from DRIFTS TPD experiments using the Redhead analysis (see details below).	164

Table C. 1 Binding energies for the various P-intermediates on the Cu ₄ /TiO ₂ (110) surface obtained from fits of the P 2p XPS spectra taken at different temperatures after exposure to 1 x 10 ⁻⁴ Torr of DMMP (see Figure C.3).....	173
Table C. 2 Binding energies for the various P-intermediates on the K/Cu ₄ /TiO ₂ (110) surface obtained from fits of the P 2p XPS spectra taken at different temperatures after exposure to 1 x 10 ⁻⁴ Torr of DMMP (see Figure C.3).	174

List of Figures

Figure 1. 1 Chemical structure of sarin and DMMP.....	3
Figure 1. 2 Schematic of single atom catalyst supported on metal oxide for oxidative decomposition of DMMP	4
Figure 1. 3 Schematic of Grand Canonical Basin Hopping algorithm.	14
Figure 2. 1 Molecular adsorption modes of sarin on TiO ₂ (110) with their adsorption energies referenced to the gas phase.	22
Figure 2. 2 The energy profile of sarin decomposition on pristine r-TiO ₂ via P-F and P-OC ₃ H ₇ bond cleavage starting from the two most stable adsorption modes (adsorption modes B and C). The decomposition via P-OC ₃ H ₇ cleavage is shown in the path B1-B3 whereas the P-F bond cleavage occurs along the path C1-C3. Elementary reaction barriers are indicated as ΔE_{act}	24
Figure 2. 3 The energy profile of sarin decomposition on pristine r-TiO ₂ via C-O bond cleavage starting from the two most stable adsorption modes C.....	25
Figure 2. 4 Sarin adsorption modes on the r-TiO ₂ surface with an O vacancy.	26
Figure 2. 5 Sarin decomposition on the r-TiO ₂ (110) surface with an O vacancy initiated via P-F (blue) or O-C (black) bond cleavage. The decomposition starts from Sarin's most stable adsorption mode (intermediate F here is written as F1, the numbering is to denote	27
Figure 2. 6 Sarin decomposition pathway on the r-TiO ₂ (110) surface with an O vacancy initiated via P-OR (R= isopropyl) bond cleavage. The sarin initial adsorption geometry is structure F = F1.	28

Figure 3. 1(a) Ex situ AC-HAADF-STEM images of the SA Pt/TiO₂ sample taken after the reduced sample went through the CO oxidation kinetic experiment, showing the singly dispersed Pt atoms as enclosed in pink circles. (b) In situ DRIFTS spectra of CO adsorption at 35 °C after H₂ reduction pretreatment. H₂ reduction pretreatment was performed at 350 °C for 2 hr. (c) Calculated structure and vibrational frequency of CO adsorbed on Pt SA supported on anatase TiO₂ which corresponds to the reduced state of the catalyst and the starting catalyst for the CO oxidation cycle. The frequency value agrees well with DRIFTS spectrum in Figure 3.1 (b). (d) Stability diagram of the different configurations of the supported Pt_{SA} on anatase TiO₂ under different gas environments (please see Figure B.6 (a) for all structures).46

Figure 3. 2 The reaction pathway for CO oxidation on PtSA/TiO₂ (a) and its respective free Gibbs Energy landscape at reaction conditions (T = 160 C°, PCO=1 kPa, PO₂=10 kPa, conversion = 5%). Surfaces with an O vacancy are represented by an inward concave. (b). The reaction pathway consists of an initiation step and a catalytic reactive cycle. Elementary steps involving adsorption or desorption processes are connected with solid lines, indicating their respective adsorption free energy barrier. For elementary reaction steps, transition states energy levels are explicitly indicated (labeled TS X) and linked by dashed lines..... 51

Figure 3. 3 In-situ/operando CO adsorption DRIFTS spectra for PtSA/TiO₂ (a) under different gas environments at 35 °C on the H₂ reduced state and (b) during CO oxidation at 160 °C and under different duration of N₂ flush of the reaction gas environment afterwards. (c) The White Line Intensity (WLI) region of the in-situ XANES spectra for Pt_{SA} after CO oxidation compared against three standards – Pt foil, Pt²⁺, and Pt⁴⁺. (d) Surface coverage along the MKM simulations for the primary Pt_{SA}/a-TiO₂ species present during CO oxidation. In the legend, we indicate the

corresponding CO vibrational frequency in cm^{-1} (above the line) and the formal Pt oxidation state derived from the Bader charge analysis (below the line; see Table S4 for more details). 54

Figure 3. 4 CO oxidation kinetic measurements on PtSA/TiO₂ with turnover frequency (TOF) calculated considering 100% Pt atoms are singly dispersed, i.e., on the surface. (a) Arrhenius plot (TOF vs 1000/RT) with the calculated apparent activation energy (E_{app}) value. E_{app} was measured between 150 and 170 °C with 1 kPa CO, 10 kPa O₂, and balance He to atmospheric pressure at 75 sccm total flow rate. (b) Effect of CO and O₂ partial pressure on TOF at 160 °C. Gas flow conditions: 0.4-1 kPa CO and 10 kPa O₂ for the effect of CO partial pressure; 1 kPa CO and 4-12 kPa O₂ for the effect of O₂ partial pressure with balance He to atmospheric pressure at 75 sccm total flow rate. (c) Surface coverage for model kinetic simulations including only part of the reaction pathways shown in Figure 2 (“black”, “black + blue”, and “black + red” paths following colors of Figure 2) and corresponding majority structures. 57

Figure 4. 1 Side and top representation of the unit cell used in the reactivity study. Highlighted Ti sites in yellow signify the rows of Ti_{5c}. 67

Figure 4. 2 Molecular adsorption modes of DMMP on Pt SA/TiO₂(101) with their adsorption energies. 68

Figure 4. 3 Molecular adsorption modes of GB on Pt SA/TiO₂(101) with their adsorption energies. 69

Figure 4. 4 Thermodynamic analysis of O-C, P-O, P-C, C-H and P-F bond cleavage for DMMP (top left) and sarin (top right). The selected ensemble of molecular adsorption for the thermodynamic study is shown on the middle bottom panel. The colors on the energy diagram correspond to each molecular adsorption mode shown. 72

Figure 4. 5 Reaction pathway for P-X (X=OCH₃, OC₃H₇ or F) bond cleavage. Pathway for DMMP shown in left and sarin shown in right. The naming nomenclature follows the ID assignment from Figure 4.3 and 4.2. 74

Figure 4. 6 Stability plot of 13 selected single metal atom catalysts plotted as a function of oxygen chemical potential. The vertical red line denotes oxygen chemical potential corresponding to the ambient condition. Each line color correspond to a chemical formula; MO_x (M: Metal, x=number of oxygen adatom). 76

Figure 4. 7 (a) Volcano plot correlating the thermodynamic drive to cleave the P-O bond with the 'barrier' across all selected 13 transition state metals single atoms. (b) the schematic of parameter defining the activity ($\Delta E_{\text{bridging}}$) and thermodynamic ($\Delta E_{\text{P-O}}$)..... 77

Figure 4. 8 (a) Comparison of the change of energy to cleave P-O vs P-F bond. (b) adsorption energy of sarin on various system compared between two different modes: on Ti sites ("Ads Ti") and on the active metal ("Ads on Metal")..... 79

Figure 4. 9 Various correlations between d-band center and (top left) the thermodynamics to cleave P-F bond, (top right) P-O bond, (bottom left) adsorption strength on Ti sites and (bottom right) the perceived barrier (the change in energy to reach the bridging intermediate from molecular adsorption). 82

Figure 5. 1 Surface characterization using (a, d) Ti 2p, (b) Cu 2p, and (e) K 2p XPS spectra and (c, f) Cu LMM Auger spectra prior to DMMP exposure for the (a–c) Cu₄/TiO₂(110) and (b–f) K/Cu₄/TiO₂(110) surfaces. 90

Figure 5. 2 Lowest energy structures for Cu₄/TiO₂(110) and K/Cu₄/TiO₂(110). Values below each structure denotes the relative stabilities (in eV) with respect to the most stable isomer. 91

Figure 5. 3 (a, d) Electronic spin density for the most stable (a) $\text{Cu}_4/\text{TiO}_2(110)$ and (d) $\text{K}/\text{Cu}_4/\text{TiO}_2(110)$ structures; (b, e) charge density difference upon adsorption of (b) Cu_4 and (e) $\text{K}-\text{Cu}_4$ adsorption on $\text{TiO}_2(110)$. The yellow and blue color denotes spin up and down density or charge accumulation and depletion, respectively. (c, f) Electronic Bader charge for (c) Cu_4 and (f) 92

Figure 5. 4 Low energy surface configurations for DMMP adsorption on (a-d) $\text{Cu}_4/\text{TiO}_2(110)$ and (e-h) $\text{K}/\text{Cu}_4/\text{TiO}_2(110)$. DMMP adsorption energies are shown below each (in eV). 93

Figure 5. 5 P 2p XPS spectra showing phosphorous surface species during exposure of 1×10^{-4} Torr of DMMP at room temperature on the surfaces of (a) Cu_4/TiO_2 , (b) $\text{K}/\text{Cu}_4/\text{TiO}_2(110)$ and $\text{K}/\text{TiO}_2(110)$. The different colored solid lines correspond to least-squares fits. 95

Figure 5. 6 C1s XPS spectra taken on the (a) $\text{Cu}_4/\text{TiO}_2(110)$, (b) $\text{K}/\text{Cu}_4/\text{TiO}_2(110)$ and (c) $\text{K}/\text{TiO}_2(110)$ surfaces under 1×10^{-4} Torr of DMMP at room temperature. The colored solid lines correspond to least squares fits of the data to three different peaks corresponding to different surface intermediates with labels C1-C3. 99

Figure 5. 7 P 2p (a,b) and C 1s (c,d) peak intensities versus temperature for the (a, c) $\text{Cu}_4/\text{TiO}_2(110)$ and (b,d) $\text{K}/\text{Cu}_4/\text{TiO}_2(110)$ surfaces exposed 1×10^{-4} Torr of DMMP at room temperature. The DMMP was pumped out of the NAP-XPS chamber prior to heating the surfaces. 101

Figure 5. 8 (a) Ti^{3+} concentration (%) as determined from fitting the Ti 2p XPS spectra at different temperatures for the $\text{Cu}_4/\text{TiO}_2(110)$ and $\text{Cu}_4/\text{K}/\text{TiO}_2(110)$ surfaces. (b) K 2p XPS peak intensity versus temperature for the $\text{Cu}_4/\text{K}/\text{TiO}_2(110)$ surface. The 300 K data points presented in parts (a) and (b) were taken under 1×10^{-4} Torr of DMMP, while DMMP was evacuated for the measurements taken at higher temperatures. 103

Figure 5. 9 Computational exploration of DMMP decomposition intermediates, combining bond dissociation at the P atom (P-C or P-OCH₃ bond cleavage) and O-C bond dissociation on (a) Cu₄/TiO₂(110) and (b) K/Cu₄TiO₂(110) surfaces. “Molecular” indicates non-dissociated chemisorbed DMMP. The adsorption energies (ΔE) of each configuration are referenced to gas phase DMMP..... 105

Figure 5. 10 Surface structures for the most stable and unique P-center containing intermediates for DMMP decomposition on Cu₄/TiO₂(110) along with their respective adsorption energies (ΔE_{ads} referenced to gas-phase DMMP) and XPS binding shifts (δ_{XPS}) for breaking one, two, and three bonds. 107

Figure 5. 11 Surface structures for the most stable and unique P-center containing intermediates for DMMP decomposition on K/Cu₄/TiO₂(110) along their respective adsorption energies (ΔE_{ads} referenced to gas-phase DMMP) and XPS binding shifts (δ_{XPS}) for breaking one, two, and three bonds. 108

Figure 5. 12 Calculated XPS binding energy shifts on P atom against its stability on Cu₄/TiO₂ (a-d) and KCu₄/TiO₂ (e-h) referenced to the molecularly chemisorbed DMMP. Plot b-d and f-h showcase the peaks obtained from isomers with one, two and three fragment transferred onto Cu₄ and Cu₄K clusters respectively. The label P-O, P-C and O-C denotes which bonds/combination of bonds are broken (P-O, P-C and O-C bonds respectively). 111

Figure 6. 2 Constructed stability diagram of Pt₆O_x as a function of oxygen chemical potential (left). Highlighted in the square are the accessible region in ambient condition. The relative stability of isomers found as function of chemical formula is plotted on the right hand side. 123

Figure 6. 3 Global minima of Pt ₆ O _x found by GCBH method. The cluster adopts the Pt ₆ O ₁₀ chemical formula (a). A and B denotes the side view. Charge density difference plot (b).	123
Figure 6. 4 Explored adsorption mode of methanol on Pt SA/TiO ₂ (101).....	124
Figure 6. 5 DFT calculated methanol oxidation pathway on Pt SA/TiO ₂ (101) starting from the most stable adsorption mode on Pt (a) and second best adsorption mode on Pt (b).....	128
Figure 6. 6 Various adsorption mode of methanol on Pt ₆ O ₁₀ /TiO ₂ (101) calculated via DFT. The numbers below denotes the adsorption energy in eV.....	130
Figure 6. 7 DFT calculated methanol oxidation pathway via PCET process without hydroxyl diffusion.	132
Figure 6. 8 DFT calculated methanol oxidation pathway via PCET process with hydroxyl diffusion.	133
Figure 6. 9 DFT calculated exploration of DMMP (left) and sarin (right) adsorption modes on Pt ₆ O ₁₀ /TiO ₂ (101). The marker denotes the site of which the phosphoryl group is binding on. Blue dots represents adsorption on Ti sites whereas grey on Pt.....	134
Figure 6. 10 Thermodynamic analysis of possible sarin decomposition pathways via P-O, P-C, P-F, O-C and C-H (propene release). Denoted in red is change of energy of the bond cleavage process which are endothermic and in green exothermic. The values under each intermediate denoted 'Eads' is referenced to the gas phase sarin.....	135
Figure A. 1 Side and Top view of pristine 2x4 r-TiO ₂ (110) surface model.	147
Figure A. 2 Top and side view of defective r-TiO ₂ (110) surface model.	147

Figure B. 1 Zeta potential of anatase TiO₂ measured as a function of pH. The pH where the zeta potential becomes zero is the point of zero charge (PZC) where the surface of TiO₂ particles would have a net charge of zero. PZC for anatase TiO₂ is ~6.4 and therefore it gets negatively charged at a pH higher than that. The Pt precursor, [Pt(NH₃)₄](NO₃)₂, dissociates into [Pt(NH₃)₄]²⁺ and 2(NO₃⁻). Based on the PZC, we therefore synthesized the PtSA/TiO₂ catalysts at pH 13.7 to electrostatically adsorb the Pt complex ([Pt(NH₃)₄]²⁺) onto the TiO₂ particles.150

Figure B. 2 BET surface area plot for the BET surface area analysis of the as-received TiO₂ powders (fresh TiO₂), calcined TiO₂ (calcination temperature 450 °C), and spent PtSA/TiO₂ (after CO oxidation kinetic measurement presented in Figure 4 (a) and (b))..... 151

Figure B. 3 PXRD patterns for fresh anatase TiO₂ (black), calcined (red) anatase TiO₂ (TiO₂ calcined at 450 °C in the same procedure as the PtSA/TiO₂), and PtSA/TiO₂ catalyst after CO oxidation kinetics experiment (green; calcined at 450 °C, oxidized at 300 °C, reduced at 350 °C, and then performed CO oxidation kinetics.). The scan for the calcined TiO₂ shows peaks only for anatase TiO₂ ensuring that TiO₂ was not converted to rutile phase during the calcination procedure (a prominent peak for TiO₂ (110) at 2θ = 27° would be present if TiO₂ was converted to rutile phase). (Note: the peak at ~50° is from the sample holder)..... 151

Figure B. 4 STEM images of PtSA after CO oxidation confirm stability of the Pt single atoms under reaction condition. Regeneration of the CO chemisorption DRIFTS spectrum after CO oxidation further confirms the stability of PtSA..... 153

Figure B. 5 CO adsorption at 35 oC on the freshly reduced PtSA/a-TiO₂ catalyst (blue) and on the same catalyst after ‘regenerating’ it following CO oxidation at 160 oC for 1 hr (red), both showing almost identical spectra which suggests stable nature of the PtSA species. After the synthesis, the

catalyst was pretreated with 10 kPa O₂ at 300 °C for 1 hour, followed by reduction under 20 kPa H₂ at 350 °C for 2 hours prior to the exposure to 0.56 kPa CO at 35 °C. This state is referred as the freshly reduced PtSA/a-TiO₂. The sample was then ‘regenerated’ through repetition of the oxidation at 300 °C (1 hr) followed by H₂ reduction at 350 °C (2 hr)..... 154

Figure B. 6(a) The stability diagram of the different configurations of PtSA. (b) The stability diagram of the different configurations of the supported PtSA on anatase TiO₂ bound with CO (the vertical lines denotes the oxidizing condition and atmospheric condition). CO helps ‘pull’ the Pt substituting Ti onto the surface. 155

Figure B. 7 Structure representation of intermediates found in pathway exploration 156

Figure B. 8 Mass spectrometer signals during 16O₂/18O₂ switching under steady-state C16O oxidation condition at 160 °C. After 16O₂ was replaced with 18O₂, we observed an instant depletion of C16O₂ signal with 16O signal (almost at the same time) which eventually reaches the baseline level, suggesting that under C16O and 16O₂ co-flow, the adsorbed C16O was only reacting with the adsorbed 16O and its reaction with lattice 16O is unlikely. If lattice 16O were involved, the C16O₂ signal would not deplete immediately after 16O being replaced with 18O. At the same time, C16O18O signal instantly rose from its baseline level suggesting that adsorbed and/or gas-phase C16O reacted with adsorbed 18O on Pt. Details of the experiment can be found in the “Experimental Methods” section in the main text. 156

Figure B. 9 CO chemisorption DRIFTS spectra (a) under N₂ flow after CO and O₂ co-flow at 35 °C, (b) under CO and O₂ co-flow as the sample is being heated up from 35 °C to reaction temperature (160 °C) showing the transition of the CO-Pt, CO-Ti⁴⁺, and gas-phase CO peak, and (c) at 35 oC with CO flow only after cooling down from CO oxidation at 160 oC under CO and

O₂ flow. The CO-Pt peak not returning to the 2115 and 2087 cm⁻¹ features shows complete and irreversible oxidization of the Pt sites under CO oxidation. 157

Figure B. 10 Progression of carbonate formation on the PtSA/a-TiO₂ catalyst after CO adsorption on the reduced catalyst, during CO and O₂ flow at 35 °C and 160 °C, followed by N₂ flush of CO and O₂, and finally under O₂ flow following the N₂ flush. 162

Figure B. 11 CO chemisorption DRIFTS peak at 35 and -75 °C after CO oxidation at 160 °C (cooled down under CO+O₂ flow). This demonstrates that mostly a single type of Pt site is present after CO oxidation. Absence of unpopulated Pt sites from low-temperature DRIFTS can be coupled with the positive CO order to suggest that a 2nd CO (other than the chemisorbed CO on PtSA) from the gas-phase is most likely involved in the reaction cycle. 162

Figure B. 12 ¹²CO/¹³CO exchange experiment at 160 °C (a) in the presence of O₂, i.e. ¹³CO oxidation and (b) in the absence of O₂, i.e. ¹³CO pulse/flow. ¹²CO/¹³CO exchange during ¹³CO oxidation at 160 °C shows that ¹³CO does exchange with the adsorbed ¹²CO during ¹³CO oxidation with an exchange rate (~36% in 30 mins) that is slower than the turnover (~5 turnovers in 30 mins). If the chemisorbed CO was the one involved in the reaction, all ¹²CO would have been replaced by ¹³CO in 30 mins. These results indicate that a 2nd CO is involved in the reaction. The absence of gas-phase O₂ seems to promote the exchange of ¹³CO with ¹²CO, which might be because more ¹³CO are available for exchange in the absence of O₂. 163

Figure B. 13 Normalized absorbance plotted as a function of temperature for temperature-programmed desorption (TPD) of the CO adsorbed during CO oxidation on PtSA/TiO₂. TPD was performed at three different heating rate and shows similar desorption behaviour. Prior to the TPD experiments, CO oxidation was performed at 160 °C for 20 mins (details in experimental section)

to achieve the steady-state CO chemisorption peak and then the sample was cooled down to 35 °C under CO and O₂ flow followed by flushing of the gas-phase CO and O₂ using N₂. Afterwards, the sample was heated up under N₂ flow. TPD of the chemisorbed CO, corresponding to the 2115 cm⁻¹ peak, shows that the CO adsorbed on Pt is bound strongly. 164

Figure B. 14 Steady-state surface coverage of the most abundant intermediates from the Modified Microkinetic Analysis after the third and final modification of the Gibbs Free Energy landscape within the error of DFT. 167

Figure B. 15 Enthalpic energy diagram of reactive pathway calculated using DFT. 168

Figure C. 1 Temperature dependence of the Cu Auger LMM spectrum for the K/Cu₄/TiO₂(110) surface after exposure to DMMP at 1 x 10⁻⁴ Torr: (a) 300 K; (b) 600 K. (c) 900 K. The spectra are fitted as the sum of contributions from the LMM Auger peaks associated with Cu⁰ (blue lines), Cu⁺ (red lines) and the Ti 2s and satellite peaks (gray lines).170

Figure C. 2 Cu LMM Auger spectra for the (a) Cu₄/TiO₂(110) and (b) K/Cu₄/TiO₂(110) 170

Figure C. 3 DFT calculated structures and relative energies for the co-adsorption of K and Cu₄ 171

Figure C. 4 Background C 1s XPS spectra taken at room temperature prior to exposure to 172

Figure C. 5 Temperature dependence of the P 2p XPS spectrum for the Cu₄/TiO₂(110) surface after exposure to DMMP at 1 x 10⁻⁴ Torr: (a) 300K; (b) 400K; (c) 600K; (d) 800K; (e) 900K. 173

Figure C. 6 Temperature dependence of the P 2p XPS spectrum for the K/Cu₄/TiO₂(110) surface 174

Figure C. 7 Temperature dependence of the C 1s XPS spectrum after exposure to DMMP 175

Figure C. 8 Temperature dependence of the Ti 2p XPS spectrum for the K/Cu₄/TiO₂(110)..... 175

Figure C. 9 Calculated Bader charges of the P center of the decomposed DMMP intermediates on the Cu₄/TiO₂(110) surface as a function of the calculate P 2p binding energy shift. The Bader charges are colored coded by configurations resulting from (b) one, (b) two and (c) three bond cleavages on DMMP. Panel (a) includes all configurations in (b)-(d)..... 176

Figure C. 10 Calculated Bader charges of the P center of the decomposed DMMP intermediates on the K/Cu₄/TiO₂(110) surface as a function of the calculate P 2p binding energy shift. The Bader charges are colored coded by configurations resulting from (b) one, (c) two and (d) three bond cleavages on DMMP. Panel (a) includes all configurations in (b)(d). 177

Acknowledgements

I would like to sincerely acknowledge my advisor, Dr. Philippe Sautet for his guidance and support for the past five years I have spent at UCLA. Where do I even begin? His knowledge and constant push as a mentor have allowed me to not only write this thesis but accomplish so many things during my PhD program. I am truly thankful and lucky to have him as my advisor.

I would like to acknowledge Dr. George Xu Yan, Dr. Geng Sun, Dr. Simran Kumari, and Dr. Vaidish Sumaria, for their support in my endeavor in mastering the DFT calculations, from performing intricate transition state search and set-ups all the way to microkinetic modeling. I would also like to thank my experimental collaborators Dr. Constantin Walenta, Muhammad Raian Yousuf, and Dr. Michael White for their experimental insights and countless science discussions. I could not have asked for better co-workers.

Next, I would like to shout out my lab mates and friends I made in the department: Simran Kumari, Martina Rüscher, Joonbaek Jang, Hio Tong (Michael) Ngan, Tobias Göckler, Zahra AlMisbaa, Vaidish Sumaria, George Xu Yan, Robert Michael Kowalski aka. Bobby, Jasmine Dinari, Pepper Yang (for lending me your laptop whenever I mine gives up), Dongfang Cheng and Yani Guan. Enduring the path of academia wouldn't be nearly as fun without you. Thank you for the memories.

Finally, and most importantly, I would like to thank my family for their constant love and prayers. Chelsea, this is for all the laughter we shared when the days are bad. I hope you are proud of me. I would not be here without you all.

Several chapters in this dissertation contain material adapted from published and unpublished manuscripts with multiple contributing authors, as noted in the following.

Chapter 2 contains figures and text adapted with permission from Tesvara, C.; Karwacki, C. J.; Sautet, P. Decomposition of the toxic nerve agent Sarin on oxygen vacancy sites of rutile TiO₂(110). *Journal of Physical Chemistry. C./Journal of Physical Chemistry. C* **2023**, *127* (17), 8006–8015. <https://doi.org/10.1021/acs.jpcc.2c08525>. Copyright 2023 American Chemical Society." PS and CJK conceptualized and supervised the work in the article. CT performed the computational studies. The draft was prepared and edited by CT and PS. The authors acknowledge the support of this work by the US Army under Program No W911NF-21-1-0361. This work used the Extreme Science and Engineering Discovery Environment (XSEDE), which is supported by the National Science Foundation grant number ACI-1548562. This work used computational and storage services associated with the Hoffman2 Shared Cluster provided by UCLA Institute for Digital Research and Education's Research Technology Group.

Chapter 3 contains figures and text adapted with permission from Tesvara, C.; Yousuf, M. R.; Albrahim, M.; Troya, D.; Shrotri, A.; Stavitski, E.; Karim, A. M.; Sautet, P. Unraveling the CO Oxidation Mechanism over Highly Dispersed Pt Single Atom on Anatase TiO₂ (101). *ACS Catalysis* 2024, 7562–7575. <https://doi.org/10.1021/acscatal.4c01018>. Copyright 2024 American Chemical Society. PS and AMK conceptualized and supervised the work in the article. CT and DT performed the computational studies. MRY, AM, performed experimental kinetic study and characterization. AS, ES performed characterization of the samples. C.T. and P.S. acknowledge support from the U.S. Army under Program No. W911NF-21-1-0361. M.Y. and A.M.K. acknowledge support from the U.S. Army Research Laboratory and the U.S. Army Research Office

under Grant No. W911NF-20-2-0058. The views and conclusions contained in this document are those of the authors and should not be interpreted as representing the official policies, either expressed or implied, of the Army Research Office or the U.S. Government. The U.S. Government is authorized to reproduce and distribute reprints for Government purposes notwithstanding any copyright notation herein. This research used 8-ID (ISS) beamline of the National Synchrotron Light Source II, a U.S. Department of Energy (DOE) Office of Science User Facility operated for the DOE Office of Science by Brookhaven National Laboratory under Contract No. DE-SC0012704. STEM imaging was performed through support by the Cooperative Research Program of Institute for Catalysis, Hokkaido University (20A1004 and 22DS0123). This work used computational and storage services associated with the Hoffman2 Shared Cluster provided by UCLA Office of Advanced Research Computing's Research Technology Group and by the hardware at Virginia Tech's Advanced Research Computing. This work used Bridges-2 at Pittsburgh Supercomputing Center through allocation CHE170060 from the Advanced Cyberinfrastructure Coordination Ecosystem: Services & Support (ACCESS) program, which is supported by National Science Foundation grants #2138259, #2138286, #2138307, #2137603, and #2138296.

Chapter 4 contains unpublished text and figures from a manuscript currently in preparation by authors Celine Tesvara, Matthew Leonard, Alex Balboa Christopher J. Karwacki and Philippe Sautet. PS designed computational studies. ML, AB designed the experimental work. The manuscript was prepared by CT, PS. CT performed the computational studies. The authors acknowledge the support of this work by the US Army under Program No W911NF-21-1-0361. This work used the Extreme Science and Engineering Discovery Environment (XSEDE), which is supported by the National Science Foundation grant number ACI-1548562. This work used

computational and storage services associated with the Hoffman2 Shared Cluster provided by UCLA Institute for Digital Research and Education's Research Technology Group.

Chapter 5 contains text and figures adapted with permission from Bonney, M. J.; Tesvara, C.; Sautet, P.; White, M. G. Understanding the decomposition of dimethyl methyl phosphonate on Metal-Modified TiO₂(110) surfaces using ensembles of product configurations. ACS Applied Materials & Interfaces 2024. <https://doi.org/10.1021/acsami.4c01250>. Copyright 2024 American Chemical Society. PS and MW conceptualized and supervised the work in this article. CT performed computational studies. MB performed experimental studies. The authors gratefully acknowledge Dr. Ashley Head, Jason Wang, and Luolin Shi for their help in setting up and running experiments at the Center for Functional Nanomaterials. The authors acknowledge support from the U.S. Army Research Laboratory and the U.S. Army Research Office under Grant Nos. W911NF-20-2-0058 (M.J.B., M.G.W.) and W911NF-21-1-0361 (C.T., P.S.). The views and conclusions herein are those of the authors and should not be interpreted as necessarily representing the official policies or endorsements, either expressed or implied, of the ARO or the U.S. Government. The NAP-XPS measurements were performed at the Center for Functional Nanomaterials, a U.S. DOE Office of Science User Facility located at the Brookhaven National Laboratory. This work used computational and storage services associated with the Hoffman2 Shared Cluster provided by the UCLA Office of Advanced Research Computing's Research Technology Group. This work used Bridges-2 at the Pittsburgh Supercomputing Center through Allocation CHE170060 from the Advanced Cyberinfrastructure Coordination Ecosystem: Services & Support (ACCESS) Program, which is supported by National Science Foundation Grants #2138259, #2138286, #2138307, #2137603, and #2138296.

Chapter 6 contains unpublished text and figures from a manuscript currently in preparation by authors Celine Tesvara, Kristin Knight, John Morris and Philippe Sautet. PS designed computational studies. JM designed the experimental work. The manuscript was prepared by CT, PS. CT performed the computational studies. The authors acknowledge the support of this work by the US Army under Program No W911NF-21-1-0361. This work used the Extreme Science and Engineering Discovery Environment (XSEDE), which is supported by the National Science Foundation grant number ACI-1548562. This work used computational and storage services associated with the Hoffman2 Shared Cluster provided by UCLA Institute for Digital Research and Education's Research Technology Group.

Curriculum Vitae

Education

2014 -2018 B.S. (Chemical Eng.), The Pennsylvania State University, University Park, PA

2019-2021 M.S. (Chemical Eng.), The University of California, Los Angeles, CA

Awards

2023 UCLA Chemical & Biomolecular Engineering 4th Year Symposium Award

Publications at UCLA

1. C. A. Walenta, F. Xu, C. Tesvara, C. R. O'Connor, P. Sautet, C. M. Friend, Facile decomposition of organophosphonates by dual lewis sites on a Fe₃O₄(111) film. *Journal of Physical Chemistry. C./Journal of Physical Chemistry. C* **124**, 12432–12441 (2020).
2. C. Tesvara, C. Walenta, P. Sautet, Oxidative decomposition of dimethyl methylphosphonate on rutile TiO₂(110): the role of oxygen vacancies. *Physical Chemistry Chemical Physics/PCCP. Physical Chemistry Chemical Physics* **24**, 23402–23419 (2022).
3. C. Tesvara, C. J. Karwacki, P. Sautet, Decomposition of the toxic nerve agent Sarin on oxygen vacancy sites of rutile TiO₂(110). *Journal of Physical Chemistry. C./Journal of Physical Chemistry. C* **127**, 8006–8015 (2023).
4. C. Tesvara*, M. R. Yousuf*, M. Albrahim, D. Troya, A. Shrotri, E. Stavitski, A. M. Karim, P. Sautet, Unraveling the CO Oxidation Mechanism over Highly Dispersed Pt Single Atom on Anatase TiO₂ (101). *ACS Catalysis*, 7562–7575 (2024).
5. M. J. Bonney*, C. Tesvara*, P. Sautet, M. G. White, Understanding the decomposition of dimethyl methyl phosphonate on Metal-Modified TiO₂(110) surfaces using ensembles of product configurations. *ACS Applied Materials & Interfaces*, doi: 10.1021/acsami.4c01250 (2024).

* Equal co-first author

Chapter 1

Introduction

1.1. Motivation

The establishment of the Chemical Weapon Convention in April 1997 prohibits the signatory states of production and use of chemical weapons, and enforces the destruction of all chemical weapons, their precursors and production facilities. The United States is among the countries that ratified the Chemical Weapon Convention and has been actively putting efforts towards disposal and decontamination of CWA. However, the fact that not all countries have completed the weapon destruction of declared stockpile or have not ratified the convention, coupled with potential terrorist attacks remains a cause for concerns. An example of such grim event is the use of sarin gas in to inflict casualty amongst civilian in Syria¹, a country which had long been suspected to be in possession of sarin. Despite Syria declaring the materials to be destroyed in August of 2014, the famous Khan Shaykun chemical attack in April 2017 proved otherwise, killing 58 and wounding more than 300 people². Such attacks underscore the ongoing imperative to develop and provide effective decontamination catalysts, especially for the application of personal protective equipment, to ensure the safety of personnels and civilians.

Chemical Warfare Agents (CWAs) are extremely toxic chemicals that can inflict significant harms and even death. CWAs can be classified into nerve agents, blister agents, choking agents, blood agents, etc. depending on the target organs.³ Amongst all agents, nerve agents, in particular sarin, poses the most lethal (26 times more deadly than cyanide) and persisting harm (shelf life of weeks to months), as it can be easily employed in its gas phase making it the ideal chemical weapon for

war and terrorism⁴. Sarin is an organophosphorus compound with a P center, connected with an isopropoxy, a fluorine, a methyl group (**Figure 1.1**). Due to its toxicity, researchers usually substitute sarin with its simulant dimethyl methylphosphonate (DMMP). Sarin and DMMP both share the $O=P(OR_1)(X)(R_2)$ structure, where R1 and R2 are alkyl groups and X an electronegative monovalent substituent. In the case of sarin, R2 and X are an isopropoxy and a fluorine group whereas in the case of DMMP, both R2 and X are methoxy groups. The mechanism of action, and the natural decomposition pathways of Sarin alongside its fate in the environment have been thoroughly researched and accounted for in past literature reviews⁴⁻⁷. Conventional decontamination of sarin from gas phase consists of filters containing adsorbents with active materials such as silica gel, carbon or metal oxides (titania, alumina, etc.)⁸⁻¹¹. However, these measures do not disarm the toxicity of sarin, but merely trapping it before exposing it to the next phase of decontamination. Neutralization of these filtering equipment follows extreme measures such as pyrolysis, oxidation in high temperatures, or exposure to high PH conditions to induce the decomposition of the intact sarin^{9,12}. There are a few more downsides to this approach. Firstly, the filters work under limited time as they become inactive after complete saturation by the agents. Needless to say, that these filters pose significant risk to personnels during transport from point of contact/exposure to decontamination facilities. Extreme neutralization effort also degrades the filters and their effectiveness, making this process not environmentally friendly.

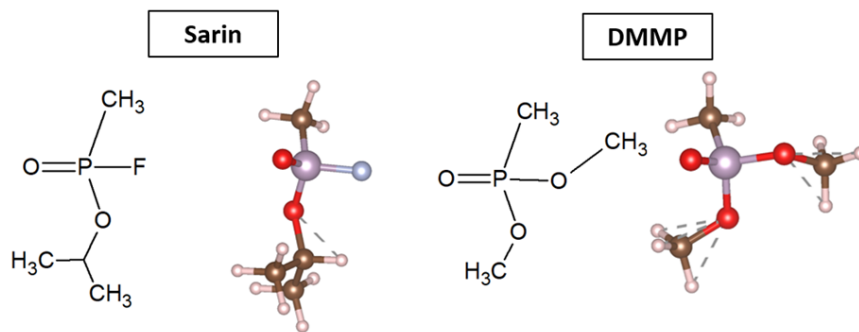


Figure 1. 1 Chemical structure of sarin and DMMP

Continual efforts to develop catalysts that can actively degrade sarin upon contact are ongoing, aiming to enhance the safety of personnel. One of such efforts is to embed the filters (in this study, metal oxides) with highly dispersed active catalyst that may induce decomposition in mild conditions. Particularly single atom catalysts (SAC) and highly dispersed nano clusters ($n < 13$) have amassed huge amounts of interest due to their newfound reactivity and promising solution for controlling the usage of highly precious (expensive) metal catalyst within the automotive industry. Combining the strong interactions between the metal oxides (filters) and the agents, with the reactivity of the highly dispersed catalyst to lower the activation barrier of the ‘trapped’ agents proposes an enticing solution for efficient CWA decontamination strategies. TiO_2 is one of the most extensively studied metal oxides in this context due to its large surface area and strong interaction with CWAs^{13–15}, including its widespread use in various applications and its high degree of understanding at the atomic level^{16–22}, making it an ideal as a trap for CWAs and support for SACs. Additionally titania often hosts various special surface structures, such as hydroxylation and defects, which have been found to act as a source of reactivity.

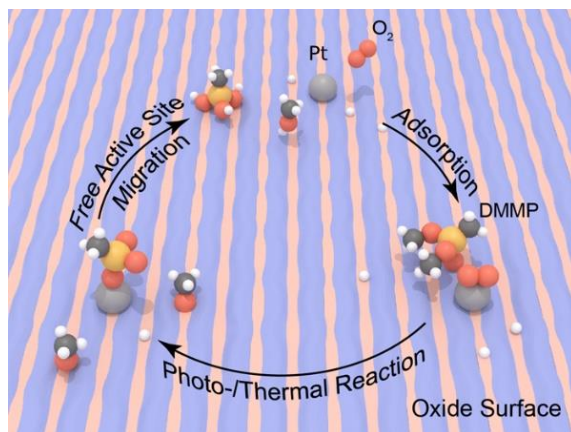


Figure 1. 2 Schematic of single atom catalyst supported on metal oxide for oxidative decomposition of DMMP

This chapter of the thesis will first focus on the current chemistries of sarin and DMMP on titania, followed by the development and use of state-of-the-art metal oxide supported highly dispersed catalyst, to finally various computational modeling techniques needed to holistically sample these highly dispersed catalysts, including its limitations.

1.2. Review on experimental (thermal) catalytic reactivity of sarin and DMMP on titania.

The most widely accepted mode of dissociation of GB on TiO_2 involves either the cleavage of P-O bond, transferring an OR alkoxy groups or the P-F bond, transferring a fluorine to the available Lewis acid sites (Ti^{4+}) on the surface. Both theoretical and experimental studies suggest that dissociation on the dry, clean surfaces of TiO_2 , both anatase and rutile are not exothermic and facile in general, particularly at room temperature. However, special deformation on the surface, oxygen vacancies, surface hydroxyls or alkaline promoters, have been hypothesized to promote decomposition by reducing activation energy barriers, triggering unique or coexisting decomposition mechanisms, or stabilizing dissociated products. Sarin decomposition on pristine,

defective (O vacancy) and hydroxylated anatase titania (α -TiO₂ (101)) has been studied using DFT and compared against DRIFTS measurements performed on P25 Degussa sample, containing mix of 17% rutile and 83% anatase phase of titania¹³. Experimentally, it was found that on room temperature, no significant signs of decomposition were observed. However, DFT calculations showed that hydroxylation and stepped surface may promote P-F bond elimination by lowering the activation barrier.

On rutile, a thermodynamic study by Quintero et. al. showed that sarin adsorption is dissociative by transferring F towards the surface Ti cation.²³ Reaction barriers were not calculated. However, a recent work using combined IR and DFT studies on UHV-dry rutile TiO₂(110) suggested that the first step of sarin decomposition most likely proceeds via propene elimination via O-C₃H₇ bond cleavages, with a barrier of 108 kJ/mol.¹³ A similar behavior is not observed, however in the experimental study using FTIR of partially hydrated surface performed in the dark by Hirakawa et.al., where production of isopropyl methyl phosphonic acid (IMPA) is shown along with changes in OH bands linked with the displacement of OH groups, suggesting P-F bond cleavage instead.²⁴ This further corroborate the findings on anatase, where hydroxyl facilitate the P-F bond cleavage. Particularly for rutile phase, past theoretical studies on titania have been focused only on the thermodynamic analysis or on the barrier for the first dissociation step and did not investigate further reaction steps nor studied the effect of oxygen vacancy. Nevertheless, past works suggest that the decomposition of sarin is inert without the intervention of defects, surface hydroxyls or elevated temperatures despite its strong interaction with the surface.

A deeper body of literature can be found with the study of sarin's non-toxic simulant, DMMP. Panayotov et al studied the thermal decomposition of DMMP on P25 Degussa titania sample using

infrared spectroscopy. Only at elevated temperatures, 295-400 K, particularly the $\nu(\text{P}=\text{O})$ modes at 1235 and 1215 cm^{-1} undergo a conversion into O-P-O groups, interacting with surface Ti sites with $\nu_a(\text{O}-\text{P}-\text{O})$ and $\nu_s(\text{O}-\text{P}-\text{O})$ modes at 1100-1097 and 1068 cm^{-1} , respectively.^{25,26} These decomposition modes, particularly at 400 K and above was attributed to the naturally occurring oxygen vacancies on the surface. However, this poses a question of whether DMMP is an accurate simulant to describe the chemistry of sarin, with the recent report showcasing the fluorine group of sarin being cleaved easily in the presence of water. Due to deeper research being done on DMMP to assess the efficiencies of filters/catalyst systems, it is crucial to compare and understand the true chemistries between sarin and DMMP.

Defects, such as oxygen vacancies or hydroxyls are known to modify DMMP decomposition pathways. FTIR studies on powder titania showed that the P-OCH₃ bond cleavage is facilitated by the presence of surface hydroxyls at temperatures starting from 214 K.²⁷ This is denoted by the shift of the P-CH₃ signal and a decrease of the surface O-H signal, and leads to the formation of adsorbed methyl phosphonic acid and possibly to the release of methanol.²⁶⁻²⁹ Another work on rutile TiO₂(110) showcase the barrier to cleave the P-O bond reduces from >2 eV to 1.4 eV³⁰. Reason behind this is the DMMP adsorbed on oxygen vacancies allows for penta-coordinated transition state prior to cleaving P-O bond, taking advantage the close distance between P center and the neighboring O_{2c} atom. It was further proved that the product formation at >500K consisting of methanol and formaldehyde could only result from a methoxy disproportionation reaction resulting from decomposed DMMP on defect sites.³¹ The behavior of DMMP adopting this penta-coordinated structure has been seen before in ZnO, zirconium hydroxide, and Zr-based metal-organic frameworks (MOFs) where DMMP is binds to surface hydroxyl groups to facilitate the release of methanol at room temperature.³²⁻³⁶ The influence of defects and different surface

morphology on the decomposition of DIMP has been observed as well. On alumina, the release of 2-propanol is observed, however on silica, the release of propene was observed instead.³⁷ To move from model molecules to real toxic nerve agents, it is important to also investigate if the reactivity of sarin with TiO₂ surfaces is similar to that of the simulant DMMP and whether a similar influence of oxide surface defects can take place with sarin decomposition chemistry.

1.3. Highly dispersed catalysts: Structure, Stability, and its relation to reactivity

In heterogeneous catalysis, the most important site of a catalyst is the exposed metals that are directly in contact with the gas reactant. As such, it makes sense to first understand the behavior of metal catalysts through the model study of defined termination of surfaces such as (111), (110), etc. However, this leaves the metal underneath the surfaces unused, and hence, inefficient. Reducing the size of the metal atoms to the extreme (single atoms and nanoparticles) helps with the inefficiency issue and various benefits, such as discrete states, unique bandgaps, and even metal support interactions that may improve reactivity. However, these benefits come but not without its drawbacks. This sub-chapter provides a short summary on supported single-atom and nanoparticles catalysts on titania.

1.3.1. Single atom catalyst

Single atom catalyst has been an emerging field of research in catalysis due to its promising performance and efficiency, as each atom is exposed and provides active sites during reactions. Perhaps one of the very first promising work of SAC is the synthesis of Pt SA supported on FeOx which showcase a high performance for CO oxidation (TOF of $138 \times 10^{-2} \text{ s}^{-1}$)³⁸. Despite its promising potential, challenges in the synthesis and stabilization remains, particularly in elevated

temperature and harsh reaction conditions.³⁹⁻⁴¹ A comprehensive investigation, employing a blend of experimental techniques (Fourier-transform infrared spectroscopy (FTIR), scanning transmission electron microscopy (STEM), and X-ray photoelectron spectroscopy (XPS)) alongside theoretical analysis (density functional theory (DFT)), was conducted on rhodium single-atom catalysts (SAC) supported on rutile TiO₂(110). The findings revealed the capability of rhodium to adjust its adsorption site and coordination in response to different gas pretreatment conditions.³⁰ Under oxidative conditions, rhodium (Rh) exhibits a tendency to replace the surface Ti_{5c} (five-fold coordinated titanium), while under reducing conditions, Rh tends to favor surface support rather than substituting titanium. A recent study conducted by DeRita and colleagues explored the deposition of platinum (Pt) as stable isolated atoms on anatase TiO₂ nanoparticles. The research demonstrated that Pt can be deposited in this form under various pretreatment conditions, including oxidative (heated to 300 °C in 100% O₂), mild reduction (heated to 250 °C in 10% H₂), and harsh reduction (heated to 450 °C in 10% H₂). Notably, the study revealed that the local coordination and oxidation/charge state of Pt single-atom species are influenced by these pretreatment conditions. This, in turn, affects the stability and activity of the supported Pt atoms. For instance, at 300 °C oxidation, Pt substitutes six-fold coordinated Ti, while at 250 °C reduction or 450 °C reduction, Pt forms adsorbed Pt(O₂) species or adsorbed Pt(OH) species, respectively; with the Pt remaining as isolated atoms.¹⁶ In another study, Thompson et al. showed that reduction pretreatment under CO induced the formation of supported Ir SA is on anatase; forming a gem-dicarbonyl ligand environment and binding to two lattice O from TiO₂. Under CO oxidation atmosphere, the Ir SA ligand environment changes where Ir is coordinated to one CO (monocarbonyl), one lattice O, and two other O from gas-phase O₂ dissociation.⁴²

As we have observed, reducing the number of active sites into a singular atom does not simplify the reaction at hand, but rather introduces a whole new degree of freedom in understanding the root of the catalytic activity of the system. The intricate dynamics of SAC during catalyst pretreatment and under operational conditions complicate the correlation between the catalytic activity for highly dispersed single atoms with the characterized/local geometric structure (resting state), if gleaned solely from experimental observations. This complexity is heightened by the difficulty in tracking the evolution of the local coordination of these isolated SAC species during oxidation, specifically through the reaction cycle, unless multiple intermediates can be captured experimentally. Furthermore, while there were studies where structural nuances of these isolated active sites (for example the work by DeRita on Pt single atom) and their responsive behavior to pretreatment conditions have been examined, the origins of their activity, the kinetics of their reactions, rate-determining intermediates, and comprehensive reaction pathways and mechanisms remain elusive. Unraveling these specifics is crucial for establishing guiding principles that will enable the future design of active and efficient Pt catalysts composed of isolated single atoms.

1.3.2. Nanoparticles

Nanoparticles (NPs) are garnering significant scientific interest due to their intriguing properties, different from their bulk counterparts. Past literature has shown improvement of catalytic activity due to the metal-oxide interaction, particularly the charge transfer phenomena. But also, like SAC, NP exhibit dynamic fluxionality driven by the reaction conditions. One would expect this since it is well understood that under realistic conditions, atoms constituting active sites are in constant motion, vibrating and diffusing due to temperature effects. Particularly at high reaction temperatures, it is evident that substantial restructuring and fluxionality are to be expected. This

poses several key challenges; unlike its metal counterparts with defined sets of active sites, the active sites undergo both structural transformations and variations in coverage. A few select examples are shown by the works of Geng et. al. on Cu_4O_x clusters supported on the amorphous alumina, which adopt various stoichiometries depending on the oxygen chemical potential present. This has a huge implication in our understanding of the reactive cluster state responsible for the reaction in the reaction conditions. It was found that in reaction conditions exist metastable states which are only 0.1-0.3 eV less stable than the global minima, which has reactive oxygen that allows for thermodynamic drive to perform oxidative propane dehydrogenation (difference in reactivity >1 eV). Considering the low barrier to restructuring, many of these metastable states are very much accessible and contributing to the overall reaction seen experimentally yet difficult to observe experimentally. In another study, the stability of Pt SA_3H_x cluster was studied for the activation of methane. Using global minimization methods (explain in later part of this chapter) and reaction condition selected as 400 °C and 0.5 bar of H_2 , it was found that Pt SA_3H_{26} is the most stable configuration. Despite so, around 19 metastable states were observed which are accessible in reaction condition. Select interesting structures which exhibit vacancies that create PtH_3 and PtH_4 coordination was found, and using the Boltzmann distribution it was found that the relative occurrence probabilities of these isomers of the catalyst are 5.1%, and 0.89% only with respect to the global minima. In typical experimental characterizations, the presence of these isomers is close to impossible to detect. These metastable states also contribute significantly to the overall reactivity, offering barrier for C-H activation of 0.6 eV, 0.4 eV less than the global minima. Despite their fluxionality, NP can act as surface modifier to enhance the reactivity of the support. Past work showcases NP being able to act as a proton source, donating electrons to the surface to facilitate the formation of defects, which in turn increases the activity of the said catalyst^{43,44} .

Thus, to understand the role of NP, one must be able to probe the accessible ‘state’ of the supported NP in reaction condition, to gain a full picture of the effects it has on the support. More importantly, it is key to probe these states in a way that can be correlated with experimental observation. Considering the short lifespan of these metastable states, it is difficult to characterize it experimentally as traditional spectroscopy techniques often produce unresolved spectra.

1.4. Modeling highly dispersed metal catalysts in realistic conditions

Due to the highly dynamic stability behavior and sensitivity towards reaction conditions, exploring all possible structures of highly dispersed metal catalysts in a comprehensive manner is a rather tricky process. As mentioned before, few techniques can be used to efficiently sample the potential energy surfaces. This section reviews briefly the basis theory for the global sampling method used in this thesis.

1.4.1. Ab initio Thermodynamics

While DFT allows for accurate calculation of the total energy of a system, it is ultimately important to achieve agreement with thermodynamics such that the effect of pressure and temperature can be considered while sampling the potential energy surface. This is especially important for a highly dispersed catalyst which is known to be very sensitive towards the reaction condition. The term ‘ab initio’ thermodynamic arises, namely a technique to apply the total energy obtained from first principle calculations to derive thermodynamic properties such as the Gibbs Free energy of formation. Using the assumption of ‘constrained equilibrium’, select species of a system (usually gas phase reactant) can be said to be in equilibrium with an arbitrary reservoir, matched to the experimental condition of steady state catalysis. Thus, the stability diagram as a function of

temperature and pressure can be built to determine the most stable structure at different reaction conditions.

The derivation of the thermodynamic properties of both the solid and the gas phase of a system has been thoroughly explained in Karsten et. al works. If we take an example of formation energy of Pt₂O_x supported on titania, at a given temperature T and partial pressure of reactant i, p_i , the Gibbs formation energy of the system can be described as

$$G_{formation} = E_{Surf+Pt_2.xO_{ad}} - E_{Surf} - 2E_{Pt(bulk)} - x \mu_O \quad (1-1)$$

With the chemical potential of the oxygen being described by

$$\mu_O(T, p) = \frac{1}{2}E_{O_2} + \frac{1}{2}E_{O_2}^{ZPE} + \Delta\mu_O(T, p^0) + \frac{1}{2}k_B T \ln\left(\frac{p}{p^0}\right) \quad (1-2)$$

Where x denoted the number of O adatoms adsorbing on the surface. We can see that the free energy of formation depends on the chemical potential of oxygen. Since the oxygen chemical potential is constructed as a function of temperature and pressure, one can construct a stability diagram by comparing the Gibbs free energy of various structures at realistic reaction conditions. Despite its simple formulation, this technique allows for better understanding of the stability of highly dispersed catalyst that may be difficult to probe even using state-of-the-art experimental spectroscopy, thus providing important insights into the role of SAC towards the decomposition of CWA.

1.4.2. Grand Canonical Basin Hopping

For single atoms interacting with gas phase species (N total atom less than 5), performing manual permutations and exploration is possible, and could be advantageous as one can construct ensemble that is based on a chemist's intuition. Unlike metal surfaces, the surface of titania is often decorated with kinks and trenches made of both Ti^{5+} and bridging oxygen. Having chemical intuition on where the metal atoms may systematically adsorb will accelerate the search process. However, as the number of adsorbed atoms increases, so is the configurational space (in exponential). Several algorithms to quickly sample accessible metastable states have been proposed to tackle this issue, ranging from Genetic Algorithm (GA) to Basin Hopping. In understanding the stability of highly dispersed and reactive nanoclusters, it is advantageous to use the so called Grand Canonical Basin Hopping algorithm, as it allows for sampling method that can be highly personalized towards the system by while incorporating thermodynamic information at the same time.

The grand canonical basin-hopping algorithm was first introduced by Calvo et. al. In this algorithm, Calvo proposed a grand canonical based algorithm to evaluate the free energy of the system on the fly during global optimization while at the same time incorporating modifiers to sample the stability of system with different size and composition. In the grand canonical ensemble, the volume, temperature T , and chemical potential of the gas reservoir μ are fixed, whereas the energy and number of particles, N , can fluctuate, hence one can optimize the size and composition of the catalyst of interest as a function of chemical potential of the gas phase reservoir and temperatures.

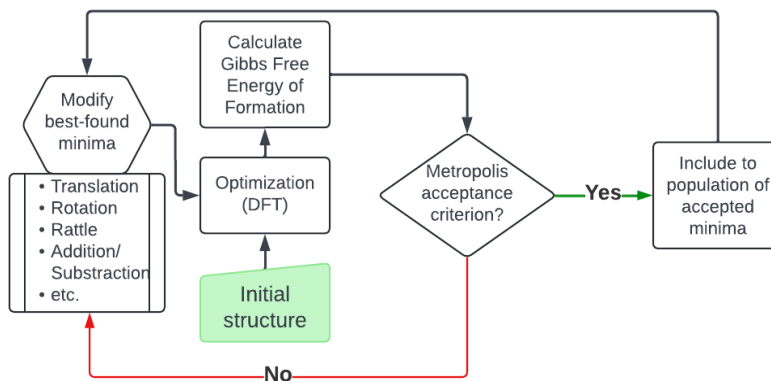


Figure 1. 3 Schematic of Grand Canonical Basin Hopping algorithm.

The algorithm is illustrated in **Figure 1.3**. In Basin Hopping, the potential energy surface is explored by hopping from one local minimum of the potential energy surface to another. These hops involve a set of randomly chosen ‘modifier’, set by the user, which could consist of randomly moving one or more atoms, or all atoms, in the system to new positions, followed by a local geometry optimization. The acceptance or rejection of each new structure is determined by an acceptance criterion of a calculated property (for example the Gibbs Free energy of formation), typically using the Metropolis criterion, although other acceptance schemes such as threshold acceptance and Tsallis statistics have been proposed. This thesis utilizes an in-house code, developed using the Atomic Simulation Environment (ASE) package, to conduct GCBH explorations. These explorations simultaneously explore the configuration and composition space to minimize the free energy (or formation energy) of the system in question, typically a supported metal cluster under the specific oxidation condition/fixed oxygen chemical potential. This method has been proved to be effective in exploring ensemble of accessible metastable states in various reaction conditions and systems as this method allows for customized modifiers that can be fine tuned for each specific systems.⁴⁵⁻⁵¹

1.5. Thesis Objectives

This thesis aims to understand the potential of highly dispersed single atom catalyst or nanocluster deposited on titania to facilitate the decomposition of sarin and its simulant DMMP at low temperatures. This thesis will be divided into 6 chapters, where chapter 2 discusses the baseline reactivity of sarin and DMMP with undoped pristine titania on rutile alongside the effect of the presence of oxygen vacancies, as well as comparing it with anatase. Chapter 3 will delve into the intricacies of the stability of single atoms deposited on anatase titania and understanding its oxidative abilities using CO as probe molecules. Microkinetic analysis will be employed to elucidate the highly convoluted reaction pathways of a seemingly simple reaction such as CO and the role that the Pt plays in activating CO and O₂. Chapter 4 would also discuss Pt SA for the decomposition of the OR group of sarin and DMMP. Chapter 5 will focus on the role of highly dispersed Cu₄ cluster in a highly controlled UHV environment towards the decomposition of DMMP. Soft landed Cu₄ cluster with and without alkaline promoter potassium on rutile TiO₂(110) was found to facilitate the decomposition of DMMP in highly controlled environments. Lastly, chapter 6 will discuss the exploration of the stability of highly dispersed Pt cluster in oxidative condition and how it alters the surface. Exhaustive sampling of accessible metastable states will be performed with GCBH, and we showcase the role of Pt of activating O₂ to facilitate decomposition of sarin & DMMP using methanol dehydrogenation as a probe reaction.

Chapter 2

Decomposition of the Toxic Nerve Agent Sarin on Oxygen Vacancy

Sites of Rutile TiO₂(110)

2.1. Introduction

One of the most used and dangerous chemical warfare agents (CWAs) is the nerve gas agent sarin (commonly referred to as GB), with its prevalent use dating back from the first world war, and more recently for terrorist attacks.⁴ However there is a lack of understanding of the molecular interaction and decomposition mechanisms of sarin on different types of materials, which poses a critical challenge in practical applications toward the neutralization of CWAs.

Metal oxides are often the customary material chosen as the base material for protective equipment as they are efficient in trapping pollutants, present high surface areas, and are chemically stable.⁵²⁻
⁵⁴ The ideal metal oxide should be able to strongly adsorb CWAs and simultaneously decompose CWAs under ambient conditions, transforming them into benign compounds. To understand the interaction of such CWAs with oxide surfaces, most experimental studies substitute CWAs with simulants. Accordingly, experimental studies regarding sarin on metal oxides often replace sarin with dimethyl methylphosphonate (DMMP). The basis of this choice lies in the similarities of chemical structures between sarin and DMMP. It is unclear however if DMMP is a good simulant of sarin for the decomposition chemistry at oxide surfaces.

Past works have shown that the decomposition of DMMP is indeed sensitive to the type of metal oxide used, and the presence of defects and contaminants. FTIR studies showed that aluminum

oxide, magnesium, and lanthanum oxides are able to cleave the P-OCH₃ bond of DMMP at room temperature, and in the case of Fe₂O₃, Fe₃O₄, and CeO₂ activation of the P-CH₃ bond to produce dimethyl ether are also observed.⁵⁵⁻⁶⁰ In the case of ceria, the formation of product (methanol and formaldehyde) can only be seen above 575K, signaling decomposition via P-OCH₃ between 300 to 550K.⁵⁶ On the other hand, combined experimental and theoretical studies showed that in the case of rutile-phased oxides in ultra-high vacuum conditions such as SnO₂ and TiO₂, the decomposition of DMMP via P-OCH₃ bond cleavage have considerably high barriers, and thus decomposition may be initiated via O-CH₃ bond cleavage instead.^{31,61} Similar phenomenon occurs for the decomposition of another sarin surrogate, diisopropyl methylphosphonate, on alumina. Ab Initio Molecular Dynamics predicted that decomposition via the O-C bond cleavage would lead to a release of propene at high temperatures (700-1000 K).⁶² Experimental studies combining X-ray photoelectron spectroscopy and temperature-programmed desorption of DMMP decomposition on rutile TiO₂ (110) under ultra-high vacuum show a broad signal for intact DMMP desorption and suggest low reactivity of TiO₂ up to 550 K.⁶³

Defects, such as oxygen vacancies or hydroxyls are known to modify DMMP decomposition pathways. FTIR studies on powder titania showed that the P-OCH₃ bond cleavage is facilitated by the presence of surface hydroxyls at temperatures starting from 214 K.²⁷ This is denoted by the shift of the P-CH₃ signal and a decrease of the surface O-H signal, and leads to the formation of adsorbed methyl phosphonic acid and possibly to the release of methanol.²⁶⁻²⁹ This is similar to the behavior of DMMP observed on ZnO, zirconium hydroxide, and Zr-based metal-organic frameworks (MOFs) where DMMP is transformed into penta-coordinated phosphor-center intermediate by surface hydroxyl groups prior to the release of methanol at room temperature.³²⁻

³⁶ Our previous work on rutile TiO₂(110) also showed the effect of oxygen vacancies in facilitating

the P-OCH₃ bond cleavage, reducing its barrier from >2 eV to 1.4 eV and rendering the process possible at 600K. It was also found that the product formation (methanol and formaldehyde) could only result from a methoxy disproportionation reaction resulting from decomposed DMMP on defect sites.³¹ The influence of defects and different surface morphology on the decomposition of DMMP has been observed as well. On alumina, the release of 2-propanol is observed, however on silica, the release of propene was observed instead.³⁷ To move from model molecules to real toxic nerve agents, it is important to also investigate if the reactivity of sarin with TiO₂ surfaces is similar to that of the simulant DMMP and whether a similar influence of oxide surface defects can take place with sarin decomposition chemistry.

Experimental studies on sarin are rare, but the decomposition chemistry of sarin has been the subject of theoretical investigations. Cluster studies on MgO showed that the cleavage of the P-F bond has a barrier of 0.95 eV and that the fluorine ion stayed on the cluster. However, the presence of surface hydroxyl groups may reduce the barrier to 0.43 eV, resulting in the release of HF.⁶⁴ A combined XPS and DFT work on MoO₂(110) showed that the decomposition of sarin most likely proceeds via the elimination of propene, with surprisingly low barriers around 54 kJ/mol, in contrast to the case of DMMP where the lowest barrier is calculated to 116 kJ/mol on the same surface.⁶⁵ Additional work on ZnO hints at the possibility of different decomposition reactivity between sarin and DMMP as the barrier to cleave the P-OR bond of DMMP on ZnO was found to be 1.77 eV, 0.6 eV higher than the barrier to cleave the P-F bond of sarin on pristine ZnO, which is 1.17 eV.^{32,66} On titania, a thermodynamic study by Quintero et. al. showed that sarin adsorption is dissociative by transferring F towards the surface Ti cation, which would be analogous to DMMP's P-OCH₃ bond cleavage.²³ Reaction barriers were not calculated. However, a recent work using combined IR and DFT studies on UHV-dry rutile TiO₂(110) suggested that the first step of

sarin decomposition most likely proceeds via propene elimination via O-C₃H₇ bond cleavages, with a barrier of 108 kJ/mol.¹³ A similar behavior is not observed, however in the experimental study using FTIR of partially hydrated surface performed in the dark by Hirakawa et.al., where production of isopropyl methyl phosphonic acid (IMPA) is shown along with changes in OH bands linked with the displacement of OH groups, suggesting P-F bond cleavage instead.²⁴ On alumina, both processes (propene formation and P-F bond cleavage) are deemed to be possible; the experimental IR work of Kuiper et.al. suggests two decomposition channels of sarin, via a P-F bond cleavage or the dealkylation to produce propene.⁶⁷ To the best of our knowledge, past theoretical studies on titania have been focused only on the thermodynamic analysis or on the barrier for the first dissociation step and did not investigate further reaction steps nor studied the effect of oxygen vacancy.

Finally, despite the fact that DMMP is structurally similar to sarin, it is still now an open question whether DMMP can accurately depict the decomposition chemistry of sarin due to the difference in chemical groups (methoxy on DMMP vs -F and -OC₃H₇ on sarin). Thus, in this study, we will focus on investigating the decomposition pathways of sarin on rutile TiO₂(110) from quantum chemical calculations and compare these pathways with our previous work on DMMP decomposition on the same surface.³¹ TiO₂ was chosen as it has been suggested as a promising material to quickly adsorb toxic agents and their degradation products. This can be seen by the strong adsorption energies of DMMP on dry rutile TiO₂(110), found in previous works.^{23,68-72} Our work here aims not only to provide full and detailed decomposition studies of sarin on titanium oxide but also to serve as a benchmark comparison of the difference between sarin and DMMP decomposition on titania. Additionally, we will also investigate the effect of surface oxygen vacancy on the sarin decomposition pathways, in comparison with DMMP, and link our

computational results with vibrational spectroscopy experiments through vibrational frequency calculations.

2.2. Methods

2.2.1. Computational Set-up

The density functional theory calculations were done using the Vienna Ab initio Simulation Package (VASP).^{73,74} The Perdew-Burke-Ernzerhof (PBE) functional was used with Hubbard U correction of 4.2 eV on Ti sites to adjust the incorrect description of Ti 3d orbitals.^{75,76} The U value 4.2 eV was taken as it correctly depicts the electronic structure features observed experimentally with TiO₂, particularly the localized nature of electrons on surfaces with oxygen vacancies.⁷⁷ The dDsC dispersion correction was used to describe long-range van der Waals interactions.⁷⁸⁻⁸⁰ The electron kinetic energy cutoff is set at 500 eV.⁸¹⁻⁸³ The electronic energies and atomic forces were converged within 10⁻⁶ eV and 0.03 eV/Å, respectively. The spurious dipole-dipole interaction between neighboring slabs in the z-direction was corrected using the Harris correction (Makov-Payne).⁸⁴

The transition states were calculated using the Nudged Elastic Band Method using 8 images.

The adsorption energies/reaction pathway energies are calculated with equation 1:

$$E_{ads/intermediate} = E_{surf+DMMP} - E_{clean\ surface} - E_{Sarin(g)} \quad (2-1)$$

2.2.2. Computational Model

The 2x4 TiO₂(110) surface was cut from the bulk. The calculated bulk lattice constants using a gamma-centered k-points mesh of 4x4x4 are: $a = 4.65 \text{ \AA}$ and $c = 3.02 \text{ \AA}$ ⁸⁵⁻⁸⁷ The surface lattice vectors are: $a = 13.16 \text{ \AA}$ and $b = 12.07 \text{ \AA}$ (Figure A.1). The surface consists of four O-Ti-O trilayers (12 atomic layers). A vacuum distance of 15 Å is set between slabs to avoid periodic interaction in the z-direction. The bottom-most three atomic layers are frozen to mimic the bulk. To model the defective surface, one oxygen atom in the bridging site (O_{2c}) was removed (Figure A.2) as it was found to be the most stable vacancy site.⁸⁸⁻⁹⁰ The removal of 1 O_{2c} represents a vacancy site coverage of 0.125 ML, which agrees well with the experimentally observed vacancy coverage of r-TiO₂(110) crystals (between 0.08 to 0.15 ML)⁹¹⁻⁹³. All surface calculations use the k-point mesh of 1x1x1. Literature and our test calculations³¹ showed that using a k-points mesh of 3x3x1, larger surface or thicker surface models show no significant difference compared to our selected 2x4 surface calculated at the gamma point.³¹

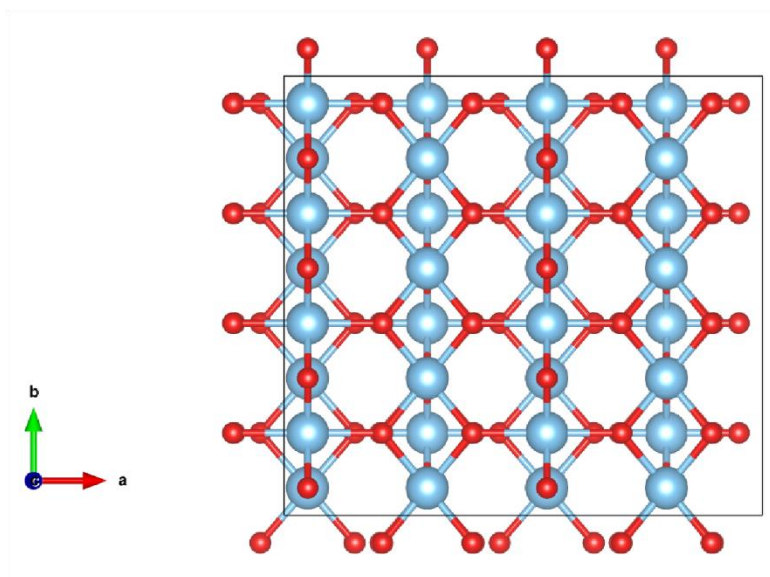


Figure 2. 1 Top view of 2x4 rutile TiO₂(110) used for optimization. The surface consist of 2 Ti_{sc} rows and 2 O_{2c} rows.

2.3. Results

2.3.1. Pristine surface

The most stable sarin adsorption geometries on pristine $\text{TiO}_2(110)$ from our DFT calculations can be seen in Figure 2.2. Sarin adsorbs molecularly via the interaction between the O atom of the P=O group and a surface Ti cation (distance 2.09 Å) with an adsorption energy of -1.80 eV (Figure 2.2A). An additional bond either between the oxygen of sarin's isopropoxy group and a surface Ti (2.60 Å) or fluorine with Ti (2.59 Å) further stabilizes the geometry with total adsorption energies of -1.92 and -1.94 eV respectively (Figure 2. 2 B and C). Finally, the adsorption geometry via the interactions of -F or $-\text{OC}_3\text{H}_7$ group with surface Ti atoms (with distances of 2.40 Å and 2.51 Å respectively) yields the weakest adsorption energy of -1.13 eV (Figure 2. 2, D). Overall, our calculations showed that $\text{TiO}_2(110)$ is an excellent trap for sarin due to the strong molecular binding. The adsorption energy of sarin is however significantly weaker than that of its simulant DMMP (by 0.41 eV).

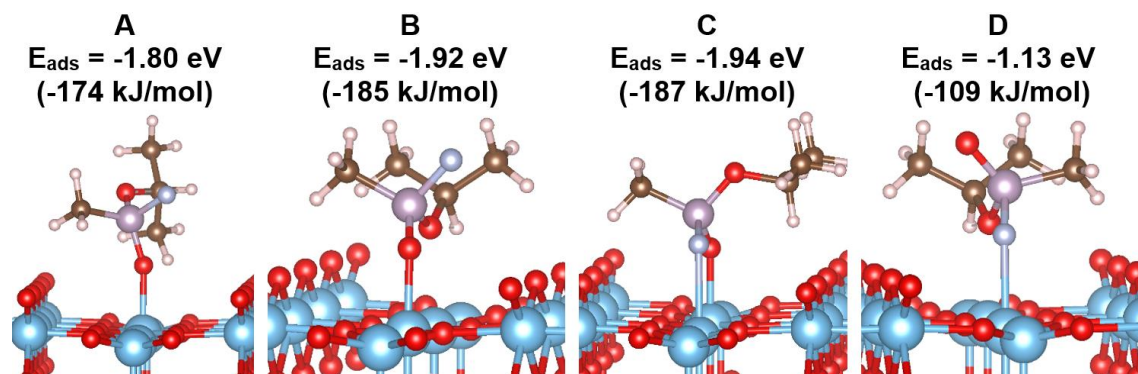


Figure 2. 2 Molecular adsorption modes of sarin on $\text{TiO}_2(110)$ with their adsorption energies referenced to the gas phase.

The decomposition pathway initiated via the P-OC₃H₇ cleavage starts from geometry B of Figure 2. 2 and follows the B1-B3 pathway, whereas the pathway initiated via the P-F bond cleavage starts from geometry C of Figure 2. 2 and follows the C1-C2 pathway. Note that B1 is identical to B and C1 identical to C. The cleavage of either the P-OC₃H₇ or the P-F bond has significantly high barriers, P-F being the least difficult bond to break (2.27 eV and 1.77 eV respectively). The P-OC₃H₇ bond cleavage transfers an isopropoxy towards a Ti_{5c} site and yields the B2 intermediate. B2 is more stable by 0.64 eV than the molecularly adsorbed sarin B1. On the other hand, the P-F bond cleavage to leave F on Ti_{5c} yields intermediate C2 which is 0.96 eV more stable than C1. A similar behavior persists for the second decomposition step (TS-B2 and TS-C2), where we can see that the P-F bond is easier to cleave than the P-OC₃H₇ bond, although both bond cleavages still have considerably high barriers (1.53 and 1.67 eV respectively). We conclude that decomposition is unlikely to happen via the P-F or the P-OC₃H₇ bond cleavage on the pristine surface, unless at high temperature.

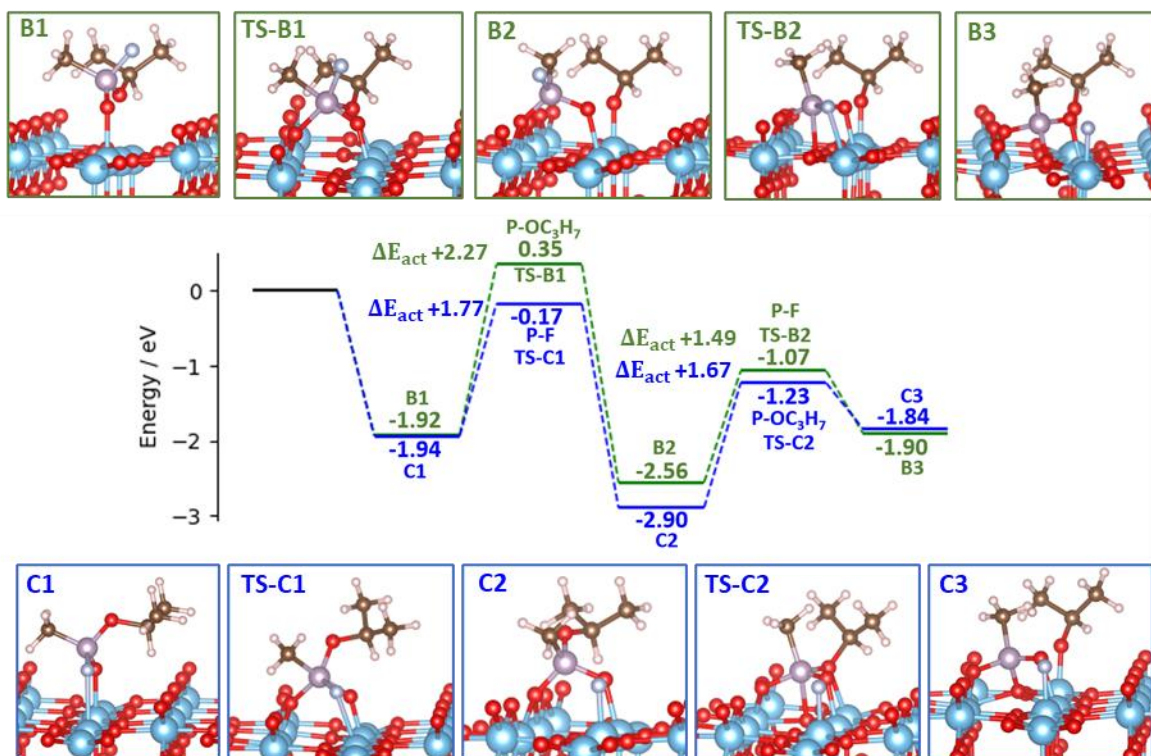


Figure 2. 3 The energy profile of sarin decomposition on pristine $r\text{-TiO}_2$ via P-F and $\text{P-OC}_3\text{H}_7$ bond cleavage starting from the two most stable adsorption modes (adsorption modes B and C). The decomposition via $\text{P-OC}_3\text{H}_7$ cleavage is shown in the path B1-B3 whereas the P-F bond cleavage occurs along the path C1-C3. Elementary reaction barriers are indicated as ΔE_{act} .

On the other hand, decomposition via the $\text{O-C}_3\text{H}_7$ bond cleavage, transferring C_3H_7 towards a nearby O_{2c} is more likely (Figure 2. 4). The barrier for this step stood at 1.17 eV, rendering it a possible pathway at 455 K (via Transition State Theory). Further P-F bond cleavage as the second step also has a comparable low barrier of 1.00 eV. It is interesting to note that the removal of C_3H_7 reduces the barrier to cleave the P-F bond, compared to the case in Figure 2. 3. However, the release of products such as HF and propene does not seem to be possible at low temperatures (Figure 2. 4, intermediate C4*) as the barrier for C-H cleavage to form propene is 1.60 eV, which requires temperatures around ~ 610 K to overcome. Note that at any point during the decomposition

pathway, the P-containing intermediate may rearrange to a more stable configuration. We see such a case here where from C2* after O-C bond cleavage, the IMPA-like intermediate can rearrange first to an η_1 structure and be stabilized as an η_2 structure (C2* η_2), maximizing the P-O-Ti interactions. This rearrangement of the C2* intermediate competes with the P-F bond cleavage. We will now investigate the effect of O vacancies on the surface toward the barriers associated with either P-F, P-OC₃H₇, or O-C₃H₇ bond cleavage.

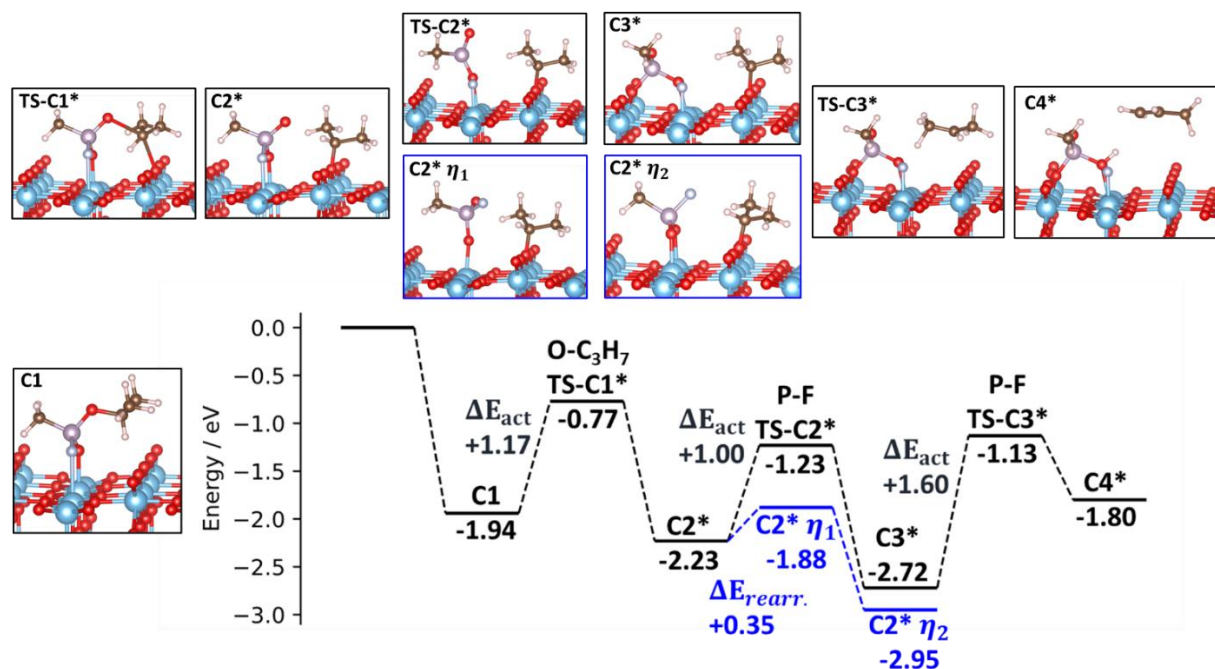


Figure 2. 4 The energy profile of sarin decomposition on pristine *r*-TiO₂ via C-O bond cleavage starting from the two most stable adsorption modes C.

2.3.2. The effect of O vacancy

With the presence of an oxygen vacancy site, the most stable molecular sarin adsorption geometries involve the P=O group occupying the vacancy site (Figure 2. 5) with two possible isomers depending on which group interacts with Ti_{5c} (geometry E and F). In geometry E, in addition to P=O occupying the vacancy, there is a stabilizing interaction from a F-Ti_{5c} interaction. This

geometry has an adsorption energy of -1.95 eV. Similarly, with geometry F, there is an additional interaction between the oxygen of the isopropoxy substituent and a surface Ti_{5c} , bringing the adsorption energy to -2.20 eV, which is the most stable configuration found. Further sarin decomposition initiated via P-F and O-C bond cleavage may follow geometry E, whereas decomposition initiated with P-OR bond cleavage may follow geometry F.

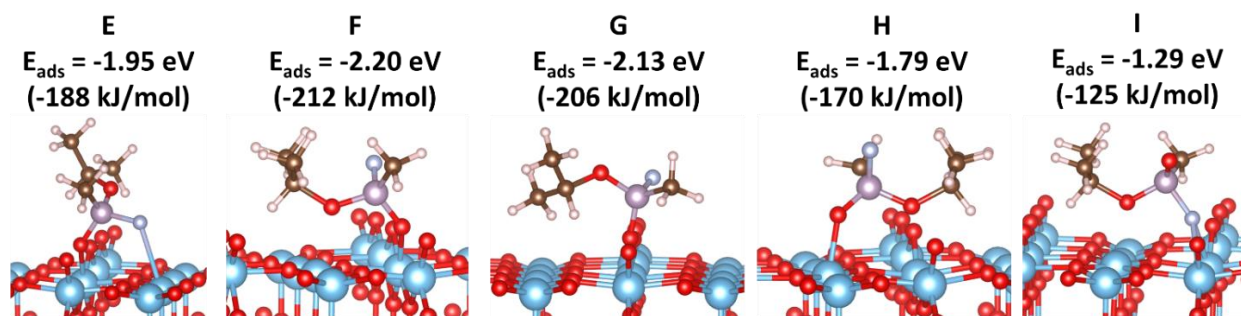


Figure 2. 5 Sarin adsorption modes on the $r-TiO_2$ surface with an O vacancy.

Figure 2. 6 shows the reaction pathway for O- C_3H_7 (E1-E2-E3) or P-F (E1-E4) bond cleavage starting from geometry E (E1=E). Since geometry F=F1 is more stable, it has also been included in the diagram, as the resting state of the molecule, and for the first step overall activation energies starting from F is indicated in the Figure 2. 6. The barrier to cleave the O- C_3H_7 bond from E1 is 1.4 eV (1.65 eV from F), which is higher than the case on the pristine surface (1.17 eV) and yields a stable intermediate E2 at -2.43 eV. Further P-F bond cleavage (E2-E3) as the second step is also exothermic by 0.35 eV (E3) with a barrier of 1.25 eV. Interestingly if we opt to first cleave the P-F bond (E1-E4), the barrier for this step is now greatly reduced from 1.77 eV (on the pristine surface) to only 0.85 eV from E1 (1.1 eV from F1). This process yields an intermediate E4 which is 0.79 eV more stable than the molecularly adsorbed sarin. Though further decomposition to cleave the P-OR bond from E4 is endothermic by 0.68 eV (not shown in Figure 2. 6), the intermediate may undergo C-H bond cleavage instead to produce gas phase propene. The barrier

to release propene is 1.53 eV and the reaction is slightly exothermic by 0.16 eV (E4-E5). This pathway shows that the O vacancy defect facilitates the P-F bond cleavage and enables it at a temperature as low as 425 K, even if starting from the most stable structure F (compared to 675K on the pristine surface, see table S1 and S3 in the SI).

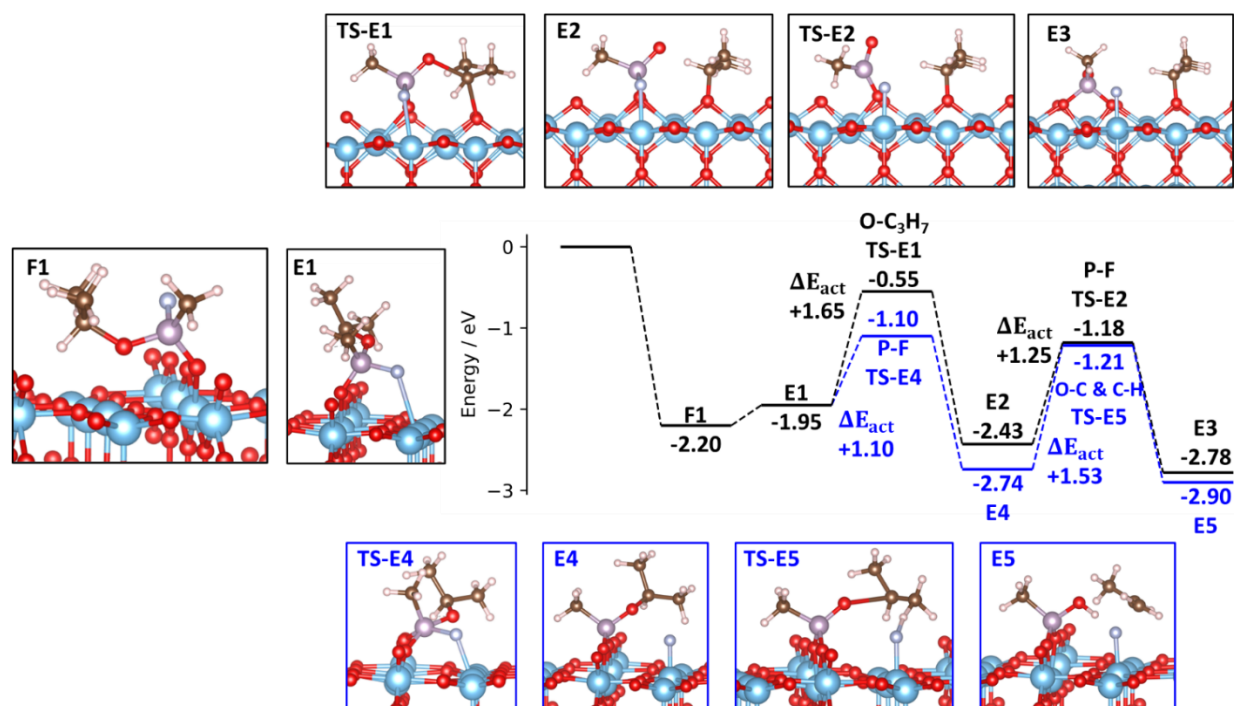


Figure 2. 6 Sarin decomposition on the *r*-TiO₂ (110) surface with an O vacancy initiated via P-F (blue) or O-C (black) bond cleavage. The decomposition starts from Sarin's most stable adsorption mode (intermediate F here is written as F1, the numbering is to denote

A similar barrier decrease can also be seen for the decomposition initiated with the P-OR bond cleavage from geometry F (Figure 2. 7). Oxygen vacancies reduce the barrier to cleave the P-OR bond from 2.27 eV (pristine surface) to 1.05 eV (defective surface), and this cleavage can occur at 410K (table S3 in SI). The P-OC₃H₇ bond cleavage transition state shows a hexa-coordinated P atom, with an extra P-O bond involving a three-fold O atom on TiO₂, trans to the P-F bond. This

additional P-O interaction stabilizes the transition state and is not present in the initial state F1 nor in the product state F2 of that elementary step. The following step to cleave the P-F bond remains relatively more facile in comparison to the case of pristine surface as well with a barrier of 1.01 eV.

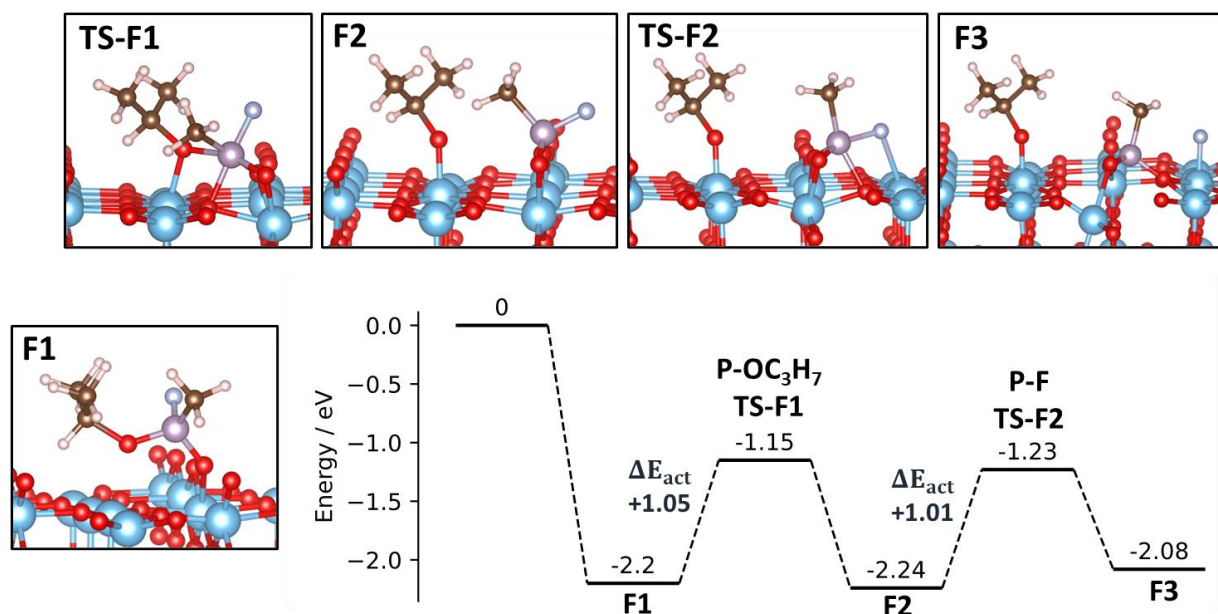


Figure 2. 7 Sarin decomposition pathway on the *r*-TiO₂ (110) surface with an O vacancy initiated via P-OR (R= isopropyl) bond cleavage. The sarin initial adsorption geometry is structure F = F1.

2.3.3. Vibrational analysis

To strengthen the interaction with experimental observation on the nature of adsorbed sarin and decomposition intermediates, vibrational analysis calculations were performed on the molecularly adsorbed species and selected intermediates which are accessible at 500 K from our pathways (following previous experimental work by Tsyshevsky et.al.¹³). However, it is known that the PBE functional tends to underestimate frequencies in comparison to the experiment. A work by Le et. al. comparing experimental and theoretical frequencies for sarin adsorbed intact on anatase

TiO₂(101) suggested that PBE underestimates sarin characteristic modes by 60 cm⁻¹ in comparison to experimental observation.⁹⁴ In order to better understand the intrinsic error on frequencies from our first principle calculations, IR frequencies for gas phase sarin were calculated with the DFT PBE-dDsC functional as a benchmark and compared with the experimental result (Table 1). In comparison to the experiment, PBE-dDsC underestimates IR frequencies by ~ 50 cm⁻¹. This value is used here as a correction shift term when comparing the frequencies of the molecularly adsorbed sarin and the intermediates obtained after thermal treatment.

Table 2. 1 Experimental and calculated vibrational frequencies for gas phase sarin. Experimental data is from ref¹³.

IR band assignment	GB vapor phase (exp.)	GB vapor phase (theory)	Δ
v(P–O)	1303	1250	-53
v(C–O–(P))	1020	978	-42
v(P–F)	845	792	-53
δ (P–CH ₃)	1328	1285	-43

Table 2 shows the characteristic IR frequencies for molecularly adsorbed sarin prior to the thermal decomposition treatment. The four best geometries of molecularly adsorbed sarin were chosen to represent the ensemble of surface species (on the pristine surface, structures A, B, and C from Figure 2. 2, on the defective surface with O vacancies, structures E and F from Figure 2. 5). Corrected values (shown in parenthesis in table 2) show good agreement with experimental observation. The ensemble of frequencies observed experimentally in the range 1271-1200 cm⁻¹ can be assigned to the P=O bond stretch, more or less weakened by the interaction with surface Ti (dative bond P=O-Ti) compared to the gas phase species. Such frequencies are seen for the chemisorption structures on the pristine surface, structures A, B, and C, wherein A sarin is

interacting with the surface with only one P=O-Ti bond while in B and C, an additional P-OPr-Ti or P-F-Ti interaction is created. The modes associated with these frequencies are not purely located on the P-O bond but show small couplings with deformations on other ligands of P. For C, which is the most stable chemisorption structure, one mode is lowered to 1125 cm⁻¹ and can be described as a P=O stretch, coupled with the O of the alkoxy ligand in a symmetric (O-P-O) stretch modes, which is seen in the experiment. Adsorption modes on defective surface E and F (P=O occupies an O vacancy with either F or O-Pr interacting with Ti) also show similar (O-P-O) stretch modes. Amongst all structures, these calculated (O-P-O) stretching modes at 1125-1173 cm⁻¹ are slightly overestimated in comparison with the experimental peak assigned to (O-P-O) at 1090-1145. All sarin adsorption configurations possess the (C-O-(P)) stretch modes and the (P-CH₃) seen experimentally, with significant weakening of the frequency for geometry B and F. Note that the experiment was performed on a powder P25 sample which contains a mixture of anatase and rutile phase of titania. Vibrational modes on the anatase phase of the sample might differ somewhat and are not included in the calculation.

Table 2. 2 IR band assignment comparison between sarin adsorption experiments at room temperature (ref 13) and theoretical frequencies for molecularly adsorbed sarin. Corrected frequencies are shown in parentheses. *Data unavailable in reference.

IR band assignment	exp	Molecularly adsorbed				
		theory (A)	theory (B)	theory (C)	theory (E)	theory (F)
$\nu(\text{P-O})$	1271-1200	1180, 1190 (1230, 1240)	1171, 1167 (1221, 1217)	1159 (1209)		
$\nu_s(\text{O-P-O})$	1090			1075 (1125)		
$\nu_{as}(\text{O-P-O})$	1145				1116 (1156)	1123 (1173)

$\nu(\text{C-O-P})$	1038	1007 (1057)	921, 917 (971, 967)	998 (1048)	1033 (1083)	924 (974)
$\nu(\text{P-F})$	*	836 (886)	836 (886)	727 (777)	819 (869)	845 (895)
$\delta(\text{P-CH}_3)$	1320	1298 (1348)	1296 (1346)	1299 (1349)	1291 (1341)	1293 (1341)

Table 2.3 shows the characteristic IR frequencies for decomposed sarin after thermal treatment. Experiment at 500 K shows a decrease of intensity for the modes in the region 1271-1200 cm^{-1} , an increase in the broad region 1200-900 cm^{-1} , mainly at 1145-1135 and 1095-1075 cm^{-1} , and a decrease at 1038 cm^{-1} . From the calculated reaction profiles, on the pristine surface, the most abundant decomposition intermediate should be $\text{C2}^*\eta_2$ (Figure 2. 4), where the sarin O-C bond is cleaved, followed by a rearrangement to form two Ti-O-P interactions. Consistently with the experiment, no mode occurs in the 1271-1200 cm^{-1} region, while O-P-O stretching modes arise at 1114 and 1088 cm^{-1} , associated with the Ti-O-P-O-Ti linkage formed in $\text{C2}^*\eta_2$. Since the O-C bond is cleaved, no mode occurs at 1038 cm^{-1} (where the C-O-(P) stretching mode of chemisorbed sarin was). The vacancy defects pose a challenge to IR spectroscopy because of their low concentration. The most abundant intermediate after decomposition on the defective surface should be the intermediate E4, following sarin P-F bond cleavage. The release of propene from this intermediate is not accessible at 500 K. This intermediate is similar to IMPA and has three P-O bonds, two with the surface (one of them corresponds to the filling of the vacancy by the oxo (P=O) of sarin), hence generating three modes. One of them occurs at 1132 cm^{-1} , close the 1145-1135 cm^{-1} enhanced region in the experimental spectrum. The other two (1029, 1054 cm^{-1}) are lower. The C-O-(P) stretch is present but it is shifted to 1073 cm^{-1} , which is close to the experimental IR band peak assigned to O-P-O stretching, hence compatible with the decrease in the experiment around 1038 cm^{-1} , initial value of the C-O-(P) stretch in intact chemisorbed sarin.

Table 2. 3 IR band assignment comparison of decomposed sarin after heating to 500 K between the experiment and theory. A negative sign (-) indicates disappearing bands and a positive sign (+) indicates increasing bands.

IR band assignment	Heated to 500 K		
	exp	theory (C2* η_2)	theory (E4)
$\nu(\text{P-O})$	1271-1200 (-)		
$\nu_s(\text{O-P-O})$	1095-1075 (+)	1038 (1088)	1082(1132)
$\nu_{as}(\text{O-P-O})$	1145-1135 (+)	1064 (1114)	994, 979 (1054, 1029)
$\nu(\text{C-O-P})$	1038 (-)		1023 (1073)
$\nu(\text{P-F})$	*	821 (871)	
$\delta(\text{P-CH}_3)$	1310	1294 (1344)	1278 (1328)

Therefore, the calculated vibrational frequencies validate the surface species obtained with our total energy calculations, with an ensemble of sarin chemisorbed structures at low temperatures, and intermediates of decomposition from C-O or P-F bond cleavage after thermal treatment.

2.3.4. Discussion

The complete decomposition pathways of sarin on the pristine and defective surface of rutile $\text{TiO}_2(110)$ have been investigated via DFT calculations. On the pristine surface, the most stable sarin adsorption geometries involve the dative $\text{P=O} \cdots \text{Ti}_{5c}$ bond, with an additional stabilizing interaction from either the isopropoxy or fluorine groups, with adsorption energies of -1.92 eV (-185 kJ/mol) or -1.94 eV (-187 kJ/mol), respectively. Our results agree very well with the data for other rutile metal oxides. The adsorption of sarin has previously been theoretically studied on

MoO₂(110) where the most stable structure found is identical to that of structure C (P=O-Ti and F-Ti binding modes) in Figure 2. 2, with a stronger adsorption energy of -229 kJ/mol.⁶⁵ The differences in adsorption energies may be attributed to the difference in surface cation acidity between titania and molybdenum. Additionally, our result agrees well with the work of Quintero et al. on rutile TiO₂ (sarin adsorption of -178 kJ/mol vs -187 kJ/mol). A slight difference may be attributed to the difference in dispersion correction employed.²³

On the pristine surface, the cleavage of the P-OC₃H₇ or P-F bond of sarin was found to have high barriers (2.27 eV and 1.77 eV respectively). This behavior has been observed as well on DMMP, where the cleavage of a P-OCH₃ bond requires overcoming a barrier higher than 2 eV.³¹ On the pristine surface, the P-F bond of sarin is less difficult to cleave compared to the P-OC₃H₇ bond, but still, the barrier is large. On the defective surface, both barriers to cleave the P-OC₃H₇ or P-F bond are considerably lowered and they become similar in magnitude. The barriers calculated with respect to the most stable isomer F1 of sarin are 1.1 and 1.05 eV, for the P-F and P-OC₃H₇ bond cleavage respectively. These bonds can therefore be broken on defective TiO₂ at moderate temperature (~425 K).

Calculations of vibrational frequencies of chemisorbed species and intermediates enable the validation of the dominant species proposed by the DFT reaction profiles and the interpretation of the experimental spectra in details. Two main results arise. First, Intact chemisorbed sarin configurations can introduce new O-P-O stretching frequencies, compared to the gas phase spectrum, seen in the room temperature experiment at 1145 and 1090 cm⁻¹. This is especially the case for the most stable configuration C. When interpreting their room temperature experimental spectrum, Tsyshevsky et al. interpreted the two new IR modes (1145 and 1090 cm⁻¹) as arising

from decomposition products of sarin via P-F or P- O(Pr) bond cleavage (Pr stands for the isopropoxy moiety). Our vibrational calculations provide an alternative interpretation as intact chemisorbed sarin can explain the features at 1145 and 1090 cm^{-1} which is consistent with DFT calculations (ours and those from Tsyshevsky et al.) which show a sizeable barrier ($>1\text{eV}$) for decomposition which cannot be passed at room temperature.

Second, our vibrational analysis showed that dissociated sarin formed after temperature treatment reinforces the occurrence of frequencies at 1145 and 1090 cm^{-1} while decreasing modes in the higher range of 1200-1271 cm^{-1} . In the presence of oxygen vacancies, unavoidable on rutile titania in UHV conditions, decomposition at moderate temperature ($\sim 425\text{ K}$) can involve P-F or P-OC₃H₇ bond cleavages. The barriers are very similar for these two pathways, but P-F bond cleavage is more exothermic so products from P-F bond cleavage should dominate on the surface (intermediate E4). O-C bond cleavage is favored on the pristine surface, and afterward, the remaining surface intermediate may rearrange to a more stable adsorption geometry. Such a rearrangement is very accessible as the barrier is very low ($+0.35\text{ eV}$) and the reaction is quite exothermic (Figure 2. , 4 C2* to C2* η_2 $\Delta E = -0.72\text{ eV}$). If the intermediate adopts the C2* η_2 conformation, further decomposition is unlikely. Our frequency calculations show that both the formation of C2* η_2 and E4 agree with the experimental spectra where Tsyshevsky et.al observe the disappearance of 1200-1271 cm^{-1} and an increase of intensity around 1145 and 1090 cm^{-1} frequencies.

Table 2. 4 Barrier comparison of the first step of sarin decomposition via P-O, P-F, and O-C bond cleavage on pristine and defective surface

Bond cleaved	Pristine surface (activation T in K)	Defective surface (activation T in K)
P-OC ₃ H ₇	2.27 eV (>800 K)	1.05 eV (~410 K)
P-F	1.77 eV (~675 K)	1.10 eV (~425 K)
O-C ₃ H ₇	1.17 eV (~455 K)	1.39 eV (~535 K)

Upon decomposition, the P-containing intermediate persists on the surface, as P coordinates itself with surface oxygens. Gas products such as propene may arise from the alkoxy resulting from the decomposition via C-H bond cleavage. However, the barrier to cleave C-H is very high and both P-containing intermediates and alkoxy may poison the surface over time. The phenomenon of surface passivation for sarin is expected and has been before observed on DMMP and DIMP on titania and other metal oxides experimentally such as cupric, manganese, alumina, and iron oxides.

31,58,95-97

It is also interesting to note that F⁻ is stable on Ti sites. An experimental (FTIR) work by Hirakawa et.al. suggests that the formation of F-Ti species is favorable on fully hydrated powder titania in which all the Ti sites are occupied with water and proton molecules. Upon F⁻ ion injection towards a hydrated titania surface, Hirakawa et. al. observed $\nu(\text{OH})$ and $\delta(\text{H}_2\text{O})$ shift, which indicates that either the dissociated water molecules (Ti-OH and proton on O_{2c}) or molecular H₂O on Ti sites are substituted by F⁻ ions.²⁴ Our calculations agree well, as we see large stabilization of the intermediates in steps involving the formation of Ti-F species on the surface, compared to the intermediates which involve the formation of Ti-OC₃H₇. On a defective surface, P-F bond cleavage

and subsequent Ti-F and P-containing (similar to IMPA) surface intermediate formation are exothermic by 0.79 eV. The P-F bond cleavage renders the following P-OC₃H₇ bond cleavage difficult, which is in agreement with the experimental observation reporting the presence of IMPA-like surface fragments.^{13,24}

Our results shed light on the question of whether DMMP is a good enough simulant for sarin decomposition reactivity. The decomposition profiles of sarin and its simulant DMMP show similarities but also key differences. Similarities are: (1) strong adsorption of both molecules which involves the dative P=O---Ti_{5c} bond, (2) difficult P-OR/P-F bond cleavage on the pristine surface, the O-C bond being the easiest to cleave on the pristine surface, and (3) the decrease of the barrier for P-OR (or equivalently P-F) bond cleavage in the presence of O vacancies. The key difference between sarin and DMMP chemistries lies in the presence of the P-F bond itself in sarin and not in DMMP. The P-F bond cleavage is significantly less difficult than the P-OR bond cleavage on the pristine surface. Additionally, the Ti-F formation upon P-F bond cleavage is much more favorable than the Ti-OC₃H₇ formation. As a consequence, there is a pathway initiated by P-F bond cleavage for sarin, which is absent for DMMP. The most obvious difference is in the case of the O vacancy containing TiO₂(110) surface with a first decomposition step of sarin by P-F bond cleavage possible at 425 K (with much higher exothermicity), while the reactivity of DMMP starts at 600K by P-OR or O-C cleavage.³¹ The F substituent also has an influence in facilitating the P-OR bond cleavage of sarin in the presence of the O vacancy, the energy barrier being 1.05 eV for sarin versus 1.4 eV for DMMP. An additional bond between P and surface O atoms is created in the transition state for P-OC₃H₇ bond cleavage of sarin: the electronegative F ligand positively polarizes P, which is more prone to interact with surface O atoms.

Therefore, DMMP is not an accurate simulant of sarin for chemical reactivity since sarin is significantly more reactive for decomposition than DMMP.

2.3.5. Conclusion

In conclusion, our analysis shows that the reactivity of sarin on pristine rutile titania is low, despite the strong adsorption energy, and that decomposition most likely initiates via the O-C bond cleavage (barrier 1.17 eV) while P-OR (R= C₃H₇ isopropyl) or P-F cleavage is highly activated (barriers larger than 2 eV). In contrast on the defective rutile surface containing O vacancies, a first decomposition step by P-OR or P-F cleavage can occur at moderate temperature (~425K), with a barrier of ~1.1 eV. The transition state for the P-OR bond cleavage is stabilized by an additional interaction between P and surface O, facilitated by the electronic effect of the F ligand. These relatively easy initial decomposition paths for sarin on rutile TiO₂ in the presence of O vacancies are in sharp contrast with the reactivity of the less toxic simulant DMMP, for which the decomposition only initiates at 600K on the same O vacancy-containing model surface. The formation of the Ti-F bond stabilizes the system significantly which gives thermodynamic preference towards the P-F bond cleavage. The produced surface IMPA-like intermediate is unlikely to undergo further decomposition via P-OC₃H₇ bond cleavage. It may react to produce propene, but the reaction is significantly activated and requires a higher temperature (585 K). Frequency calculation indicates that intact molecular adsorption of sarin can explain the experimental spectrum at room temperature, while further decomposition by C-O or P-F bond cleavage, presumably at O vacancies, is responsible for the spectral evolution seen at 500K, in agreement with calculated barriers. This theoretical work, therefore, reconciles theory and experiments for the sarin decomposition pathway on TiO₂ surfaces, proposes a pathway for initial

moderate temperature decomposition by P-F or P-OC₃H₇ cleavage on O vacancies, and demonstrates the limited accuracy of DMMP as a reactivity simulant for sarin.

Chapter 3

Unraveling the CO Oxidation Mechanism over Highly Dispersed Pt Single Atom on Anatase TiO₂(101)

3.1. Introduction

Pt group metals (PGM) are widely used in many industrial catalytic processes. However, their expense and scarcity led to much attention and effort towards singly dispersed supported metal atoms as these systems provide maximum metal utilization, well-defined active sites, and in some cases improved catalytic efficiency. Moreover, metal single atoms offer unique electronic properties due to unsaturated coordination environment and better access to frontier orbitals for interaction with the support atoms, which allows for chemical transformations that would otherwise be difficult^{38,98–109}. To utilize the full potential of the single-atom catalysts, however, it is important to understand structure-activity relations and to obtain mechanistic insights for the relevant reaction.

As Pt is an important catalyst for many industrial applications, including CO oxidation for automobile pollution control, Pt single-atom (Pt_{SA}) catalysts have been investigated extensively in recent years^{38,100,104–106,108–112}. Amongst metal oxide supports for single atom catalysts, titanium dioxide (TiO₂; Titania) has been gaining popularity due to its affordability, ease of access, and established routes of synthesis in the literature^{113,114}. Titania exists in three crystal structures, namely anatase, brookite and rutile at temperatures below 773 K^{115–118}. There are not many studies on brookite itself as support for single atoms, not only because it is a metastable phase, but also because it is difficult to synthesize¹¹⁹. Due to its higher surface area and less constrained structure,

anatase is often found to be the common product phase during the synthesis of titania¹²⁰. Although both rutile and anatase can anchor metal single atoms, the synthesis of supported single atoms on anatase TiO₂ is more accessible and has already been performed^{110,121,122}. The ease of synthesis, stability at low temperatures, and ability to stabilize single atoms make anatase TiO₂ an ideal candidate as a metal single atom catalyst support.

Despite Titania's ability to stabilize single metal atoms, the determination of their stability and intrinsic reactivity under operating reaction conditions is intricate due to the heterogeneity in the local coordination of these active metal sites and the dynamic changes in their coordination under different chemical environment and reaction conditions^{110,123–126}. A combined experimental (Fourier-transform infrared spectroscopy (FTIR), scanning transmission electron microscopy (STEM), and X-ray photoelectron spectroscopy (XPS)) and theoretical (density functional theory (DFT)) study on Rh single-atom catalyst (SAC) on rutile TiO₂(110) showed that Rh may adapt its adsorption site and coordination depending on the gas pretreatment condition¹²⁴. In oxidative conditions, Rh may substitute the surface Ti_{5c} (five-fold coordinated Ti), whereas in reducing conditions, Rh prefers to be supported on the surface instead of substituting Ti. A recent work by DeRita *et al.*¹¹⁰ on TiO₂-supported Pt single atoms showed that Pt can be deposited as stable isolated atoms on anatase TiO₂ nanoparticles under various pretreatment conditions: oxidative (300 °C in 100% O₂), mild reduction (250 °C in 10% H₂) and harsh reduction (450 °C in 10% H₂). Interestingly, it was shown that the local coordination and oxidation/charge state of Pt single-atom species depend on these pretreatment conditions, which in turn impact the stability and activity of the supported Pt atoms. For instance, 300 °C oxidation, 250 °C reduction or 450 °C reduction resulted in Pt substituting six-fold coordinated Ti, adsorbed Pt(O₂) species, or adsorbed Pt(OH) species, respectively. The Pt atoms remained isolated in all cases with the Pt(OH) species being

mobile and adsorbed on both step and terrace sites. In another recent study, Thompson *et al.*⁴² showed that Ir SA is adsorbed/supported on anatase TiO₂ after CO reduction pretreatment with a *gem*-dicarbonyl ligand environment and binding to two lattice O from TiO₂. Under CO oxidation atmosphere, the Ir SA ligand environment changes where Ir is coordinated to one CO (monocarbonyl), one lattice O, and two other O from gas-phase O₂ dissociation.

The dynamic nature of SA Pt species during catalyst pretreatment and under reaction environment makes it challenging to describe the catalytic activity of highly dispersed single atoms in a level that connects to the characterization/local geometric structure (resting state) from experiment alone. This is more so because evolution of the local coordination of these isolated Pt species during CO oxidation, i.e. the evolution through the reaction cycle is difficult to follow experimentally unless more than one intermediate can be isolated⁴². Moreover, although the structural details of the isolated Pt sites, their dynamic response to pretreatment environments causing difference in local coordination, and its influence on chemical reactivity have been studied by DeRita *et al.*¹¹⁰, the origin of their activity and reaction kinetics, rate-determining intermediates, and detailed reaction pathways and mechanism are still missing. It is important to understand these details for achieving guiding principles so that active and efficient Pt catalysts consisting of isolated single atoms can be designed in the future.

Additionally, it is crucial to understand what role oxygen atoms from the TiO₂ lattice play in the CO oxidation mechanism, given that TiO₂ is a reducible support. This will allow for optimal selection and tuning of support for single-atom Pt group catalysts. Previously, it has been reported for CeO₂-supported Pt nanoparticles that reactive and mobile/labile support lattice oxygen (O*) can be supplied by the interfacial sites at the Pt-CeO₂ interface, where labile/reactive O* can travel

from distance to react with the adsorbed CO at the interfacial Pt sites, thus enhancing CO oxidation reactivity^{127,128}. However, the involvement of reactive labile lattice oxygen for CO oxidation on TiO₂-supported Pt single-atom is still unknown.

In this work, we describe the dynamic structure of stable and uniform Pt single atoms (Pt_{SA} hereafter) deposited on the surface of anatase TiO₂, their reactivity towards CO oxidation, and the detailed mechanism of the reaction by combining experimental methods (DRIFTS, STEM, X-ray absorption spectroscopy (XAS) and kinetic studies) and computational approaches from first principles (DFT and microkinetic modeling). We studied the local coordination environment of the Pt single atoms and the CO adsorption behavior on these isolated sites after reduction and during CO oxidation to identify the rate-controlling intermediate(s) and step(s). We show that the starting catalyst after reduction is a supported (adsorbed) Pt atom on anatase-TiO₂ (101) with one oxygen vacancy (Pt_{ads}O_{vac1}). Upon exposure to CO and O₂ it turns into Pt(CO) without O vacancy, and initiates the reaction cycle with competing branching pathways involving Langmuir–Hinshelwood or Eley-Rideal type CO oxidation. We demonstrate that the first chemisorbed CO generally binds strongly on Pt and that a second gas-phase CO can be involved favorably in the reaction resulting in the experimentally observed Eley-Rideal step. Furthermore, microkinetic modelling reveals that the fractional CO and O₂ reaction orders originate from multiple competing rate-determining intermediates and transition states. These results demonstrate that CO oxidation may undergo multi-branch convoluted reaction pathways even on a simple supported single-atom system.

3.2. Computational Methods

Anatase TiO₂(101) was chosen as the support because it is the most stable facet, followed by the (010) and the (001) facets with surface energies of 0.44, 0.53 and 0.9 J.m⁻², respectively, with the

(101) facet dominating (>94%) the surface of nanoparticles^{42,43}. The Vienna Ab Initio Simulation Package was used for the density functional theory computations (VASP)^{44,45}. All calculations were performed using the Perdew-Burke-Ernzerhof (PBE) functional to describe the exchange and correlation energy. In order to correctly include the van der Waals interactions, the dDsC dispersion correction was added⁴⁶⁻⁴⁸. The electron-ion interactions were described by the Projector Augmented Wave (PAW) approach. One-electron functions were developed on a plane wave basis set and a 500 eV cutoff was chosen⁴⁹⁻⁵¹. Following the Dudarev approach, Ti was given an effective Hubbard U (DFT+U) parameter of 4.2 eV due to the onsite coulomb repulsion of the Ti 3d orbitals^{52,53}. The value of 4.2 eV was chosen because it accurately captures the characteristics of the electronic structure that were seen with TiO₂ in experimental settings, particularly the localized nature of electrons on surfaces with oxygen vacancies⁵⁴. The electronic energies were converged within a 10⁻⁶ eV accuracy and atomic force convergence criterion was set to 0.03 eV/atom. The transition states structures and energies were calculated using the Nudged Elastic Band Method including 8 images.

The periodic slab of anatase TiO₂ (101) was cut from a TiO₂ bulk of lattice constant: a = 3.83 Å and c = 9.63 Å. The *ab initio* thermodynamics analysis to study the stability of Pt_{SA}/a-TiO₂(101) was performed using the following equation:

$$G = E_{TiO_2(surface)+Pt_{SA}} - E_{TiO_2(surface)} - \frac{1}{4}E_{Pt_4(bulk)} \quad (3-1)$$

To account for the anharmonicity of the vibrational spectra simulation, the values obtained by the simulation are usually normalized with respect to a reference, where CO gas is the common choice. However, CO gas is not an appropriate structure to obtain a scaling factor for Pt(+2) species as

it fails to reproduce the CO stretches of Pt(II)-CO complexes ($\text{PtCl}_2(\text{CO})_2$).⁵⁵ Hence, in this work, the CO stretch is normalized by $\text{PtCl}_2(\text{CO})_2$ instead of CO gas phase to account for this error.

3.3. Results and Discussion

3.3.1. Synthesis, Structure, and Stability of $\text{Pt}_{\text{SA}}/\text{a-TiO}_2(101)$

We confirm the presence and the stability of isolated Pt atoms on anatase TiO_2 using *ex-situ* microscopy and *in-situ* DRIFTS. *Ex-situ* aberration-corrected high-angle annular dark-field scanning transmission electron microscopy (AC-HAADF-STEM) images collected after CO oxidation kinetics experiments (in Figure 3.1 (a) and Figure C.4) show singly dispersed Pt atoms (enclosed in dashed pink circles) on the TiO_2 surface even after enduring the high-temperature reduction pretreatment (350 °C) and prolonged reaction gas environment (after several hours of CO oxidation kinetics measurement at 160 °C). *In-situ* CO adsorption DRIFTS at 35 °C on the H_2 -reduced state shows a symmetric peak at $\sim 2073 \text{ cm}^{-1}$ (Figure 3.1 (b)) in the ν_{CO} region corresponding to the C-O vibrational frequency on the reduced Pt_{SA} . The 2073 cm^{-1} peak observed experimentally matches the DFT-calculated frequency for the most stable adsorbed structure of the Pt_{SA} under these conditions (2065 cm^{-1} ; structure labelled “ $\text{Pt}_{\text{ads}}\text{O}_{\text{vac1}}$ ” in Figure 3.1 (c)). This suggests consistency between the synthesized Pt_{SA} species and the modeled $\text{Pt}_{\text{SA}}/\text{a-TiO}_2(101)$ species. An almost identical CO chemisorption peak was obtained after regenerating the catalyst following CO oxidation, showing the stable nature of the $\text{Pt}_{\text{SA}}/\text{a-TiO}_2$ catalyst (see Figure B5). Thus, STEM and DRIFTS show that Pt stays as single-atom species supported on anatase TiO_2 during CO oxidation. Our DFT calculations and *in-situ* DRIFTS show that $\text{Pt}_{\text{SA}}/\text{a-TiO}_2(101)$ can adopt different configurations depending on pretreatment condition and gas environment. Figure 3.1 (d) shows the sensitivity of the $\text{Pt}_{\text{SA}}/\text{a-TiO}_2(101)$ structure on the condition prior to CO

exposure. In reducing conditions, Pt_{SA} is most stable as supported on the two-fold-coordinated surface oxygen (O_{2c}) vacancy sites formed on a-TiO₂ (structure “Pt_{ads}O_{vac1}” in Figure 3.1 (c)). As discussed earlier, the measured C-O vibrational frequency on the reduced Pt_{SA} species was 2073 cm⁻¹ which matches well with the DFT-calculated frequency of 2065 cm⁻¹ corresponding to Pt adsorbed on TiO₂ with one O vacancy sites (structure “Pt_{ads}O_{vac1}” in Figure 3.1 (c), (d), and Figure B.6 (a)). This state represents the initial reduced state of the catalyst before exposing it to the oxidizing reaction environment, *i.e.* CO + O₂ flow. In contrast, in oxidizing conditions under O₂ (high oxygen chemical potential; right-hand side of the stability diagram in Figure 3.1 (d)), the most stable species corresponds to Pt_{SA} substituting a six-fold-coordinated Ti sites (structure “Pt_{subTi}” in Figure 3.1 (d) and Figure B.6 (a)). The behavior of Pt_{SA} substituting the Ti cation as dopant has been seen before on rutile TiO₂. Tang *et al.*³⁰ showed a thermodynamic analysis on rutile TiO₂ where Rh prefers to substitute the bridging Ti_{6c} (six-fold-coordinated Ti) sites. Meanwhile, a combined FTIR and DFT work by Thang *et al.* suggested that Pt_{SA} most likely adopts the supported/adsorbed structure²⁷. However, a follow up work by DeRita *et al.* confirmed the dynamic nature of Pt_{SA}: substituted Pt on six-fold-coordinated Ti (Ti_{6c}) site upon oxidation conditions and supported/adsorbed Pt_{ads}O₂ species after mild reduction¹⁶. Since the catalyst in this study undergoes reduction prior to CO oxidation, the subsequent DFT modeling of the reaction pathways follows the reduced “Pt_{ads}O_{vac1}” structure, as per agreement found by DRIFTS and DFT-calculated C-O vibrational frequency.

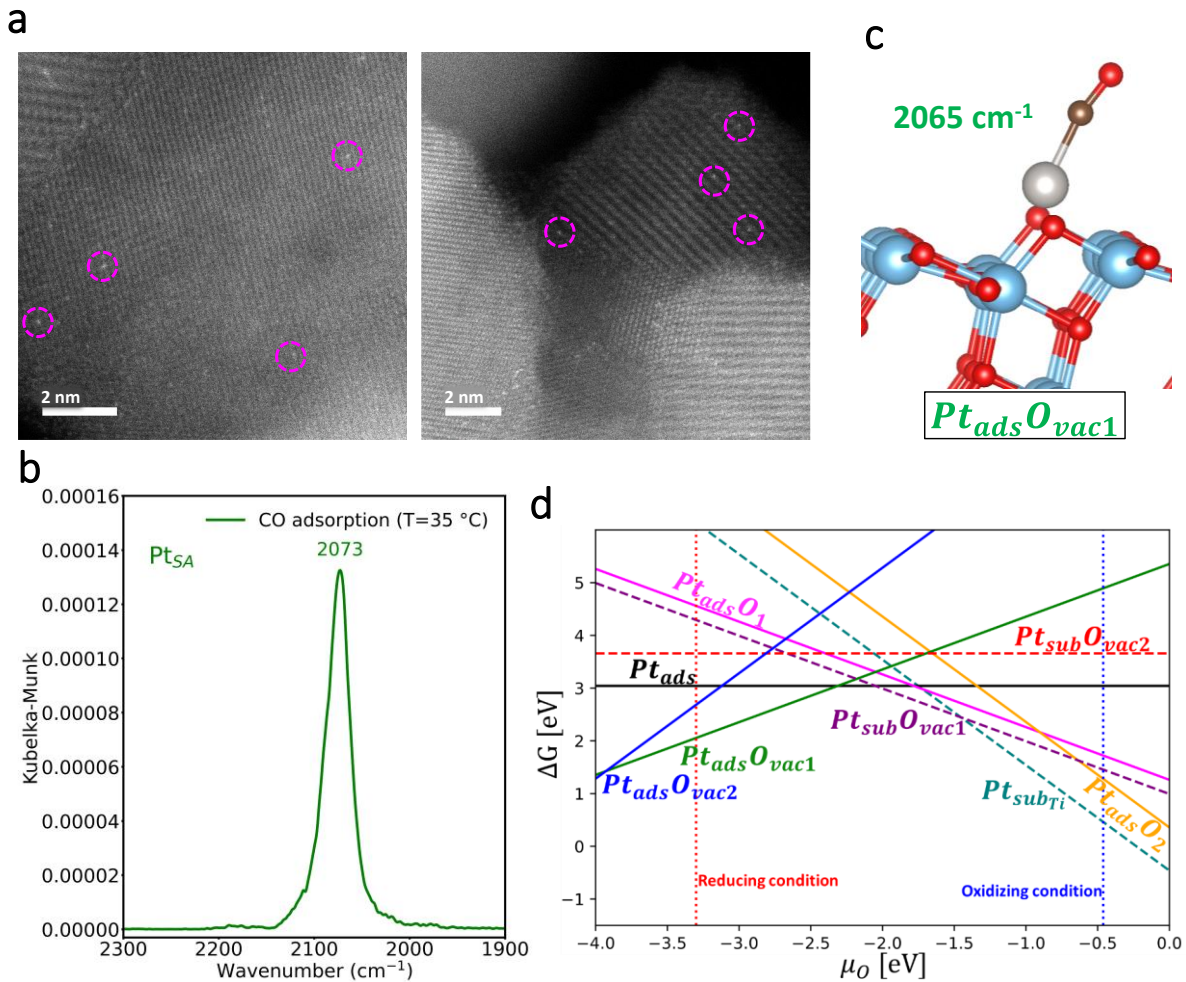


Figure 3. 1(a) Ex situ AC-HAADF-STEM images of the SA Pt/TiO₂ sample taken after the reduced sample went through the CO oxidation kinetic experiment, showing the singly dispersed Pt atoms as enclosed in pink circles. **(b)** In situ DRIFTS spectra of CO adsorption at 35 °C after H₂ reduction pretreatment. H₂ reduction pretreatment was performed at 350 °C for 2 hr. **(c)** Calculated structure and vibrational frequency of CO adsorbed on Pt SA supported on anatase TiO₂ which corresponds to the reduced state of the catalyst and the starting catalyst for the CO oxidation cycle. The frequency value agrees well with DRIFTS spectrum in Figure 3.1 (b). **(d)** Stability diagram of the different configurations of the supported Pt_{SA} on anatase TiO₂ under different gas environments (please see Figure B.6 (a) for all structures).

To further understand how CO would affect the stability of Pt_{SA}/a-TiO₂(101), a similar study was conducted with the presence of CO absorbed on all the Pt_{SA} species, with the CO chemical potential corresponding to the conditions $P_{CO} = 1$ kPa and $T = 25$ °C. Upon exposure to CO, Pt(CO) structure on the pristine TiO₂ surface where Pt is supported/adsorbed on TiO₂ (“Pt_{ads}” structure in Figure B.6 (b)) becomes the most stable configuration in a large range of reducing condition oxygen chemical potential, while in oxidizing conditions, Pt substituting Ti_{6c} (“Pt_{subTi}” in) is still the most thermodynamically stable species followed by the metastable supported/adsorbed “Pt_{ads}O₂” structure (see structures in Figure B.6 (b)). The crossing in stability between the Ti-substituting Pt_{SA} and the supported Pt_{SA} now occurs at a much higher chemical potential (-0.9 eV, compared to -1.75 eV prior to CO exposure). Therefore, the interactions between CO and Pt decrease the thermodynamic driving force for restructuring the Pt atom from adsorbed to substituted in oxidizing conditions.

3.3.2. Elucidation of CO Oxidation Pathway and Active Species

The oxidation pathways of CO and its Gibbs Free energy diagram were explored using DFT at experimental conditions ($T = 160$ °C, $P_{CO} = 1$ kPa, $P_{O_2} = 10$ kPa) and 5% conversion (Figure 3.2 (a) and (b), respectively). The supported/adsorbed Pt_{ads}O_{vac1} structure was the starting configuration (structure I in Figure 3.1(c) and Figure 3.2(a)). Calculations show that the reaction consists of an initiation step and a reactive cycle where the system does not return to the initial catalyst configuration. The initiation step consists of CO and O₂ adsorption on structure I, followed by an Eley-Rideal (ER) type CO oxidation using a gas-phase CO to ultimately form Pt(CO) (structure IV in Figure 3.2(a)). The initiation step is very facile as the adsorbing O₂ heals the vacancy and provides a reactive O adatom, resulting in a large thermodynamic driving force and a small barrier to form CO₂ even at room temperature via the ER mechanism (Figure 3.2 (b)). This

is shown experimentally as the fresh reduced Pt_{SA} catalyst with a CO vibrational frequency of 2073 cm⁻¹ gets oxidized when exposed to O₂ (Figure 3.3 (a)) and the CO peak blueshifts from 2073 cm⁻¹ to two peaks positioned at 2087 and 2115 cm⁻¹ upon O₂ flow. Upon CO re-adsorption the intensity of both peaks increases, indicating a role of both CO and O₂ in the initiation cycle. Notably, the co-flow, or reversing the order of CO and O₂ flow at 35 °C on the reduced Pt_{SA} state also led to the same two peaks with similar intensity (Figure B.7 (a)). These two peaks, positioned at 2087 and 2115 cm⁻¹, merge into a single peak positioned at 2115 cm⁻¹ in the initial stages of heating the catalyst (Figure B.7(b)), which is the same peak observed under steady state at 160 °C (Figure 3.3 (b)), and suggests that the initiation step is facile, but not barrierless, in agreement with the DFT calculated initiation pathway in Figure 3.2. Furthermore, the CO-Pt peaks obtained experimentally upon exposure to O₂ followed by CO or CO and O₂ co-flow on the reduced Pt_{SA} agree well with DFT-calculated vibrational frequencies of the states in the initiation cycle. Specifically, upon O₂ healing the O vacancy, the frequency shifted from 2065 cm⁻¹ (experimental 2073 cm⁻¹) (starting CO-Pt_{ads}O_{vac1} structure) to 2081 cm⁻¹ (structure II in Table B.3), forming an adsorbed Pt(O)(CO) species (structure II in Figure 3.2 (a)). Finally, flowing CO leads to CO₂ formation via an Eley-Rideal step and results in the formation of state IV with a calculated CO vibrational frequency of 2106 cm⁻¹, all in very good agreement with the experimental results in Figure 3.3 (a). Importantly, the Pt_{SA} remains in the same state as in Figure 3.3 (b) when cooled to room temperature (Figure B.7 (c); red spectrum) indicating that this is an irreversible initiation cycle. As will be discussed below, this is further shown by our calculations as well.

In summary, the initiation pathway starts with structure I and results in a reduced Pt(CO) species without O vacancy (intermediate IV, Figure 3.2(a)). From this Pt(CO) species, the reaction can continue via O₂ adsorption in an η²-manner on Pt (intermediate V). The dissociation of this O₂

results in intermediate VI (Pt(O)(O)(CO)). From intermediate VI, two possible pathways arise: the formation of CO₂ via an LH mechanism (black path) that results in the reduced Pt(O) intermediate (structure VIII(a)) or via an ER mechanism involving an additional CO from gas phase, which is prone to formation of carbonate (red path, structure VIII(b)). Carbonate formation during CO oxidation has been observed from experiment via DRIFTS (Figure B.8), supporting this red ER pathway. Both pathways form a Pt(O) species adsorbed with CO (Pt(CO)(O), intermediate IX) upon adsorption of CO (VIIIa-IX, black path) or release of CO₂ (VIIIb-IX, red path).

From this Pt(CO)(O) species (structure IX), the reaction can continue via O₂ adsorption in a bridging manner between Pt and Ti, immediately followed by an Eley-Rideal CO oxidation from the gas phase to form CO₂ with the remaining O adatom (O_{ad}) of Pt(O)(CO)(O₂) (intermediate X(a), blue path). The barrier along this blue pathway is +0.58 eV (TS IIIa-IV). The release of CO₂ yields an isomer of intermediate V - the Pt(CO)(O₂) species (intermediate XII(a)). Rearrangement of Pt(CO)(O₂) to a more stable isomer is facile via desorption and re-adsorption of O₂ (XII(a)-IV-V). Alternatively, the Pt(CO)(O) species can absorb another CO (intermediate X(b), black path). This path is only limited by the CO adsorption barrier (0.46 eV) and will initiate a LH type mechanism for the second CO₂ formation. The barrier to form CO₂ from intermediate XI(b) [Pt(CO)(CO)(O)] is very low (0.14 eV, TS 2), and the subsequent release of CO₂ regenerates the initial Pt(CO) structure (intermediate IV). We note that the Pt does not return to state I, confirming that the catalyst changes irreversibly after the initiation cycle as was seen from experiment as well (Figure B.7).

It is interesting to note that both the initiation steps and the reactive pathway do not involve lattice oxygen of TiO₂ since all the pathways involve either an Eley-Rideal or Langmuir Hinshelwood

type of mechanism with an O adatom on Pt. This behavior has recently been shown with other TiO₂ supported SAC. A work by Liu *et al.* showcased the CO oxidation kinetics on Ir₁/TiO₂ to follow mostly an Eley-Rideal mechanism and not Mars-van Krevelen mechanism that would involve oxygens from TiO₂ lattice.^{36,37}

Our mechanistic exploration shows a rich complexity of pathways involving different branches with similar barriers. Determining the favored path is therefore not directly possible from the reaction profile and requires microkinetic modeling as will be discussed below.

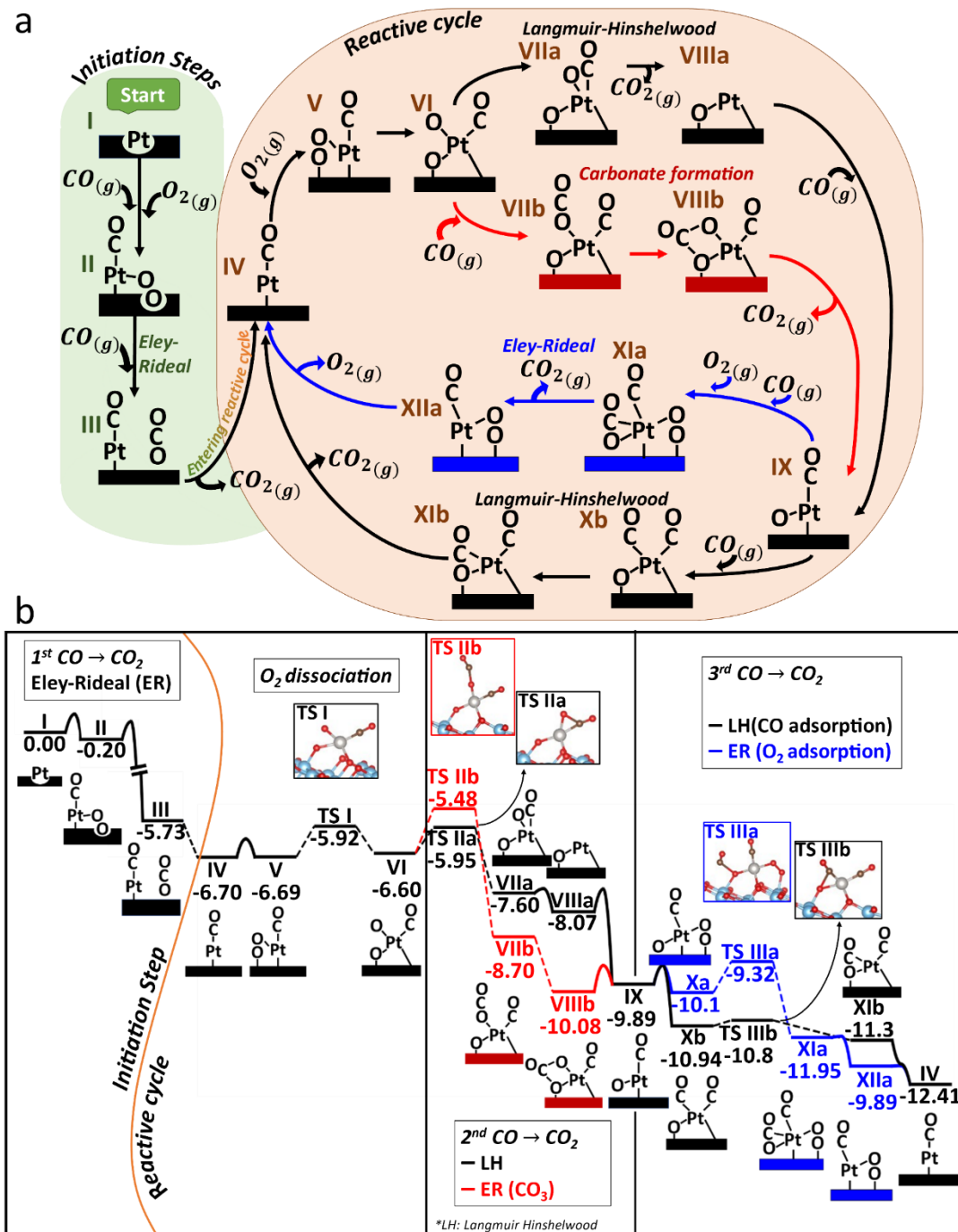


Figure 3. 2 The reaction pathway for CO oxidation on PtSA/TiO₂ (a) and its respective free Gibbs Energy landscape at reaction conditions ($T = 160\text{ C}^\circ$, $PCO=1\text{ kPa}$, $PO_2=10\text{ kPa}$, conversion = 5%). Surfaces with an O vacancy are represented by an inward concave. (b). The reaction pathway consists of an initiation step and a catalytic reactive cycle. Elementary steps involving adsorption or desorption

processes are connected with solid lines, indicating their respective adsorption free energy barrier. For elementary reaction steps, transition states energy levels are explicitly indicated (labeled TS X) and linked by dashed lines.

3.3.3. Kinetics of CO oxidation: Microkinetic Analysis

Microkinetic Modeling (MKM) was employed to further understand the kinetics of CO oxidation on Pt_{SA}/a-TiO₂(101). As the system does not return to the initial Pt_{ads}O_{vac1} structure (intermediate I) at steady-state, the microkinetic modeling was built on elementary reaction steps which describe the reactive cycle only. A list of elementary reaction steps describing the reactive cycle was built for the microkinetic analysis (**Table B.2**). The MKM employed Gibbs Free energies at experimental reaction conditions (T = 160 °C, P_{CO} = 1 kPa, P_{O₂} = 10 kPa, conversion = 5%). Details of the MKM setup are listed in the supporting information (**Table B.2** and associated discussion).

The MKM was run towards steady state. The most abundant intermediates on the surface were Pt(CO) (structure IV, 35.5%), Pt(O₂)(CO) (structure V, 26.8%), Pt(CO)(CO₃) (structure VIII(b), 19.6%), and Pt(O)(O₂)(CO) (structure X(a), 16.8%) (all shown in **Error! Reference source not found.** (d)). We note here that intermediates IV and V are the most abundant species under steady-state and have CO vibrational frequencies of 2106 and 2116 cm⁻¹, respectively, providing a detailed interpretation of the CO vibrational frequency of 2115 cm⁻¹ that we experimentally observe during steady-state CO oxidation at 160 °C (**Figure 3.3** (b)). However, species VIII(b) and X(a) were not observed as distinct peaks in DRIFTS (**Figure 3.3** (b)) likely due to their small contribution and their CO vibrational frequency (2137 and 2156 cm⁻¹, respectively; **Table B.3**) falling in the same range as the large gas-phase CO peak. It is important

to note that CO bound on structure IV and V are strongly chemisorbed with calculated binding energy of -3.76 eV and -1.51 eV, respectively. Strong CO binding is observed experimentally as well from temperature-programmed desorption (TPD) of the chemisorbed CO observed during steady-state CO oxidation (**Figure 3. 3 (b)**). The estimated binding energy was ~140 kJ/mol or -1.45 eV (see **Figure B.11**, **Table B.5**, and associated discussion for TPD procedure and analysis). Since any adsorbed O₂ would be desorbed during the TPD process, this experimental value would correspond to the CO binding energy on structure IV rather than on structure V.

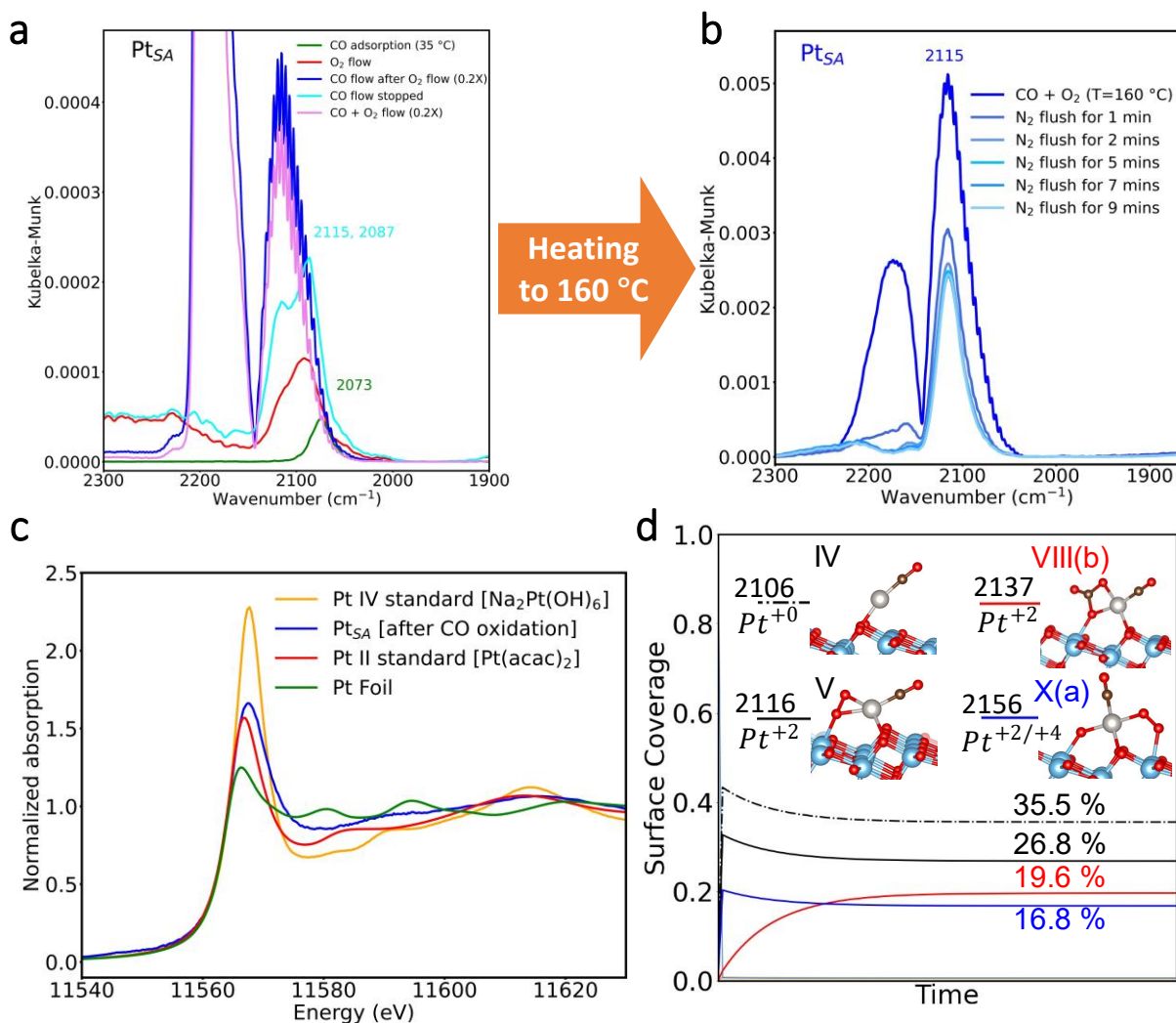


Figure 3. 3 In-situ/operando CO adsorption DRIFTS spectra for PtSA/TiO₂ (a) under different gas environments at 35 °C on the H₂ reduced state and (b) during CO oxidation at 160 °C and under different duration of N₂ flush of the reaction gas environment afterwards. (c) The White Line Intensity (WLI) region of the in-situ XANES spectra for Pt_{SA} after CO oxidation compared against three standards – Pt foil, Pt²⁺, and Pt⁴⁺. (d) Surface coverage along the MKM simulations for the primary Pt_{SA}/a-TiO₂ species present during CO oxidation. In the legend, we indicate the corresponding CO vibrational frequency in cm⁻¹ (above the line) and the formal Pt oxidation state derived from the Bader charge analysis (below the line; see Table B.4 for more details).

The MKM ensemble of surface species with significant coverage is consistent with the Gibbs Free Energy landscape, which suggests that there are few competing turnover frequency-determining intermediates (TDI), particularly intermediates IV and V. To estimate the oxidation state of the Pt_{SA} species, we performed *in-situ* XAS at 35 °C after CO oxidation at 160 °C and compared the XANES white line intensity region against that of Pt foil, Pt II [Pt(acac)₂], and Pt IV [Na₂Pt(OH)₆] standards (Figure 3. 3 (c)). It is evident from the similar white line intensity of the Pt_{SA} and Pt(acac)₂ that the Pt_{SA} species after CO oxidation is close to Pt²⁺. From Bader charge analysis (Table B.4), the Pt oxidation state (Figure 3. 3 (d)) of the most abundant intermediates (structure IV and V) during steady-state CO oxidation (at 160 °C) were found to be 0 and +2 (Bader charge 0.16 and 0.82, respectively; see methods for calculation details and Table B.3-4), respectively. To be consistent with the conditions of the XANES measurements, we ran microkinetic modeling of the CO oxidation at 27 °C and found that structure V (Pt(O₂)(CO)) is more stable and hence more probable than structure IV. Therefore, a Pt oxidation number of +2 is predicted by simulations under conditions similar to the experimental XANES measurements, suggesting consistency with the experimentally observed oxidation state.

CO oxidation rate measurements under strict kinetic control (Figure 3. 4 (a) and (b)) show apparent activation energy of 69±2 kJ/mol and fractional CO and O₂ reaction orders of 0.55±0.15 and 0.36±0.10, respectively. The reaction orders obtained from MKM are 0.24 and 0.46 respectively for CO and O₂, qualitatively agreeing with the experimental values.

The turnover frequency (TOF) at 160 °C obtained from MKM on the other hand is significantly overestimated at 3.3×10³ (mol CO₂).(mol surface Pt)⁻¹.s⁻¹, compared to the experimental value of 3.8×10⁻³ (mol CO₂).(mol surface Pt)⁻¹.s⁻¹, indicating that the DFT calculation underestimated

barriers in the reaction network, which is a general behavior.³⁷⁻⁴⁰ This is also reflected in the calculated apparent activation energy of 45 kJ/mol compared to the experimental value of 69±2 kJ/mol. A summary of the computational and experimental CO oxidation kinetics is presented in Table 3. 1.

Table 3. 1 Turnover Frequency (TOF), CO and O₂ reaction orders, and apparent activation energy (E_{app}) obtained from microkinetic modeling under experimental conditions. TOF, CO order, and O₂ order values are at 160 °C and apparent activation energy was measured between 150 and 170 °C.

Kinetic parameter	Value obtained from MKM	Value obtained from experiment
TOF (1/s)	3.3×10^3	3.8×10^{-3}
CO order	0.24	0.55±0.15
O ₂ order	0.46	0.36±0.10
E _{app} (kJ/mol)	45	69±2

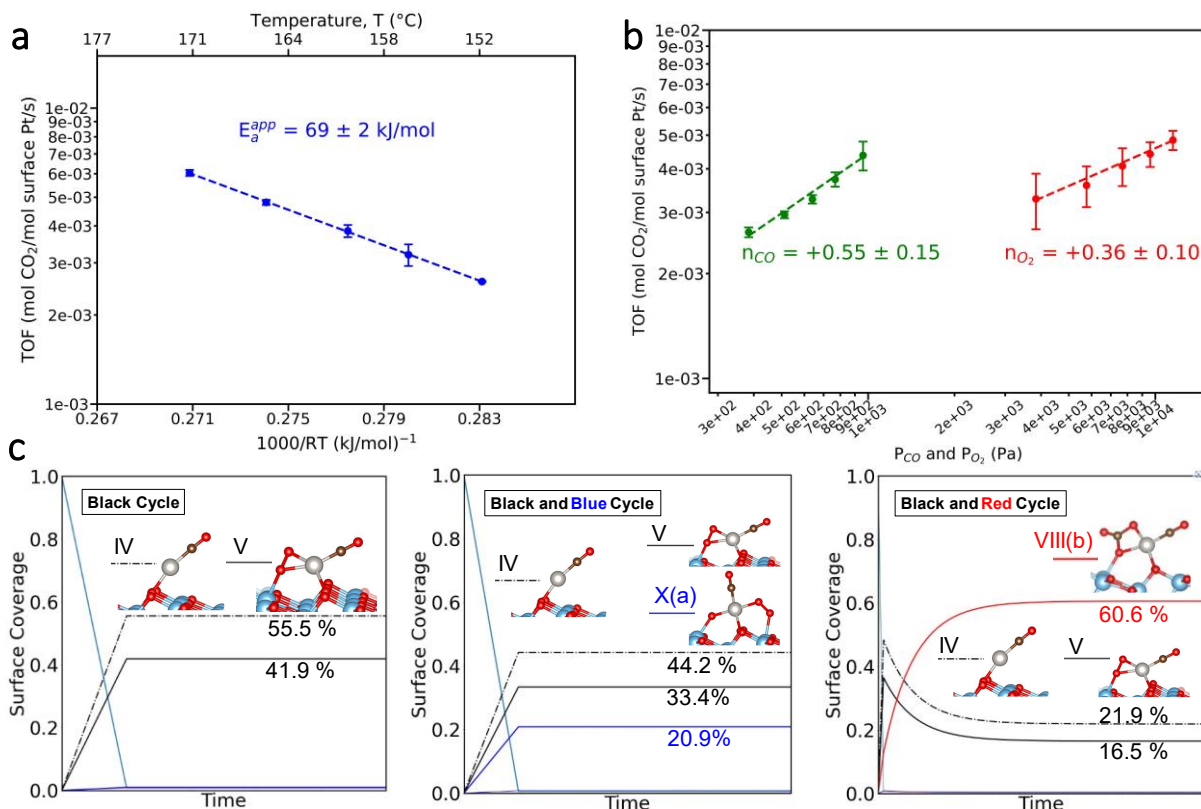


Figure 3. 4 CO oxidation kinetic measurements on PtSA/TiO₂ with turnover frequency (TOF) calculated considering 100% Pt atoms are singly dispersed, i.e., on the surface. (a) Arrhenius plot (TOF vs 1000/RT) with the calculated apparent activation energy (E_{app}) value. E_{app} was measured between 150 and 170 °C with 1 kPa CO, 10 kPa O₂, and balance He to atmospheric pressure at 75 sccm total flow rate. (b) Effect of CO and O₂ partial pressure on TOF at 160 °C. Gas flow conditions: 0.4-1 kPa CO and 10 kPa O₂ for the effect of CO partial pressure; 1 kPa CO and 4-12 kPa O₂ for the effect of O₂ partial pressure with balance He to atmospheric pressure at 75 sccm total flow rate. (c) Surface coverage for model kinetic simulations including only part of the reaction pathways shown in Figure 3.2 (“black”, “black + blue”, and “black + red” paths following colors of Figure 3.2) and corresponding majority structures.

On supported nanoparticles, fractional orders indicate competitive adsorption of CO and O₂ on the metal and/or a two-site mechanism where CO adsorption proceeds on the metal site while O₂ activation proceeds on the metal-support interface. However, on supported single atom catalysts

the reaction pathway can be more complex due to the ability to adsorb more than one molecule at the same time as shown above (Figure 3.2) and can involve more than one kinetically relevant step.^{36,37} Therefore, a detailed discussion of the experimental and simulated kinetics requires the computation of the TOF-determining transition states (TDTS), obtained with a degree of rate control (DRC) analysis⁴¹ (shown in Table 3.2). Several TDTS are obtained along the branches of the pathway. The greatest DRC (0.45) is obtained for the O₂ dissociation step along the black pathway (V-TSI-VI). However, the second Eley-Rideal CO₂ formation along the blue pathway (X(a)-TS IIIa-XI(a)) also provides a significant DRC (0.24), together with the first CO₂ formation along the black pathway (VI-TS IIa-VII(a)). Overall, the MKM results summarized in Table 1, Table 3.2, and Figure 3.3 (d) show that fractional CO and O₂ order come from multiple competing rate-determining processes. Our computational results suggest that there is an ensemble of active surface species and pathways persisting on the catalyst during reaction.

Table 3.2 Computed Degree of Rate Control obtained from the Microkinetic Modeling (MKM) at reaction conditions ($T = 160$ °C, $P_{CO} = 1$ kPa, $P_{O_2} = 10$ kPa, conversion = 5%) for the TOF-determining transition states (TDTS)

Label	Reaction	Type of reaction	DRC
R5	$Pt(CO)(O_2)[V] \rightarrow TS\ I \rightarrow Pt(CO)(O)(O)[VI]$	Surface, O ₂ dissociation	0.45
R9	$Pt(O)(CO)(O_2)[X(a)] + CO_{gas} \rightarrow TS\ IIIa$ $\rightarrow Pt(CO)(CO_2)(O_2)[XI(a)]$	Eley-Rideal, CO ₂ formation	0.24
R6	$Pt(CO)(O)(O)[VI] \rightarrow TS\ IIa$ $\rightarrow Pt(O)(CO_2)[VII(a)]$	Surface, CO ₂ formation	0.18

R8	$Pt(O)(CO)[IX] + O_{2gas}$ $\rightarrow Pt(O)(CO)(O_2) [X(a)]$	Adsorption	0.05
-----------	---	------------	------

3.3.4. Origin of Partial Orders and Apparent Activation Energy

The main TDTS of the complete reaction network (TSI) and the main TDI (IV and V) are located along the black pathway, associated with the re-oxidation of the catalyst. The resulting reaction order depends on the choice of the TDI species: If structure IV is selected, one O₂ adsorption step occurs between TDI and TDTS so that the O₂ order is 1; If structure V is selected, O₂ is already adsorbed, hence the order is zero. Since both IV and V have TDI nature, the overall order is a weighted average, hence close to 0.5. No CO adsorption occurs between TDI and TDTS along this pathway, so that the CO order should be zero. This is confirmed by a model MKM simulation where only the black pathway of Figure 3.2 is included (see Figure 3.4 (c) and Table 3.3) where the O₂ order is mainly unchanged while the CO order drops to 0.03.

Table 3. 3 Results from the decomposed microkinetic analysis of the three simpler reactive cycles within the complete reaction cycle

	All combined	Black	Black + Blue	Black + Red
TOF (s⁻¹)	3.3 x 10 ³	5. 3 x 10 ³	4.2 x 10 ³	2.1 x 10 ³
CO order	0.24	0.03	0.33	0.01
O₂ order	0.46	0.53	0.38	0.2
E_{app} (eV)	0.47	0.38	0.29	1.15

The origin of the partial CO order is located in the blue pathway. Structure XI(a) along this path has a significant coverage (~ 0.17) and hence some TDI nature, associated with TS IIIa as a TDTS (DRC 0.24). This Eley-Rideal CO oxidation step obviously sees a CO adsorption between the TDI and the TS, so that the CO order is 1, but no O₂ adsorption so that the O₂ order is zero. The combined orders when mixing the blue pathway with the black pathway depend on the weight in the rate. A model MKM simulation including only the black and blue paths gives 0.33 and 0.38 for the CO and O₂ order, in good agreement with our qualitative discussion above.

The involvement of a 2nd CO from the gas-phase (during the ER steps) has been confirmed by multiple *in-situ* DRIFTS experiments. The CO adsorption peak after cooling down (under CO and O₂ flow) from steady-state CO oxidation (at 160 °C) to 35 °C and -75 °C shows identical shape and intensity (Figure B.9). This shows that there are no bare Pt sites (without chemisorbed CO) during steady-state CO oxidation, indicating that the positive CO order is not due to weak CO adsorption on bare Pt sites, but rather due to a 2nd CO from the gas phase reacting with adsorbed and/or interfacial oxygen. To investigate further, we performed ¹³CO/¹²CO exchange experiments at 160 °C both in the presence and absence of O₂, i.e. ¹³CO oxidation and ¹³CO pulse (Figure B.10 (a) and (b), respectively). Exchange of ¹³CO with ¹²CO occurs during CO oxidation, as evident from the evolution of the peak centered at $\sim 2066\text{ cm}^{-1}$, but with an exchange rate ($\sim 36\%$ in 30 mins) that is slower than the turnover number in the equivalent time (~ 5 turnovers in 30 mins) suggesting a 2nd CO is likely involved but that this is not the only CO oxidation pathway. If the chemisorbed CO was the only one involved in the reaction, all ¹²CO would have been replaced by ¹³CO in 30 mins because of the 5 turnovers observed. Interestingly, the absence of gas-phase O₂ seems to promote the exchange of ¹³CO with ¹²CO, which was also observed for Ir₁/TiO₂³³. The

experimental results therefore confirm the simultaneous presence of ER and LH CO oxidation steps in the mechanism as proposed by our calculations (black and blue paths).

The red pathway introduces the TDI structure VIII(b) ($\text{Pt}(\text{CO}_3)(\text{CO})$) with overall coverage 0.2 and explains the carbonate formation leading to partial poisoning of the active site. A model simulation including only the black and red paths (Figure 3. 4 (c)) provides a higher carbonate coverage (0.6) compared to its overall coverage. This is due to the fact that in the overall system, the blue pathway opens up an extra channel to consume structure IX and hence the carbonate structure VIII(b) (Figure 3.2).

If we now focus on the apparent activation energy, it also has a composite nature. Since the activation energy is an enthalpy, it should be obtained from the enthalpy differences for the TOF-determining processes (see Figure B.13 in Appendix B). Contributions from the initial O_2 dissociation pathway (black path) are -0.25 eV for IV-TSI and $+0.76$ eV for V-TSI, while from the red path, the carbonate decomposition corresponds to an enthalpy of $+1.5$ eV (CO_2 release), and from the blue path, X(a)*-TS3(a) is associated to a barrier of 0.33 eV. The overall computed value is 0.47 eV, corresponding to a rate-weighted combination of the various active pathways, while model simulations with only part of the paths can provide strongly altered values (**Error! Reference source not found.**). For example, only “black + red” path shows an effective barrier of 1.15 eV, while the “black + blue” path shows an effective barrier of 0.29 eV.

The overall kinetics and kinetic parameters therefore result from the combination of different reaction branches in the mechanism. Small energy differences in the profile can change the contribution of each path in the reaction rate and affect the orders and apparent activation energy. Computational results can be sensitive to errors in Free Energy values from various

approximations (DFT energy, entropy values), meaning it is very challenging to obtain accurate values³⁷. The impact of the sensitivity of the DFT accuracy is further illustrated in the supporting information (Figure B.12 and associated discussion). Combining theory and experiment is hence essential to provide detailed insights in such cases where reaction channels/branches compete.

3.3.5. Conclusions

In this study, we investigated the mechanism of CO oxidation on a single-atom Pt supported on anatase TiO₂ (Pt_{SA}/a-TiO₂) using a combination of DFT calculations, microkinetic analysis, experimental kinetic measurements, and several *in-situ/operando* spectroscopic techniques. Despite remaining as isolated atoms, Pt_{SA} species shows dynamic coordination behavior under different gas environments, *i.e.*, oxidative, reductive, and reactive. We show that despite the apparently simple system of a supported single Pt atom, the CO oxidation reaction on Pt_{SA}/a-TiO₂ involves a complex reaction mechanism consisting of initiation steps followed by a reactive cycle involving multiple competing pathways. As shown by the combination of DFT calculations and DRIFTS experiments, under reducing conditions the initial catalyst consists of a Pt_{SA} structure having an adsorbed/supported Pt atom on the anatase-TiO₂ (101) with one oxygen vacancy. The initiation steps consist of CO adsorption and healing of O vacancy with an O₂ molecule, followed by an Eley-Rideal type CO oxidation on the surface O₂ species involving another gas-phase CO and forming the supported Pt(CO) structure. The subsequent reactive cycle starts from the oxidation of Pt(CO) with O₂, and proceeds via competitive CO oxidation events occurring either from chemisorbed CO (Langmuir-Hinshelwood mechanism) or from additional gas phase CO (Eley-Rideal mechanism) forming a Pt(O)(CO) species. Another CO oxidation step follows, also through competition between two mechanisms, completing the cycle to form the initial Pt(CO) species. Microkinetic modeling reveals that the most abundant intermediates during steady-state

CO oxidation are Pt(CO) and Pt(O₂)CO, both exhibiting CO stretching frequencies close to the experimentally observed value of 2115 cm⁻¹. The kinetic measurements and the microkinetic modeling simulations from first principles show fractional positive CO and O₂ orders, originating from an O₂ dissociation and an Eley-Rideal CO₂ formation steps exhibiting the highest degree of rate control. Our study also shows that the reaction pathways proceed with the involvement of oxygen adatoms directly provided by O₂ dissociation, and not lattice oxygens as it would be the case for a Mars-van Krevelen mechanism. Our results show that microkinetic modeling is sensitive to the uncertainties in energies and barriers from DFT, and without experiments, could lead to incorrect conclusions regarding reaction rate, dominant reaction pathway, and most abundant reaction intermediates. Overall, our findings shed light on the intricate reaction pathways followed by even a seemingly simple single-atom catalyst system for a model CO oxidation reaction.

Chapter 4

Chemical Warfare Agent decomposition on Pt SA/a-TiO₂(101): reactivity & establishing descriptors

4.1. Introduction

The persistent threat posed by chemical warfare agents (CWAs) necessitates the development of effective and efficient neutralization methods. Among various strategies, the combination of metal oxide as a support for single-atom catalysts has emerged as a promising solution due to the unique opportunities to entrap agents on metal oxide^{30,64,97,129–133} and enhance decomposition by utilizing the reactivity of single atom catalyst^{13,131,134–137}. Recent advances in the study of DMMP/GB decomposition on SAC supported on MOF showcases examples of fruition of this idea. Cu supported on MOF UiO-66 was seen to be able to facilitate decomposition whereas the MOF was able to entrap the agent efficiently^{138,139}. Cu deposited as isolated metal cations was shown to be able to actively catalyze the decomposition of DMMP. Furthermore, DFT calculations show that these cations prevent the over binding of phosphate decomposition products at the zirconia node by occupying the bridged binding sites. The cationic states of Cu were calculated to be Cu (I) and Cu (II), with their oxidation states varying based on the pretreatment methods. The two combined factors of reduced Lewis acid strength and the obstruction of the zirconia node sites showcase the role of Cu SAC as an active site to facilitate the catalyst performance compared to the pristine MOFs.

The addition of SAC or nanoparticles could also alter the state of the electronic states on the surface, making it more favorable to form defects. It has been established before that defects such

as oxygen vacancies and hydroxyls may facilitate decomposition of CWA^{25,26,31,132,137,140,141}. Changing the PH or dissociative adsorption of H₂O on the surface was shown to facilitate the P-F bond cleavage onto the surface. Work by Son and Li et. al. showcases the doping of titania with Au NP encourages the presence of additional oxygen atoms at the Au/TiO₂ interface^{43,44,142}. This oxygen adsorption leads to charge depletion from the Au atoms, thereby creating more accessible vacant states to accept electrons from TiO₂. It is interesting to note that DFT calculations was able to reveal that the specific facet of titania (Au/TiO₂(001)) interface exhibits the greatest charge depletion.

This chapter continues to investigate the reactivity of Pt₁/a-TiO₂(101) towards various CWAs, aiming to identify the key reactive species and elucidate the underlying mechanisms of decomposition. Furthermore, we explore a range of descriptors that govern the reactivity of this catalyst system by first investigating the stability of 13 supported metal catalyst on anatase, followed by its reactivity using the key intermediates found during the decomposition of GB on the Pt system. These descriptors include properties that may be inherent to the metal: d-band center and Lewis acidity. This study aims to deepen the understanding of CWA decomposition mechanisms on Pt₁/a-TiO₂(101) and to establish a set of reliable descriptors that can predict catalytic performance. This work not only contributes to the field of chemical defense but also enhances our understanding of single-atom catalysis in environmental detoxification applications.

4.1.1. Computational Set-up

For the density functional theory (DFT) simulations, the Vienna Ab Initio Simulation Package (VASP) was employed⁷³. These calculations utilized the Perdew-Burke-Ernzerhof (PBE) functional to define exchange and correlation energies, complemented by the dDsC dispersion

correction to accurately account for van der Waals forces^{79,80}. The electron-ion interactions were modeled using the Projector Augmented Wave (PAW) method, and a plane wave basis set with a 500 eV cutoff was adopted^{83,143}. Titanium d orbitals was assigned an effective Hubbard U parameter of 4.2 eV, following the Dudarev approach to DFT+U, to capture the electronic structure details consistent with experimental observations of TiO₂, especially the localized electron behavior on surfaces with oxygen vacancies^{144,145}. The calculations aimed for electronic energy convergence within 10⁻⁶ eV and atomic force convergence at 0.03 eV/atom. Transition state structures and energies were determined using the Nudged Elastic Band Method with eight intermediate images.

The computational model utilized a periodic slab of anatase TiO₂(101) cut from a bulk TiO₂ crystal with lattice constants $a = 3.83 \text{ \AA}$ and $c = 9.63 \text{ \AA}$. Supported PtO₂ structure was chosen as it was shown to be the most stable supported Pt structure in oxidation condition shown in the literature. The surface lattice vectors are: $a = 19.35 \text{ \AA}$ and $b = 16.76 \text{ \AA}$ (Figure 4. 2.). The large unit cell was chosen in order to avoid intra-cell interaction error. The surface consists of four O-Ti-O trilayers (12 atomic layers). A vacuum distance of 15 Å is set between slabs to avoid periodic interaction in the z-direction. The bottom-most three atomic layers are frozen to mimic the bulk. The transition states were calculated using 8 images on a smaller test unit cell ($a = 11.61 \text{ \AA}$ and $b = 11.18 \text{ \AA}$). Found TS was recalculated to confirm the negligible effect of cell size towards the calculated barrier.

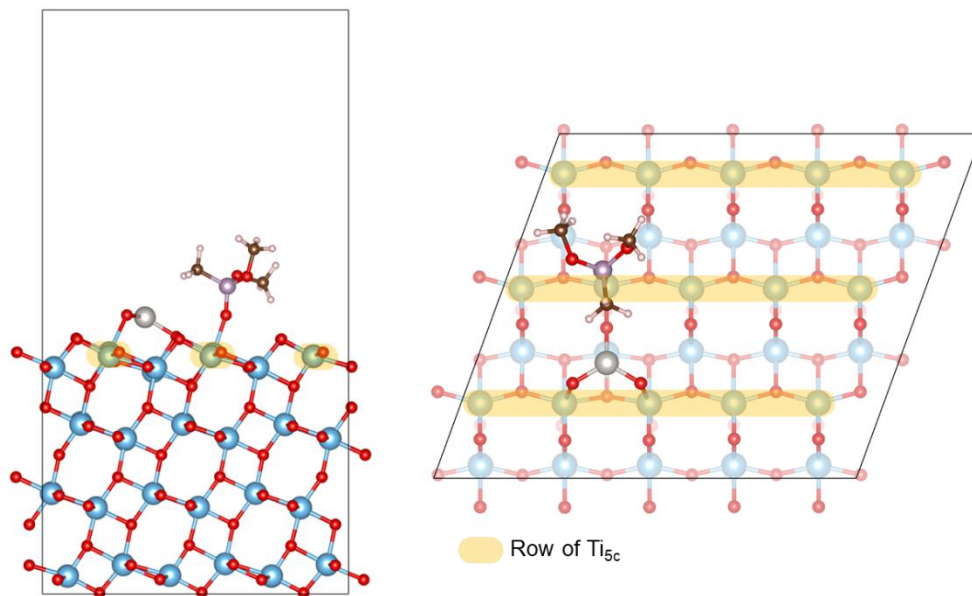


Figure 4. 1 Side and top representation of the unit cell used in the reactivity study. **Highlighted Ti sites in yellow signify the rows of Ti_{5c} .**

4.2. Results & Discussions

The binding modes and strength of DMMP and GB were calculated and shown on **Figure 4.1** and **Figure 4.2**. Overall, the adsorption of DMMP and GB with strongest adsorption energies of -1.93 eV and -1.61 eV, respectively. The most stable binding mode of DMMP follows an η_2 configuration (Ti-O-P=O-Ti) creating 2 P-O-Ti bond interactions with 2 Ti_{5c} sites (**Figure 4.1 A & B**). Adsorption via the phosphoryl group on Ti (P=O-Ti) bond only (denoted as η_1) reduces the adsorption energy by around ~ 0.3 eV (**Figure 4.1 C & D**). Adsorption on Pt sites on the other hand, is not very strong. DMMP physisorbs on Pt SA unless the Pt SA rearranges by cleaving the Pt-O_{2c} bond to accommodate DMMP via the phosphoryl P=O group to form the P=O-Pt bond (**Figure 4.1 E-F**).

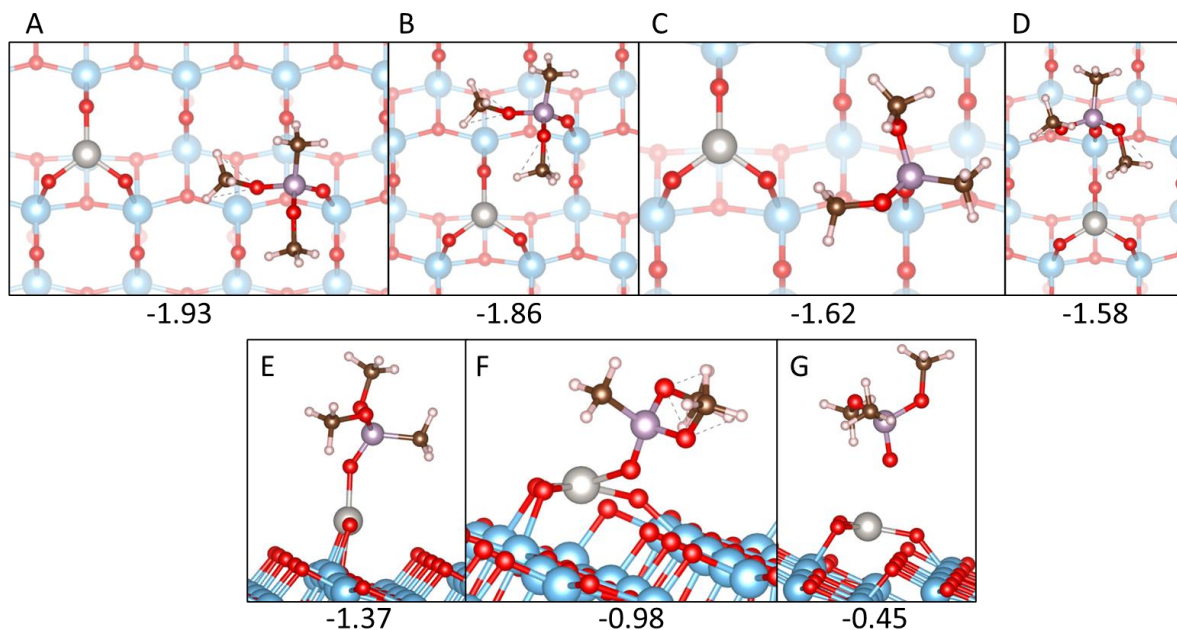


Figure 4. 2 Molecular adsorption modes of DMMP on Pt SA/TiO₂(101) with their adsorption energies.

Different adsorption behavior was seen on GB (**Figure 4.2**). Sarin adsorbs most favorably on rearranged Pt SA via dative P=O-Pt bond (**Figure 4.2 A**). Second best configuration adopts series of η_1 -adsorbed GB on Ti sites surrounding the Pt SA. Unlike DMMP, the η_2 configuration either via additional interaction of -F-Ti or $-(C_3H_7)O-Ti$ does not offer additional stabilization (**Figure 4.2 D, F, G**). The size and steric effects of the functional groups of sarin results in it having weaker binding with Pt/titania overall. Sarin's isopropyl group is bulkier than DMMP's methoxy groups, causing more steric hindrance and reducing the molecule's ability to approach and interact with the adsorption surface closely. Additionally, the presence of the fluorine atom in sarin can influence its electronic properties and interactions with the surface and does not offer stabilization with surface Ti sites. On the other hand, DMMP's smaller methoxy groups allow for closer and more effective interaction with the surface, leading to stronger adsorption. Similar to DMMP however, GB physisorbs weakly on the un-rearranged Pt SA species on the surface (**Figure 4.2 I-K**).

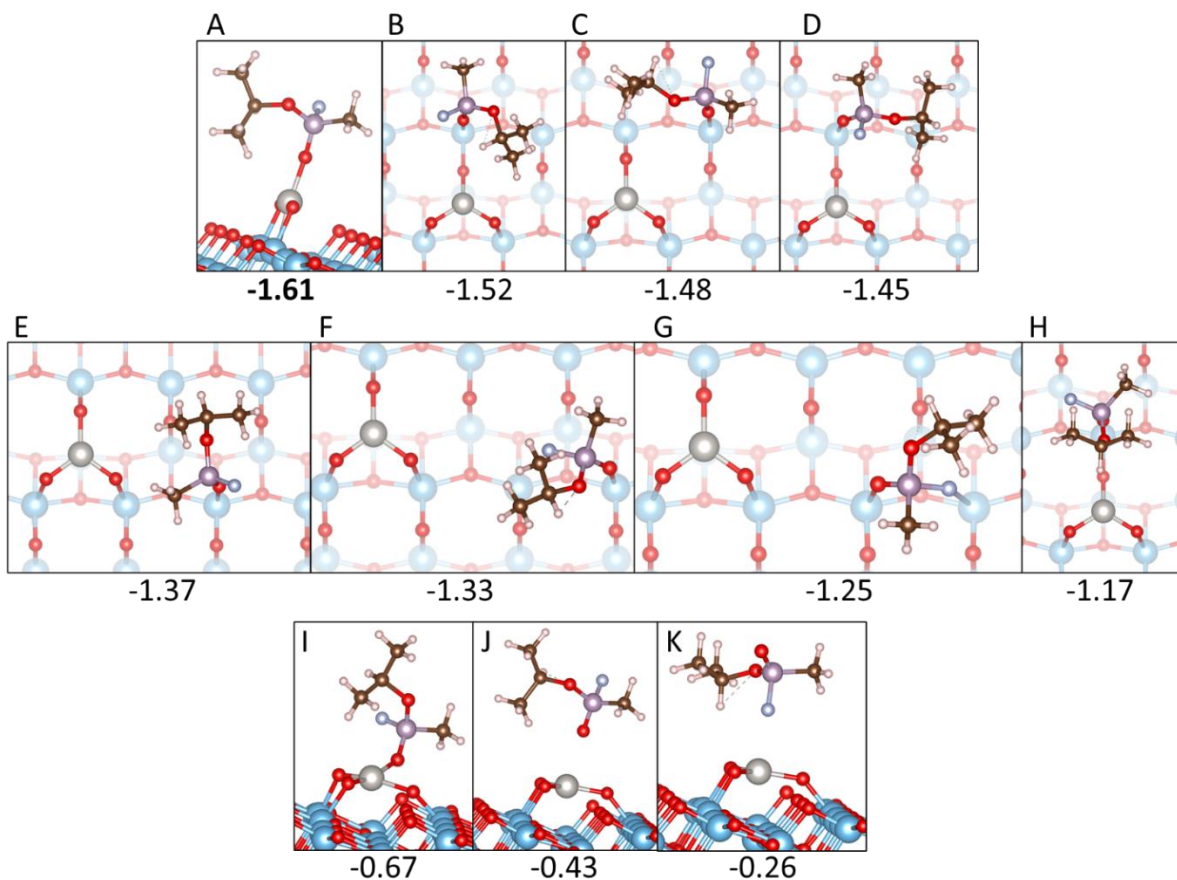


Figure 4. 3 Molecular adsorption modes of GB on Pt SA/TiO₂(101) with their adsorption energies.

4.2.1. Thermodynamic analysis

To quickly identify probable decomposition pathways upon adsorption, select ensembles of most stable and interesting molecular adsorption modes are used to investigate the thermodynamics of decomposition of both DMMP and GB via all possible bond cleavages (Figure 4.3). Yellow, green and black highlight represent structures being adsorbed on the titania whereas the blue highlight represents GB/DMMP adsorbed on the restructured Pt SA.

Let us first look at the thermodynamics of DMMP (**Figure 4.3 top left**). DMMP adsorbed on Pt can favorably cleave an O-C bond, transferring a -CH₃ group to an oxygen adatom, forming the

remaining $(\text{O})_2\text{P}(\text{CH}_3)(\text{OCH}_3)$. For adsorption modes where DMMP is adsorbed on Ti sites, however, there are clear endothermic trends to cleave the O-C bond cleavage. This was the opposite behavior compared to the undoped surface, in which the O-C bond cleavage was the most facile pathway.

In the case of P-O bond cleavage, DMMP adsorbed on Ti on the same Ti_{5c} row as the PtSA catalyst via η_1 mode (yellow) and those on different row via η_2 mode (black) are not viable for P-O and P-C bond cleavages for a couple of reasons: (1) the adsorbed DMMP is limited by distance to perform P-X cleavage, while transferring a methoxy or methyl onto the Pt and (2) the long pathway (>6 Angstrom) for P center to rebind with the nearest surface O_{2c} . As we have found in the literature, long pathway for P-O rebinding after P-X bond cleavage results in extremely high barrier and thus is unlikely to happen. An exception was intermediate ‘green’ where the DMMP is adsorbed on the neighboring Ti_{5c} row of those on which Pt SA resides. This positioning creates an accessible pathway to cleave P-O or P-C bond while keeping the P center fully coordinated with surface O_{2c} . Both of these processes (P-O and P-C) are exothermic by -1.17 and 1.39 eV for P-O and P-C respectively.

GB seems to exhibit a similar trend with DMMP, where O-C bond cleavage is in general endothermic no matter which site GB is being adsorbed and exothermic trend for P-X bond via GB adsorbing via η_1 mode on the neighboring Ti sites across the active Pt SA (green). It is interesting to note that the drive to cleave the P-X bond are not all of the same strength with P-C being the most favorable, followed by P-O and P-F bond. This behavior was seen before in the literature where P-F bond was deemed to offer less thermodynamic drive, but lower barrier to cleave. From adsorption to P-O, P-F and P-C bond cleavage, the energy stabilization stands at (ΔE ,

eV), 0.82, 0.72 and 1.47 eV respectively. There is a stark difference in the P-C bond cleavage behavior between GB and DMMP, perhaps due to the difference in electronic properties stemming from the -F group.

Literature suggests that C-H bond cleavage to trigger propylene release is the most favorable channel of decomposition seen on the pristine surface. Our calculations showcase that this process is uphill in electronic energy by average of ~ 0.7 eV, although this does not rule out the possibility that the release of propylene may allow for this process to be favorable due to the contribution of the propylene gas phase entropy. We conclude that DMMP/GB adsorbing on Ti via η_1 mode (green) is the most reactive adsorption mode and further kinetic study was performed on this intermediate.

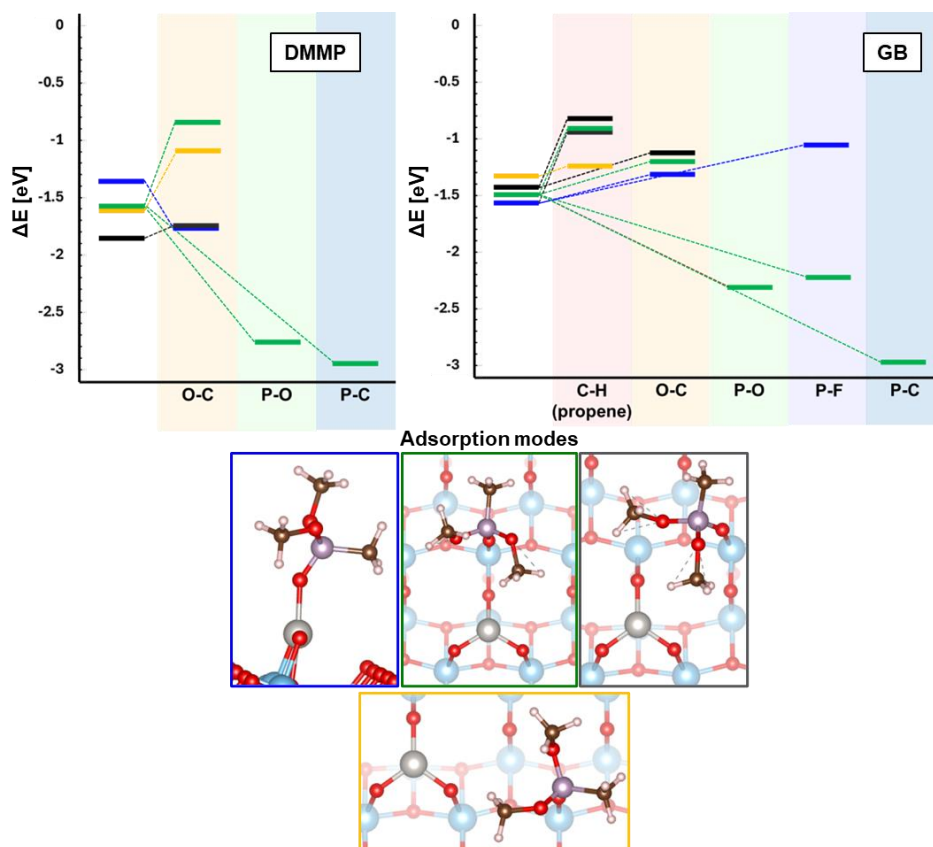


Figure 4. 4 Thermodynamic analysis of O-C, P-O, P-C, C-H and P-F bond cleavage for DMMP (top left) and sarin (top right). The selected ensemble of molecular adsorption for the thermodynamic study is shown on the middle bottom panel. The colors on the energy diagram correspond to each molecular adsorption mode shown.

4.2.2. Kinetic analysis

After confirming the most reactive adsorption modes and favorable bond cleavages, the decomposition of DMMP and sarin via P-O, P-C, and P-F bond cleavage pathways was calculated alongside its barriers.

For DMMP (Figure 4. 4, left), the P-O bond cleavage results in the formation Pt-OCH₃ and a phosphoryl intermediate, with an activation barrier 1.1 eV, much lower than the previously

reported system of pristine titania (rutile) of 2.2 eV. In contrast, the P-C bond cleavage pathway exhibits a significantly higher activation barrier of 2.25 eV. This higher barrier indicates that P-C bond cleavage is a less likely pathway under standard conditions. The relatively low barrier for the P-O bond cleavage and the fact that it is the only exothermic pathway for DMMP, suggest that P-O bond cleavage would be the primary reaction channel for DMMP. However, one must remember that in order to activate DMMP, it has to reorient from the most stable adsorption mode at -1.93 eV towards the activated adsorption mode at -1.58 eV (A-D), climbing the potential energy surface uphill by 0.35 eV. This makes the effective rate limiting barrier at 1.45 eV, making this reaction possible at approximately 562 K (using Transition State Theory approximation)

Sarin, on the other hand, demonstrates a similar preference for the P-O bond cleavage pathway, resulting in the formation of an isopropyl on Pt and a phosphoryl intermediate with an activation barrier of 0.75 eV. The P-C bond cleavage in sarin, has a barrier of 2.19 eV, further supporting the conclusion that P-C bond cleavage is less favorable.

Notably, the P-F bond cleavage pathway in sarin is also energetically feasible, but with much higher barrier of 1.35 eV in comparison to the P-O bond cleavage (0.75 eV). The reasoning behind this is that unlike the transfer of isopropoxy, Pt SA was not able to stabilize the 'bridging' Pt-O₄ planar-like intermediate using the interaction with the fluorine group; where the P-F bond is elongated to facilitate the new Pt-F bond, while at the same time interacting with the surface O_{2c}. Hence, the most probable channel of decomposition on sarin would also proceed via the P-O bond cleavage, with an effective rate limiting barrier of 0.84 eV (326 K).

The reaction energy diagrams for these pathways illustrate the similar chemistry between DMMP and Sarin, with sarin being slightly more active. For both molecules, decomposition via P-O and

P-F bond can be achieved via mild heating. The lower activation barriers for the P-O bond cleavage pathways in both DMMP and sarin underscore the primary role of Pt SA in the decomposition processes, due to its unique interaction with the methoxy/isopropoxy group in the decomposition of DMMP and sarin. This finding of course raises a question of whether DMMP is a good simulant for sarin, particularly to describe the reactivity of fluorine group on sarin.

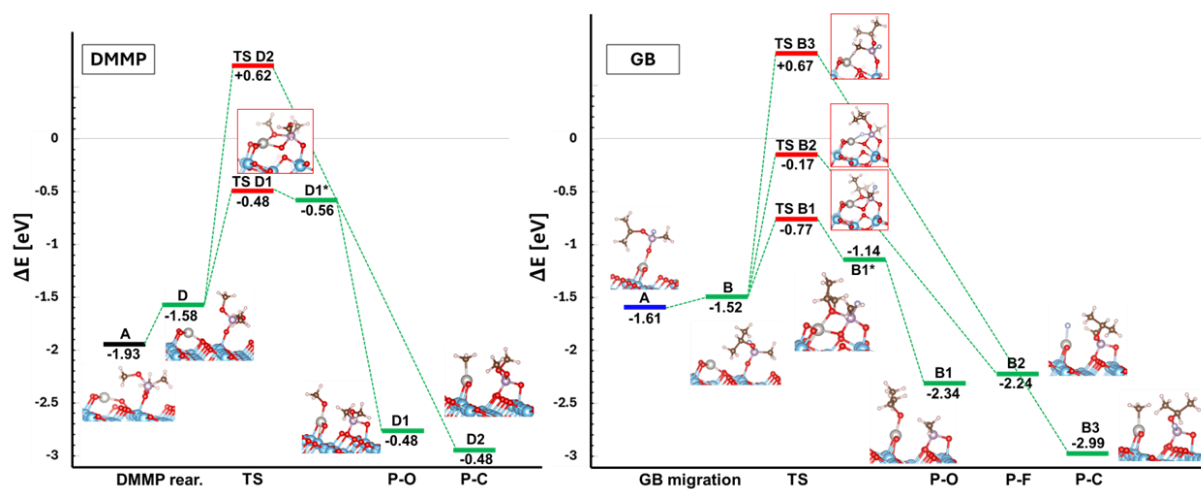


Figure 4. 5 Reaction pathway for P-X ($X=\text{OCH}_3$, OC_3H_7 or F) bond cleavage. Pathway for DMMP shown in left and sarin shown in right. The naming nomenclature follows the ID assignment from Figure 4.3 and 4.2.

4.2.3. Descriptor screening across transition metal

In our investigation, we first focused on studying the reactivity for Pt SA, which served as a benchmark for our subsequent analyses. Utilizing key intermediates and the so called ‘bridging’ state identified in this preliminary reactivity study, we expanded our scope to screen the reactivity of ten additional metals. This comprehensive screening aimed to identify metals that exhibit optimal reactivity and stability for our target reactions.

The stability of 10 selected transition state metal as a single atom supported on anatase titania was explored and calculated using the ab initio thermodynamic principles. As shown in stability diagram (Figure 4. 6), amongst all 10 metals, the system tends to adopt either an MO or MO₂ type of species on the surface (M=Metal). The stability diagram generally follows the electronegativity trend of the periodic table very well. Highly oxophilic (less electronegative) transition metals such as Pt, Ir, Rh and Ru adopt the MO₂ structure whereas highly electronegative species adopt the MO structure. Few metals with oxophilicity in between the two extremes are Co, Fe and Pd which seems to have competing MO and MO₂ stable states. This can also be correlated very well with the respective metal oxidation states. Metals that exist in more cationic phase (eg. Pt⁴⁺, Rh⁶⁺, etc.) tends to adopt the MO₂ states. This would also imply that the presence of less oxophilic metals such as Ag, Cu which exist in +1 oxidation state as a single atom seems to be unlikely. Although it is unlikely, for the sake of comparison, these systems will be included in the descriptor and reactivity study. Based on the stability diagram, 13 systems were chosen for further descriptor search: AgO, CuO, PdO, PdO₂, NiO, CoO, CoO₂, FeO, FeO₂, PtO₂, RhO₂, RuO₂, IrO₂.

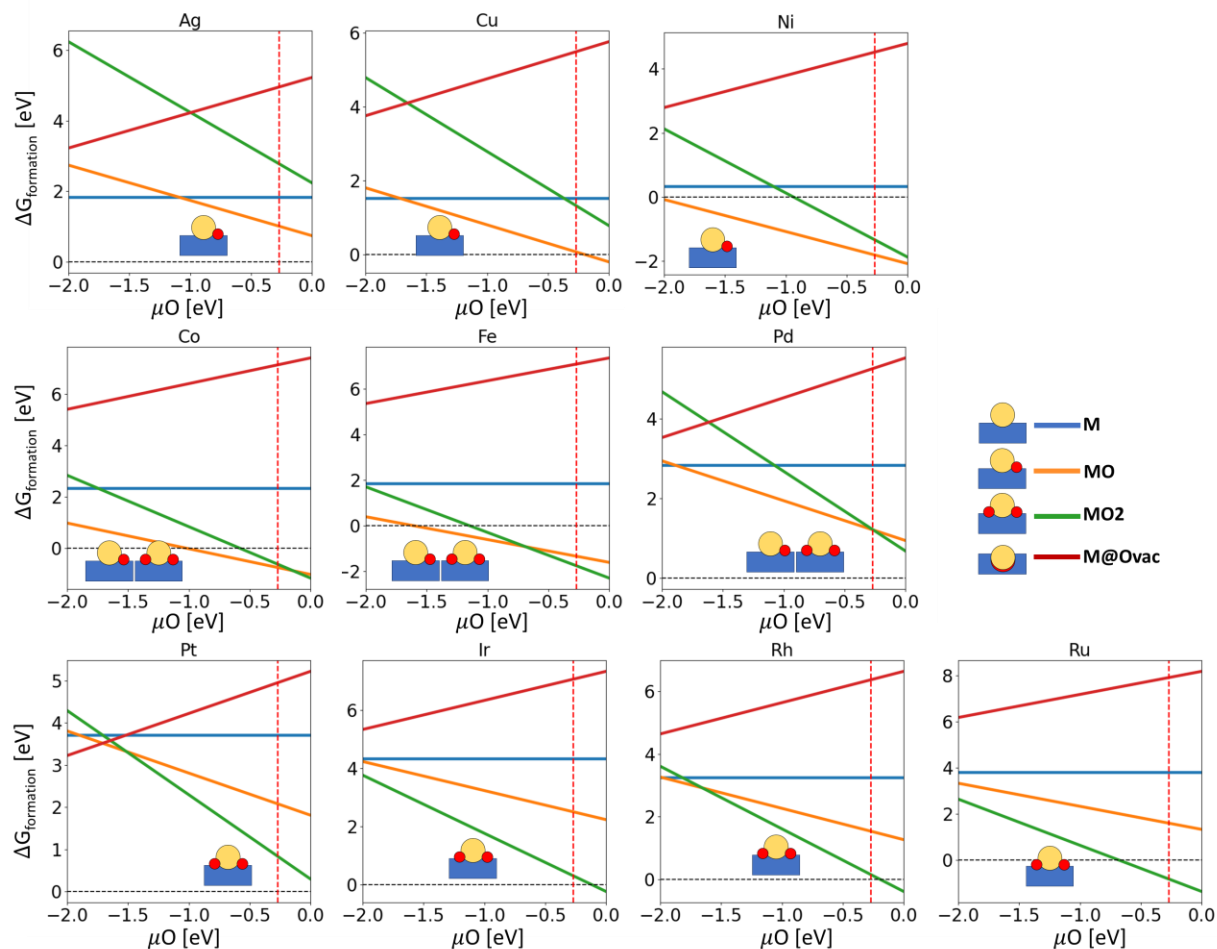


Figure 4. 6 Stability plot of 13 selected single metal atom catalysts plotted as a function of oxygen chemical potential. The vertical red line denotes oxygen chemical potential corresponding to the ambient condition. Each line color correspond to a chemical formula; MO_x (M : Metal, x =number of oxygen adatom).

In heterogeneous catalysis, the volcano plot is a common way to visualize the relationship between catalytic activity and the binding energy of a key intermediate. The plot typically shows catalytic activity on the y-axis and a descriptor, such as the adsorption energy of the intermediate, on the x-axis. The characteristic volcano shape suggests that there is an optimal binding energy that maximizes catalytic activity. If the binding is too weak, the intermediate does not adsorb

sufficiently, leading to low activity. Conversely, if the binding is too strong, the intermediate cannot desorb easily, also resulting in low activity. At the peak of the volcano, the binding energy is just right, resulting in the highest catalytic activity.

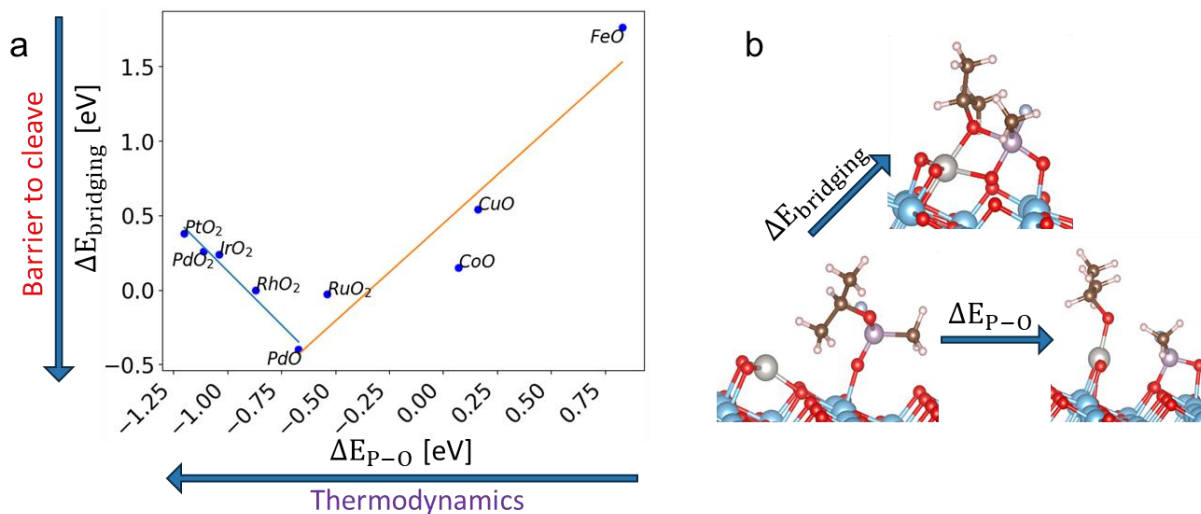


Figure 4. 7 (a) Volcano plot correlating the thermodynamic drive to cleave the P-O bond with the 'barrier' across all selected 13 transition state metals single atoms. (b) the schematic of parameter defining the activity ($\Delta E_{bridging}$) and thermodynamic (ΔE_{P-O}).

A volcano plot-like relationship was discovered in relation between the 13 d-transition metal for based on the key intermediates found in the decomposition pathway on Pt system, namely: (1) the quasi-stable 'bridging' Pt-O-P structure, as it facilitates the P-O bond cleavage, (2) the cleaved P-O bond intermediate (Figure 4. 7). In this particular 'volcano' plot, the trend illustrates the relationship between the thermodynamic drive to decompose the isopropoxy group and its kinetic (barrier). What is interesting to note, is that there is an interesting correlation; metals on the right side of the volcano plot, with weak (even endothermic) thermodynamic drive, correlates with more unstable TS-like bridging state to cleave the P-O bond. This is clear, since the binding of the metals is endothermic with the isopropoxy, it would less likely facilitate the formation of the bridging

intermediate. Conversely, catalysts on the left side, with stronger binding energies, also exhibit low activity because the isopropoxy binds too strongly, hindering the formation of the penta-coordinated P-center of the GB with the surface O_{2c} . Amongst metal which have favorable thermodynamic, fortunately, the energies of the bridging intermediate seems to be on a rather acceptable range that can be accessed with a mild heating.

Among the systems investigated, PdO, RhO₂, and RuO₂ were found at the peak of the volcano plot, indicating their optimal balance between the thermodynamic drive to cleave P-O and accessibility of the bridging intermediate, ideal to facilitating efficient decomposition. On the other hand, it is interesting to note that metal with either low oxophilicity or interesting magnetic properties such as AgO, NiO, FeO₂ and CoO₂ does not exhibit stable 'bridging' intermediate. For Ag, this could be due to the mismatch of the oxidation state that was enforced upon it being supported as AgO species (Ag (II)) and its commonly found oxidation states which are Ag(I) or Ag(III). Not to mention Ag (and Ni) is a metal with low oxophilicity, yielding to weak interaction with the isopropoxy. This can be seen by the ΔE_{P-O} of Ag and Ni being +0.13 and -0.08 eV respectively. One could also argue the fact that FeO₂ and

CoO₂ does not have a bridging state lies in its metal-oxygen bonds nature. If we take for example Pt-O and Pd-O, the nature of the metal-oxygen bonds in Pt and Pd oxides includes significant π -backbonding due to the availability of d-orbitals. This backbonding stabilizes the planar MO₄ geometry. Whereas Co-O and Fe-O do not have the same extent of d-orbital overlap with oxygen p-orbitals of the isopropoxy. This limits the ability of these metals to stabilize planar structures through π -backbonding, making them favor octahedral or other non-planar structures for increased stability.

It is also interesting to note that this volcanoic relationship does not give a holistic picture towards the complete reactivity behavior between the screened metals. One would expect that the ability to cleave the P-O bond would translate into the P-F bond. This is not entirely true. Figure 4. 8, a showcase the relationship between the drive to cleave the P-O and the P-F bond. Metals with high electronegativity and low oxophilicity have significantly huge deviation from the expected

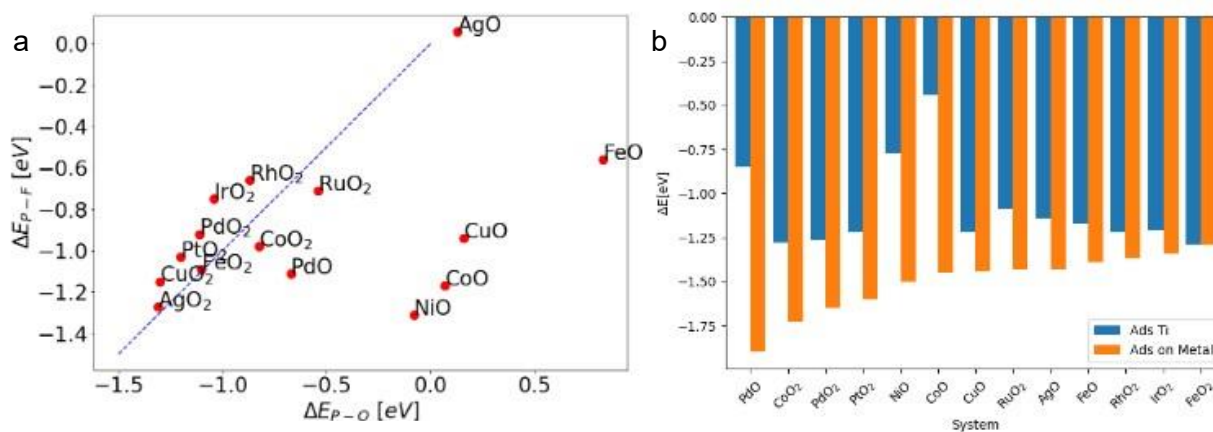


Figure 4. 8 (a) Comparison of the change of energy to cleave P-O vs P-F bond. (b) adsorption energy of sarin on various system compared between two different modes: on Ti sites ("Ads Ti") and on the active metal ("Ads on Metal")

Another point that one should consider is the energy required to bring the simulant or agent from the most stable adsorption mode towards the activated adsorption mode. Figure 4. 8 (right) showcase the adsorption energy trend across the system on two adsorption modes: on M site and on Ti (activated) site. There is a wide range of adsorption energy on the metal site from -1.34 (FeO₂) To -1.90 eV (PdO), a deviation range of 0.56 eV in comparison to GB adsorbing on the Ti sites (average of ~-1.25 eV across all metal, not including few exceptions: PdO, NiO, CoO; to be discussed later). This imbalance in adsorption energy is important because as we have shown before, the GB must migrate to the nearby Ti site to allow active metal to initiate favorable decomposition of P-X bond. Previous volcano plot suggested that PdO to be a promising candidate due to the ideal thermodynamic drive and accessible ‘bridging’ (TS) state. However, the strong adsorption of GB on Pd (-1.90 eV) and weak adsorption on Ti (-0.85 eV) means that on this system, GB must climb 1.05 eV in potential energy surface before initiating the P-X bond decomposition. This means, even though the bridging state of GB on PdO is more stable than molecularly adsorbed GB (-0.40 eV w.r.t. adsorbed GB on Ti), giving the illusion that P-O bond cleavage is barrierless, the potential effective barrier will still stand at 1.05 eV to account for GB diffusion from Pd site to Ti site. Morris et.al. suggest that Ti sites with stronger Lewis acidity helps increase the binding strength and dissociation of P-O bond cleavage of DMMP on titania. The strong adsorption of GB on these few select system may indicate a different pathway at play that is different from what we have seen on the Pt SA system. Secondly, adsorption of GB on Ti site seems to show consistent stable strength across d-transition metals with few exceptions: PdO, NiO, CoO. Suggesting that the metal modified the electronic structure of the Ti sites. Literature suggests that the deposition of these metal can significantly increase the formation of oxygen vacancy, which could alter the binding strength of GB on Ti sites.

4.2.4. Relating the activity with the d-state center of active SAC

The d-state (or d-band on bulk metal) center is one of the most used concepts to understand the catalytic activity of transition metals. Nørskov et. al. show that the position of the d-band center relative to the Fermi level can influence the strength of adsorption of reactants and intermediates on the metal surface, in which this understanding can be further expanded towards the Sabatier principle to ultimately guess the performance of a catalyst. This understanding is key to describe why certain metals are better catalysts than others.

Figure 4.9 showcases the relationship between few key reactivity parameters such as the thermodynamic drive to cleave P-O/P-F bond, perceived barrier, and adsorption on Ti sites. For all catalytic parameters chosen, there is a clear linear correlation for metal systems that have d-state center lower than -1.8 eV. As the d-state of the metals become farther than the Fermi level (lower than -1.8 eV), the thermodynamic drive to cleave either P-O or P-F bond cleavage increases and the binding strength of sarin on Ti sites increases as well (Figure 4. 9), indicating that metals with deeper d-state center may exhibit better P-X bond cleavage thermodynamics overall and are more unlikely to be poisoned by the molecular adsorbed sarin on the metal active sites. This correlation agrees well with the work of Nørskov et. al. which showcases the deeper d-band allows for deeper/more stable bonding orbitals with the adsorbed molecule. This signify that the metals with deeper d-state center will form stronger binding with the isopropoxy or fluorine fragment. On the other hand, deeper d-state suggests higher barrier to cleave the P-X bonds, in agreement with the Sabatier/volcano relationship found previously.

This simple correlation showcases that by simply checking an inherent parameter of the active metal catalyst such as d-state center, one can quickly predict the performance of the catalyst to

decompose CWA. Not only that, the inverse relationship between the thermodynamic drive of decomposition and the barrier suggests that there is an ideal d-state center values that optimizes the potential of both parameters, highlighting the potential predicting power of this simple descriptor to find previously unexplored catalyst systems.

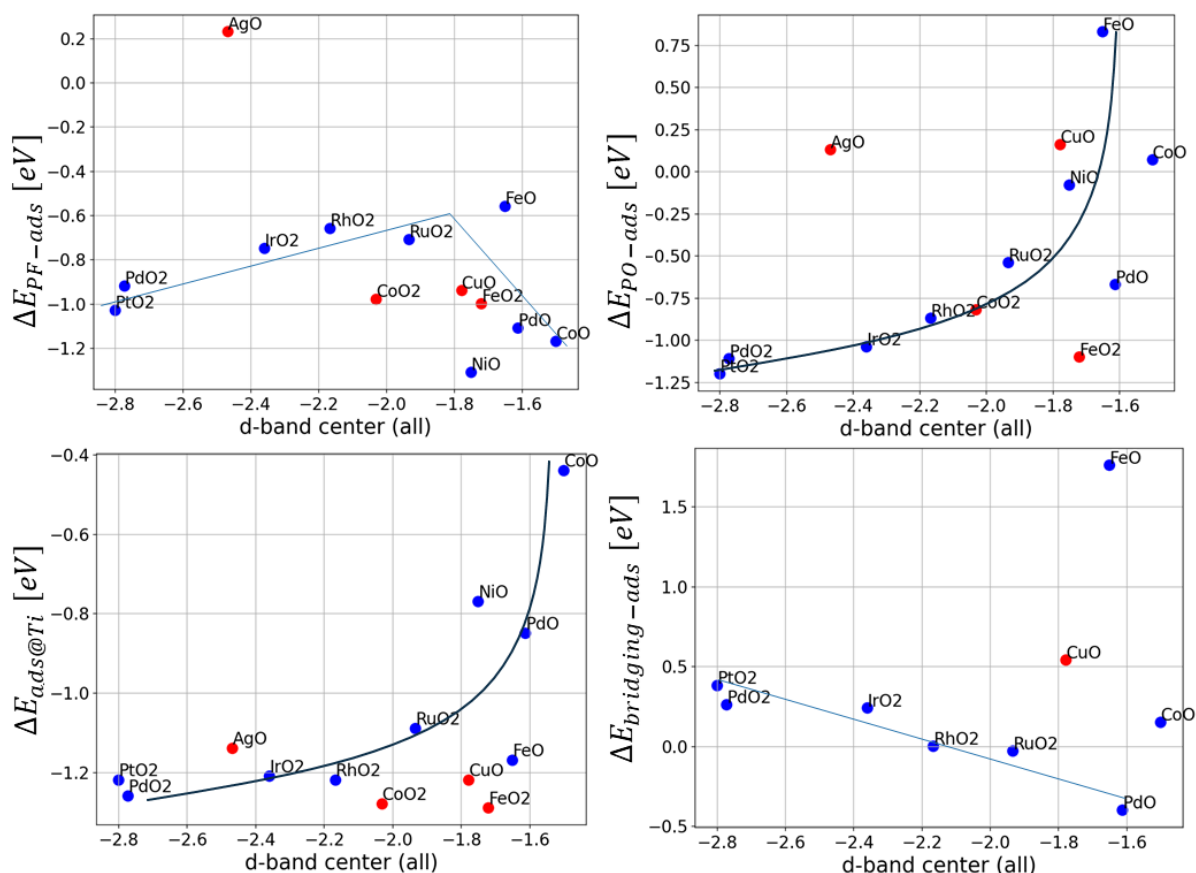


Figure 4.9 Various correlations between d-band center and (top left) the thermodynamics to cleave P-F bond, (top right) P-O bond, (bottom left) adsorption strength on Ti sites and (bottom right) the perceived barrier (the change in energy to reach the bridging intermediate from molecular adsorption).

4.2.5. Conclusion

In conclusion, we have studied the reactivity of Pt SA/a-TiO₂(101) catalyst towards sarin and its simulant DMMP using DFT. We show the different adsorption behavior between sarin and

DMMP, where DMMP prefers to adsorb via η_2 configuration on 2 Ti sites whereas sarin adsorbs stronger on the active Pt SA due to the steric hindrance of creating the similar η_2 configuration. However, a quick thermodynamic study shows that the two reactant seems to follow a similar pathway, where the DMMP/Sarin migrate to a Ti_{5c} site via η_1 binding mode ('activated molecular adsorption') on the neighboring row close to the active PtSA site before starting the decomposition. DMMP and Sarin decompose most favorably via the P-X (X=methoxy, methyl, isopropoxy and fluorine) bond cleavage, with P-O and P-F bond cleavage showing acceptable barrier ranging from 0.75 to 1.35 eV w.r.t activated molecular adsorption mode and thus can be achieved with a mild heating. This low activation barrier can be attributed to the Pt SA ability to stabilize the isopropoxy/methoxy group of sarin/dmmp in their penta-coordinated P center (binding with surface bridging oxygen). In order to do this, Pt SA adopts a very stable PtO_4 -planar like structure.

Using decomposition on Pt SA as a base, several key intermediates were chosen to establish reliable descriptors for predicting catalytic performance. The stability of 13 different d-transition metal/titania system studied in ambient condition. Metals with low oxidation state exist on the surface adopting the MO (M=Metal) chemical formula whereas metal that can adopt higher oxidation states adopt the MO_2 chemical formula. Key intermediates such as decomposed GB via P-O bond and P-F bond and the bridging intermediate were recalculated on the 13 metal systems to uncover an interesting 'volcano'-like relationship, where the metals which exhibit too low or too high thermodynamic drive to cleave P-O suffers in terms of kinetics. A deeper study of the inherent properties of the metal shows linear correlation between Lewis acidity of the metal system and its d-band center. We showcase that linear correlation can be established for reactivity pertaining to the P-O bond cleavage, specifically for metals with more Lewis acidity. Overall this study has deepened the understanding of CWA decomposition mechanisms on Pt SA/a- $TiO_2(101)$

and has established a set of descriptors that can be helpful in predicting catalytic performance of SAC/titania system.

Chapter 5

Decomposition of Dimethyl Methyl Phosphonate on Surface Modified TiO₂(110): Cu Clusters and Alkali Atoms

5.1. Introduction

The addition of an active transition metal (TM) to the oxide surface as a supported nanoparticle (NP) appears to enhance DMMP reactivity. There seems to be a correlation between the enhanced reactivity and the reducibility of the oxide. Despite this higher activity, the strong binding of the remaining POx residue also results in difficulties of the removal, which often poisons the surface.¹¹⁻¹⁶ More recent studies of single metal atoms supported on the metal oxide nodes of metal organic frameworks (MOFs), e.g., Cu@MOF-UiO-66, suggest that the isolated metal cation can be active for promoting DMMP decomposition, while also blocking the bridged binding site for phosphate decomposition products on the zirconia node. Unlike larger Cu NPs which are metallic, the single Cu atoms incorporated into the MOF were found to be cationic, Cu(I) and Cu(II), with the distribution of oxidation states dependent on pretreatment. Theoretical studies on the Cu@UiO-66 system show that the weaker Lewis strength of the Cu cations and the blocking of zirconia node sites should result in overall better performance than the pristine MOFs. In chapter 2, we showed that reduced Ti³⁺ cations at O-vacancies act as adsorption sites for DMMP, but with a slightly lower adsorption energy compared with the pristine surface, consistent with the lower cation acidity.²⁹ Oxygen vacancies are shown to play an important role in reducing the barrier for P-OCH₃ cleavage, but the barrier values remain rather high and decomposition is unlikely below ~600 K consistent with experiments on bare TiO₂(110).^{26,29}

In this work, we explored the decomposition of DMMP on ultrasmall Cu_4 clusters supported on a reducible support, $\text{TiO}_2(110)$, with and without the presence of an alkali metal modifier, i.e., K atoms. This combination of materials adopts many modifications expected to improve CWA decomposition and catalyst regeneration by decreasing the metal particle size to promote the formation of cationic Cu atoms via direct interaction with the titania support; (2) use of a reducible oxide, TiO_2 , to allow the formation Ti^{3+} cations with lower Lewis strength via O-vacancy formation; (3) adding an alkali modifier (K) to further increase the basicity of the oxide support to weaken DMMP interactions. The co-deposition of an alkali atom, K, is hypothesized to enhance the basicity and reducibility of the TiO_2 support via electron transfer, e.g., $\text{K} + \text{Ti}^{4+} \rightarrow \text{K}^+ + \text{Ti}^{3+}$.³⁰⁻³⁴ The increased basicity of the surface is expected to weaken the strength of the $\text{P-O-Ti}^{3+/4+}$ bonds, making it easier to remove the final PO_x decomposition products.³⁵⁻³⁶

Surfaces of $\text{Cu}_4/\text{TiO}_2(110)$ and $\text{K}/\text{Cu}_4/\text{TiO}_2(110)$, noted hereafter as Cu and K-Cu, respectively, were tested for reactivity with DMMP using near ambient pressure XPS at a pressure of 1×10^{-4} Torr of DMMP. The P 2p and C 1s core level spectra were used to identify surface intermediates resulting from adsorption and decomposition of DMMP and their stabilities on the surfaces from room temperature to 800 K. Detailed ab initio DFT calculation were performed to determine the structures of the Cu and K-Cu surfaces and elucidate the complex decomposition pathways that involve synergistic interactions between Cu_4 , K and the TiO_2 surface. The calculations show that the Cu_4 clusters strongly promote P-O, O-C and P-C bond cleavage of DMMP by stabilizing the products of these decomposition and are highly fluxional with atomic structures that depend on the configuration of fragments bound to the surface. Moreover, the large number of energetically accessible configurations of decomposition products results in a near

continuous distribution of calculated P 2p chemical shifts that proposes an alternative approach to assigning broad, unresolved core level spectra.

5.2. Computational methods

The density functional theory (DFT) calculations in this study were performed using the Vienna Ab initio Simulation Package (VASP). The Perdew-Burke-Ernzerhof (PBE) functional was employed, along with a Hubbard U correction of 4.2 eV applied to Ti sites to better describe the onsite coulomb repulsion of the Ti 3d orbitals. This particular U value of 4.2 eV was chosen to accurately represent the electronic structure observed experimentally in TiO₂, particularly in relation to the localized nature of electrons on surfaces with oxygen vacancies. The dDsC dispersion correction was implemented to account for long-range van der Waals interactions. The one electron orbitals are developed on a basis set of plane waves, with a cutoff energy set at 500 eV and the convergence criterion were established at 10⁻⁶ eV for electronic energies and within 0.03 eV/Å for atomic forces. To correct for the spurious dipole-dipole interaction between neighboring slabs in the z-direction, the Harris correction (Makov-Payne) was applied. Transition states were determined using the Nudged Elastic Band Method with eight intermediate images, with climbing image turned on after the forces of all images are below 0.1 eV.

The adsorption energies and reaction pathway energies for systems with Cu₄ and Cu₄K were calculated using Equation 1 and 2 respectively:

$$E_{DMMP_{ads}} = E_{intermediate} - E_{TiO_2+Cu_{cluster}} - E_{DMMP} \quad (5-1)$$

$$E_{DMMP_{ads}} = E_{intermediate} - E_{TiO_2+Cu_{cluster}+K} - E_{DMMP} \quad (5-2)$$

The 2x5 TiO₂(110) surface was built from the bulk crystal structure. The bulk lattice constants were computed with a gamma-centered k-points mesh of 4x4x4, resulting in values of $a = 4.65 \text{ \AA}$ and $c = 3.02 \text{ \AA}$. The 2x5 surface lattice vectors were determined from the bulk geometry as $a = 13.16 \text{ \AA}$ and $b = 15.09 \text{ \AA}$. This surface comprised four O-Ti-O trilayers, equivalent to 12 atomic layers. A vacuum distance of 15 \AA was introduced between slabs to prevent periodic interactions along the z-direction. The bottom three atomic layers were kept frozen to emulate the bulk. All surface calculations employed a k-point mesh of 1x1x1. Using a larger k-points mesh (e.g., 3x3x1) or thicker surface models did not yield significant differences compared to our selected 2x5 surface, calculated at the gamma point.

A total of 22 and 25 isomers of deposited Cu₄ clusters and Cu₄ clusters with K atoms were manually generated and explored exhaustively. The stabilities of each isomer are expressed relative to the most stable one. Subsequently 290 isomers of molecular and dissociative DMMP adsorption were explored on the Cu₄/TiO₂ and K/Cu₄/TiO₂(110) surfaces.

5.3. Results

5.3.1. Experimental Characterization of Cu₄/TiO₂(110) and K/Cu₄/TiO₂(110)

Figure 1 provides a summary of the state of the Cu and K–Cu surfaces prior to DMMP exposure. The level of reduction of the TiO₂(110) support was inferred from Ti 2p XPS spectra that were fitted to contributions from Ti⁴⁺ and reduced Ti³⁺ cations that appeared at lower binding energies. Figure 1a,d shows that the TiO₂(110) surface is only slightly reduced for both the as-prepared Cu (3.8% Ti³⁺) and K–Cu (7.5% Ti³⁺) surfaces; adding K increases surface reduction as expected for electron transfer to the TiO₂ support (Figure 1d). The Cu 2p spectrum in Figure 1b is characteristic of both surfaces with the binding energies consistent with Cu⁰ and/or Cu¹⁺ as these

oxidation states are too close to be resolved. Moreover, the K 2p binding energies are consistent with completely ionized K⁺ when deposited onto oxide surfaces (Figure 1e). (39,50) The Cu LMM Auger spectra are complicated by overlap with the Ti 2s core level and associated satellites, but the satellite peak at ~577.4 eV is largely free of overlap and was used to fix the Ti 2s contributions for the entire spectrum. The relative intensities and peak widths for the Ti 2s states were experimentally determined from the bare TiO₂(110) surface. The least-squares fits included LMM contributions from both Cu⁰ and Cu¹⁺ along with the scaled Ti 2s peaks, but the Cu⁰ contribution was found to be too small to fit with confidence (see the SI for the description of fitting). (51) The sharp peak near 570.1 eV (kinetic energy of 916.6 eV) is a signature of Cu¹⁺, whereas Cu⁰ has a characteristic peak near 568.3 eV (kinetic energy of 918.4). As shown in the SI, significant Cu⁰ contributions are only observed in LMM Auger spectra taken after exposure to DMMP and heating to 900 K (Figure C. 1). Hence, the fits shown in Figure 1c,f only include contributions from the Cu¹⁺ LMM and Ti 2s photoemission peaks; these spectra indicate that Cu¹⁺ is the dominant oxidation state in the Cu₄ clusters on the as-prepared Cu and K–Cu surfaces.

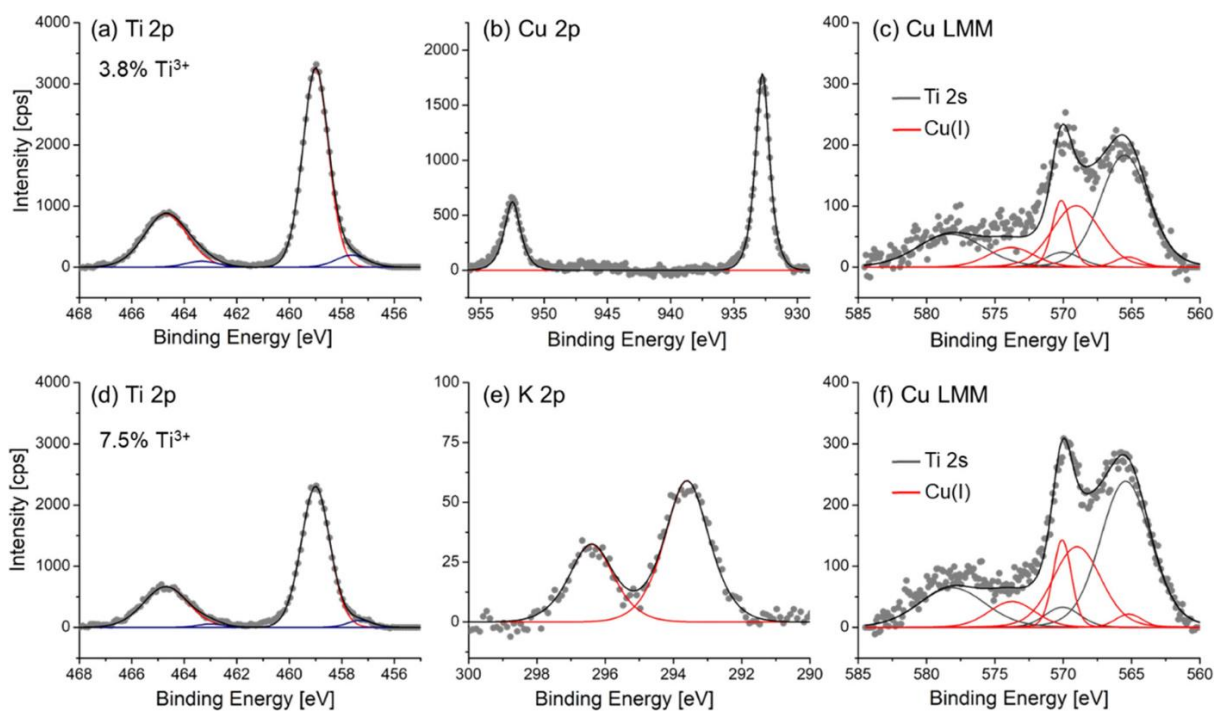


Figure 5. 1 Surface characterization using (a, d) Ti 2p, (b) Cu 2p, and (e) K 2p XPS spectra and (c, f) Cu LMM Auger spectra prior to DMMP exposure for the (a–c) $\text{Cu}_4/\text{TiO}_2(110)$ and (b–f) $\text{K}/\text{Cu}_4/\text{TiO}_2(110)$ surfaces.

5.3.2. Theoretical description of $\text{Cu}_4/\text{TiO}_2(110)$ and $\text{K}/\text{Cu}_4/\text{TiO}_2(110)$ surfaces and adsorption of molecular DMMP

The calculated lowest energy structures of the Cu and K-Cu surfaces are shown in Figure 2. The Cu_4 cluster on $\text{TiO}_2(110)$ maximizes the interaction with the surface by adopting monolayer structures, either as flat rhombus or square geometries, while the tetrahedral structure lies +0.64 eV higher in energy (Figure 5. 2, top row). The Cu atoms interact with bridging O atoms of the $\text{TiO}_2(110)$ surface. These structures are similar to those found in previous DFT calculations of Cu_4 clusters on $\text{TiO}_2(110)$.¹⁷⁻²⁰ From the Bader charge analyses shown in Figure 3C, the Cu_4 cluster donates 0.84e to the surface for the most stable configuration, which results in spin density

localization observed on the two Ti atoms located below the Cu_4 cluster (with values ~ 1 and $0.1 \mu\text{B}$, Figure 3A).

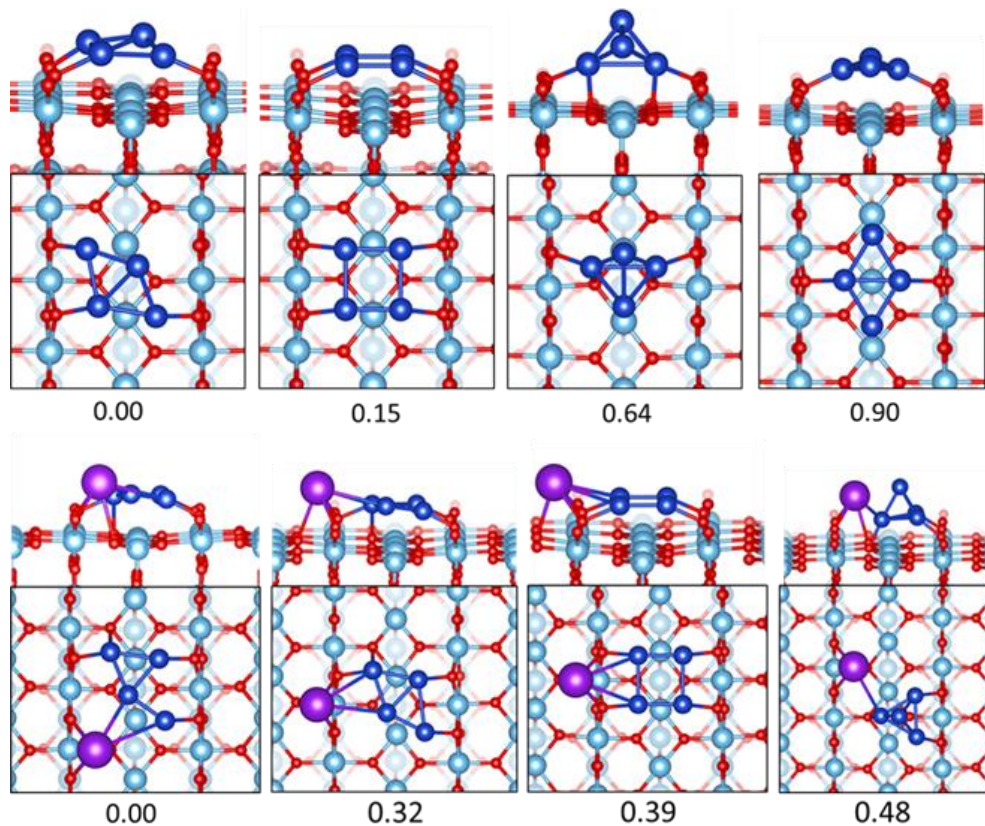


Figure 5. 2 *Lowest energy structures for $\text{Cu}_4/\text{TiO}_2(110)$ and $\text{K}/\text{Cu}_4/\text{TiO}_2(110)$. Values below each structure denotes the relative stabilities (in eV) with respect to the most stable isomer.*

The K atom prefers to interact with both TiO_2 and the Cu_4 cluster, inducing a deformation of its geometry (Figure 5. 2, bottom row). The electron charge donated to the TiO_2 surface increases to $\sim 1.4e$ with the addition of both K and Cu_4 , but the electron transfer is mostly from the K atom (Figure 3F). Here, the K atom is completely ionized, creating a localized electron on a surface Ti atom in the vicinity (spin $1 \mu\text{B}$, Figure 5. 3D). The Cu_4 cluster donates less electrons to the surface (~ 0.5) in the presence of K (Figure 5. 3F). Nonetheless, the calculations suggest

the presence of cationic $\text{Cu}^{\delta+}$ atoms on surfaces with and without K, which is in qualitative agreement with the observed Cu LMM Auger spectra (Figure 5. s 1c ad 1f).

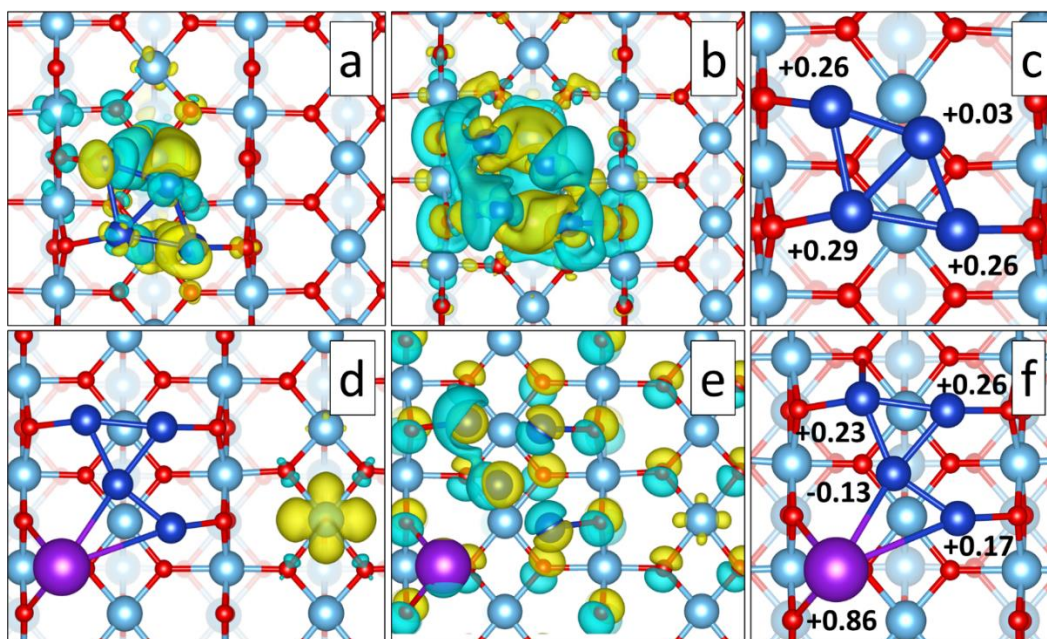


Figure 5. 3 (a, d) Electronic spin density for the most stable (a) $\text{Cu}_4/\text{TiO}_2(110)$ and (d) $\text{K}/\text{Cu}_4/\text{TiO}_2(110)$ structures; (b, e) charge density difference upon adsorption of (b) Cu_4 and (e) K-Cu_4 adsorption on $\text{TiO}_2(110)$. The yellow and blue color denotes spin up and down density or charge accumulation and depletion, respectively. (c, f) Electronic Bader charge for (c) Cu_4 and (f)

The calculated lowest energy structures for binding molecular DMMP on the Cu and K-Cu surfaces are shown in Figure 4. DMMP prefers to bind to the $\text{TiO}_2(110)$ surface and not onto the Cu_4 cluster or K atom. For the lowest energy configurations (Figure 5. s 4a and 4e), DMMP binds in an $\eta_2\text{-O-P-O}(\text{CH}_3)$ configuration to two Ti_{5c}^{4+} cations aligned along the $[001]$ direction of the $\text{TiO}_2(110)$ surface, while the second methoxy and the methyl groups are oriented perpendicular along the $[1\bar{1}0]$ direction. This DMMP adsorption structure is essentially identical to that predicted for DMMP on the bare $\text{TiO}_2(110)$ surface.^{29,51} On the Cu surface (Figure 5. 4a), the Cu_4 cluster is

located in the same row as DMMP and adopts a square geometry by forming four Cu-O bonds with nearby bridging O-atoms. This is also the case on the K-Cu surface (Fig 4e) although the

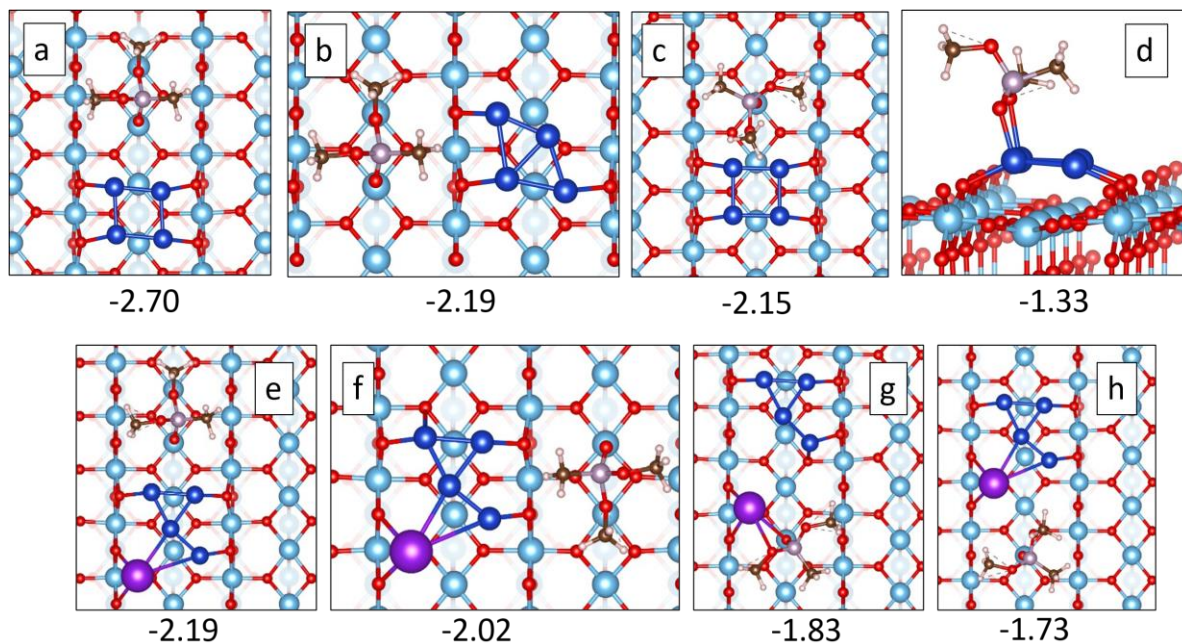


Figure 5. 4 Low energy surface configurations for DMMP adsorption on (a-d) Cu₄/TiO₂(110) and (e-h) K/Cu₄/TiO₂(110). DMMP adsorption energies are shown below each (in eV).

structure of the Cu₄ cluster is modified by direct interactions with the K atom. For the other low-lying isomer configurations, DMMP remains mostly bonded to the TiO₂(110) surface, but can also interact with the Cu₄ cluster (Figure 5. 4c) or K atom (Figure 5. 4g).

Although the lowest energy adsorption structures for DMMP on the Cu, K-Cu, and bare TiO₂(110) surfaces are essentially the same, the DMMP adsorption energies show that the addition of the Cu₄ cluster strengthens DMMP binding (-2.70 eV), while K addition destabilizes DMMP binding (-2.19 eV) relative to DMMP on the bare TiO₂ (110) surface (-2.35 eV). The latter value was recently reported by Tesvara, et al., using a similar level of DFT.^{29,51} The lower DMMP adsorption energy on the K-Cu surface is attributed to the additional electron charge donated from

the K atoms to the TiO₂ surface as indicated by the calculated Bader charges (Fig.s 3c and 3f). Lowering the binding energies of DMMP and its decomposition fragments is one of the expected outcomes of alkali addition, as electron transfer to the TiO₂ surface should effectively decrease the Lewis acidity of the Ti_{5c} cations and weaken bonds to electrophilic adsorbates like DMMP.

5.3.3. NAP-XPS results for DMMP exposure at room temperature

The P 2p spectra shown in Figure 5 for the Cu and K-Cu surfaces exposed to DMMP at RT consist of a number of overlapped peaks that extend over a range of ~8 eV. The spectrum for the Cu only surface (Figure 5.5a) could be fit to four P 2p doublets (labeled P₁-P₄) where the peak widths and doublet separations (0.85 eV) were constrained to be the similar.⁵² For the K-Cu surface (Figure 5.5b), the spectrum starts at lower binding energy and requires only three P 2p doublets to fit the data, with binding energies essentially the same as peaks P₂-P₄ in the Cu spectrum. By comparison, the K only surface exhibits only one P 2p peak (Figure 4c), with a fitted binding energy identical to peak P₁ in the Cu only spectrum. We note that the K only spectrum was obtained by moving the small NAP-XPS entrance aperture (~300 μm) to the edge of the K-Cu surface where there was no detectable Cu; the Cu₄ cluster deposition area was limited to region 3-4 mm (dia) near the center of the TiO₂(110) substrate.

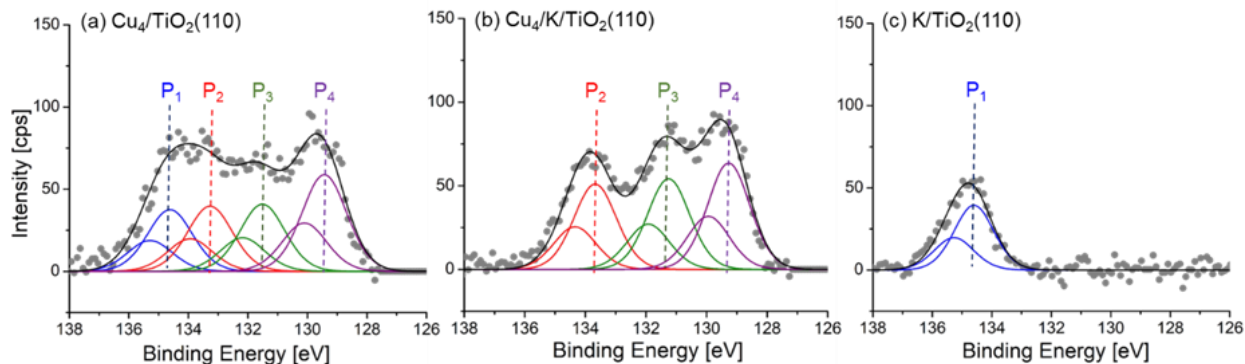


Figure 5. 5 P 2p XPS spectra showing phosphorous surface species during exposure of 1×10^{-4} Torr of DMMP at room temperature on the surfaces of (a) Cu_4/TiO_2 , (b) $\text{K}/\text{Cu}_4/\text{TiO}_2(110)$ and $\text{K}/\text{TiO}_2(110)$. The different colored solid lines correspond to least-squares fits.

Table 5. 1 Summary of P 2p and C 1s binding energies for DMMP on $\text{TiO}_2(110)$ surfaces with and without Cu_4 clusters and K atoms, along with data from previous studies on related surfaces

Surface	P ₁	P ₂	P ₃	P ₄	C ₁	C ₂	C ₃
K/Cu₄/TiO₂	----	133.7	131.3	129.3	288.8	287.0	285.5
Cu₄/TiO₂	134.6	133.3	131.5	129.4	288.9	287.2	285.4
K/TiO₂	134.6	n/a	--	--	288.7	287.3	285.8
TiO₂^a	134.9 ^g	--	--	-	--	287.7 ⁿ	286.3 ^o
Cu-NP/TiO₂^b	134.9 ^g	133.7 ^h	--	-	--	287.7 ⁿ	286.3 ^o
Ni-NP/TiO₂^c	134.5 ^g	133.7 ^h	--	129.1 ^l	--	287.8 ⁿ	286.3 ^o
Pt-NP/TiO₂^d	134.8 ^g	134.0 ^h	--	129.5 ^l	--	287.8 ⁿ	286.3 ^o 284.6 ^p
CuO^e	133.8 ^g	132.8 ⁱ	---	--	288.1 ^m	287.1 ⁿ	285.1 ^o
Cu₂O^f	134.1 ^g	133.1 ⁱ	132.1 ^j 130.0 ^k	128.9 ^l	--	286.4 ⁿ	284.2 ^o
^a Ref [26] UHV dose at RT ^b Ref [12] UHV dose at RT ^c Ref [16] UHV dose at RT ^d Ref [11] UHV dose at RT ^e Ref [21] exposure to 1x10 ⁻⁴ Torr DMMP at RT ^f Ref [22] exposure to 1x10 ⁻⁴ Torr DMMP at RT ^g Chemisorbed DMMP ^h PO _x ⁱ Methyl methyl phosphonate (MMP) O=P(OCH ₃)(CH ₃)O				^j Phosphinate, O=PH(OCH ₃)O-Cu ^k Phosphine, Cu-P-CH ₃ or O-P-CH ₃ ^l Atomic phosphorous, P-Cu or P-O ^m carbonate, CO ₃ ²⁻ ⁿ methoxy, -OCH ₃ ^o P-CH ₃ ^p Pt-CH _x			

The binding energies for the best-fit P 2p_{3/2} peaks for all three surfaces are given in Table 1 along with those obtained on related surfaces reported in the literature. The 2p_{3/2} binding energy for P₁ (134.6 eV) is similar to chemisorbed DMMP on bare TiO₂(110),²⁶ Ni and Pt nanoparticles (NPs) supported on TiO₂(110)^{11,53} and bulk Cu₂O²² and CuO²¹ surfaces. Additional support for assigning P₁ to chemisorbed DMMP comes from P 2p XPS spectra which show that P₁ disappears from the Cu surface at ~500 K (see Figures 7a and S3b). On TiO₂(110) surfaces with and without metals, chemisorbed DMMP was shown to desorb reversibly and/or decompose at temperatures > 400 K.^{11-12,16,26} Hence, we assign P₁ to intact, chemisorbed DMMP. As P₁ is the only peak observed on the K-only surface (Figure 5.5c), we conclude that the K-only surface is unreactive with respect to DMMP at RT, similar to bare TiO₂(110).^{26,29} Moreover, the fact that P₁ does not appear in the P 2p spectrum for the K-Cu surface (Figure 5.5b) indicates that intact DMMP is not stable on this surface at RT and is thereby more reactive than the Cu or K-only surfaces.

The P₂-P₄ peaks appearing at lower binding energies are assigned to the decomposition products of DMMP in line with previous studies. In particular, the P 2p spectra for the Cu and K-Cu surfaces are similar to those obtained for DMMP exposure on a polycrystalline Cu₂O surface using NAP-XPS under identical conditions, i.e., RT and 1x10⁻⁴ Torr of DMMP.²² On the Cu₂O surface, the P 2p peaks from highest to lowest binding energies were assigned to chemisorbed DMMP, methyl methylphosphonate (MMP), phosphinate, phosphine (P-CH₃), and atomic phosphorous (P).²² These assignments indicate that the degree of DMMP fragmentation and P-atom reduction increases with decreasing P 2p binding energy. Although the P 2p binding energies for the Cu₂O surface differ somewhat from those observed here (see Table 1), we can tentatively and initially assign the P₂ peaks to MMP and P₄ to atomic-P, while the P₃ peak results from unresolved contributions from other species such as phosphinate and phosphine. These

assignments will be later reanalyzed in the light of the theory simulations. The assignments for P₂ (MMP) and P₄ (atomic P) are consistent with those proposed for Ni and Pt NPs supported on TiO₂(110), and both are observed at temperatures ≥ 400 K, while only P₄ is present after heating to 850 K.^{11,53} In sharp contrast to the results presented here, larger Cu nanoparticles (4-15 nm) supported on TiO₂(110) were reported to be mostly unreactive towards DMMP at saturation coverage, with only the P₂ species present at RT and a very small contribution from P₄ after heating to > 700 K.¹² Although the DMMP exposure conditions were very different in the latter work, the results presented here (Figure 5.5) strongly suggest that the small Cu₄ clusters with and without co-deposition of K are far more reactive than larger Cu nanoparticles on the same support, TiO₂(110).

The C 1s core level spectra for the Cu and K-Cu surfaces taken under 1×10^{-4} Torr of DMMP at RT are shown in Figure 6. These spectra were obtained by subtracting the background spectrum taken under UHV prior to DMMP exposure. This eliminates contributions from adventitious carbon (C_{ad}) and other species resulting from the decomposition of background gases during the transfer and exchange of samples in the NAP-XPS instrument. The resulting spectra could be least-squares fit with three peaks, C₁-C₃, with similar, but not identical binding energies on all three surfaces. The fitted C 1s binding energies are given in Table 1. Earlier studies of DMMP on bare TiO₂(110)²⁶ and metal NP's (NPs; Cu, Ni, Pt) supported on TiO₂(110)^{11-12,53} found C 1s peaks with binding energies very close to that observed here for C₂ and C₃; the latter were assigned to methoxy (*OCH₃) and methyl (*CH₃), respectively. As shown in the calculations described later, both methoxy and methyl can be bound to the P-atom in DMMP or DMMP fragments, and as dissociation products bound to the Cu₄ clusters or Ti⁴⁺ cations on the TiO₂ surface. The higher binding energy for the C₁ peak is in the range for formate (HCOO*) and

carbonate (CO_3^*) which have been observed in IR spectra of titania-supported powder systems exposed to ambient pressures of DMMP.^{24,28} Here we will identify C_1 as an oxidized carbon species, CO_x . The fraction of CO_x is small compared to the other carbon intermediates on the all three surfaces (10-20%).

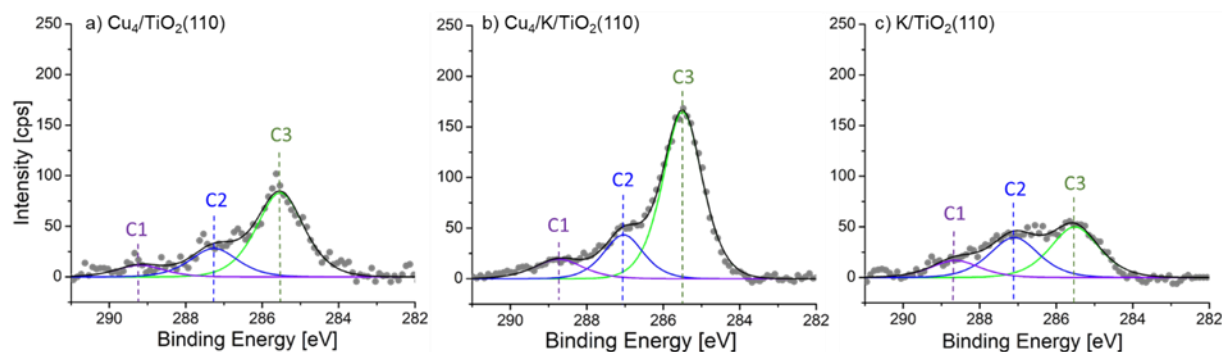


Figure 5.6 *C1s XPS spectra taken on the (a) $\text{Cu}_4/\text{TiO}_2(110)$, (b) $\text{K}/\text{Cu}_4/\text{TiO}_2(110)$ and (c) $\text{K}/\text{TiO}_2(110)$ surfaces under 1×10^{-4} Torr of DMMP at room temperature. The colored solid lines correspond to least squares fits of the data to three different peaks corresponding to different surface intermediates with labels C1-C3.*

For the bare $\text{TiO}_2(110)$ surface and larger Cu NPs on $\text{TiO}_2(111)$ surface at RT, Ma et al., measured the methoxy-to-methyl ($\text{C}_2:\text{C}_3$) peak ratio to be approximately 2:1 suggesting the presence of only intact molecular DMMP (see Scheme 1).^{12,26} Ratios ≤ 1 are typical for surfaces on which DMMP decomposes via P-OCH₃, PO-CH₃ or P-CH₃ bond cleavage. For the Cu only surface studied here, the methoxy-to-methyl ratio is 0.34 and is even smaller for the K-Cu surface, 0.26. The smaller value for K-Cu is consistent with the earlier conclusion that no molecular DMMP is present on this surface. The observed $\text{C}_2:\text{C}_3$ ratios suggest that DMMP decomposition on the Cu and K-Cu surfaces leads to a build-up of methyl fragments on the surface that could result from preferential P-CH₃ and PO-CH₃ bond cleavage of DMMP or other P-intermediates. Methoxy fragments could also be lost via secondary reactions, e.g., methanol formation followed by

desorption, but this is less likely at RT. For the K-only surface (Figure 5.6c), the ratio is C₂:C₃ ratio is larger than for Cu and K-Cu but is still less than one (0.78), which is unexpected since the P 2p spectrum suggests the presence of only unreacted DMMP on the surface (Figure 5.5c). We tentatively attribute the K-only spectrum to spillover of C-based fragments from the center of the sample, where the Cu₄ clusters are deposited, to the edges of the support where only K is present. Hence, the K-only C 1s spectrum is a likely a combination of chemisorbed DMMP and C fragments generated from the K-Cu regions (center) of the surface. Overall, the results in Figure 6 indicate that DMMP decomposition leads to a larger fraction of methyl products on the K-Cu and Cu surfaces. Moreover, the K-Cu surface is significantly more reactive as evidenced by the larger surface concentration of carbon-based intermediates (~1.8 times more than Cu only surface).

As shown in Figure C.2, the Cu LMM Auger spectra for the Cu and K-Cu surfaces during exposure of 1×10^{-4} Torr of DMMP at RT are nearly identical to the surfaces prior to DMMP exposure (see Figure 5.1c and 1f). These results show that DMMP adsorption and decomposition do not alter the Cu oxidation state, which remains mostly Cu¹⁺ in the Cu₄ clusters at RT.

5.3.4. Temperature dependence

Figure 7 shows the temperature dependence of the P-based and C-based surface species on the Cu and K-Cu surfaces following DMMP exposure at RT. Heating experiments were performed under high vacuum ($\sim 1 \times 10^{-8}$ Torr) after DMMP was pumped out of the XPS main chamber. The individual P 2p and C 1s XPS spectra at each temperature from which these curves were derived are given in SI, Figure C. 3 and S4, respectively. On the Cu surface (Figure 5.7a), the P₁, P₃ and P₄ species drop rapidly with increasing temperature with P₁ and P₃ undetectable above 400 K and 600 K, respectively. The loss of P₁ at low temperatures is consistent with the assignment to

molecular DMMP which is known to desorb and decompose on $\text{TiO}_2(110)$ above 400 K.^{11-12,26} The P_4 species, assigned to atomic-P, is more stable with $\sim 20\%$ remaining on the surface at 900 K. By contrast, the P_2 peak intensity exhibits the opposite behavior and increases by more than 3x from RT to 900 K. These temperature trends suggest that P_3 and P_4 species are being oxidized and converted to P_2 at higher temperature. This conclusion is supported by the total surface concentration of P species, which drops when heated to 600 K and then increases to $\sim 80\%$ of its initial value at 900K where it is nearly equal to the P_2 signal.

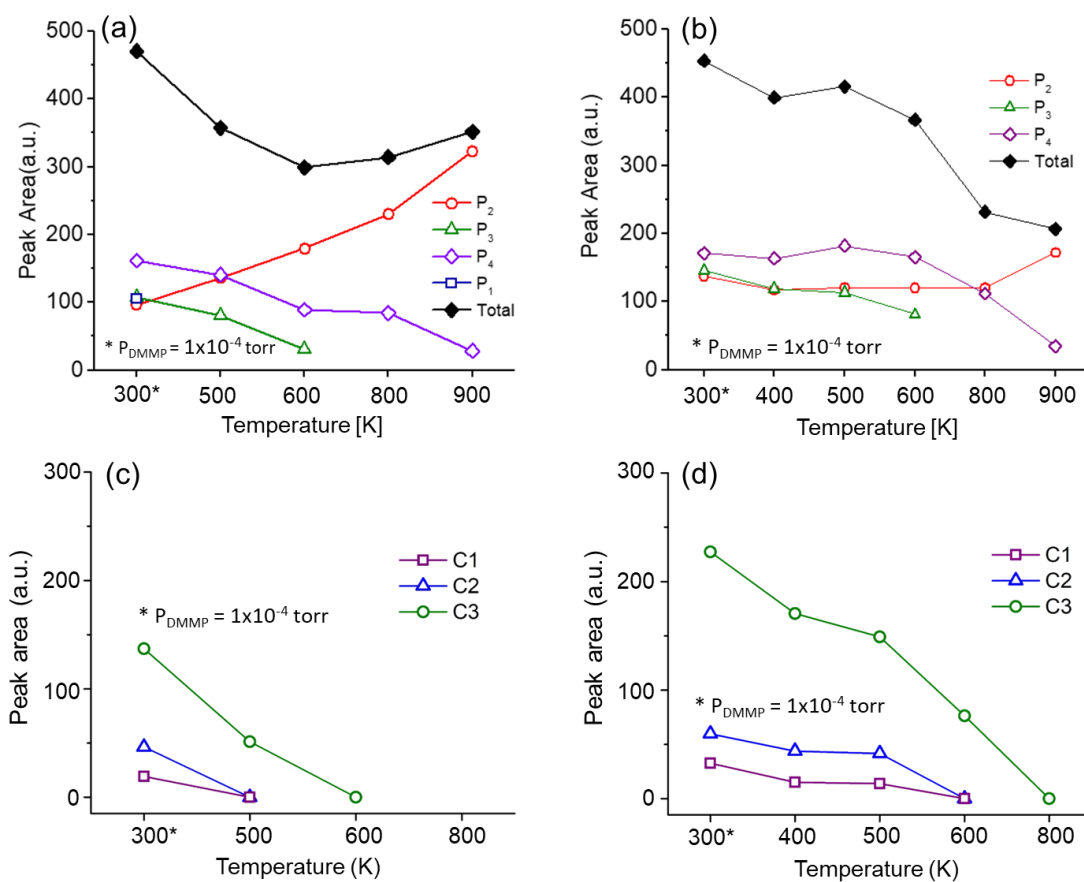


Figure 5. 7 P 2p (a,b) and C 1s (c,d) peak intensities versus temperature for the (a, c) $\text{Cu}_4/\text{TiO}_2(110)$ and (b,d) $\text{K}/\text{Cu}_4/\text{TiO}_2(110)$ surfaces exposed 1×10^{-4} Torr of DMMP at room temperature. The DMMP was pumped out of the NAP-XPS chamber prior to heating the surfaces.

The surface concentration of the reduced P_3 species on the K-Cu surface (Figure 5.7b) follows a similar trend as the Cu only surface and is undetectable above 600 K. However, the trends for the surface concentrations of P_2 , P_4 and total P are very different for the K-Cu surface as compared to the Cu only surface. Specifically, the concentrations of both P_2 and P_4 are essentially constant from RT to 600 K, while the drop in total P can be largely associated with the loss of P_3 species. Above 600 K, the P_4 species falls off rapidly to ~20% of its maximum value, while P_2 remains constant till 800 K and then increases at 900K (Figure 5.7b). The drop in the total P intensity above 600K follows the sum of $P_2 + P_4$, and is nearly the same as P_2 at 900 K. Overall, the total P present on the K-Cu surface continuously drops with increasing temperature to only ~40% of its maximum value at 900 K as compared to 80% on the Cu surface. The temperature dependent results show that the presence of K atoms enhances stability of the highly reduced P_4 species, while also promoting the removal of all P-containing decomposition products at temperatures > 600K.

The temperature dependence of the C 1s peak intensities after heating the Cu and K-Cu surfaces are shown in Figure 7c-d (the individual C 1s XPS spectra at 300 K, 500 K and 800 K for both surfaces are shown in SI, Figure C. 5). The primary difference between the Cu and K-Cu surfaces is that the initial concentrations of C-species associated with DMMP decomposition are higher on the K-Cu surface. On both surfaces, the peak intensities for C_1 - C_3 decrease rapidly with increasing temperature and are mostly undetectable above 600 K. The exception is C_3 on the K-Cu surface, where its larger initial concentration extends its detectability to > 600 K. These results show that the Cu and K-Cu surfaces are mostly free of C-based intermediates resulting from DMMP decomposition after heating to 600-800 K (see Figure C. 5c and f).

Figure 8a shows the effects of DMMP adsorption, decomposition and increasing surface temperature on the state of reduction of the TiO₂(110) support for the Cu and K-Cu surfaces (the individual Ti 2p XPS spectra with fits are given in SI, Figure C. 6). Without K, the fraction of Ti³⁺ is roughly unchanged (~4%) from the as-prepared surface (Figure 5.1a) and increases above 600 K to about 8% at 900 K. Reduction of the TiO₂(110) surface is expected at temperatures > 600 K via the formation of bridged oxygen vacancies and associated reduced Ti³⁺ cations.³³ Interestingly, the K-Cu surface exposed to DMMP becomes more oxidized when heated from 300-600 K, i.e., the Ti³⁺ percentage drops from 8% to 4%, followed by reduction at 800 K. The final state of reduction is the same for both surfaces at (~8%) at 900 K.

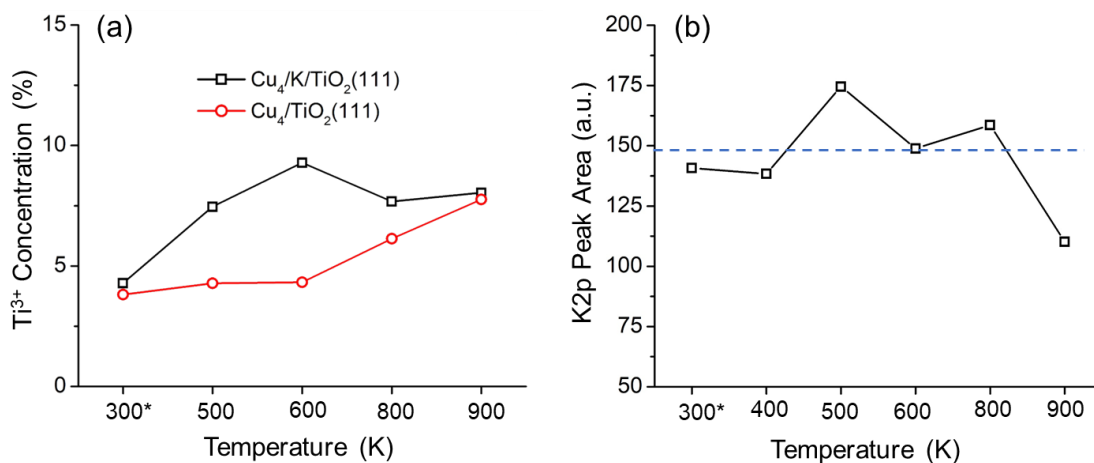


Figure 5. 8 (a) Ti³⁺ concentration (%) as determined from fitting the Ti 2p XPS spectra at different temperatures for the Cu₄/TiO₂(110) and Cu₄/K/TiO₂(110) surfaces. (b) K 2p XPS peak intensity versus temperature for the Cu₄/K/TiO₂(110) surface. The 300 K data points presented in parts (a) and (b) were taken under 1×10^{-4} Torr of DMMP, while DMMP was evacuated for the measurements taken at higher temperatures.

The unusual temperature dependence observed for the Ti³⁺ concentration for the K-Cu surface is attributed to the surface coverage of K atoms, which can be probed by the K 2p XPS

intensity. As shown in Figure 8b, the K coverage is roughly constant up to ~800 K, above which the K coverage decreases by about 30% via evaporation. The loss of K from the surface reduces electron donation to the TiO₂ support and thereby “oxidizes” the surface with a decrease in the number of reduced Ti³⁺ cations (Figure 5.8a). We expect the bonding of P-intermediates to reduced Ti³⁺ cations to be weaker (lower Lewis acidity) compared to Ti⁴⁺ so that they can be more readily removed from the surface with increasing temperature. This may explain why the K-Cu surface generates a lower concentration of oxidized P₁ species at temperatures below 800 K where the K adatoms are stable (Figure 5.8b). Moreover, the temperature dependence of highly reduced P₄ species on the K-Cu surface (Figure 5.7b) exhibits a similar profile as the K intensity (Figure 5.8b) suggesting that K enhances the stability of the P₄ species.

5.4. Discussion

A comparison of the XPS spectra for the Cu, K-Cu, and K surfaces (Figure 5.5), demonstrates that the presence of Cu₄ clusters is essential to DMMP decomposition, as no P-based fragments are observed for the K only surface. The presence of both K atoms and Cu₄ clusters on TiO₂(110) further enhances reactivity with only decomposition fragments and no molecular DMMP observed on the surface at RT. The K-Cu surface also improves the removal of the decomposition products at high temperatures. Comparing the results of this work with XPS experiments of DMMP decomposition on other related surfaces (see Table 1), we can make reasonable assignments of the fitted P 2p peaks to specific DMMP molecular fragments. Because the observed binding energies vary for different TiO₂ surfaces with different admetals, these assignments are tentative at best without other corroborating evidence such as IR vibrational spectra under the same experimental conditions. Moreover, the complexity of the ternary

K/Cu₄/TiO₂(110) system, where the decomposition fragments can bind at TiO₂, Cu₄, or K sites and their interfaces, could give rise to a much wider range of P 2p binding energies than on the surfaces of pure materials (e.g., Cu₂O) or a binary metal-on-oxide surfaces. Hence, it may be more appropriate to view the P 2p spectra as representing an overlapping distribution of chemical shifts corresponding to P atoms in many different local environments instead of assigning the incompletely resolved XPS spectra to a few specific decomposition products. Here, we used DFT calculations to sample a large number of energetically favorable decomposition configurations for DMMP on the Cu and K-Cu surfaces to better understand how the Cu₄ and K metals promote DMMP decomposition and how final state fragment distributions influence the chemical environment of the P-based fragments. The latter is reflected in the calculated P 2p chemical shifts (δ_{XPS}) and the resulting manifold of shifts can be compared to the experimental P 2p XPS spectra.

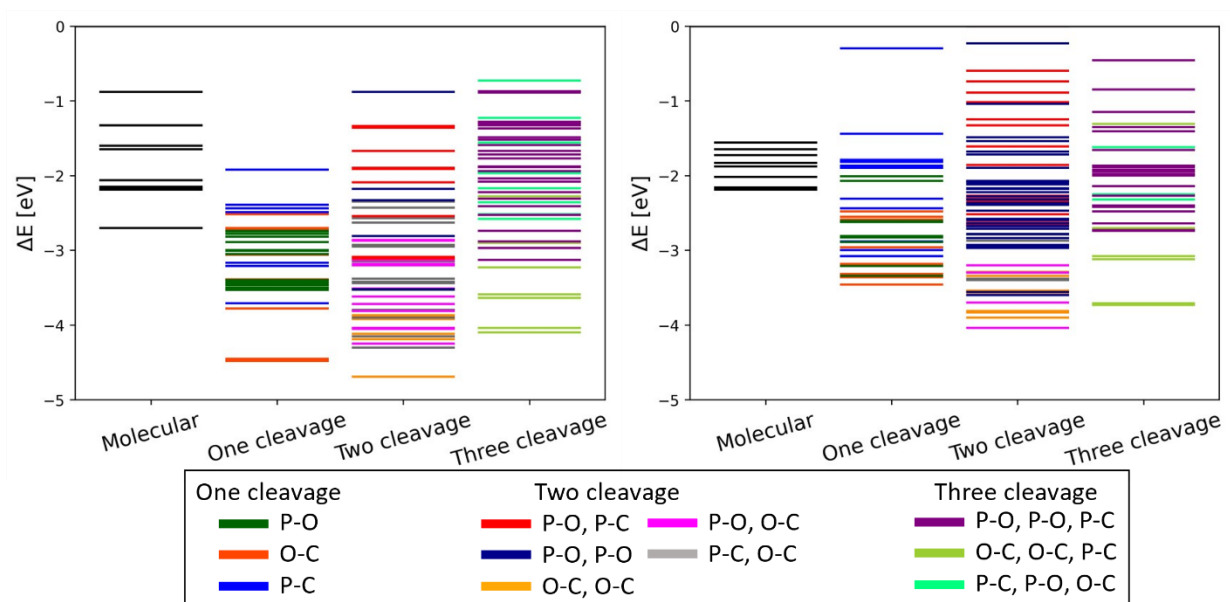


Figure 5. 9 Computational exploration of DMMP decomposition intermediates, combining bond dissociation at the P atom (P-C or P-OCH₃ bond cleavage) and O-C bond dissociation on (a)

Cu₄/TiO₂(110) and (b) K/Cu₄TiO₂(110) surfaces. “Molecular” indicates non-dissociated chemisorbed DMMP. The adsorption energies (ΔE) of each configuration are referenced to gas phase DMMP.

Possible isomers of decomposed DMMP via the cleavage of one, two, or three O-C, P-O, and P-C bonds on the Cu and K-Cu surfaces were exhaustively explored (290 configurations). The adsorption energies of the different chemisorbed DMMP and their decomposition configurations relative to the gas phase DMMP on the Cu and K-Cu surfaces are plotted in Figure 9. On both surfaces, the Cu₄ clusters provide a very strong thermodynamic drive for full DMMP decomposition with many isomer configurations having energies lower than chemisorbed DMMP, up to 2 eV (~190 kJ/mol) lower. The isomer configuration energies are systematically larger in absolute value (more negative) for the Cu compared to the K-Cu surface suggesting that the presence of K atoms weakens interactions between the dissociation products and binding sites on the K/Cu₄/TiO₂(110). The latter is consistent with the observed temperature trends in Figure 7 where P-species resulting from DMMP decomposition are more easily removed from the K-Cu surface when heated above 600 K.

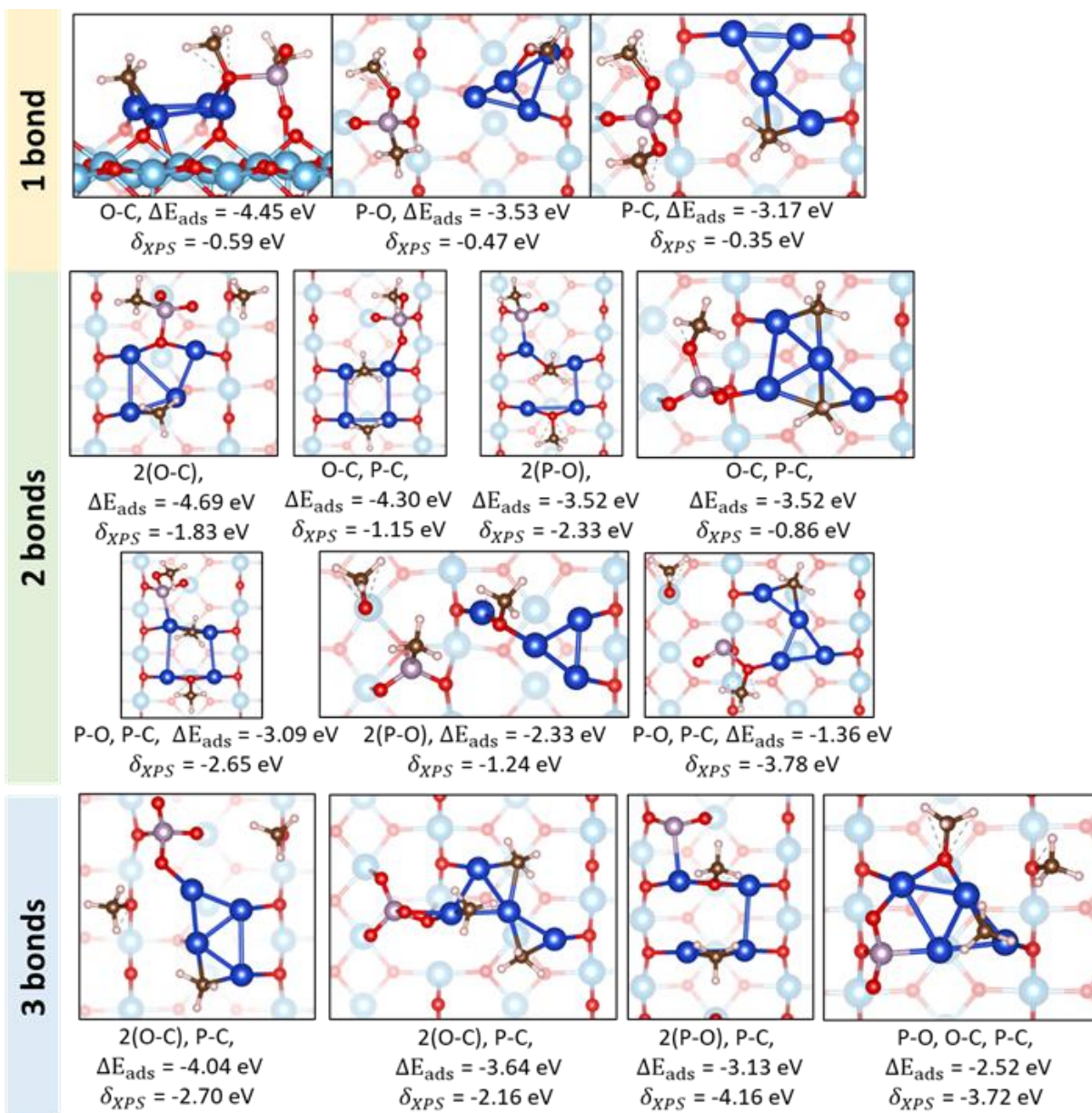


Figure 5. 10 Surface structures for the most stable and unique P-center containing intermediates for DMMP decomposition on Cu₄/TiO₂(110) along with their respective adsorption energies (ΔE_{ads} referenced to gas-phase DMMP) and XPS binding shifts (δ_{XPS}) for breaking one, two, and three bonds.

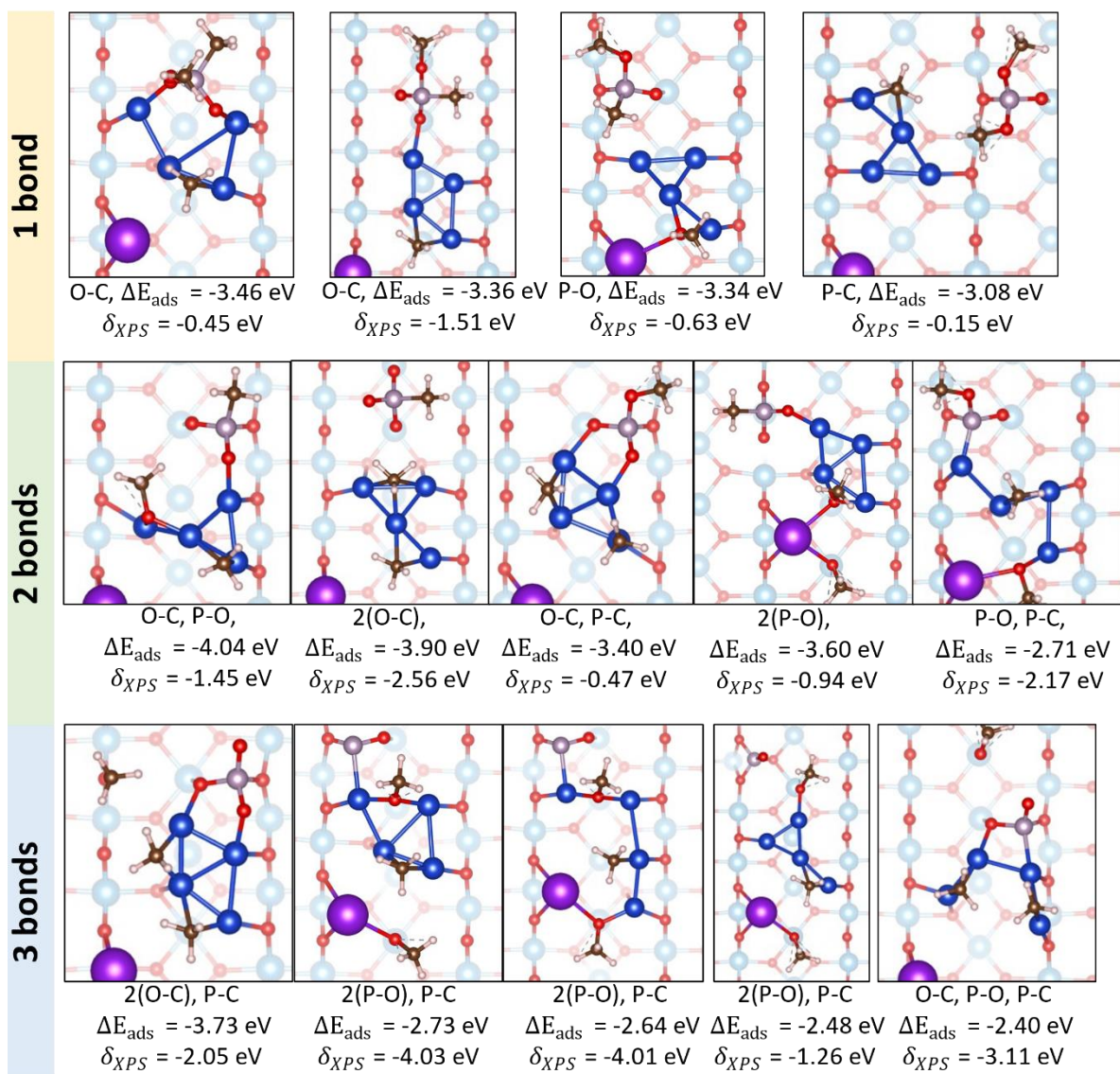


Figure 5. 11 Surface structures for the most stable and unique P-center containing intermediates for DMMP decomposition on K/Cu₄/TiO₂(110) along their respective adsorption energies (ΔE_{ads} referenced to gas-phase DMMP) and XPS binding shifts (δ_{XPS}) for breaking one, two, and three bonds.

Selected ensemble of configurations with interesting XPS binding shifts or lowest adsorption energy after breaking one, two, and three bonds in DMMP on Cu and K-Cu surfaces are shown in Figures 10 and 11, respectively. On the Cu surface, the most stable configurations resulting from 1-bond and 2-bond cleavages involve breaking O-C bonds to form CH₃ fragments,

while 3-bond cleavages that release three CH₃ fragments by breaking two O-C and one P-C bonds are thermodynamically more favorable. The released CH₃ fragments bind predominantly to the Cu₄ clusters or more rarely to O-lattice atoms of the TiO₂ support. These most stable configurations therefore generate a large fraction of methyl groups bound to Cu, in complete agreement with the very low C2:C3 ratio of peaks in the C XPS spectra discussed above. The best two-bond cleavage configuration is slightly more favorable ($\delta E_{rel} = -1.99$ eV, δE_{rel} denotes the stability of an intermediate with respect to the chemisorbed DMMP) than the best one-bond configuration ($\delta E_{rel} = -1.75$ eV), but the product of the 3-bond cleavage is somewhat less stable ($\delta E_{rel} = -1.35$ eV), although still markedly favored compared to intact chemisorbed DMMP on the TiO₂ surface.

On the K-Cu surface, breaking only one O-C bond still results in the most stable 1-bond configuration ($\delta E_{rel} = -1.27$ eV), whereas the lowest energy configuration for breaking 2-bonds involves one O-C and one P-O bond ($\delta E_{rel} = -1.85$ eV), while the result of two O-C cleavages is close in energy ($\delta E_{rel} = -1.71$). Similar to the Cu surface, two O-C and one P-C bonds are broken in the lowest energy configuration for 3-bond cleavages ($\delta E_{rel} = -1.53$ eV). In all the configurations sampled, the CH₃O and CH₃ fragments are stabilized on the Cu₄ clusters, even in the presence of K atoms. Again, a large ratio of methyl bound to Cu is formed, in agreement with the C 1s spectra. The surface structures in Figures 10-11 also highlight the dynamic (fluxional) nature of Cu₄ clusters, with marked deformations of the structure of the Cu₄ cluster to accommodate the methyl or methoxy ligands, and the wide range of molecular fragment binding sites for the remaining P-moieties that determine the local chemical environment and, thereby, the 2p binding energies of these P-fragments.

In order to identify the P-fragments that are most likely to contribute to the XPS spectra, P 2p binding energy shifts (δ_{XPS}) were calculated and plotted as a function of the stability of the

isomer configuration (Figure 12). Stability here is defined as the absolute value of the energy change with respect to chemisorbed DMMP, i.e.,

$$E_{stability} = |E_{isomer} - E_{chemisorbed\ DMMP}| \quad (5-1)$$

A more positive value hence means a more stable configuration. The calculated P 2p binding energy shifts for all the fragment configurations sampled on the Cu and K-Cu surfaces are shown in Figures 12a and 12b, respectively. The calculated shifts range from -1 to -4 eV, agreeing well with the experimental data (Figure 5). Moreover, the magnitude of the calculated shifts exhibits clear trends with (1) the number of bonds broken or fragments transferred to the surface and (2) the types of bonds cleaved. These trends are evident in Figures 12b-12d and 12f-12h, which separate the calculated shifts for fragment configurations resulting from 1-bond, 2-bond, and 3-bond cleavages. Firstly, as the degree of decomposition increases, the binding energy shift increases. Secondly, for isomers resulting from 1-bond dissociations, the largest shifts are associated with O-C bond cleavage, followed by P-O and P-C bonds, although intermediate shifts can also be seen for O-C bond cleavage (Figure 5.10). For 2-bond dissociations, isomers with a P center that possesses either phosphoryl groups (P=O) resulting from O-C bond cleavage or that underwent P-O bond cleavage generally have larger shifts. Isomer configurations with fully reduced P centers, where all the P-O and P-C bonds are cleaved, have the largest calculated shifts, close to -4 eV. These P centers re-coordinate with Cu atoms and a few surface O atoms for their stability. Correlations between the calculated P 2p binding energy shifts and the oxidation state of the P center as inferred from Bader charge analyses are shown in Figure C. 7 and Figure C. 8 for the Cu and K-Cu surfaces, respectively. The latter shows that as the degree of decomposition

increases, the Bader charge on the P atom decreases, i.e., it becomes more reduced, and the binding energy shifts to lower energies.

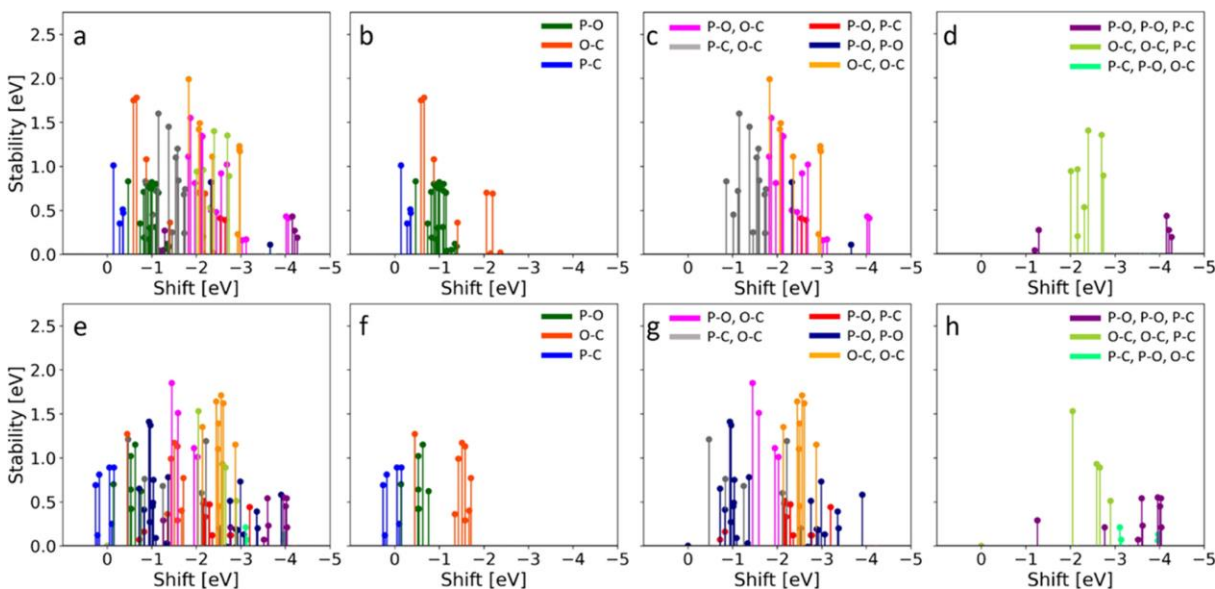


Figure 5.12 Calculated XPS binding energy shifts on P atom against its stability on Cu_4/TiO_2 (a-d) and $\text{KCu}_4/\text{TiO}_2$ (e-h) referenced to the molecularly chemisorbed DMMP. Plot b-d and f-h showcase the peaks obtained from isomers with one, two and three fragment transferred onto Cu_4 and Cu_4K clusters respectively. The label P-O, P-C and O-C denotes which bonds/combination of bonds are broken (P-O, P-C and O-C bonds respectively).

Overall, the calculated trends in Figures 12, S7, and S8 are in qualitative agreement with previous studies of DMMP decomposition where negative P 2p binding shifts (relative to intact DMMP) were attributed to fragments with fewer bonds to the P center, with atomic P species exhibiting largest shift (see Table 1). Here, we identified the P_2 peaks with a shift of about -1 eV (w.r.t. to P_1 , chemisorbed DMMP) to methyl methylphosphonate (MMP). This assignment is consistent with the calculated 1-bond shifts for O-C bond cleavage on Cu and K-Cu surfaces (Figs 12b and 12f); however, binding energy shifts near -1 eV can also include contributions from P-species resulting from 2-bond breaking processes (O-C and P-O) with similar energy stabilities

(Fig.s 12c and 12g). Similarly, the P₃ peaks with observed shifts near -3.2 eV are likely to be a mix of P-species resulting from multiple 2-bond dissociations (Figure 5.12c and 12g) on both surfaces, although configurations resulting from two O-C cleavages have the highest calculated stability. Finally, the calculations suggest that the P₄ peaks exhibiting the largest calculated (-4 eV) and observed (-5.2 eV) binding energy shifts are likely associated with P-species resulting from 3-bond dissociation processes, i.e., two P-O and one P-C or two O-C and one P-O bond cleavages (Fig.s 12d and 12h). The P 2p peaks observed in this binding energy range on other surfaces such as those listed in Table 1 are typically assigned to “atomic P.” The lowest energy structures in Figures 11 and 12 show that the most reduced species is a P-atom bonded to two O-atoms and the Cu₄ cluster on the Cu and K-Cu surfaces. Overall, the calculations show that the apparent peaks in the experimental P 2p spectra (Figure 5) are not likely associated with any specific DMMP fragment. Instead, the XPS spectra are better described by a manifold of P-atom chemical environments that depend sensitively on the final state configuration of fragments on the surface and the number and type of bonds broken (Fig.s 10-12).

5.5. Conclusions

In this work, NAP-XPS combined with DFT calculations were used to probe the reactivity of the TiO₂(110) surface modified with the deposition of ultra-small Cu₄ clusters and alkali metal (K) atoms for the decomposition of a CWA simulant, DMMP. By itself, TiO₂(110) is inactive for DMMP decomposition except at elevated temperatures. By contrast, the Cu₄/TiO₂(110) surface is found to be very reactive, with highly reduced P-species observed even at RT. The co-deposition of K atoms further enhances the reactivity and also improves the removal of the decomposition products at high temperatures. The P 2p and C 1s core level spectra, and our DFT calculations,

indicate that DMMP decomposition on Cu and K-Cu surfaces involves cleavage of P-O, P-C, and C-O bonds to form chemisorbed methoxy and methyl groups on the surface. Using comparisons with previous studies of DMMP decomposition on other related surfaces, the incompletely resolved peaks in the P 2p spectra could be tentatively assigned to specific P-based species, including DMMP, MMP, and “atomic” P. To gain a more atomistic picture of the decomposition pathways that lead to the observed decomposition products, detailed ab initio DFT calculations were performed to determine the surface distribution of decomposition products for a large number of energetically favorable final state configurations (290) resulting from 1-3 bond cleavages in chemisorbed DMMP. The calculations show that intact DMMP preferentially binds to the TiO₂(110) surface, although the binding energy is sensitive to the presence of nearby Cu₄ clusters and K atoms. Moreover, the calculations show that the Cu₄ clusters strongly promote P-O, O-C, and P-C bond cleavage in DMMP and are highly fluxional with atomic structures that depend on the configuration of fragments bound to the surface. For each configuration of final state decomposition products, the P 2p binding energy shift relative to chemisorbed DMMP was calculated. The predicted energy shifts range from -1 to -4 eV, which is in reasonable agreement with the energy widths of the experimental P 2p spectra. The magnitudes of the calculated shifts depend on the number of bonds broken and which type of bond is cleaved, e.g., P-O or P-C. The largest shifts are associated with P centers where all three P-O and P-C bonds are cleaved and re-coordinate to Cu at surface O atoms (“atomic” P species). This suggests that the broad P 2p core level spectra are better described by a near-continuous distribution of P 2p chemical shifts that arise from a large number of energetically accessible decomposition configurations. When only a few final state configurations are energetically favorable, this analysis leads to similar conclusions as the conventional peak fitting approach, where each peak can be “assigned” to a different

oxidation state. More broadly, this combined experimental and computational study sheds new light on the interpretation of core-level spectra associated with intermediates resulting from complex surface reactions.

Chapter 6

Methanol as a probe for CWA decomposition on highly dispersed Pt nanocluster on Anatase TiO₂(101)

6.1. Introduction

The reactivity of organophosphonate is hypothesized to correlate with the Lewis acidity of the active metal site^{34,129,132,136,138,146–148}. Devulapalli et. al found that the active site in UiO-67 MOFs responsible for the hydrolysis of DMNP is the metal node and is dependent on the Lewis-acidic strength of the metal, where weaker acid correspond to lower rate of hydrolysis¹⁴⁷. Similarly with DMMP, promoting the Lewis acidity of the active site by introducing highly dispersed nanoparticles could promote decomposition, as seen before in the case of Cu on TiO₂^{138,139,141,142}. The work of Panoyotov examine the reaction pathways of the chemical warfare agent simulant dimethyl methylphosphonate (DMMP) on nanoparticulate Au/TiO₂¹⁴⁹. The infrared spectral signature of adsorbed CO, a primary reaction product, was used to monitor the oxidation states of Au and Ti during the reaction. It was shown that small Au particles (<5 nm) on TiO₂ enhance the oxidative degradation of DMMP via 2 mechanism: (1) anaerobic pathway, where vapor-phase DMMP reacts upon adsorption, producing various organic compounds and adsorbed CO. This initial oxidation pathway likely involves lattice oxygen around the Au particles' periphery. The second mechanism involves charge transfer from Au particles to gas-phase oxygen, which then reacts with DMMP adsorbed on TiO₂, resulting in complete oxidation of DMMP and CO₂ release. It was hypothesized that this charge transfer is responsible for the increase of surface Ti acidity, thus altering the dative bond of DMMP to favor P-O bond cleavage. These findings suggest either

NP can: (1) alter the state of the surface or (2) rearrange dynamically by reacting with gas phase species.

In the examples above, the chemical potential of oxygen and reductive agents determines the oxidation states of Au in nanoparticulate Au oxide-supported catalysts^{149,150}. Thus, the dynamic nature of SAC seems to be extended as well to highly dispersed supported NP. As we have seen in the case of supported single atom on titania, understanding the stability of highly dispersed catalyst is not always a straightforward path. As the size of the cluster increases, the degree of freedom in which the cluster can rearrange and interact with the surface increases exponentially. Especially in reaction conditions, the structure of the catalyst may still change, hence adding another layer of difficulty when one tries to probe the state of the catalyst using traditional spectroscopy methods. This was evidenced by various studies of highly dispersed metal catalyst ranging from oxidation to electrochemistry, where the state of the active NP changes as the reaction condition changes.^{45,46,110,137,151–153}

Methanol oxidation (dehydrogenation) serves as fascinating probe reactions to understand the Lewis acidity and basicity of a site. By analyzing the products formed, we can identify the active site involved. Tatibouët¹⁵⁴ established that when methanol is exposed to catalyst with very strong acid sites, formaldehyde becomes a rate limiting intermediate, allowing it to form dioxymethylene species. These species can react with nearby methoxy groups or adsorbed methanol to produce methylal. However, at high temperatures, this reaction doesn't occur because formaldehyde desorbs faster than it reacts to form dioxymethylene species. The equilibrium then shifts towards the dissociation of methylal as the temperature rises. If both acid and basic sites on the catalyst system are stronger than required for methylal formation, dioxymethylene species

oxidize into formate species, which quickly react with methanol to produce methyl formate or further oxidize into carbon oxides. Conversely, if strong acid sites and very weak basic centers are present, only dimethyl ether is formed. Thus, the variety of products formed in methanol oxidation and dehydrogenation may guide us on the nature of the catalytic sites involved.

Extensive research has been carried out to understand the mechanistic details of methanol oxidation on noble-metal catalysts. In one notable study, Yoon et al. investigated methanol oxidation on various oxide-supported platinum catalysts¹⁵⁰. Their findings indicated that a TiO₂ support enhances selectivity towards partial oxidation products, such as formaldehyde and methyl formate, due to increased charge transfer from TiO₂ to Pt. Furthermore, by controlling the growth of titania particles, they discovered that partial oxidation products preferentially form on the Pt/TiO₂(001) facets. Complementing this work, Reece et al. employed a combination of microkinetic modeling and transient product analysis to unravel the mechanistic steps of methanol oxidation on nanoporous Au¹⁵⁵. Their study revealed that increasing the partial pressure of CH₃OH led to higher selectivity for methyl formate. This was attributed to the high surface coverage of methoxy groups, which enabled a coupling mechanism where two methoxy species reacted to produce methyl formate. Importantly, their research demonstrated that the pathway to methyl formate formation was distinct from the overoxidation pathway leading to CO₂ and H₂O. A work by Sapienza et. al. employed a combination of packed-bed reactor experiments and high-vacuum surface science techniques to unravel the reaction mechanism of methanol oxidation on a Pt/TiO₂ catalyst¹⁵⁶. The reactor studies revealed that under mild reaction conditions, methyl formate is the primary product, while complete combustion to CO₂ occurs at elevated catalyst temperatures. Surface science investigations further elucidated that CO₂ production proceeds through a surface-bound formate intermediate via multiple proton-coupled electron-transfer steps. Interestingly

water, produced during the initial methanol adsorption, is crucial for activating the oxidative pathways of this Pt-based catalyst. Hence it seems that Pt enhances the Lewis acidity of titania which can be beneficial for the decomposition of GB/DMMP. Understanding these findings and translating it to the reactivity of DMMP or GB remains to be an interesting question for computational scientists to address, as the electronic effects between the metal NP and its support is tightly correlated with its stability in the reaction condition while the experimental elucidation using traditional spectroscopy methods remains limited.

In this chapter we explored the stability of Pt₆O_x supported on anatase TiO₂(101) and all of its accessible metastable states under reaction condition using the grand canonical basin hopping algorithm. We then performed methanol reactivity studies as a probe in understanding the role of the Pt NP in oxidative conditions, by observing its electronic effect towards the support and the product formed from all possible oxidation pathways; particularly in comparison to the single atom. It was found that Pt SA facilitate the formation of methoxy species, followed by two accessible pathways, the CO₂ + 2H₂O formation and the dioxomethylene species that can react to form methyl formate. On Pt cluster, we observe the cluster would be partially oxidized in oxidative conditions, adopting the Pt₆O₁₀ chemical formula. Pt₆O₁₀ adopts a bilayer structure made of planar PtO₄-subunits. Analysis of isomers found by GCBH reveals that this cluster is a very stable global minima, while providing active O adatoms that may participate in oxidation reactions. Methanol dehydrogenation study reveals the role of surface O adatoms in

6.2. Computational Methods

6.2.1. VASP set-up

The density functional theory (DFT) simulations was calculated using the Vienna Ab Initio Simulation Package (VASP)⁷³. The Perdew-Burke-Ernzerhof (PBE) functional was used for defining the exchange and correlation energies, along with the dDsC dispersion correction to accurately account for van der Waals forces^{79,80,157,158}. The Projector Augmented Wave (PAW) method was employed to model electron-ion interactions, and a plane wave basis set with a 500 eV cutoff was adopted^{81,83}. To capture the electronic structure details consistent with experimental observations of TiO₂, particularly the localized electron behavior on surfaces with oxygen vacancies, titanium d orbitals were assigned an effective Hubbard U parameter of 4.2 eV, following the Dudarev approach to DFT+U¹⁴⁵. The calculations aimed for electronic energy convergence within 10⁻⁶ eV and atomic force convergence at 0.03 eV/atom. Transition state structures and energies were determined using the Nudged Elastic Band (NEB) method with eight intermediate images.

6.2.2. Cell size for reaction pathway optimization

The computational model involved a periodic slab of anatase TiO₂(101) cut from a bulk TiO₂ crystal with lattice constants $a = 3.83 \text{ \AA}$ and $c = 9.63 \text{ \AA}$. A supported PtO₂ structure was selected based on its stability under oxidation conditions as demonstrated in the literature. The surface lattice vectors were $a = 19.35 \text{ \AA}$ and $b = 16.76 \text{ \AA}$ (Figure D.1). A large unit cell was chosen to minimize intra-cell interaction errors, and the surface consisted of four O-Ti-O trilayers (12 atomic layers). A 15 Å vacuum gap was set between slabs to avoid periodic interactions in the z-direction, with the bottom-most three atomic layers fixed to simulate bulk conditions. Transition states were initially calculated using eight images on a smaller test unit cell ($a = 11.61 \text{ \AA}$ and $b = 11.18 \text{ \AA}$),

and the found transition state was recalculated to confirm the negligible effect of cell size on the calculated barrier.

6.2.3. Global optimization using GCBH

The GCBH explorations are carried out by an in-house code (CatalApp^{50,159,160}) developed by Sun et.al., which is developed based on the Atomic Simulation Environment (ASE) package in python. GCBH efficiently explores the configuration and chemical composition of the cluster by minimizing the free energy of the supported Pt₆O_x cluster at the specific oxygen chemical potential.

$$G(Pt_6O_x@TiO_2) = E(Pt_6O_x@TiO_2) - \sum_{j=1}^{M_{species}} \mu_j N_j$$

Where, $E(Pt_6O_x@TiO_2)$ is the DFT calculated electronic energy of the system which is approximated as the free energy of the slab. This algorithm assumes that the vibrational contributions are ignored for slab systems considering that those contributions are negligible. The grand canonical treatment comes from the chemical potential of reacting gas phase species, where μ_j is the chemical potential of element type j , and N_j is the number of element type j in the system. To understand the effect of oxidation condition, only the number of oxygen is varied. The oxygen potential is sampled at 4 different equilibrium conditions: -0.27 eV (ambient condition), -0.5 eV, -0.75 eV, and -1 eV. The reason for the different points of sampling is because the nature of basin hopping in which it hops towards the most stable basin, which is defined by the Gibbs Free energy of formation. These basins are calculated at a specific, pre-defined oxygen chemical potential equilibrium, and thus the algorithm would risk under sampling the basins (chemical formula) that could be favorable otherwise at different value of oxygen chemical potential. For example, in

ambient conditions, the oxygen chemical potential is known to be of small (absolute) value, and thus one would expect the adsorption/formation of supported oxide would be probable. On the other hand, in reducing conditions, the oxygen chemical potential increases (in absolute) value. As a result, the Gibbs free energy of conformers with less oxygen adsorbed in the system would have much higher basin than those with more oxygen adsorbed in the system. these process is highly unlikely (oxygen chemical potential is very low) and hence the algorithm would risk undersampling conformers with less oxygen adsorbed on the cluster. By sampling across ranges of oxygen chemical potential, we ensure to sample most stable conformers at across wide range of oxygen pressure.

A total of 9 metallic Pt₆ deposited on smaller unit cell of anatase ($a = 11.61 \text{ \AA}$ and $b = 11.18 \text{ \AA}$) are used as initial geometries for 9 different basin hopping, each rerun with the 4 oxygen chemical potential (a total of 36 separate basin hopping run). Select modifiers were employed to ensure proper sampling: translation, rotation, rattling (parts of the clusters), random displacement of oxygen adatoms and addition/deletion of O atoms on Pt₆ sites to create a grand canonical ensemble of Pt₆O_x. Each GCBH step consists of three steps: (a) generating new structure using the before-mentioned modifiers and the previous local minimum, (b) local optimization of the new-found structure, and (c) the acceptance or rejection of the optimized new structure. Throughout this process, the modifiers was not applied on the surface, however, the surface is allowed to relax alongwith the Pt₆ cluster. Hence, any structural effects of the NP towards the support is properly sampled. The newly generated structure is optimized in step (b) using the BFGS algorithm in ASE until the maximum force on the atoms is below 0.03 eV/\AA . In step (c), the acceptance probability of the new structure is determined by the Metropolis algorithm, which depends on the free energies of the new (G_i^{+1}) and old (G_i) structures. A temperature of 1500 K is used for this calculation to

ensure the sampling process does not converge too quickly. Note that this high temperature is only for the BH acceptance probability and is different from the temperature of the O₂ reservoir.

6.3. Results & Discussion

6.3.1. Pt₆O_x stability and its electronic effect

To explore the possible chemical stoichiometry and its geometry diversity of Pt₆ cluster, the GCBH algorithm was used to explore the potential energy surface globally. Figure 6.2 showcases the calculated Gibbs Free energy of formation of the most stable conformers of each chemical formula found (Pt₆O_x, x=0-14) during the GCBH exploration. In ambient condition (red line) the most stable chemical formula is Pt₆O₁₀, where the Pt is partially oxidized to form combination of Pt⁺² and Pt⁺⁴ species, confirmed by Bader charge analysis referenced to the bulk PtO and PtO₂ (Figure D.1). The most stable Pt₆O₁₀ cluster adopts a bilayer structure, composed of series of planar PtO₄-like building blocks (Figure 6.3). Comparison of the relative Gibbs free energy of formation of all found conformation as a function of number of oxygens in the chemical formula showcase the stable nature of this particular Pt₆O₁₀ species, where most isomers are around 1.25 eV less stable than the global minima. This could partly be explained by the structure of the global minima itself, suggesting that the linkage of PtO₄ subunit is highly stable and thus it is not prone to restructuring or diffusing (since the PtO₄ subunit is anchored onto the surface oxygens). The partly oxidized Pt₆ also showcase the ability of the cluster to provide active O species, with the free energy cost to remove the oxygen as low as 0.68 eV, compared to the bridging oxygen of the undoped pristine anatase (>4 eV).

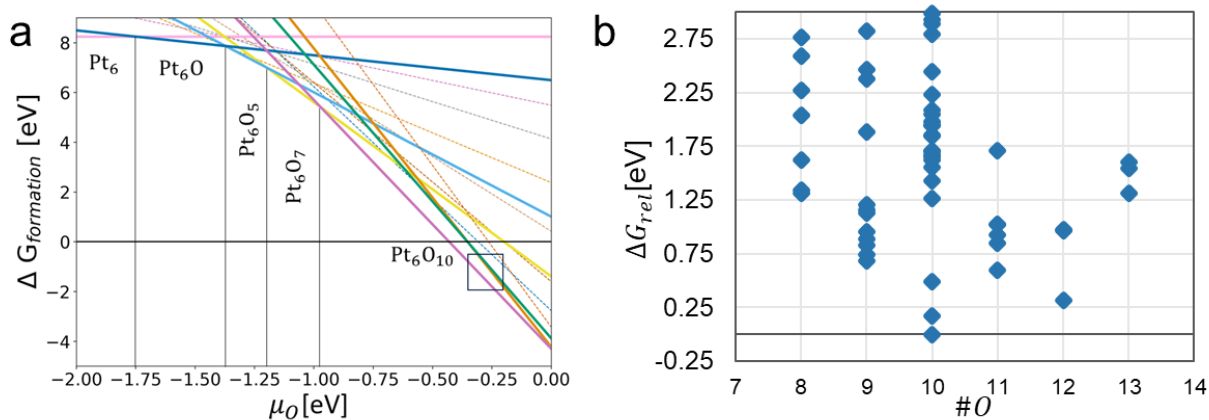


Figure 6. 1 Constructed stability diagram of Pt_6O_x as a function of oxygen chemical potential (left). Highlighted in the square are the accessible region in ambient condition. The relative stability of isomers found as function of chemical formula is plotted on the right hand side.

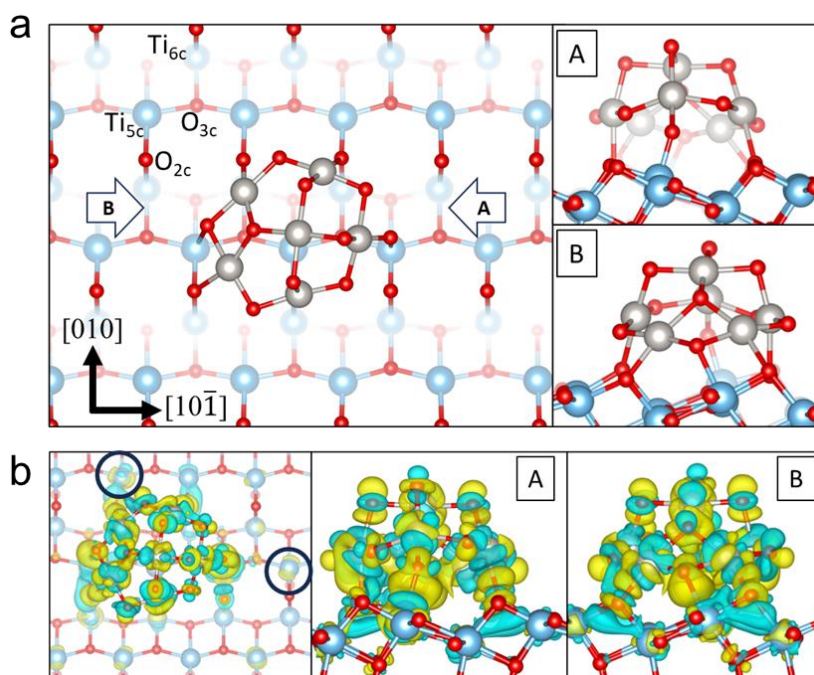


Figure 6. 2 Global minima of Pt_6O_x found by GCBH method. The cluster adopts the Pt_6O_{10} chemical formula (a). A and B denotes the side view. Charge density difference plot (b).

6.3.2. Methanol reactivity on Pt SA

Methanol is used as a probe to understand the effect of highly dispersed SAC and NP towards CWA decomposition in preventing catalyst poisoning and increasing the lewis acidity of the surface. Firstly, the study was conducted on single atom system, the supported PtO₂ species on a-TiO₂. Methanol still adsorbs most favorably on Ti sites, with adsorption energy comparable to the pristine system without SAC (**Figure 6. 4**) at -1.16 eV (-1.17 eV on pristine), indicating that the Pt species is unlikely altering the electronic structure of the support. Second best adsorption mode follows Methanol adsorbing on PtO₂ species. On the other hand, rearrangement of the PtO₂ species by breaking a Pt-O_{2c} bond with the surface weakens the methanol binding energy to (Figure 6. 4 b, -0.74 eV).

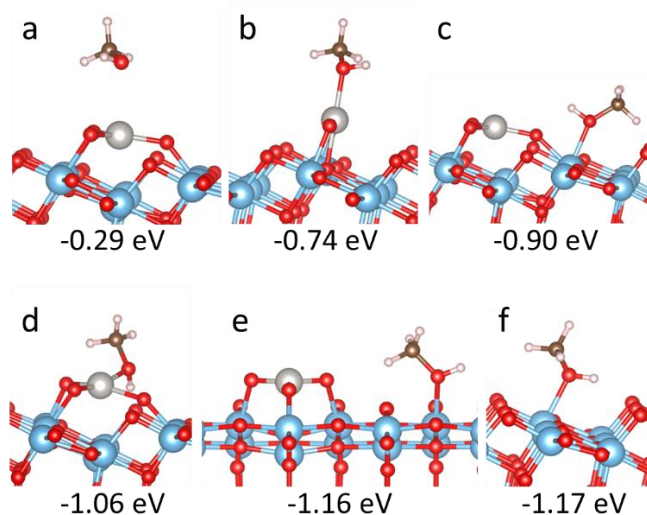


Figure 6. 3 Explored adsorption mode of methanol on Pt SA/TiO₂(101)

The methanol reactivity proceeds via O-H abstraction Figure 6. 5, transferring a proton to a nearby surface bridging oxygen to form methoxy. The increase of Pt-OCH₃ binding triggers the rearrangement of the PtO₂ catalyst by breaking the Pt-O_{2c} bond. Subsequent C-H abstraction to

form formaldehyde and an Pt-O_{ad}H species is facile with barrier of 0.97 eV (**Figure 6. 5**, I to III). Upon formation of formaldehyde, the second C-H cleavage to form the second O_{ad}H requires very high barrier (>2.2 eV, brown path). The oxidation then follows two possible pathway: (1) the formyl (OCH) pathway and (2) the formate (OCHO) pathway. The first pathway follows the rearrangement of the Pt active site, (OPt(O_{ad}H)-CH₂O) by Pt breaking the Pt-O_{ad}H bond and reattaches to nearby surface oxygen (OPt(O_{2c})-CH₂O) (intermediate III-IVb). This transformation is slightly uphill by 0.38 eV, however from here on the OCH formation has a much lower barrier of 0.8 eV, making TS Vb as the effective rate determining transition state (RDTS) and η_1 -formaldehyde (III) as the rate determining intermediate (RDI). This change in activity can be attributed due to Pt being less reduced and more stable as rebinds with the bridging oxygen, allowing it to activate the remaining oxygen adatom. The effective barrier is thus 1.18 eV, which is possible to be overcome at ~457 K.

Second pathway (formate formation) begins with the carbon of the η_1 -formaldehyde binding with the O_{ad} on Pt, forming an η_2 -dioxomethylene (IVa). This step is downhill by 0.2 eV, with barrier of 0.25 eV making this step very facile. After the facile formation of dioxomethylene (CH₂O₂), one prominent pathway involves the formation of formate (HCOO⁻). Dioxomethylene can interact with the Pt site to cleave a C-H bond, leading to the formation of formate (OCHO) and Pt-H, which is a key intermediate in many literature studying methanol oxidation reactions. A significant resulting pathway from this formate formation is the formation of methyl formate (HCOOCH₃). This formate can couple with a nearby methoxy (CH₃O) species present on Ti sites (O-H cleavage was found to be favorable nevertheless). This coupling reaction results in the formation of methyl formate, The formation of methyl formate is particularly a notable because it confirms the experimental observation in mild oxidation reaction found previously, whereas

harsher condition would see overoxidation to CO_2 , which was seen on the other possible minority pathway (Figure 6. 5 b). These reaction pathways highlight the versatile nature of dioxomethylene as an intermediate and its role in facilitating selective oxidation processes on catalytic surfaces.

A minority oxidation pathway follows the rearrangement of PtO_2 active site prior to any O-H cleavage of methanol (Figure 6. 5, b). This pathway creates interesting products, particularly H_2O and CO , which are prone to be oxidized further into CO_2 . Methanol being adsorbed on rearranged Pt SA directly allows for it to protonate all its -H to the more active O adatom near Pt. Similarly, the pathway begins with the deprotonation of the O-H group in methanol, forming methoxy (CH_3O). The methoxy intermediate then undergoes successive dehydrogenation steps, but interestingly without the direct formation of formaldehyde. Upon forming methoxy, the presence of nearby OH facilitates C-H abstraction to form a hydroxylated dioxomethylene (HOCH_2O) (Figure 6. 5, b, II-III). From here on, a proton coupled electron transfer (PCET)-like process by cleaving another C-H to form H_2O and Pt stabilized CHO radical is quite facile. We note that the process resembles somewhat a PCET, where a nearby OH activate a proton to form H_2O from the formaldehyde whereas Pt is storing the electron to stabilize the remaining radical. Another round of 'PCET' like process on the very reactive formyl and OH complete the formation of CO and another H_2O . The generated CO , in the presence of excess oxygen, can be further oxidized to CO_2 as the catalyst reoxidizes/ goes into steady state, confirmed by the study of CO oxidation on PtSA system as shown previously, completing the oxidation pathway of methanol. This sequence of reactions illustrates the comprehensive breakdown of methanol to carbon dioxide and water, emphasizing the role of the PtO_2 active site rearrangement in facilitating efficient proton and electron transfers essential for the complete oxidation process. It is interesting to note that a previous work by Sapienza et. al. albeit on a bigger Pt loading, suggests the autocatalytic nature

of methanol oxidation on Pt cluster supported on anatase. The adsorption of methyl formate, a key intermediate seen during normal methanol oxidation, in anhydrous condition only results in dissociative adsorption as methoxy and formate. However, co-adsorption with O₂ and water allows methyl formate to fully oxidize the methoxy as other forms of carbonates. Sapienza et. al. also see formations of hydroxyls on the surface, a process that we have seen on the single atom study. We could compare the process of the first C-H bond cleavage with and without the help of surface OH, seen on pathway a and b. Without nearby OH (Figure 6. 5 a, I-II), the C-H deprotonation barrier stands at 0.96 eV, whereas with surface OH (Figure 6. 5 b, II-III) the barrier goes down to 0.75 eV. We discovered the role of nearby OH to stabilize the formed hydrogenated DOM which is otherwise difficult to proceed.

From a simple study of a single atom system, we've discovered the various role Pt can do to facilitate the O-H and C-H abstraction steps during methanol oxidation. Firstly, Pt site helps activate the methanol O-H (or C-H for methoxy) proton by providing oxygen adatom from the gas phase. Pt and oxygen adatoms can participate in a 'PCET'-like process, where oxygen adatom activates a proton, while Pt act as electron sink to stabilize the remaining carbonate species. Secondly, these oxygen adatoms may form OH, which could participate in stabilizing the remaining formaldehyde during the second and third C-H proton transfer. In order to see whether this role stays true in a bigger cluster, a test with Pt₆O₁₀ is performed.

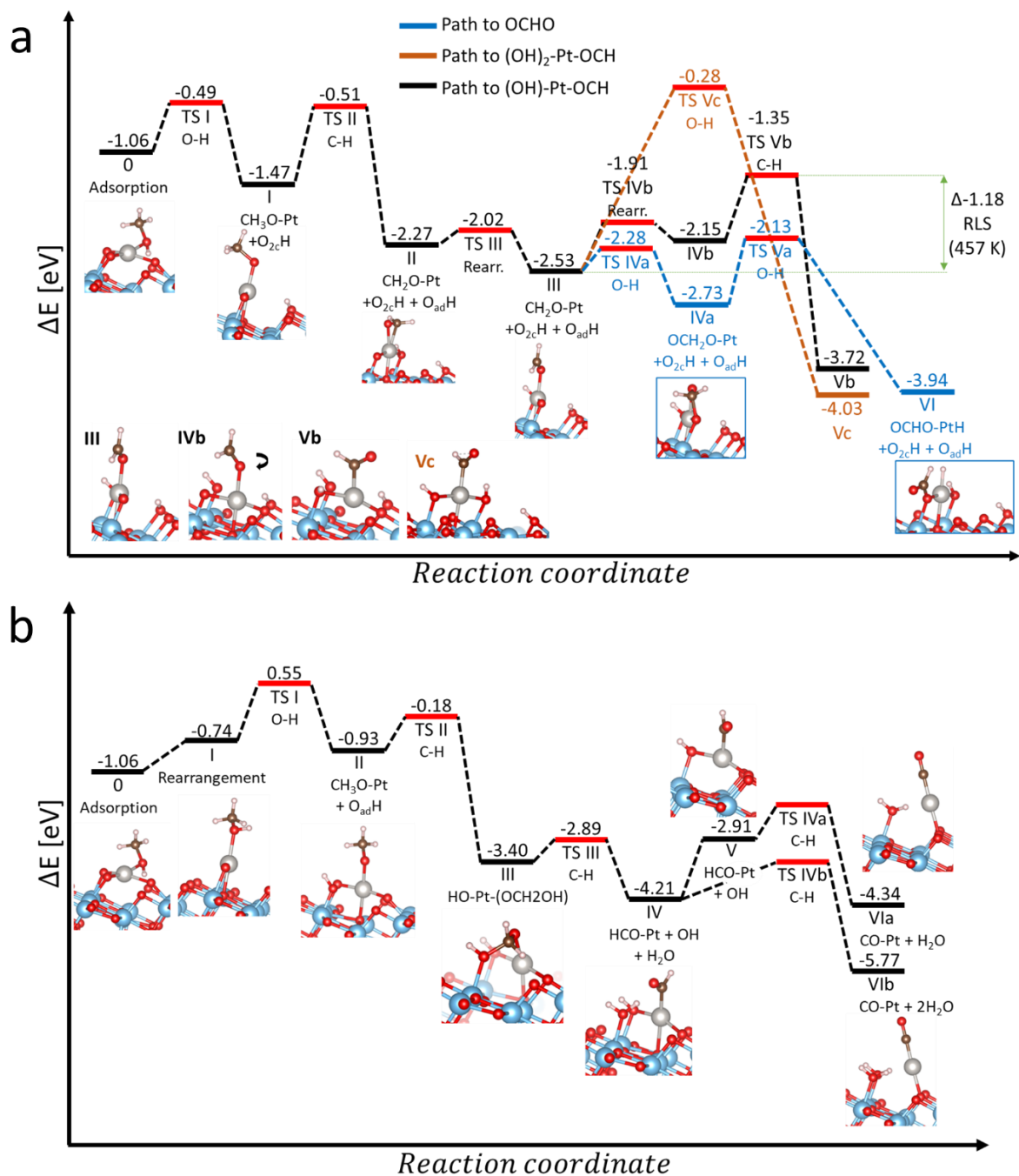


Figure 6. 4 DFT calculated methanol oxidation pathway on Pt SA/TiO₂(101) starting from the most stable adsorption mode on Pt (a) and second best adsorption mode on Pt (b).

6.3.3. Methanol adsorption on Pt₆O₁₀ NP

Figure 6. 6 shows DFT calculated adsorption behavior of methanol on a Pt₆O₁₀/TiO₂. The results reveal that methanol preferentially adsorbs on the Ti sites rather than the Pt sites (a, b, c) with slightly stronger binding compared to the pristine surface (-1.17 eV). Various adsorption isomers on various Ti sites in the interface were explored, showing slight differences (-1.40 to -1.26 eV) in adsorption energies, indicating that the cluster affects the Ti_{5c} sites. Unlike the single atom however, methanol adsorption on Pt sites exhibited a lower energy and can only chemisorb on the top layer of the Pt cluster (-0.67 eV, d). The PtO₄ subunit on the interfacial layer of the cluster can only physisorb the methanol. A plausible hypothesis for the weaker adsorption of methanol on the Pt cluster compared to Pt SA sites is related to the geometric and electronic structure of the Pt atoms. In the Pt cluster, the Pt atoms tend to adopt a stable PtO₄ planar configuration, where each Pt atom is surrounded by four oxygen atoms. This configuration maximizes the coordination and stability of the Pt atoms, making additional adsorption sites less energetically favorable. In contrast, isolated Pt atoms or single Pt atoms on the support are typically only three-coordinated, lacking the complete stabilization provided by the PtO₄ structure. This can be evidenced by the most stable adsorption mode on PtSA, where methanol adsorbs in an angle that completes the PtO₄ planar structure while accommodating the 2 oxygen adatoms and a surface bridging oxygen. Consequently, these under-coordinated Pt atoms are more prone to interact with adsorbates like methanol. However, in the Pt cluster, since the Pt atoms already achieve a stable configuration with their oxygen neighbors, the adsorption of methanol results in weaker binding energy compared to the more under-coordinated Ti sites on the TiO₂ support, which offer more favorable adsorption conditions. Further reactivity studies are then focused on the most stable adsorption mode, where methanol is interacting with surface Ti_{5c}.

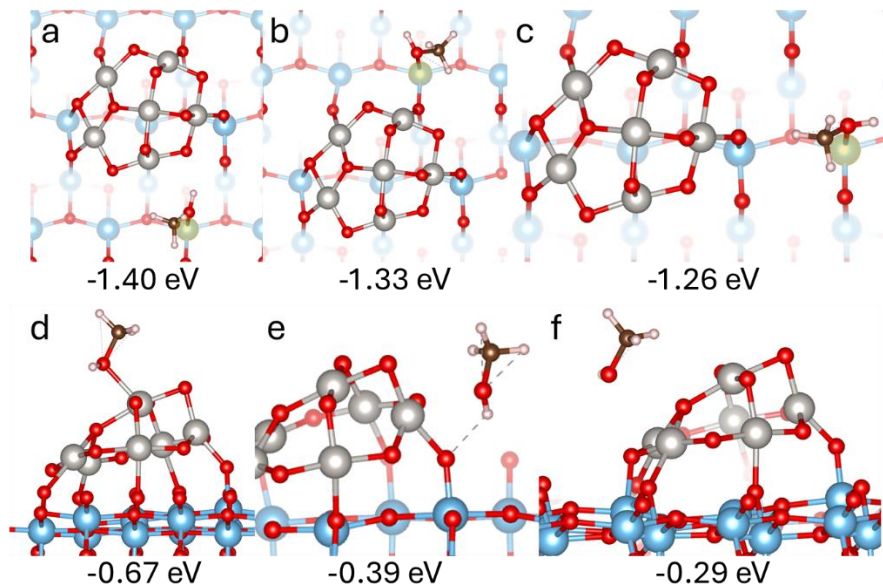


Figure 6. 5 Various adsorption mode of methanol on $Pt_6O_{10}/TiO_2(101)$ calculated via DFT. The numbers below denotes the adsorption energy in eV.

6.3.4. Methanol reactivity on Pt_6O_{10} NP: Proton Coupled Electron Transfer (PCET)

Building on the work of Sapienza et al., which suggests that the generation of reactive hydroxyl species derived from methanol participate in several proton-coupled electron transfer (PCET) reactions, we explore an initial methanol oxidation pathway on oxidized Pt cluster. During each PCET step, a proton is removed from the methanol fragment bound to the surface, while the Pt cluster or the support's band states accept the freed electron, resulting in a reduction of the catalyst at each stage. Further computational calculations show the roles of Pt clusters and hydroxyl groups on mechanistic pathways of methanol oxidation. Methanol initially adsorbs onto the Ti support rather than directly onto the Pt cluster. Once adsorbed, O-H dissociation to form methoxy (CH_3O) is generally very facile (+0.55 eV barrier). This step typically happens even at the TiO_2 support without any dopants, where methanol transfer an H to a nearby bridging oxygen. The next step is the dehydrogenation of methoxy to form formaldehyde (CH_2O). This involves the breaking of a

C-H bond, transferring an H to another O adatom available on the clusters, followed by the concerted formation of a C-Pt bond (Figure 6. 7 intermediate II). Interestingly the barrier to achieve this bond cleavage is difficult (+1.80 eV) even with the assistance of oxygen adatoms. To free up more active O adatoms, H can diffuse throughout the cluster, with barrier of ~0.6 eV (intermediate II-III). Second C-H abstraction to form HCO also encounter high barrier similar to the first activation of C-H, making this path difficult.

From this initial study, it does not seem that the PCET happens solely on the surface. Past studies note that the oxidation state of the Pt particles and local environment of the hydroxyl groups involved are still currently unknown. Looking at the low barrier of H diffusion across the cluster, we further probe whether reaction can proceed better when the hydroxyls can be transferred onto other site of the cluster, or even the support, which in turn can help reducing the Ti sites, making it more active.

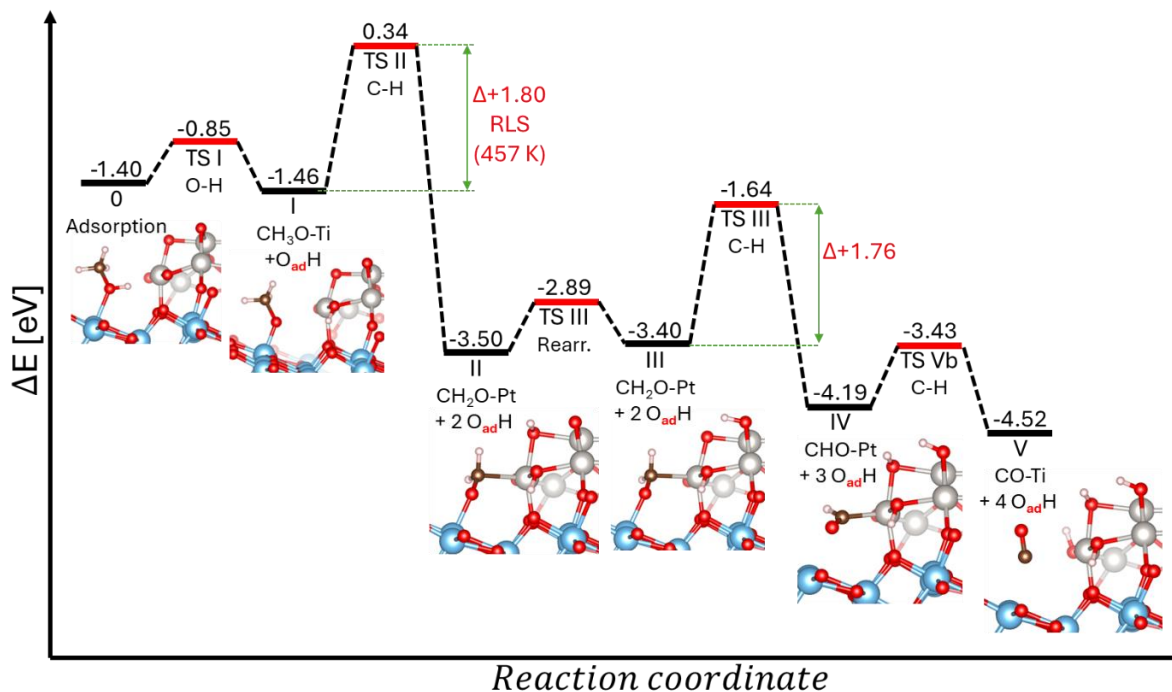


Figure 6. 6 DFT calculated methanol oxidation pathway via PCET process without hydroxyl diffusion.

As shown on Figure 6. 7, the hydroxylated surface was able to reduce the Ti_{5c} site, allowing for the PCET process to create formaldehyde to have a significantly lower barrier. We hypothesize that further C-H abstraction can then occur after H migration towards the support, agreeing with the past. Here we showcase that the role of the oxygen adatoms on the cluster, as active O species to abstract the proton out of the methanol and Pt which acts as an electron sink. The formation of DOM however was not seen in the cluster study, rather the formyl species. This, coupled with the ease of hydroxyl transfer along the cluster to create available active oxygen adatoms makes the possibility for full oxidation towards CO_2 more probable than in the single atom system.

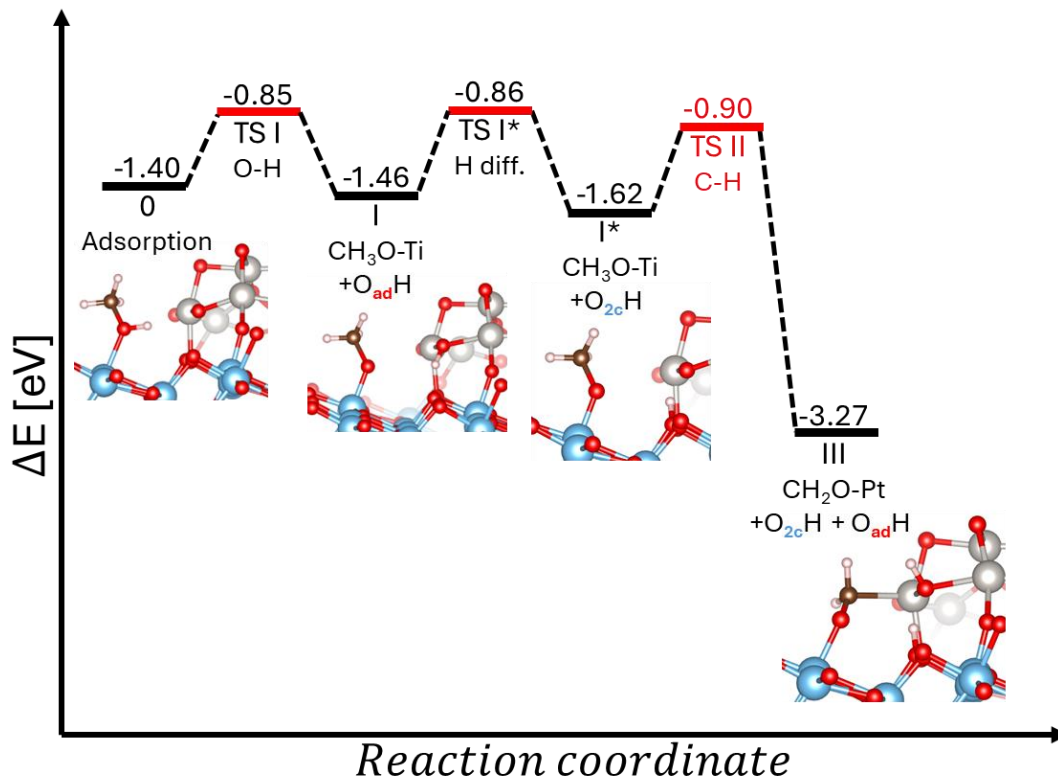


Figure 6. 7 DFT calculated methanol oxidation pathway via PCET process with hydroxyl diffusion.

6.3.5. CWA thermodynamics on Pt6O₁₀ NP

The adsorption of dimethyl methylphosphonate (DMMP) and Sarin on the Pt₆O₁₀/TiO₂ catalyst predominantly occurs at the titanium (Ti) sites on the TiO₂ support (Figure 6. 9) either via the singular P=O-Ti bond or the Ti-O-P-O-Ti (DMMP), denoted by the blue dots. The binding energies ranges between ~-2 to ~-1.5 eV, with DMMP adsorption being slightly stronger mainly due to the variation of size, conformation and interaction of the functional groups with the surface. We found these values to be comparable to the adsorption energy of DMMP/Sarin on a pristine surface. Interestingly, DMMP and sarin interacts weakly with the Pt cluster, with the strongest binding mode being on top of the PtO₄ subunit residing in the top layer of the cluster. The PtO₄ subunit on

the interface with titania is does not interact strongly with either of the nerve agent. This adsorption trend is in similar behavior with what we have seen for methanol.

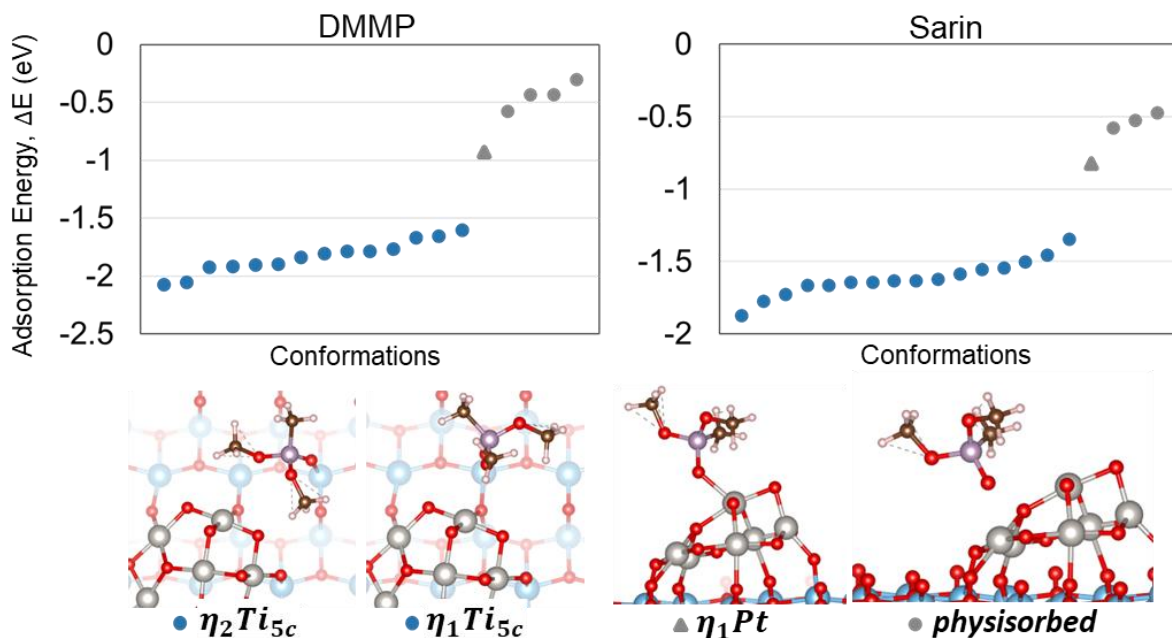


Figure 6. 8 DFT calculated exploration of DMMP (left) and sarin (right) adsorption modes on $Pt6O_{10}/TiO_2(101)$. The marker denotes the site of which the phosphoryl group is binding on. Blue dots represents adsorption on Ti sites whereas grey on Pt.

The thermodynamic analysis of sarin decomposition pathways provides critical insights into the role of the Pt NP as sarin breaks specific bonds, with select intermediates illustrated in Figure 6.10. This analysis focuses on the P-O, P-C, P-F, O-C, and C-H bonds, with the energy changes for each bond cleavage process color-coded for clarity: red for endothermic and green for exothermic reactions. The starting molecular adsorption structure was chosen to be the η_1 -configured sarin to allow more interaction with the Pt catalyst. The figure details each intermediate's energy adsorption values (E_{ads}), referenced to gas-phase sarin.

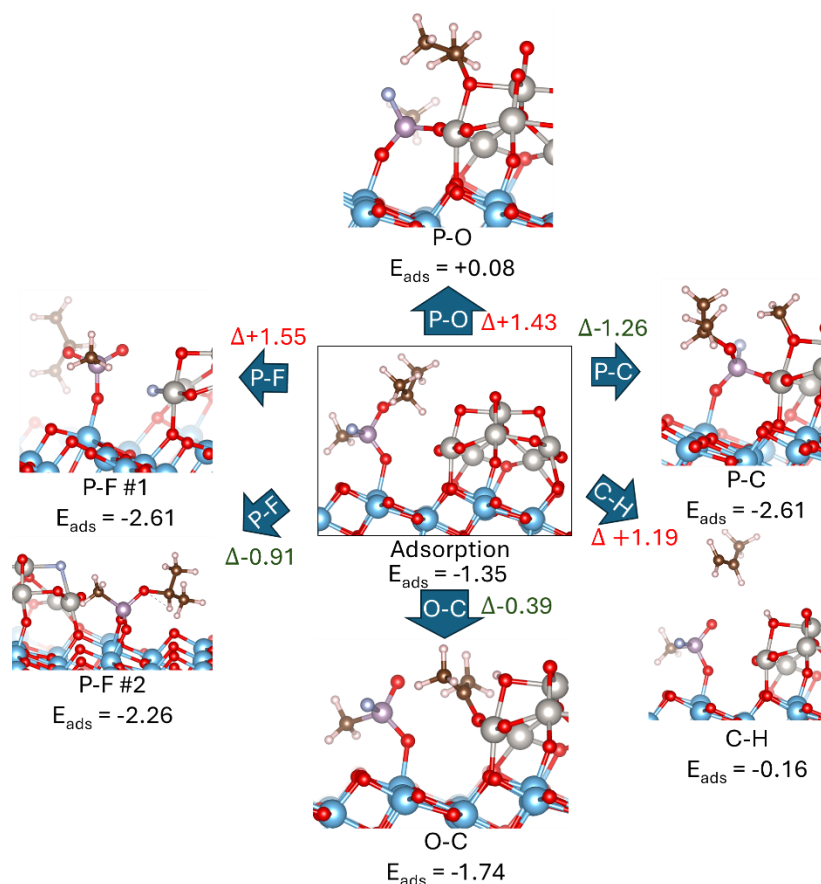


Figure 6. 9 Thermodynamic analysis of possible sarin decomposition pathways via P-O, P-C, P-F, O-C and C-H (propene release). Denoted in red is change of energy of the bond cleavage process which are endothermic and in green exothermic. The values under each intermediate denoted ‘E_{ads}’ is referenced to the gas phase sarin.

The P-O bond cleavage (highlighted in red) is an endothermic process by +1.43 eV. In order to transfer a methoxy and accommodate the remaining phosphoryl intermediate, the cluster must rearrange, by shifting an O adatom on the top layer upwards. Similarly, the P-F bond cleavage via the substitution of the -F group with O adatom from the cluster is also an endothermic reaction by +1.55 eV. The lack of stabilization by the transferred fragment onto the Pt NP after a P-F or P-O bond leads to an endothermic process in general. Rearrangement of the location of the -F group

and the remaining isopropyl methyl phosphonate (IMPA)-like intermediate to adopt η_2 -adsorption mode can help stabilize the system to be more favorable (Figure 6.10, 'P-F #2'). The general endothermic behavior to cleave P-O and P-F bonds followed by unfavorable deposition of decomposition fragment onto the Pt NP is in opposite behavior to our previous work on Cu₄ on rutile TiO₂(110), where we showcase the role of Cu₄ in stabilizing the decomposition fragment (methoxy) after the P-O bond cleavage and thus provide the thermodynamic drive for further decomposition. We contribute the endothermic change in energy due to the fact that this bond may require a significant input of energy to break the already stable PtO₄ subunit. Unlike Cu₄ which is highly fluxional and can accommodate the decomposition fragment, Pt₆O₁₀ is composed of highly stable PtO₄ subunit, making it unlikely to rearrange to accommodate the fragment. This is evidenced by the difference of energy between the global minima of Pt₆O₁₀ and other isomers of the same chemical formula found via GCBH (Figure 6.2 b). Thus, despite the Pt NP being able to provide active oxygen adatoms to restabilize the P center in sarin, making this cleavage is still a thermodynamically challenging step.

In contrast, the cleavage of the P-C bond is an exothermic reaction by -1.26 eV. This pathway does not involve any rearrangement of the Pt NP. The oxygen adatoms activate the methyl fragment whereas another O adatom stabilize the P-center, making it a thermodynamically favorable process. The exothermic nature of P-C bond cleavage suggests the prominent role of the O adatom in activating role which does not require the rearrangement of the cluster itself. Another example is the the O-C bond cleavage (transferring a methyl onto an oxygen adatom) which is as expectedly found to be another exothermic process by -0.34 eV, even without the need of the remaining phosphoryl intermediate to adopt the η_2 - adsorption mode. Both process (P-C and O-C) bond cleavage transfer a methyl fragment onto the cluster without the need of rearrangement and

maintain the tetrahedral coordination of the P center with oxygen. The fact that P-C bond cleavage have much bigger exothermic drive than O-C bond (P-C vs O-C) showcase the role of the oxygen adatoms to stabilize the P-center. Finally, the C-H bond cleavage, associated with the release of propene, is an endothermic process. This C-H bond is known to be difficult to break, despite the eventual release of propene, a relatively stable product. However, rearrangement of phosphoryl intermediate and the entropic contribution from the released propene may facilitate this process.

It is interesting to note that the thermodynamic of sarin decomposition in the Pt NP system completely contrasts with the Pt SA system, where the Pt SA is able to stabilize either the isopropoxy, the methyl or the fluorine group from any P-X bond cleavage (X: functional groups). The strongly stable bilayer PtO₄ building blocks highlight the give and take of providing active O adatoms to stabilize P-center while at the same time providing open site for the fragment to stabilize. The contrast behavior between Pt SA and Pt NP truly mimics the methanol adsorption behavior between the two systems, signifying that methanol can be used as a probe to see how decomposition fragment interact with a catalyst system.

6.4. Conclusions

The exploration of the Pt₆ cluster's chemical stoichiometry and geometry using the GCBH algorithm has identified Pt₆O₁₀ as the most stable formula under ambient conditions, attributable to its bilayer structure of planar PtO₄-like building blocks. This configuration, with partially oxidized Pt+2 and Pt+4 species, demonstrates significant stability, while providing active oxygen adatoms, with a free energy cost to remove oxygen as low as 0.68 eV. Utilizing methanol oxidation as a probe, we investigated the role of Pt single atom catalysts (SAC) and nanoparticles (NP) on stabilizing the decomposition products of sarin and DMMP. Methanol adsorption and oxidation on

the PtO₂/TiO₂ system indicated minimal electronic alteration by Pt, with methanol oxidation proceeding through O-H abstraction and subsequent C-H abstractions. After formation of initial formaldehyde, two facile oxidation pathways are observed: formyl and formate, with the latter being more facile due to the lower barrier for formate formation from dioxomethylene. A minority pathway involves PtO₂ rearrangement, leading to formation of water and CO₂ through proton-coupled electron transfer (PCET)-like processes. These findings highlight the critical role of Pt and oxygen adatoms in facilitating proton and electron transfers, essential for complete methanol oxidation.

On Pt₆O₁₀ cluster, methanol initially adsorbs onto the Ti support, where O-H dissociation to form methoxy (CH₃O) occurs with a low barrier (+0.55 eV). The subsequent dehydrogenation of methoxy to formaldehyde (CH₂O) has a high barrier (+1.80 eV). However, H diffusion either to the surface or to another oxygen adatoms site across the cluster can free the initial O adatom and is relatively easy (~0.6 eV). After transferring a hydroxyl to the surface, the barrier to form CH₂O reduces to 0.72 eV, suggesting that hydroxyl transfer to other cluster sites or the support could enhance reactivity. Our findings indicate that PCET involves both the surface and the Pt cluster, with oxygen adatoms playing a crucial role in stabilizing intermediates and facilitating further oxidation steps.

Lastly we compare the methanol oxidation reactivity to CWA. The adsorption of dimethyl methylphosphonate (DMMP) and sarin on the Pt₆O₁₀/TiO₂ catalyst primarily occurs at the titanium (Ti) sites on the TiO₂ support, with binding energies ranging from ~-2 to ~-1.5 eV, slightly stronger for DMMP due to its size and functional group interactions. Both DMMP and sarin interact weakly with the Pt cluster, with the strongest binding mode on the Ti sites, similar to methanol adsorption

behavior. The thermodynamic analysis of sarin decomposition on Pt NP reveals that P-O and P-F bond cleavages are endothermic processes, requiring +1.43 eV and +1.55 eV, respectively. These processes involve rearrangements of the Pt NP and result in an overall destabilizing effect due to the lack of stabilization of the transferred fragments. In contrast, P-C bond cleavage is exothermic by -1.26 eV, and does not require Pt NP rearrangement, making it a thermodynamically favorable process. Similarly, the O-C bond cleavage is exothermic by -0.34 eV. These pathways demonstrate the role of oxygen adatoms in stabilizing the P-center without necessitating cluster rearrangement. The C-H bond cleavage, associated with propene release, is endothermic due to the difficulty in breaking this bond, despite the stable product formed. Interestingly, the Pt NP system's behavior contrasts with the Pt SA system, where Pt SA can stabilize various decomposition fragments, highlighting the complex interplay of active oxygen adatoms and the stability of the PtO₄ subunits in facilitating or hindering sarin decomposition. These findings provide a comprehensive understanding of the mechanistic pathways and thermodynamics of methanol and CWA oxidation on Pt-based catalysts, offering valuable insights for future catalytic design and application.

Chapter 7

Conclusion

This dissertation employs DFT modeling to understand the characteristic of highly dispersed metal catalysts ($n=1-6$), its interaction with the titania support and activity under reaction condition using various probe reactions such as CO oxidation and methanol dehydrogenation to understand its viability for chemical warfare agent decomposition, namely sarin (GB) and its simulant DMMP (dimethyl methyl phosphonate). We showcased that titania works exceptionally well to trap the nerve agents, as well as stabilizing highly dispersed clusters on the surface. Not only that, using CO as probe reaction it was found that the stability of these catalyst remains dynamic even in reaction conditions, offering unique reactivity despite making confirmation with experiment elusive. We found that Pt single atoms facilitate P-X bond cleavage for both sarin and DMMP; using these key intermediates and transition states, we established reactivity trend towards decomposition of CWA across the transition state metals. Finally, we moved to nanoclusters ($n=4$ & 6) and examined the role of size, environment and its interaction with support towards reactivity. We showcased that in UHV conditions, Cu_4 and alkali promoters such as K can donate electrons to the surface which reduces the Lewis acidity of the Ti sites, hence decreasing the overbinding of the DMMP which in turn increase its reactivity.

In the first chapter of this thesis, we study the basic reactivity of sarin on rutile $\text{TiO}_2(110)$. Sarin binds strongly to Ti_{5c} sites despite being slightly weaker than DMMP. As expected, the reactivity of sarin on pristine rutile via P-F or P-O bond is low (>1.8 eV), with the most active bond cleavage being the O-C bond, transferring a C_3H_7 group to the nearby surface bridging oxygen. This reactivity can be improved in the presence of defect, which facilitates sarin to adsorb

on the oxygen vacancy sites, allowing for shorter pathway towards P-F or P-O bond cleavage (~1.4 eV) making it possible at higher temperatures. An ensemble of molecularly adsorbed and kinetically accessible decomposed sarin intermediates was then selected to calculate the key vibrational stretches and compared with experimental IR stretches. We confirmed that peaks at ~1200 cm correspond to the phosphoryl group creating dative O=P-Ti bond while the peaks between 1100-1000 cm⁻¹ correspond to the bidentate Ti-O-P-O-Ti bonds. Upon increasing the heat, the 1200 cm⁻¹ peaks decreases whereas the 1100-1000 cm⁻¹ peaks increase, signaling decomposition taking place. This is consistent with the vibrational analysis showing that the 1200 cm⁻¹ peaks being absent of the kinetically accessible intermediate. Despite the low reactivity, we concluded that titania is a great trap for DMMP and Sarin, with both system having similar chemistry on the surface. The creation of oxygen vacancies adds additional electrons on to Ti_{5c} sites, increasing its Lewis acidity while at the same time reduces its binding strength with the P containing intermediates, which also contribute to the overall reactivity of the agents.

In the second chapter we began to investigate the stability of single atom catalyst supported on anatase. Anatase was selected as the support as it was found to exhibit higher reactivity compared to rutile while maintaining strong interaction with CWAs. Using ab initio thermodynamics, after reducing pretreatment, Pt resides on an oxygen vacancy site, confirmed via computed vibrational stretch and DRIFTS. As the system enters the oxidative reactive conditions, Pt undergoes initiative steps, consisting of first healing the oxygen vacancies with O₂, followed by a cycle of Eley-Rideal CO oxidation to form a reduced PtCO. Each of these steps in the initiation path were captured by timed DRIFTS spectra where it shifts upwards from 2073 (computed:), to 2087 () to finally a mixture of 2115 and 2087 before resolving to steady state 2115 upon introduction of O₂ and CO. All these stretches agree with the DFT calculations very well. Experimental kinetic studies

showcase peculiar partial order behavior of CO and O₂, suggesting multiple competing pathways at hand. To understand the state observed during steady state, meticulous pathway searches with DFT indeed showcases multiple competing mechanisms, each convoluted with another, in the reactive cycle in which all of them have a significant degree of rate control. Using microkinetic modeling, we showcase the ensemble of intermediates: PtCO, PtCO(O₂), PtO(O₂)CO and Pt(CO)(CO₃), all having CO vibrational stretch close to the experimentally observed steady state values at 2115 cm⁻¹. We also unravel how the degree of rate control of each pathway can impact the overall CO and O₂ reaction order via deconvoluted, satellite microkinetic modeling of each found reaction cycle. DFT found pathway also points several branching pathways which features 2 CO species being adsorbed on the active Pt sites along the reaction pathway, whereas some that only feature 1 CO species. This was further confirmed by experimental C13 experiment, establishing the source of the fractional CO and O₂ order. We also highlighted the accuracy of the microkinetic modeling in predicting the turnover frequency which is incredibly sensitive towards the energy accuracy obtained by DFT.

In the third chapter, we continued to model the reactivity of CWAs in the presence of Pt SA catalysts on anatase TiO₂(101). Our study revealed distinct adsorption behaviors between sarin and DMMP, with DMMP favoring adsorption via an η₂ configuration on two Ti sites, while sarin adsorbs more strongly on the active Pt single atom (SA) due to steric hindrance. A quick thermodynamic study indicated that both reactants follow a similar pathway, migrating to a Ti_{5c} site via an η₁ binding mode before decomposition. The decomposition of DMMP and sarin most favorably occurs via P-X (X = methoxy, methyl, isopropoxy, and fluorine) bond cleavage, with P-O and P-F bond cleavages showing acceptable barriers ranging from 0.75 to 1.35 eV relative to the activated molecular adsorption mode, achievable with mild heating. This low activation barrier

is attributed to the Pt SA's ability to stabilize the isopropoxy/methoxy group in a penta-coordinated P center, adopting a stable PtO_4 -planar-like structure.

Building on the decomposition pathways observed on Pt SA, we selected several key intermediates to establish reliable descriptors for predicting catalytic performance. We studied the stability of 13 different d-transition metal/titania systems under ambient conditions, finding that metals with low oxidation states adopt the MO (M=Metal) formula, while those with higher oxidation states adopt the MO_2 formula. By recalculating key intermediates such as the decomposed GB via P-O and P-F bond cleavages and the bridging intermediate on these metal systems, we uncovered a 'volcano'-like relationship. Metals with either too low or too high thermodynamic drive to cleave P-O suffer in terms of kinetics. A deeper investigation revealed a linear correlation between the Lewis acidity of the metal system and its d-band center, particularly for reactivity involving P-O bond cleavage. This study has enhanced our understanding of CWA decomposition mechanisms on Pt SA/a- $\text{TiO}_2(101)$ and established a set of descriptors useful for predicting the catalytic performance of SAC/titania systems.

In the fourth chapter, we investigated the role of bigger cluster and alkali modifiers soft landed on titania in UHV condition for decomposition of CWAs. The reactivity of dimethyl methyl phosphonate (DMMP) was studied on rutile $\text{Cu}_4/\text{TiO}_2(110)$ and $\text{K}/\text{Cu}_4/\text{TiO}_2(110)$ surfaces using DFT, supporting the observation of near ambient pressure x-ray photoelectron spectroscopy (NAP-XPS). It was found that mass selected Cu_4 clusters and potassium (K) atoms improved the reactivity and recyclability of the TiO_2 surface after exposure to DMMP. Using NAP-XPS, we observed the formation of DMMP by-products via the measurements of the phosphorous (P) 2p and carbon 1s core level spectra shifts. Systems with Cu_4 show many convoluted, unresolved peaks

of P 2p that signifies ensembles of products on the surface. The co-deposition of K atoms and Cu₄ clusters further improves the reactivity with no intact DMMP detectable.

To further understand the role of the clusters, detailed DFT calculations were performed to determine the surface structures and energetically accessible pathways on the Cu₄/TiO₂(110) and K/Cu₄/TiO₂(110) surfaces. Firstly we found that Cu₄ prefers to maximize contact with the surface, adopting a monolayer rhombus coordination with potassium residing near the interfacial sites. Our Bader charge analysis further confirms the source of reactivity of the system co-deposited with K, where there are significant electron transfers from Cu₄ and K towards interfacial Ti_{5c} sites. The addition of K as alkali promoter weakens the Lewis acidity of Ti sites, making the binding energy of DMMP (intact and decomposed) weaker, which in turn facilitates further decomposition. The calculations show that DMMP and P-containing reaction products preferentially bind to the titania, whereas the molecular fragments, i.e., methoxy and methyl, bind to both the Cu₄ clusters and TiO₂. This stabilization provides the thermodynamic drive to cleave the P-O, O-C, and P-C. One of the reasons Cu₄ was able to stabilize these fragments is because these Cu₄ clusters are highly fluxional, in order to accommodate the configuration of fragments that are bound to them. To fully understand the state of the accessible surface species, 290 intermediates consisting of various degree of DMMP decomposition (1-3 bond cleavages) was explored. For each configuration, the P 2p binding energy shift relative to chemisorbed DMMP was calculated. The calculated energy shifts range from -1 to -4 eV, which align well with the observed energy widths of the experimental P 2p spectra. The extent of these shifts varies depending on the specific bonds broken, such as P-O or P-C bonds. Notably, the most significant shifts occur at P centers where all P-O and P-C bonds are severed and subsequently re-coordinate to Cu on surface O atoms, forming "atomic" P species. This observation supports the idea that the broad P 2p core level spectra are best

represented by an almost continuous range of P 2p chemical shifts, stemming from numerous energetically feasible decomposition configurations. When only a limited number of final state configurations are energetically favorable, the findings align with traditional peak fitting methods, where each peak corresponds to a distinct oxidation state. Overall, this combined experimental and computational investigation offers a new point-of-view into interpreting core-level spectra related to intermediates from complex surface reactions.

Although the result from Cu₄ deposition is promising, the study did not include the effect of ambient conditions towards the stability of the cluster and hence. In chapter 6, we investigated the affect of ambient oxidative condition towards highly dispersed Pt₆ nanocluster supported on titania and its activity using various methanol as a probe reaction. The exploration of the Pt₆ cluster's chemical stoichiometry and geometry using the GCBH algorithm identified Pt₆O₁₀ as the most stable formula under ambient conditions, attributed to its bilayer structure of planar PtO₄-like building blocks with partially oxidized Pt⁺² and Pt⁺⁴ species. This configuration demonstrates significant stability and provides active oxygen adatoms, with a free energy cost to remove oxygen as low as 0.68 eV. Utilizing methanol oxidation as a probe, we investigated the role of Pt single atom catalysts (SAC) and nanoparticles (NP) in stabilizing the decomposition products of sarin and DMMP. Methanol adsorption and oxidation on the PtO₂/TiO₂ system indicated minimal electronic alteration by Pt, with oxidation proceeding through O-H abstraction and subsequent C-H abstractions. Two primary oxidation pathways were observed: formyl and formate, with the latter being more facile. These findings highlight the critical role of Pt and oxygen adatoms in facilitating proton and electron transfers essential for complete methanol oxidation.

Moving on to chemical warfare agents (CWA), we found that dimethyl methylphosphonate (DMMP) and sarin adsorb primarily at titanium sites on the TiO₂ support of the Pt₆O₁₀/TiO₂

catalyst, with binding energies slightly stronger for DMMP. Both agents interact weakly with the Pt cluster, similar to methanol adsorption behavior. Thermodynamic analysis revealed that P-O and P-F bond cleavages in sarin are endothermic processes, while P-C and O-C bond cleavages are exothermic and thermodynamically favorable. The Pt NP system's behavior contrasts with the Pt SA system, which can stabilize various decomposition fragments. These insights into the mechanistic pathways and thermodynamics of methanol and CWA oxidation on Pt-based catalysts provide valuable guidance for future catalytic design and application.

Appendix A

Supporting information for chapter 2.

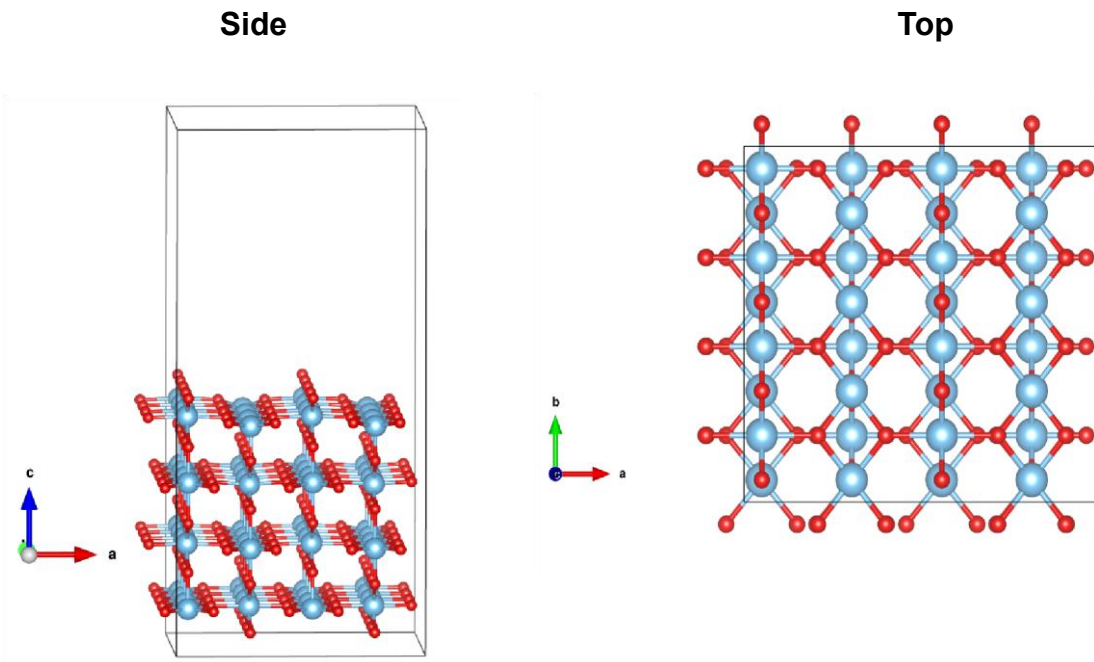


Figure A. 1 Side and Top view of pristine 2×4 $r\text{-TiO}_2(110)$ surface model.

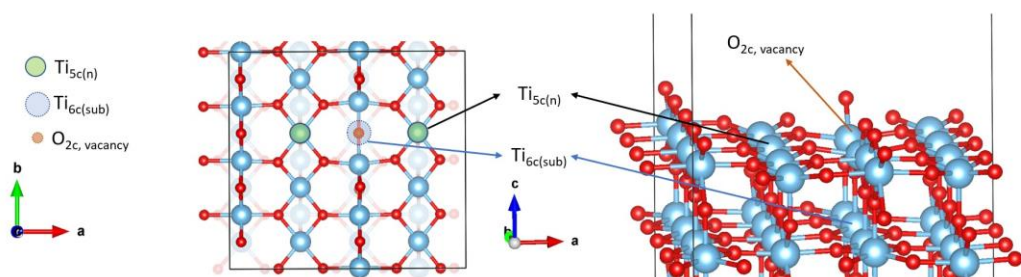


Figure A. 2 Top and side view of defective $r\text{-TiO}_2(110)$ surface model.

Figure A. 1 and A. 2 shows the surface model used in this work. There are 4 types of atoms exposed on the surface, depending on their coordination, namely Ti_{5c} , Ti_{6c} , O_{2c} , and O_{3c} . These atoms form rows in the $[001]$ direction. The top-most layer consists of repeating O_{2c} rows

(bridging oxygen row), O_{3c} rows, and Ti_{5c} rows. Ti_{6c} rows reside beneath the top-most O_{2c} bridging oxygen row.

A1. Reaction Rate Constant Calculated using the Transition State Theory

The kinetic rate constant for each elementary step of sarin's decomposition was calculated using the Transition State Theory approximation, with vibrational contribution to entropy neglected:

$$k = \left(\frac{k_b T}{h}\right) \exp\left[-\frac{E_{TS}-E_R}{k_b T}\right] \quad (\text{A-1})$$

Where E_{\cdot} is the energy of the transition state and E is the energy of the reactant.

Table A.1 and A2 list the kinetic rate constant on the pristine (Table S1) and defective (Table S2) surfaces. The activation temperature of each step (where $k \sim 1 \text{ s}^{-1}$) is also listed.

Table A. 1 Reaction rate constants [1/s] at 300 K of Sarin on the pristine surface starting from intermediate C

C1 to C2	C2 to C3	C1 to C2*	C2* to C3*	C3* to C4*
P-F	P-O	O-C	P-F	C-H
2.02 E-17 s ⁻¹ (1.10 s ⁻¹ at 675K)	1.34 E-15 s ⁻¹ (1.12 s ⁻¹ at 635K)	1.80 E-7 s ⁻¹ (1.24 s ⁻¹ at 455K)	1.72 E-8 (1.33 s ⁻¹ at 390K)	1.30 E-14 (1.24 s ⁻¹ at 615K)

Table A. 2 Reaction rate constants [1/s] at 300 K of Sarin on the pristine surface starting from intermediate C

B1 to B2	B2 to B3
P-O	P-F
3.3 E-26 s ⁻¹ (7.38 E-2 s ⁻¹ at 800K)	8.74 E-13 (1.29 s ⁻¹ at 575K)

Table A. 3 Reaction rate constants [1/s] at 300 K of Sarin on the defective surface starting from intermediate E

F1 to E1 to E2	E2 to E3	F1 to E1 to E4	E4 to E5	F1 to F2	F2 to F3
O-C	P-F	P-F	O-C and C-H	P-O	P-F
1.65 E-15 s ⁻¹ (0.97 s ⁻¹ at 630K)	7.99 E-9 s ⁻¹ (1.2 s ⁻¹ at 485K)	2.57 E-6 s ⁻¹ (0.93 s ⁻¹ at 425K)	2.53 E-8 s ⁻¹ (1.21 s ⁻¹ at 585K)	1.76 E-5 s ⁻¹ (1.23 s ⁻¹ at 410K)	8.20 E-5 (1.07 s ⁻¹ at 425K)

Appendix B

Supporting information for chapter 3.

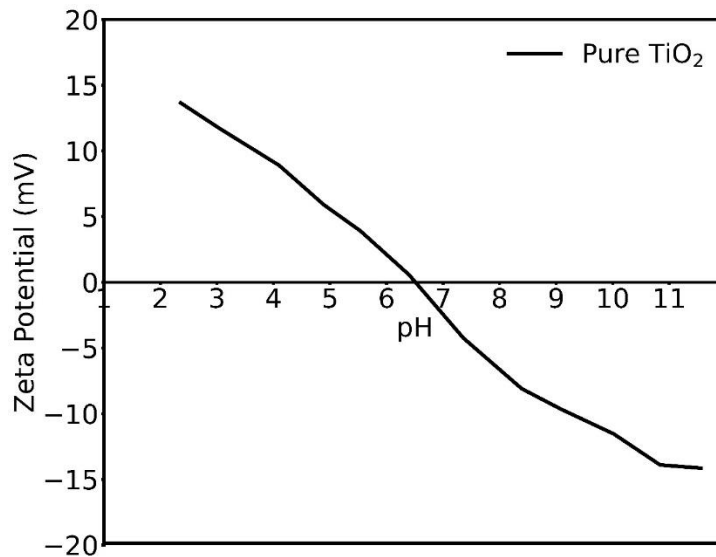


Figure B. 1 Zeta potential of anatase TiO₂ measured as a function of pH. The pH where the zeta potential becomes zero is the point of zero charge (PZC) where the surface of TiO₂ particles would have a net charge of zero. PZC for anatase TiO₂ is ~6.4 and therefore it gets negatively charged at a pH higher than that. The Pt precursor, [Pt(NH₃)₄](NO₃)₂, dissociates into [Pt(NH₃)₄]²⁺ and 2(NO₃⁻). Based on the PZC, we therefore synthesized the PtSA/TiO₂ catalysts at pH 13.7 to electrostatically adsorb the Pt complex ([Pt(NH₃)₄]²⁺) onto the TiO₂ particles.

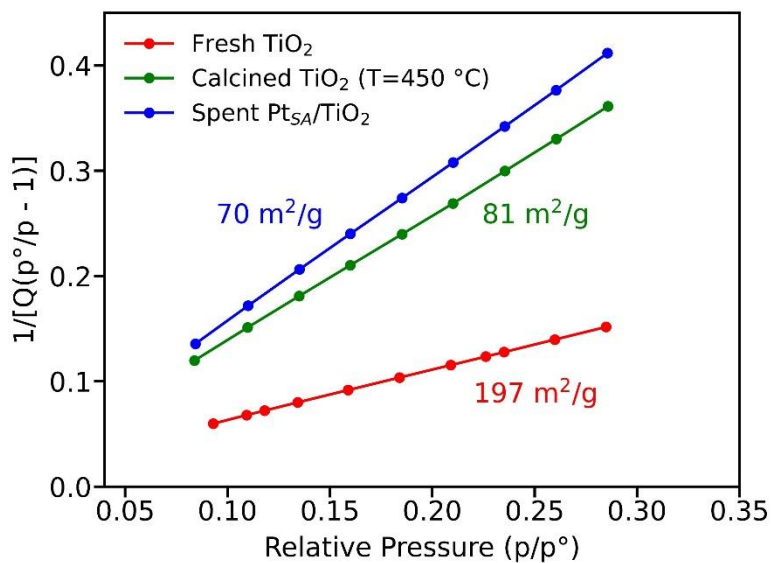


Figure B. 2 BET surface area plot for the BET surface area analysis of the as-received TiO_2 powders (fresh TiO_2), calcined TiO_2 (calcination temperature $450 \text{ }^\circ\text{C}$), and spent PtSA/TiO_2 (after CO oxidation kinetic measurement presented in Figure 4 (a) and (b)).

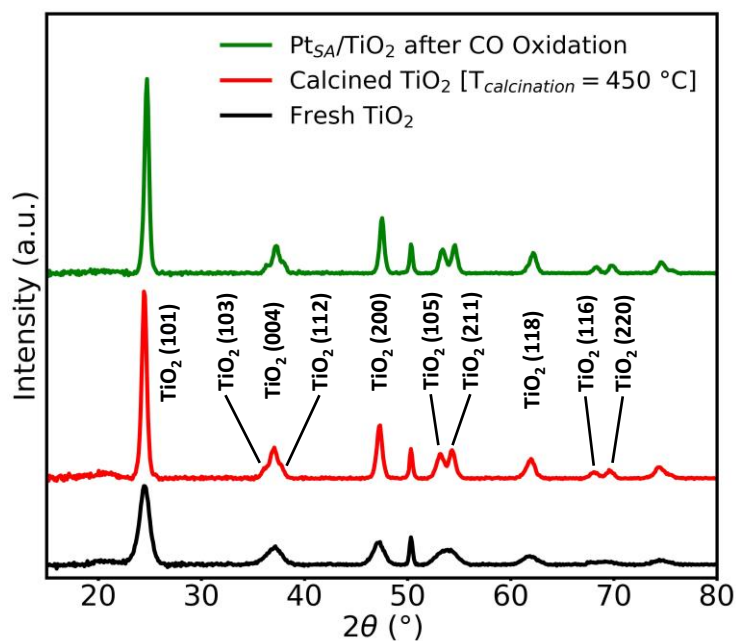


Figure B. 3 PXRD patterns for fresh anatase TiO_2 (black), calcined (red) anatase TiO_2 (TiO_2 calcined at $450 \text{ }^\circ\text{C}$ in the same procedure as the PtSA/TiO_2), and PtSA/TiO_2 catalyst after CO oxidation kinetics

experiment (green; calcined at 450 °C, oxidized at 300 °C, reduced at 350 °C, and then performed CO oxidation kinetics.). The scan for the calcined TiO₂ shows peaks only for anatase TiO₂ ensuring that TiO₂ was not converted to rutile phase during the calcination procedure (a prominent peak for TiO₂ (110) at 2θ = 27° would be present if TiO₂ was converted to rutile phase). (Note: the peak at ~50° is from the sample holder)

Table B. 1 Average crystallite size of TiO₂ in the fresh TiO₂, calcined TiO₂, and the spent PtSA/TiO₂ (after CO oxidation kinetics experiment on the reduced PtSA/TiO₂) samples calculated using the Scherrer equation and the line broadening of TiO₂ (101) and TiO₂ (200) diffraction peaks.

Sample	Fresh TiO ₂	Calcined TiO ₂ (450 °C)	Spent Pt _{SA} /TiO ₂
Average Crystallite Size (nm)	9.0	17.8	20.5

Scherrer equation:

$$D_p = \frac{0.94 \times \lambda}{\beta \times \cos\theta}$$

Here, D_p: average crystallite size [nm], β: line broadening at half the maximum intensity, also known as full width at half maximum (FWHM) [radians], θ: Bragg angle [°], λ: X-ray wavelength [nm] (λ_{CuKα} = 0.15418 nm)

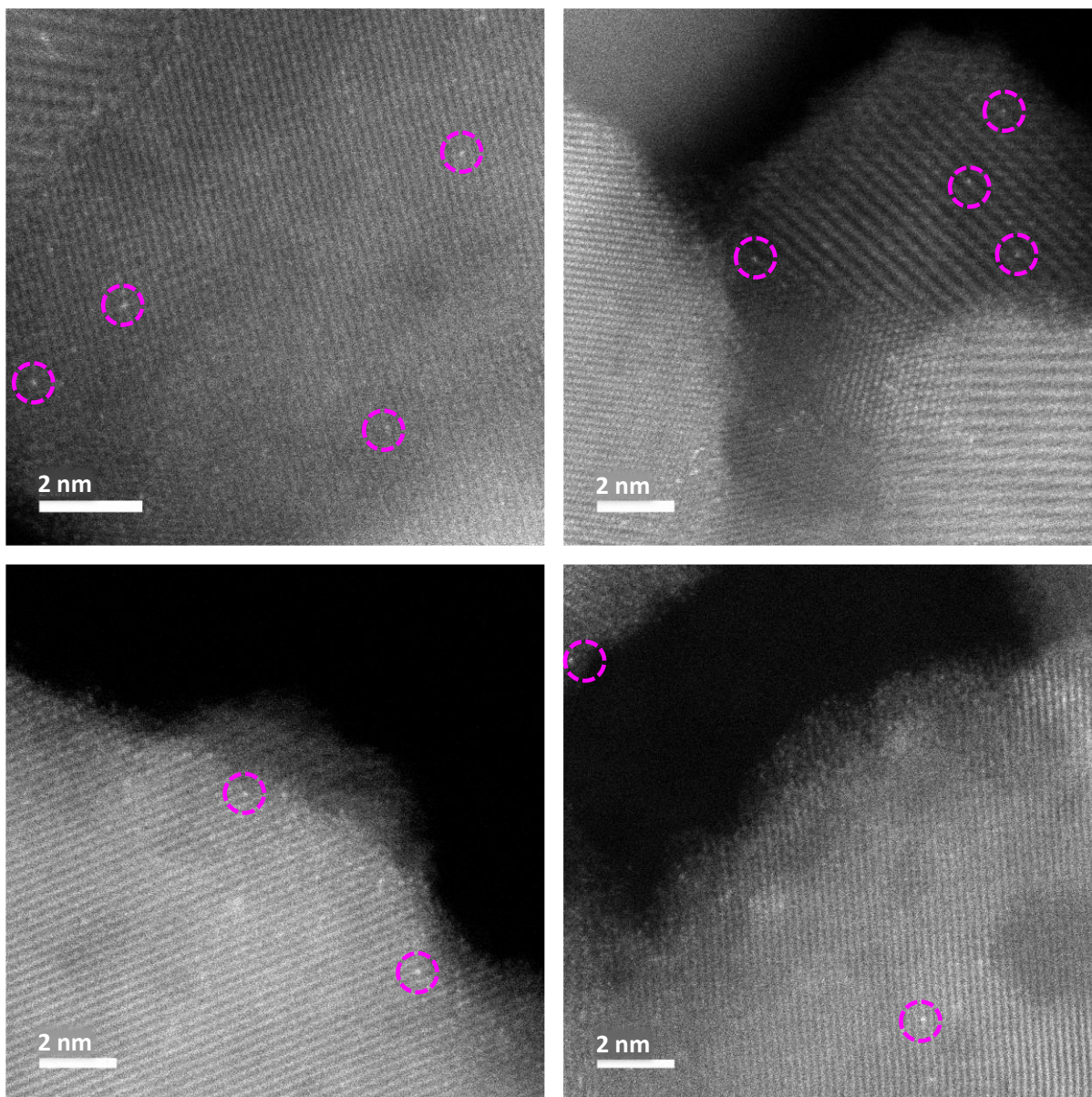


Figure B. 4 STEM images of PtSA after CO oxidation confirm stability of the Pt single atoms under reaction condition. Regeneration of the CO chemisorption DRIFTS spectrum after CO oxidation further confirms the stability of PtSA.

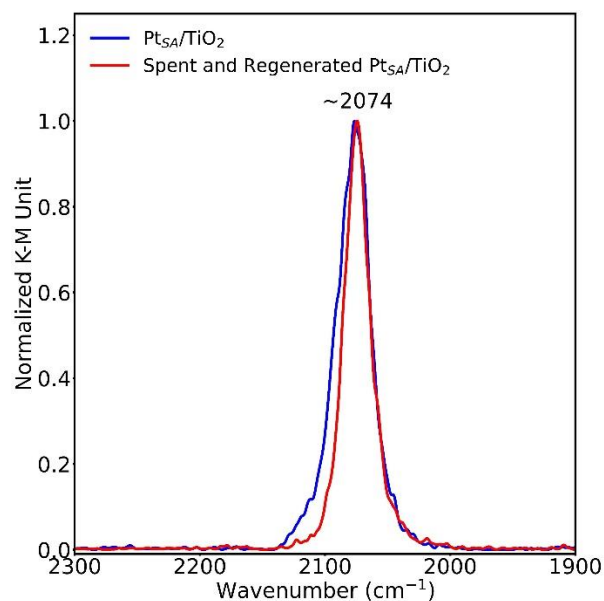


Figure B. 5 CO adsorption at 35 oC on the freshly reduced PtSA/a-TiO₂ catalyst (blue) and on the same catalyst after ‘regenerating’ it following CO oxidation at 160 oC for 1 hr (red), both showing almost identical spectra which suggests stable nature of the PtSA species. After the synthesis, the catalyst was pretreated with 10 kPa O₂ at 300 °C for 1 hour, followed by reduction under 20 kPa H₂ at 350 °C for 2 hours prior to the exposure to 0.56 kPa CO at 35 °C. This state is referred as the freshly reduced PtSA/a-TiO₂. The sample was then ‘regenerated’ through repetition of the oxidation at 300 °C (1 hr) followed by H₂ reduction at 350 °C (2 hr).

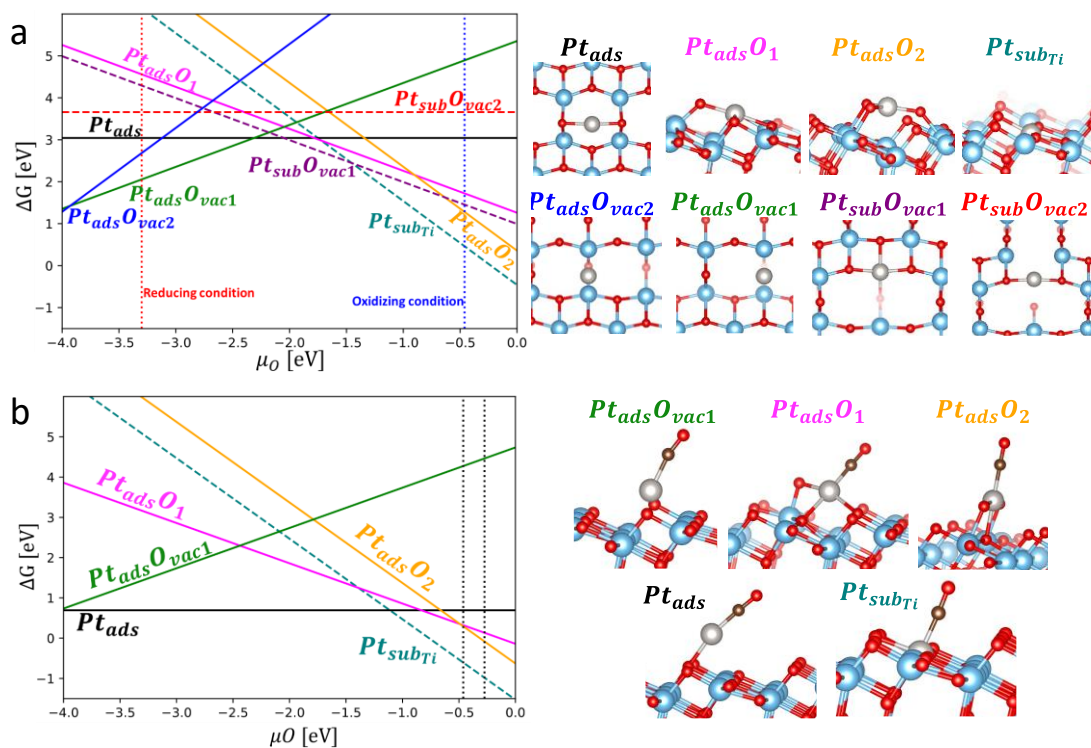


Figure B. (a) The stability diagram of the different configurations of PtSA. (b) The stability diagram of the different configurations of the supported PtSA on anatase TiO_2 bound with CO (the vertical lines denotes the oxidizing condition and atmospheric condition). CO helps ‘pull’ the Pt substituting Ti onto the surface.

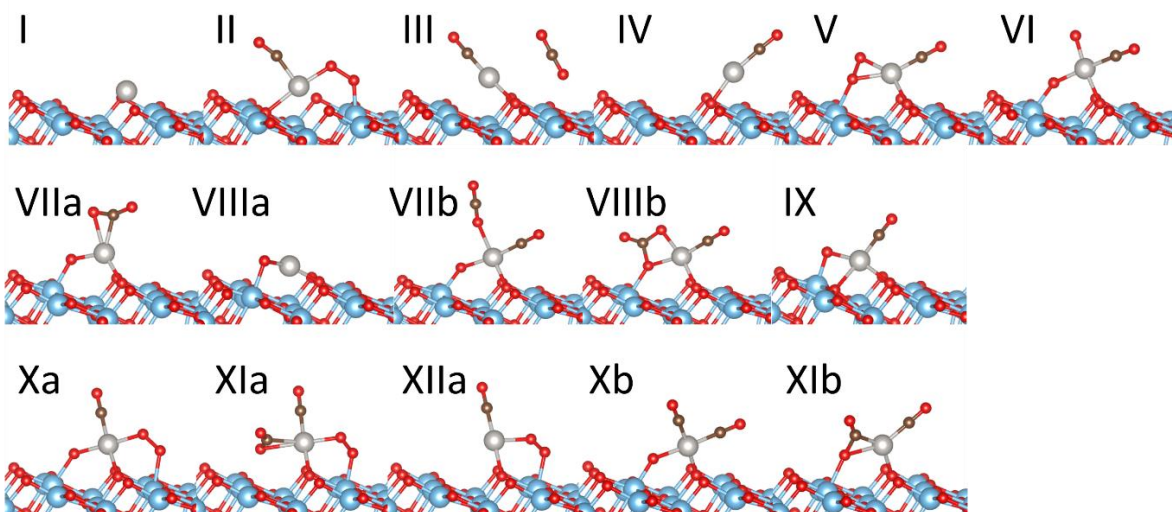


Figure B. 7 Structure representation of intermediates found in pathway exploration

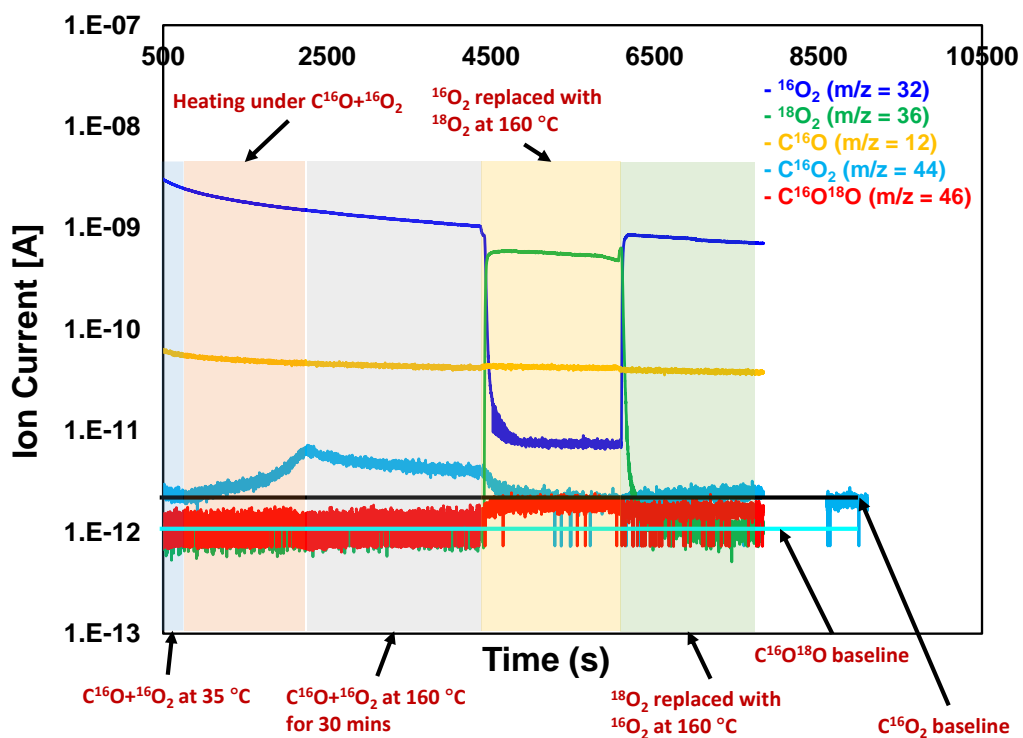


Figure B. 8 Mass spectrometer signals during $^{16}\text{O}_2/^{18}\text{O}_2$ switching under steady-state C^{16}O oxidation condition at $160\text{ }^\circ\text{C}$. After $^{16}\text{O}_2$ was replaced with $^{18}\text{O}_2$, we observed an instant depletion of C^{16}O_2 signal with ^{16}O signal (almost at the same time) which eventually reaches the baseline level, suggesting that

under $C^{16}O$ and $^{16}O_2$ co-flow, the adsorbed $C^{16}O$ was only reacting with the adsorbed ^{16}O and its reaction with lattice ^{16}O is unlikely. If lattice ^{16}O were involved, the $C^{16}O_2$ signal would not deplete immediately after ^{16}O being replaced with ^{18}O . At the same time, $C^{16}O^{18}O$ signal instantly rose from its baseline level suggesting that adsorbed and/or gas-phase $C^{16}O$ reacted with adsorbed ^{18}O on Pt. Details of the experiment can be found in the “Experimental Methods” section.

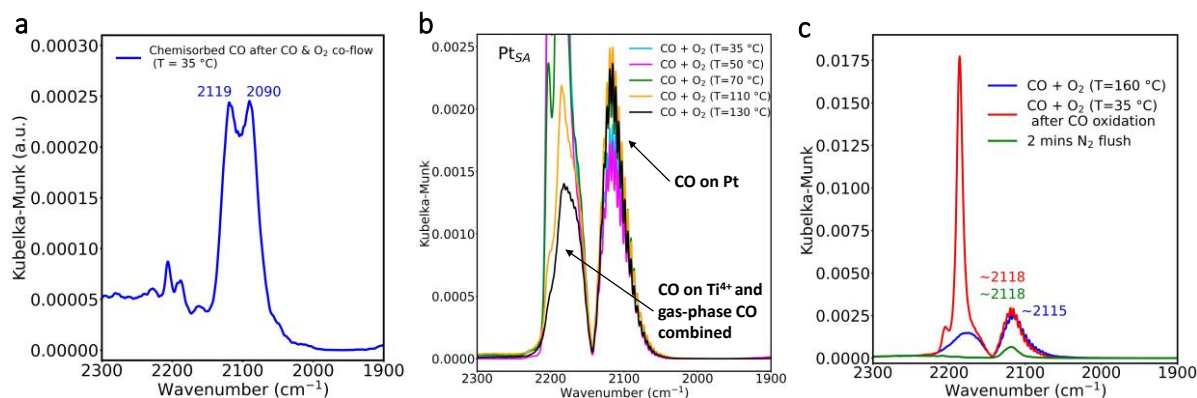


Figure B. 9 CO chemisorption DRIFTS spectra (a) under N_2 flow after CO and O_2 co-flow at 35 °C, (b) under CO and O_2 co-flow as the sample is being heated up from 35 °C to reaction temperature (160 °C) showing the transition of the CO-Pt, CO-Ti $^{4+}$, and gas-phase CO peak, and (c) at 35 °C with CO flow only after cooling down from CO oxidation at 160 °C under CO and O_2 flow. The CO-Pt peak not returning to the 2115 and 2087 cm^{-1} features shows complete and irreversible oxidization of the Pt sites under CO oxidation.

B1. Microkinetic Modeling Methodology

DFT based microkinetic modelling was employed to quantitatively compare the theoretically proposed reaction pathway to experimental measurements. The model consists of 13 elementary steps (Table S2), following the ‘reactive cycle’ found from the Gibbs free energies pathways (intermediate IV onwards) calculated by DFT. Transition State Theory was used to calculate the forward and reverse rate constant of surface reactions¹⁶¹:

$$k_{surf,i} = \frac{k_B T}{h} \exp\left(-\frac{\Delta G_{act}^0}{RT}\right)$$

Whereas collision theory was used to calculate the rate of reaction steps involving adsorption and desorption of gas molecules. The equilibrium constant ($K_{ads,i}$) was used to calculate the rate of desorption step:

$$k_{ads,i} = \frac{\sigma A_{site} P^0}{\sqrt{2\pi m_{gas} k_B T}}$$

$$K_{ads,i} = \frac{\exp(-\Delta G_{ads,i}^0)}{k_B T}$$

$$k_{des,i} = \frac{k_{ads,i}}{K_{ads,i}}$$

where σ is the sticking coefficient (assumed as 1), A_{site} is the area of the active site, P^0 is the standard state pressure, m_{gas} is the mass of the adsorbing/desorbing gas molecule, and k_B is Boltzmann's constant. Each Pt is assumed as an active site; hence the area can be approximated from the Pt neutral radii (135 pm), which gives an approximately $\sim 1E^{-20}$ m² of footprint area (A_{site}).

The rate of each elementary step i was calculated using the following equation:

$$r_i = k_i^{forward} \prod_j \alpha_{j,surf}^{v_{ji}^{forward}} \prod_j \alpha_{j,gas}^{v_{ji}^{forward}} - k_i^{reverse} \prod_j \alpha_{j,surf}^{v_{ji}^{reverse}} \prod_j \alpha_{j,gas}^{v_{ji}^{reverse}}$$

where $k_i^{forward}$ and $k_i^{reverse}$ are the forward and reverse rate constants for elementary step i, $v_{ji}^{forward}$ and $v_{ji}^{reverse}$ are the stoichiometric coefficients of reactant in the forward and reverse directions, respectively. $\alpha_{j,surf}$ is the surface coverage fraction for surface intermediates j reactant and $\alpha_{j,gas}$ is the ratio of the partial pressure to the standard pressure, P_i/P^0 , for gaseous reactant.

The changes of each intermediate coverage as the function of time can then be written as a set of ordinary differential equation (ODEs), which can be used to solve for the steady state coverage.

$$\frac{d\theta_i}{dt} = - \sum_i v_{ji}^{forward} r_i + \sum_i v_{ji}^{reverse} r_i$$

$$\theta_{Pt(O)CO}(t = 0) = \sum_i \theta_{PtO_xCO_y,i} = 1$$

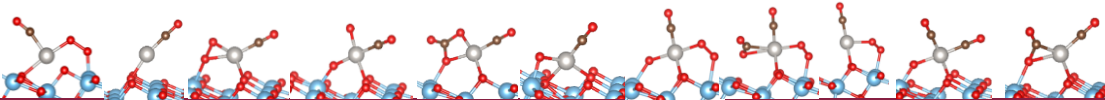
Where $\theta_{Pt(O)CO}$ are the surface coverage of initial Pt(O)(CO) intermediate at the beginning of reactive cycle and $\theta_{PtO_xCO_y,i}$ are the coverages of all other Pt species on the surface. The set of ODEs are numerically solved until the system reached steady state coverage (50s).

The calculation of the activation barrier of adsorbing molecule gases follows the works done by Vlachos *et al.* where one can calculate the activation barrier of gas adsorption by equating the rates obtained from the collision theory and the rates obtained from the transition state theory.¹⁶²

Table B. 2 Elementary reaction steps used for the microkinetic modeling (MKM).

Label	Reaction (Black Cycle)	Type of reaction
R0	$\text{Pt}(\text{CO})[\text{IV}] + \text{O}_{2_{\text{gas}}} \rightarrow \text{Pt}(\text{CO})(\text{O}_2)[\text{V}]$	Adsorption
R1	$\text{Pt}(\text{CO})(\text{O}_2)[\text{V}] \xrightarrow{\text{TSI}} \text{Pt}(\text{CO})(\text{O}_2)_2[\text{VI}]$	Surface, O ₂ dissociation
R2	$\text{Pt}(\text{CO})(\text{O}_2)_2[\text{VI}] \xrightarrow{\text{TSIIa}} \text{Pt}(\text{O})(\text{CO}_2)[\text{VII(a)}]$	Surface, CO ₂ formation
R3	$\text{Pt}(\text{O})(\text{CO}_2)[\text{VII(a)}] \rightarrow \text{Pt}(\text{O})[\text{VIII(a)}] + \text{CO}_{2_{\text{gas}}}$	Desorption
R4	$\text{Pt}(\text{O})[\text{VIIIa}] + \text{CO}_{\text{gas}} \rightarrow \text{Pt}(\text{O})(\text{CO})[\text{IX}]$	Adsorption
R5	$\text{Pt}(\text{O})(\text{CO})[\text{IX}] + \text{CO}_{\text{gas}} \rightarrow \text{Pt}(\text{O})(\text{CO})_2[\text{X(b)}]$	Adsorption
R6	$\text{Pt}(\text{O})(\text{CO})_2[\text{X(b)}] \xrightarrow{\text{TSIIIb}} \text{Pt}(\text{CO})(\text{CO}_2)[\text{XI(b)}]$	Surface, CO ₂ formation
R7	$\text{Pt}(\text{CO})(\text{CO}_2)[\text{XI(b)}] \rightarrow \text{Pt}(\text{CO})[\text{IV}] + \text{CO}_{2_{\text{gas}}}$	Desorption
<hr/>		
Label	Reaction (Blue Cycle)	Type of reaction
R8	$\text{PtO}(\text{CO})[\text{IX}] + \text{O}_{2_{\text{gas}}} \rightarrow \text{PtO}(\text{CO})(\text{O}_2) [\text{X(a)}]$	Adsorption
R9	$\text{PtO}(\text{CO})(\text{O}_2)[\text{X(a)}] + \text{CO}_{\text{gas}} \xrightarrow{\text{TS2b}} \text{Pt}(\text{CO})(\text{CO}_2)(\text{O}_2) [\text{XI(a)}]$	Eley-Rideal, CO ₂ formation
R10	$\text{Pt}(\text{CO})(\text{CO}_2)(\text{O}_2)[\text{XI(a)}] \rightarrow \text{Pt}(\text{CO})(\text{O}_2)[\text{XII(a)}] + \text{CO}_{2_{\text{gas}}}$	Desorption
R11	$\text{Pt}(\text{CO})(\text{O}_2) [\text{XII(a)}] \rightarrow \text{Pt}(\text{CO})[\text{IV}] + \text{O}_{2_{\text{gas}}}$	Desorption
<hr/>		
Label	Reaction (Red Cycle)	Type of reaction
R12	$\text{Pt}(\text{CO})(\text{O})_2[\text{VI}] + \text{CO}_{\text{gas}} \rightarrow \text{Pt}(\text{CO})(\text{CO}_3) [\text{VIIIb}]$	Activated adsorption
R13	$\text{Pt}(\text{CO})(\text{CO}_3)[\text{VIIIb}] \rightarrow \text{Pt}(\text{O})(\text{CO}) [\text{IX}] + \text{CO}_{2_{\text{gas}}}$	Desorption

Table B. 3 Vibrational Stretch of CO on various intermediates during CO oxidation obtained from DFT calculation.



Intermediate	II	IV	V	VI	VIIIb	IX	Xa	Xla	Xlla	Xb	Xlb
Pt Bader Charge	0.120	0.164	0.823	1.216	0.891	0.844	1.106	0.908	0.672	0.932	0.567
$\nu_{\text{PtCl}_2(\text{CO})_2}$ ($\lambda = 1.023$)	2081	2106	2116	2156	2137	2147	2156	2150	2034	2193 / 2124	2123

Table B. 4 The Bader charge analysis of various Pt states of the $\text{Pt}_{\text{SA}}/\text{TiO}_2$. The most stable Pt states (supported and dopant) adopts +4 oxidation state.

System	Pt charge	Pt oxidation state
PtO (bulk)	+0.845	+2
PtO ₂ (bulk)	+1.561	+4
PtsubTi _{5c}	+1.472	+4
PtsubTi _{5c} +O _{vac}	+0.917	+2
PtO ₂ (intermediate I)	+1.180	+2/+4
PtO (intermediate IV)	+0.571	+2

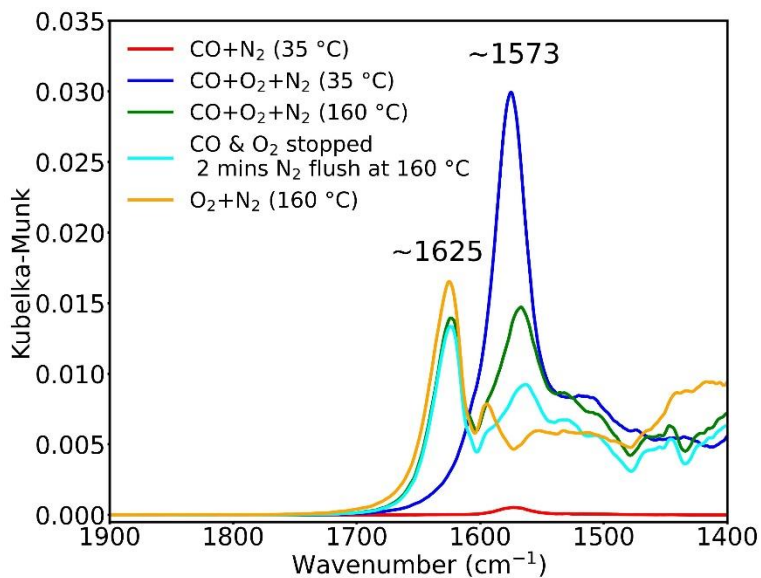


Figure B. 10 Progression of carbonate formation on the PtSA/a-TiO₂ catalyst after CO adsorption on the reduced catalyst, during CO and O₂ flow at 35 °C and 160 °C, followed by N₂ flush of CO and O₂, and finally under O₂ flow following the N₂ flush.

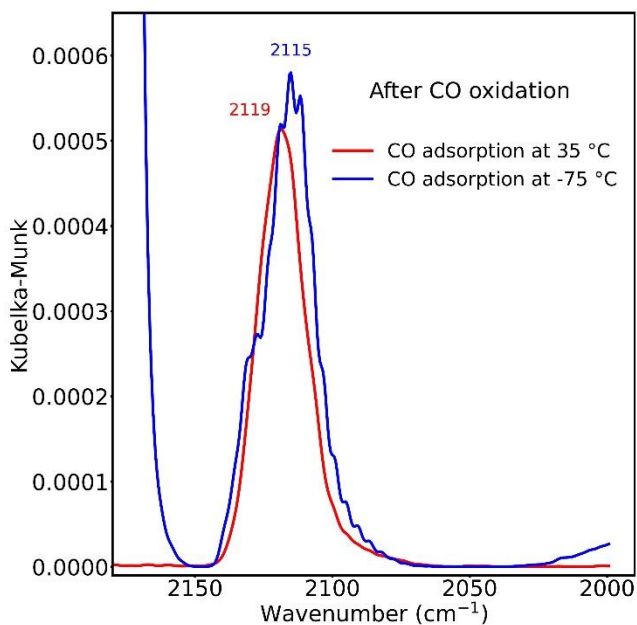


Figure B. 11 CO chemisorption DRIFTS peak at 35 and -75 °C after CO oxidation at 160 °C (cooled down under CO+O₂ flow). This demonstrates that mostly a single type of Pt site is present after CO

oxidation. Absence of unpopulated Pt sites from low-temperature DRIFTS can be coupled with the positive CO order to suggest that a 2nd CO (other than the chemisorbed CO on PtSA) from the gas-phase is most likely involved in the reaction cycle.

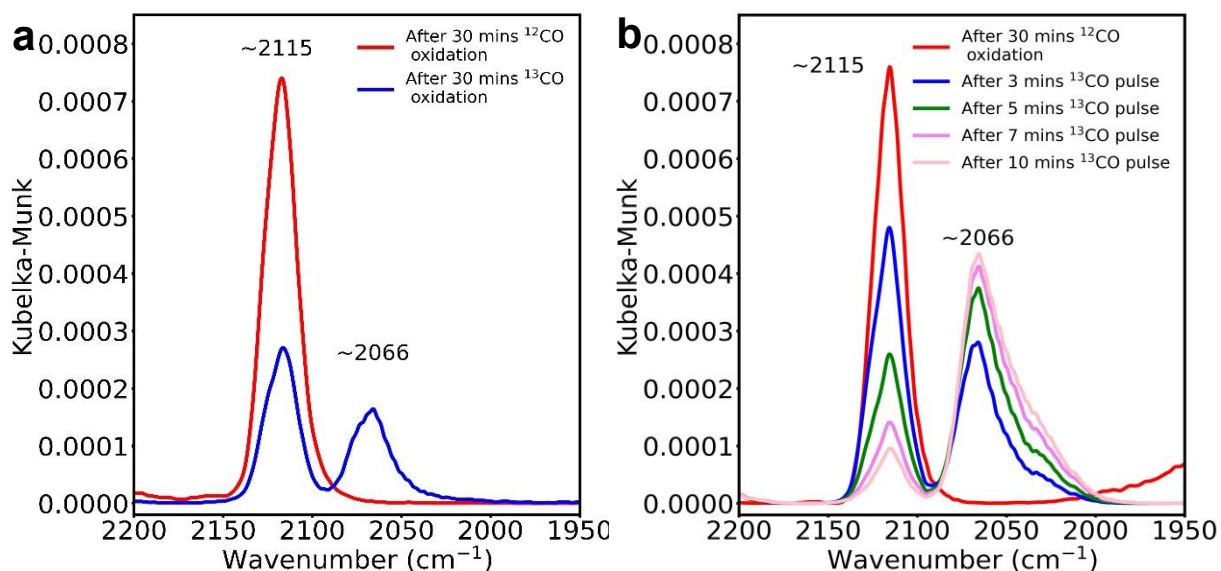


Figure B. ¹²CO/¹³CO exchange experiment at 160 °C (a) in the presence of O₂, i.e. ¹³CO oxidation and (b) in the absence of O₂, i.e. ¹³CO pulse/flow. ¹²CO/¹³CO exchange during ¹³CO oxidation at 160 °C shows that ¹³CO does exchange with the adsorbed ¹²CO during ¹³CO oxidation with an exchange rate (~36% in 30 mins) that is slower than the turnover (~5 turnovers in 30 mins). If the chemisorbed CO was the one involved in the reaction, all ¹²CO would have been replaced by ¹³CO in 30 mins. These results indicate that a 2nd CO is involved in the reaction. The absence of gas-phase O₂ seems to promote the exchange of ¹³CO with ¹²CO, which might be because more ¹³CO are available for exchange in the absence of O₂.

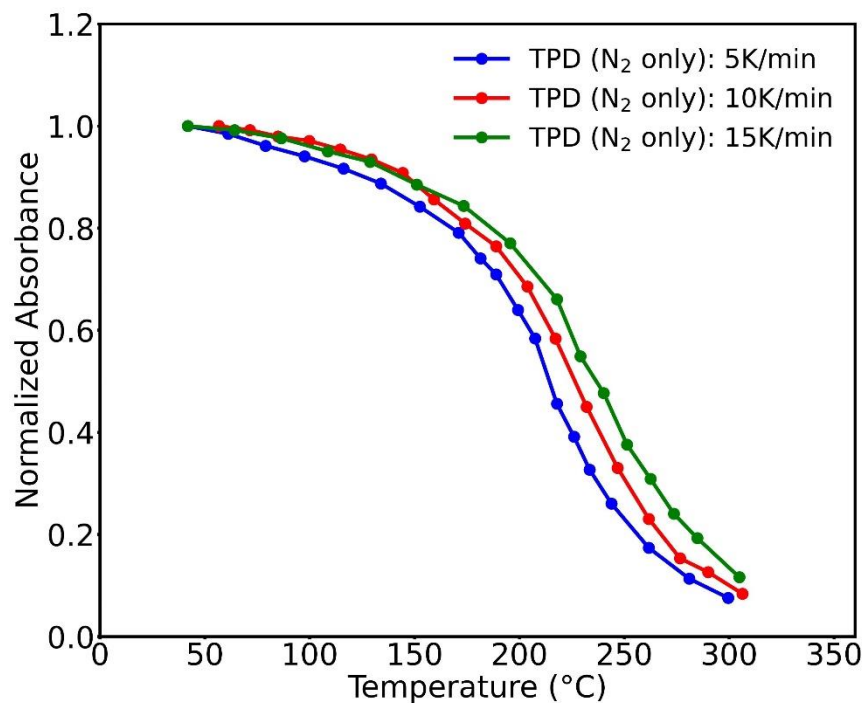


Figure B. 13 Normalized absorbance plotted as a function of temperature for temperature-programmed desorption (TPD) of the CO adsorbed during CO oxidation on PtSA/TiO₂. TPD was performed at three different heating rate and shows similar desorption behaviour. Prior to the TPD experiments, CO oxidation was performed at 160 °C for 20 mins (details in experimental section) to achieve the steady-state CO chemisorption peak and then the sample was cooled down to 35 °C under CO and O₂ flow followed by flushing of the gas-phase CO and O₂ using N₂. Afterwards, the sample was heated up under N₂ flow. TPD of the chemisorbed CO, corresponding to the 2115 cm⁻¹ peak, shows that the CO adsorbed on Pt is bound strongly.

Table B. 5 Binding energy (heat of adsorption) of the chemisorbed CO on the Pt SA/a-TiO₂ catalysts during steady-state CO oxidation reaction estimated from DRIFTS TPD experiments using the Redhead analysis (see details below).

TPD heating rate	T _{max} (°C)	E _{des} (kJ/mol CO)
5 K/min	207	140
10 K/min	210	138
15 K/min	218	139

B2. Redhead Analysis using CO chemisorption DRIFTS spectra from TPD

To estimate the heat of adsorption of CO chemisorbed on Pt_{SA} species during CO oxidation, DRIFTS was utilized to perform temperature-programmed desorption (TPD) of these chemisorbed CO species. Briefly, the sample was cooled down to 35 °C under CO and O₂ flow after performing steady-state CO oxidation for ~20 mins at 160 °C. CO and O₂ flow were then stopped, and the sample was heated at different rates (in separate experiments) under only N₂ flow while DRIFTS spectra were being recorded simultaneously. These DRIFTS spectra for each experiment were plotted as a function of temperature (not shown). The absorbance value of each of these spectra was then measured using OMNIC™ Series Software by Thermo Fisher Scientific Inc. and were normalized by the maximum value (absorbance of the DRIFTS spectrum at room temperature). The normalized absorbance values are plotted in Error! Reference source not found.. The CO desorption rate was calculated using the normalized absorbance values with the following formula:

$$\text{Desorption Rate} = \frac{A_1 - A_2}{T_2 - T_1}$$

Here, A denotes normalized absorbance value and T denotes temperature. A₁ and A₂ are the normalized absorbance at T₁ and T₂, respectively.

After the desorption rates were calculated at different temperatures, the temperature corresponding to the maximum CO desorption rate was then obtained and used for the Redhead analysis^{163,164}. Assuming CO desorption is a first-order process, the formula for Redhead analysis to calculate the heat of adsorption is as follows:

$$E_{des} = R T_{max} \left[\ln \left(\frac{\nu T_{max}}{\beta} \right) - 3.46 \right]$$

Here, E_{des}: activation energy of desorption [J.mol⁻¹];

R: gas constant [J.mol⁻¹.K⁻¹];

T_{\max} : temperature corresponding to maximum desorption rate [K];

ν : pre-exponential factor [s^{-1} for first-order desorption];

β : heating rate, dT/dt [$K \cdot s^{-1}$];

If the adsorption process is not activated, then E_{des} becomes the heat of adsorption of the desorbing gas¹⁶⁴. This condition is true in our case as the adsorbing gas is CO. We also assumed that the desorption process is first-order in nature and the associated pre-exponential factor is $10^{13} s^{-1}$. The latter takes into consideration that the transition state of the desorbing molecule is similar to the chemisorbed state. A sample calculation is given below.

For 5 K/min heating rate:

$$T_{\max} = 207 \text{ }^{\circ}\text{C} = 481 \text{ K}$$

$$B = 5 \text{ K/min} = 0.083 \text{ K/s}$$

$$E_{des} = 8.314 \times 481 \times \left[\ln \frac{10^{13} \times 481}{0.083} - 3.46 \right] = 140390 \frac{J}{mol} = 140 \frac{kJ}{mol}$$

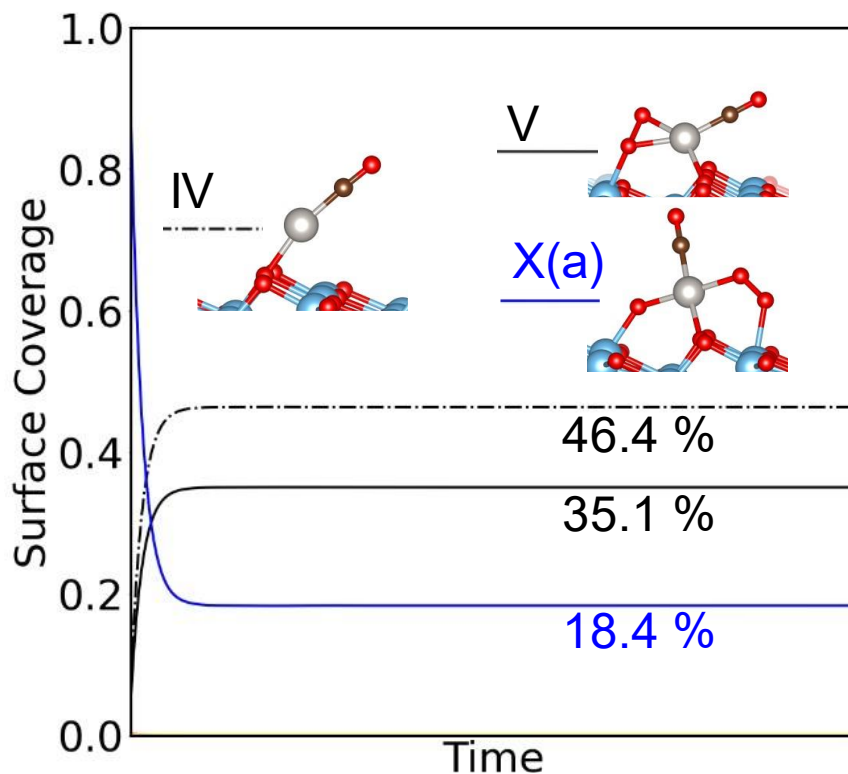


Figure B. 14 *Steady-state surface coverage of the most abundant intermediates from the Modified Microkinetic Analysis after the third and final modification of the Gibbs Free Energy landscape within the error of DFT.*

Microkinetic sensitivity towards DFT inaccuracies

To probe the sensitivity of MKM towards inherent DFT inaccuracies, a series of modifications within the error of DFT towards the Gibbs Free energy pathways were applied in order to tune the results closer towards the experimental results. Three main modifications and their results are reported succinctly below.

Details of the modification of the Microkinetic Analysis:

1. All TS are increased by 0.2 eV (leads to TOF reduced to 24 s^{-1})
2. To encourage CO E-R pathway, intermediates of blue pathway are stabilized by 0.125 eV. This value was found as going too low will take all the rate determining behavior from black pathway (O_2 adsorption + dissociation), leads to CO and O_2 order equal to 0.27 and 0.24

- Final effort, lowering intermediate IV, V (by 0.08 eV) and XIa (0.08 eV) as much as possible to further lower the TOF and E_{app}

Implications of combined modifications:

- Highest CO and O₂ order attainable are 0.27 and 0.24, respectively.
- TOF is now 2.1, whereas apparent activation energy increases to 0.84 eV
- Conclusion:** although MKM is inadequate to explain TOF, it can explain the source of CO and O₂ order and concurrent analysis with experimental observation is key to fully comprehend the kinetics of the entire reaction network

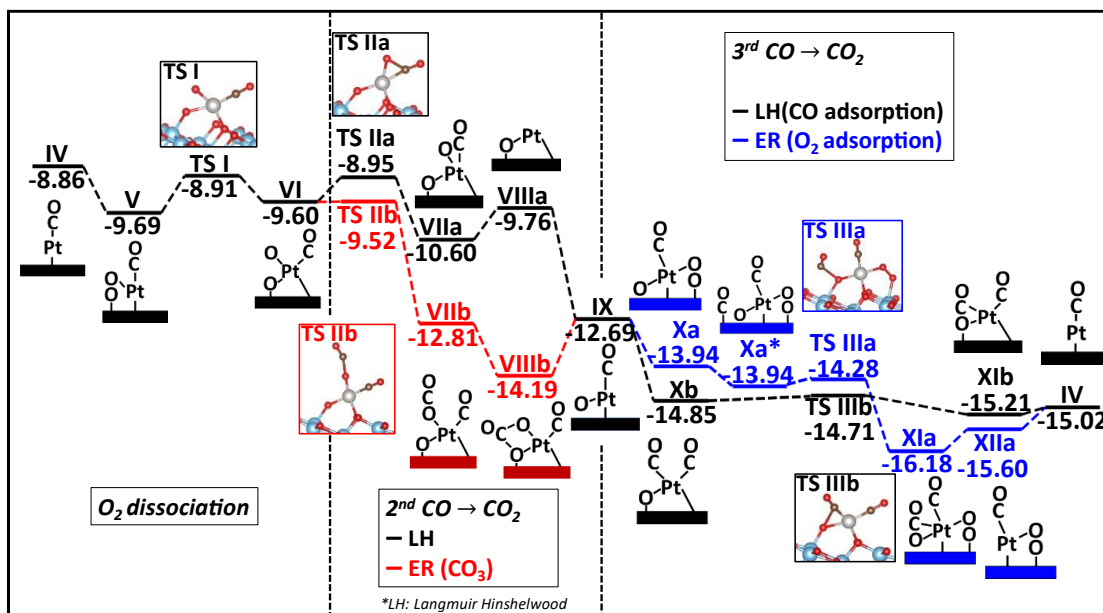


Figure B. 15 Enthalpic energy diagram of reactive pathway calculated using DFT.

Appendix C

Supporting information for chapter 5.

C1. Fitting of Cu LMM Auger Spectra

For the $\text{Cu}_4/\text{TiO}_2(110)$ and $\text{K}/\text{Cu}_4/\text{TiO}_2(110)$ surfaces studied in this work, the Cu LMM Auger spectrum is overlapped by peaks from the Ti 2s photoemission peaks at the Al K_{α} x-ray energy (1486.7 eV). The Cu 2p XPS spectra do not show the characteristic shake up peaks associated with Cu(II), so the Auger spectra were fitted with LMM contributions from Cu(0) (blue) and Cu(I) (red) as well as Ti 2s (grey) peaks, with the latter being fixed by matching the intensity of the satellite at peak at 577.4 eV which is free of overlaps. The relative intensities and peak widths for the Ti 2s states were experimentally determined from the bare $\text{TiO}_2(110)$ surface. The contributions of Cu(0) and Cu(I) to the Auger spectra were least squares fit using peak parameters determined in reference [1]. In that work, a collection of empirically fit spectra for various Cu compounds with differing oxidation states (0, +1) and ligands were used to quantify the line-shapes, FWHM and relative peak positions and intensities for Cu(0) and Cu(I). The most prominent peak for Cu(I) lies near 569.9 eV while Cu(0) exhibits a narrower, characteristic peak near 568.0 eV.¹ The experimental Auger LMM spectra for the $\text{K}/\text{Cu}_4/\text{TiO}_2(110)$ and $\text{Cu}_4/\text{TiO}_2(110)$ samples from RT to 600 K exhibit a distinct feature at 569.8 eV which can be assigned to Cu(I), whereas this feature drops in intensity at 900 K and new peak appears at 568.1 eV consistent with the appearance of Cu(0). The least squares fits shown in Figures 1, S1 and S2 using the peak parameters in reference [1] confirm these qualitative assignments with Cu(I) being the dominant Cu species at RT to 600 K (red peaks), while Cu(0) is more prominent after annealing to 900 K (blue lines, Figure

C.1c). The contribution of Cu(0) at temperatures ≤ 600 K was too small relative to the Ti 2s peak to be fit with confidence, but at 900 K the Cu(0) contribution is $\approx 65\%$ of the total Cu signal. Note also that the total intensity of Cu LMM peaks decrease substantially between 600 K and 900K, i.e., 42% of the total signal 600 K to 23% at 900K.

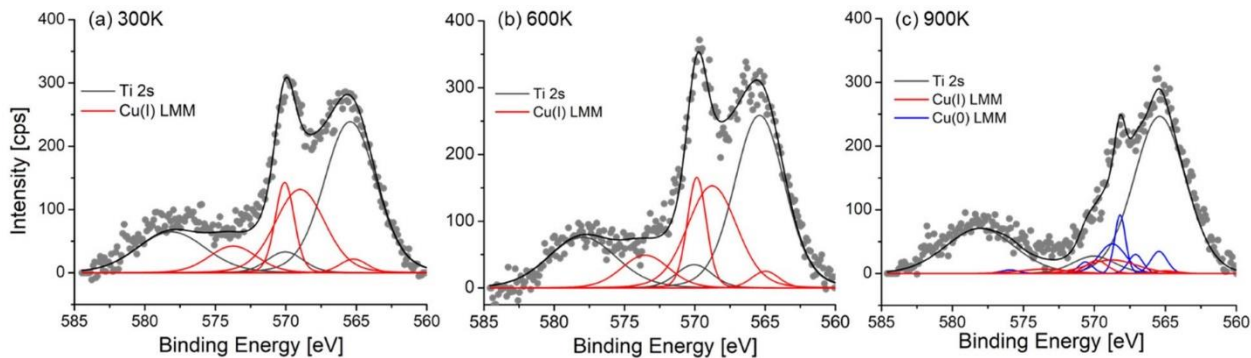


Figure C. 1 Temperature dependence of the Cu Auger LMM spectrum for the $K/Cu_4/TiO_2(110)$ surface after exposure to DMMP at 1×10^{-4} Torr: (a) 300 K; (b) 600 K. (c) 900 K. The spectra are fitted as the sum of contributions from the LMM Auger peaks associated with Cu0 (blue lines), Cu+ (red lines) and the Ti 2s and satellite peaks (gray lines).

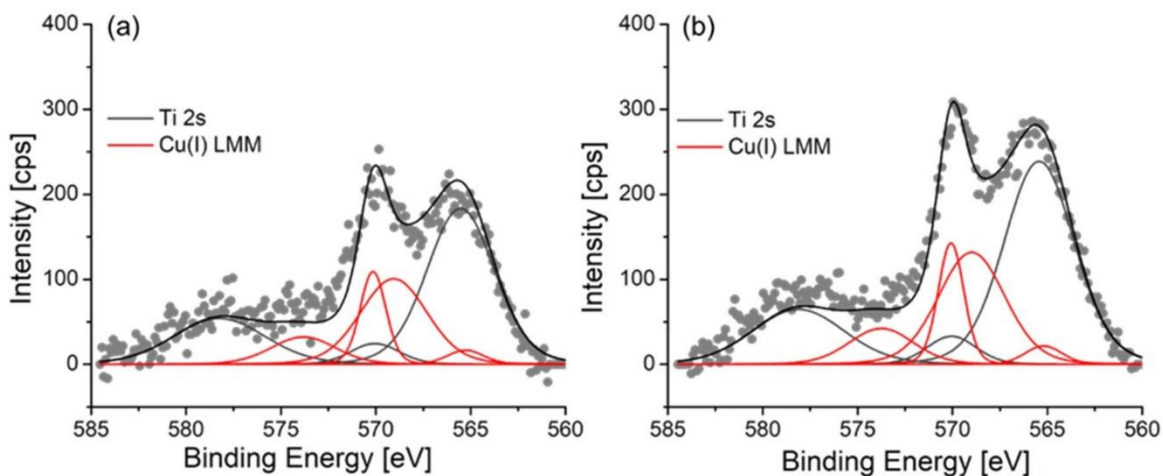


Figure C. 2 Cu LMM Auger spectra for the (a) $Cu_4/TiO_2(110)$ and (b) $K/Cu_4/TiO_2(110)$

surfaces during exposure of 1×10^{-4} Torr of DMMP at room temperature. The spectra are fitted as the sum of contributions from the LMM Auger peaks associated with Cu(I) (red lines) and the Ti 2s and satellite peaks (gray lines).

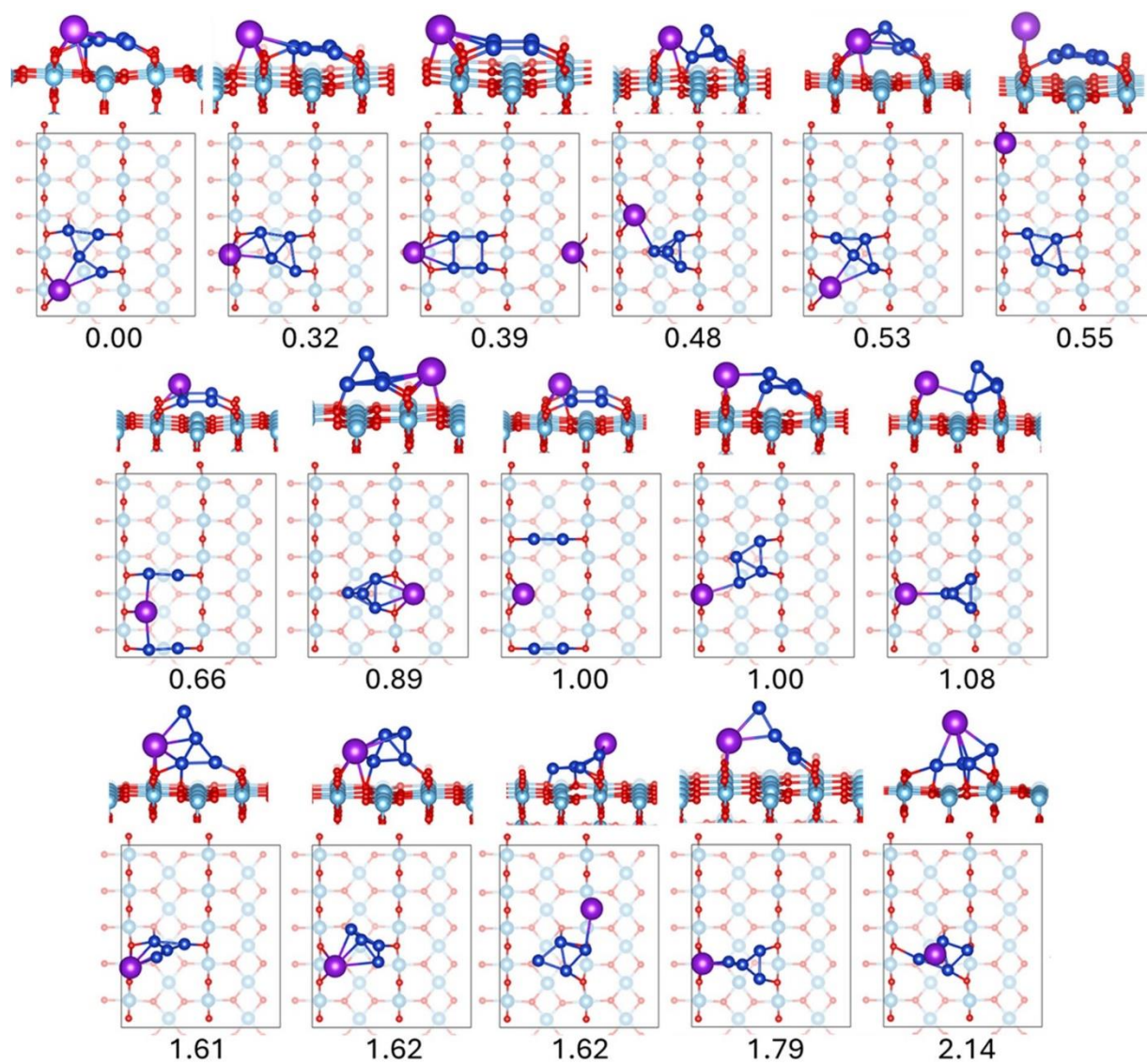


Figure C. 3 DFT calculated structures and relative energies for the co-adsorption of K and Cu_4 on $\text{TiO}_2(110)$ sorted by relative stabilities. Atom colors: Ti: light blue; O: red; Cu: dark blue; K: purple; P: grey; C: brown.

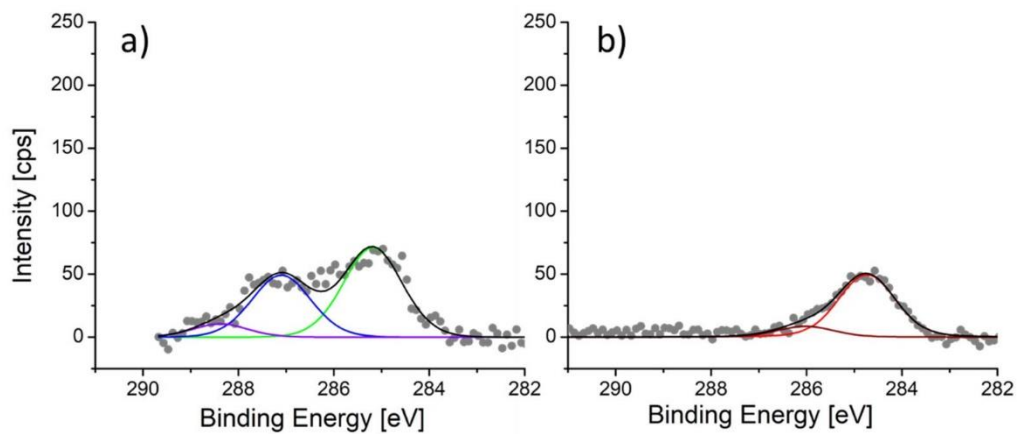


Figure C. 4 Background C 1s XPS spectra taken at room temperature prior to exposure to DMMP for the (a) Cu₄/TiO₂(110) and (b) K/Cu₄/TiO₂ surfaces. Note that the C 1s spectrum for the K only surface is the same as the K-Cu surface (b) since it was taken in a region of the K-Cu surface where there was no detectable Cu as determined by XPS.

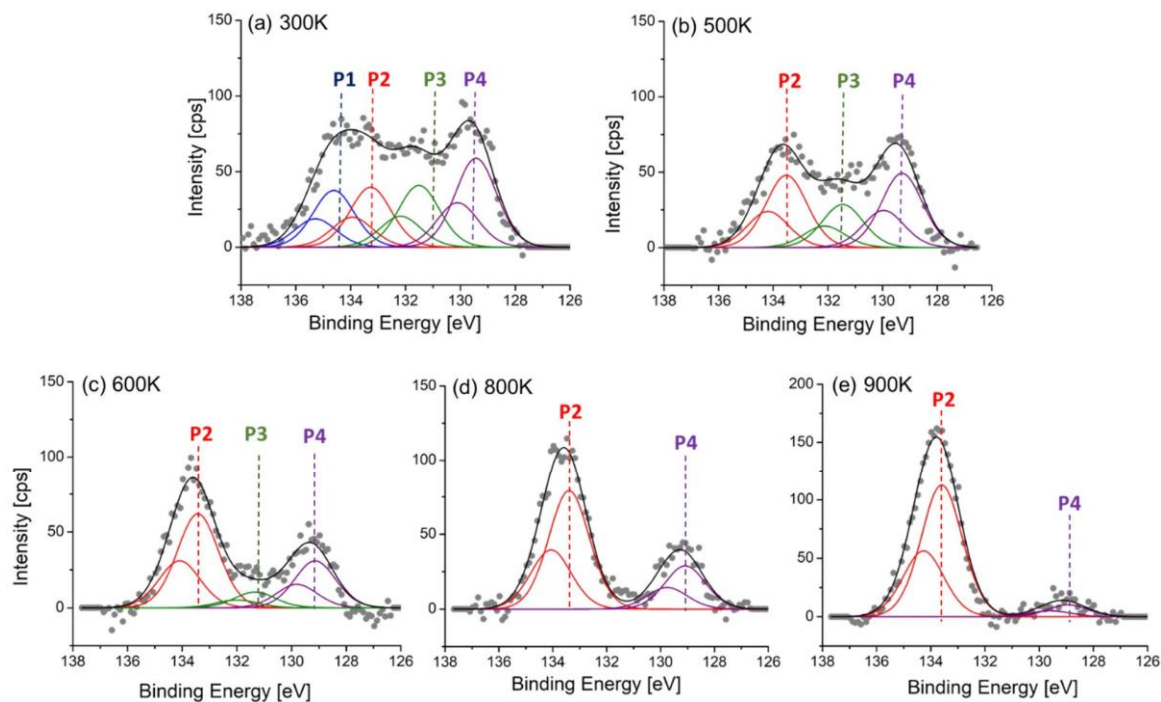


Figure C. 5 Temperature dependence of the P 2p XPS spectrum for the Cu₄/TiO₂(110) surface after exposure to DMMP at 1 x 10⁻⁴ Torr: (a) 300K; (b) 400K; (c) 600K; (d) 800K; (e) 900K.

Table C. 1 Binding energies for the various P-intermediates on the Cu₄/TiO₂(110) surface obtained from fits of the P 2p XPS spectra taken at different temperatures after exposure to 1 x 10⁻⁴ Torr of DMMP (see Figure C.3).

Temperature	P ₁	P ₂	P ₃	P ₄
300	134.5	133.3	131.6	129.4
500	--	133.5	131.5	129.3
600	--	133.4	131.3	129.1
800	--	133.4	--	129.1
900	--	133.6	--	128.9

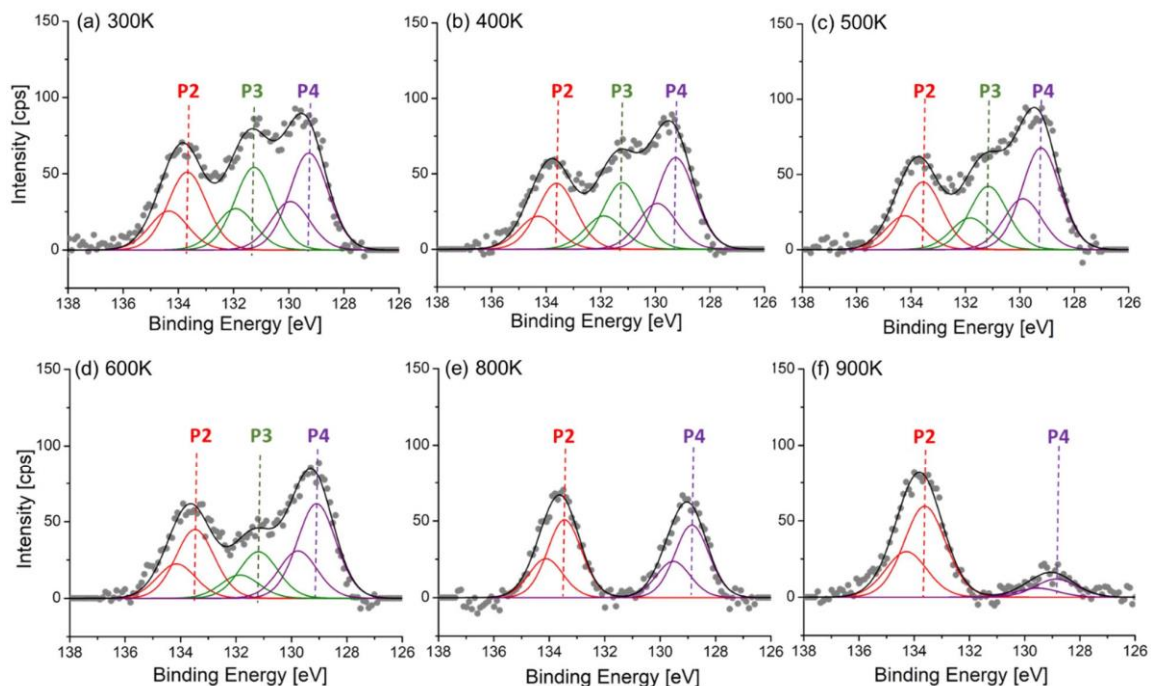


Figure C. 6 Temperature dependence of the P 2p XPS spectrum for the K/Cu₄/TiO₂(110) surface after exposure to 1 x 10⁻⁴ Torr of DMMP at (a) 300 K; (b) 400K; (c) 500K; (d) 600K; (e) 800K; (f) 900K.

Table C. 2 Binding energies for the various P-intermediates on the K/Cu₄/TiO₂(110) surface obtained from fits of the P 2p XPS spectra taken at different temperatures after exposure to 1 x 10⁻⁴ Torr of DMMP (see Figure C.3).

Temperature	P ₂	P ₃	P ₄
300	133.6	131.2	129.2
400	133.6	131.2	129.2
500	133.5	131.2	129.2
600	133.4	131.2	129.1
800	133.4	---	128.8
900	133.6	---	128.8

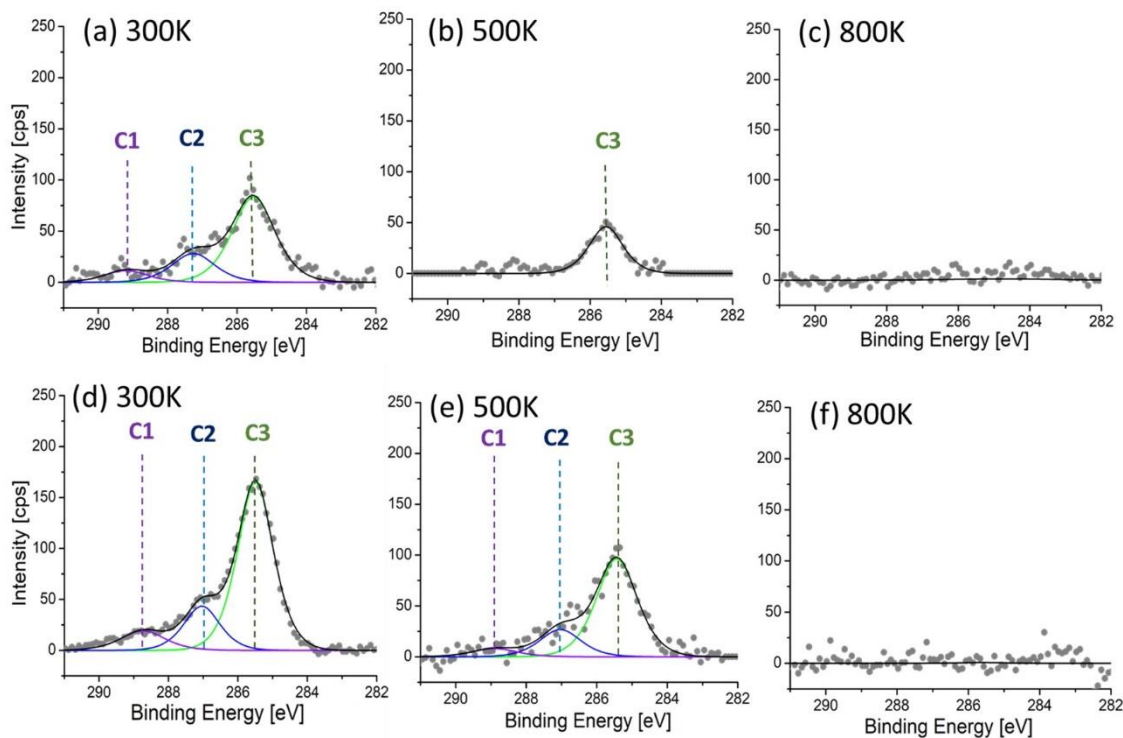


Figure C. 7 Temperature dependence of the C 1s XPS spectrum after exposure to DMMP at 1×10^{-4} Torr for the $\text{Cu}_4/\text{TiO}_2(110)$ surface: (a) 300K; (b) 500K; (c) 600K; and the $\text{K}/\text{Cu}_4/\text{TiO}_2(110)$ surface; (d) 300K; (e) 500K; (f) 600K.

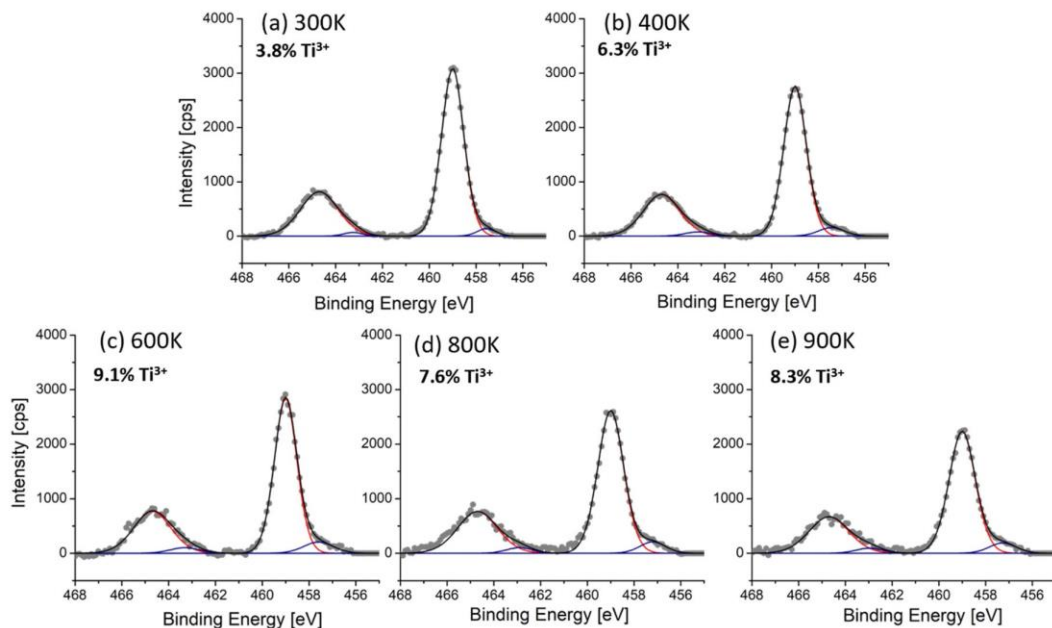


Figure C. 8 Temperature dependence of the Ti 2p XPS spectrum for the $\text{K}/\text{Cu}_4/\text{TiO}_2(110)$

surface after exposure to DMMP at 1×10^{-4} Torr: (a) 300K; (b) 400K; (c) 600K; (d) 800K; (e) 900K.

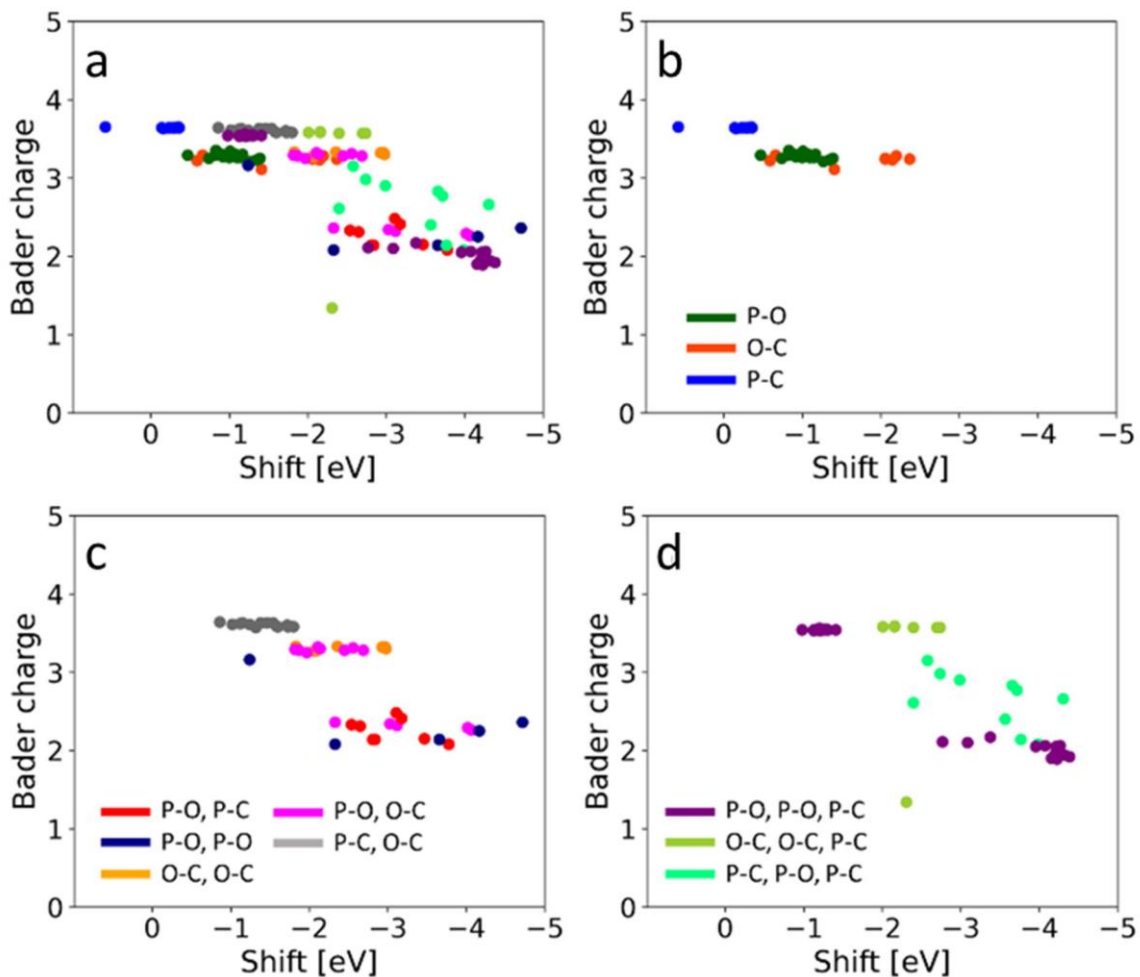


Figure C. 9 Calculated Bader charges of the P center of the decomposed DMMP intermediates on the $\text{Cu}_4/\text{TiO}_2(110)$ surface as a function of the calculate P 2p binding energy shift. The Bader charges are colored coded by configurations resulting from (b) one, (b) two and (c) three bond cleavages on DMMP. Panel (a) includes all configurations in (b)-(d).

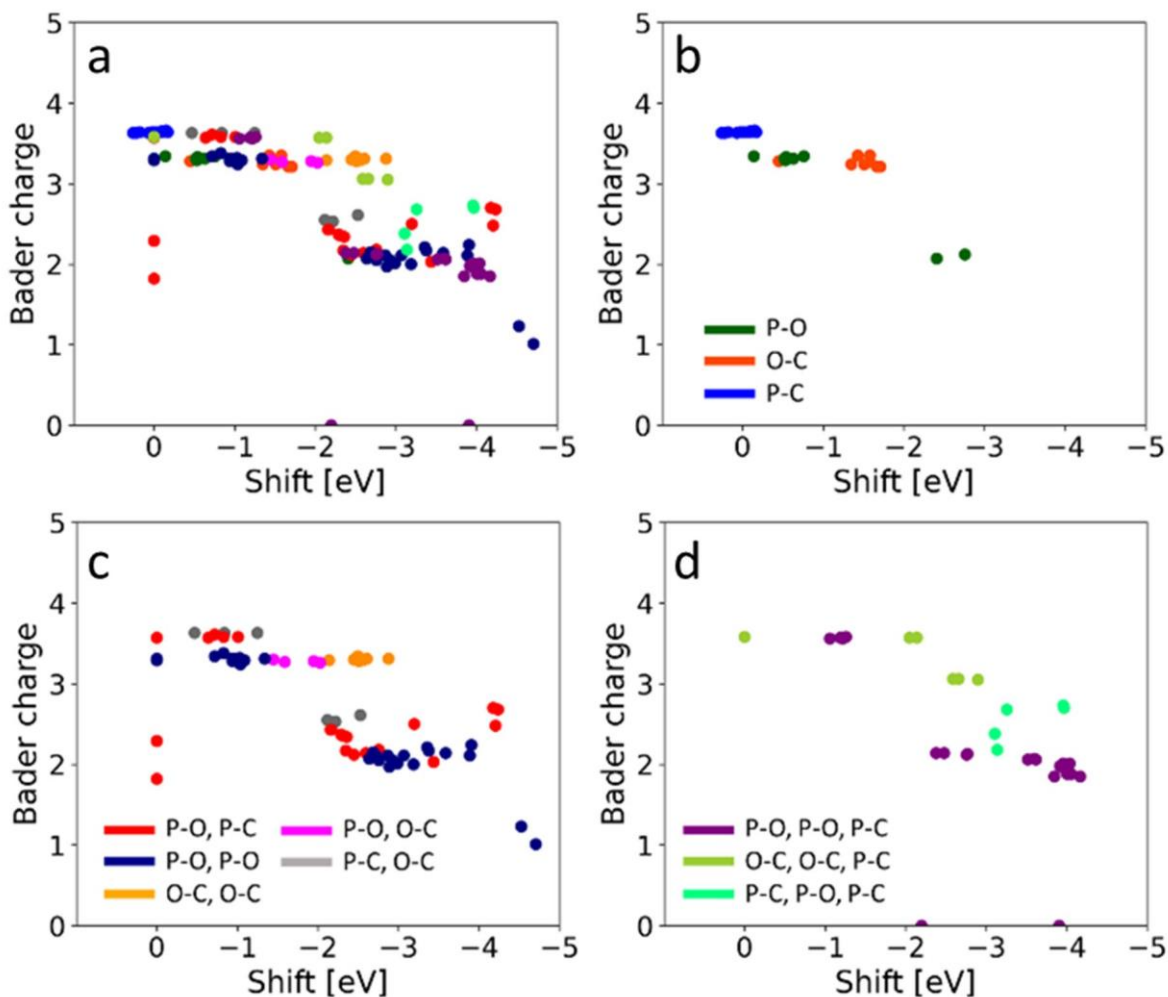


Figure C. 10 Calculated Bader charges of the P center of the decomposed DMMP intermediates on the K/Cu/TiO₂(110) surface as a function of the calculate P 2p binding energy shift. The Bader charges are colored coded by configurations resulting from (b) one, (c) two and (d) three bond cleavages on DMMP. Panel (a) includes all configurations in (b)(d).

Bibliography

- (1) Chulov, M. Sarin Used in April Syria Attack, Chemical Weapons Watchdog Confirms. *The Guardian*. 2017.
- (2) Zarocostas, J. Syria Chemical Attacks: Preparing for the Unconscionable. *The Lancet* **2017**, 389 (10078), 1501. [https://doi.org/10.1016/S0140-6736\(17\)30997-2](https://doi.org/10.1016/S0140-6736(17)30997-2).
- (3) Moyer, R. A.; Sidell, F. R.; Salem, H. Nerve Agents. In *Encyclopedia of Toxicology: Third Edition*; 2014. <https://doi.org/10.1016/B978-0-12-386454-3.00635-7>.
- (4) Yanagisawa, N. The Nerve Agent Sarin: History, Clinical Manifestations, and Treatment. *Brain Nerve* **2014**, 66 (5), 561–569.
- (5) Kaczmarek, A.; Gorb, L.; Sadlej, A. J.; Leszczynski, J. Sarin and Soman: Structure and Properties. *Struct Chem* **2004**. <https://doi.org/10.1023/B:STUC.0000037910.26456.59>.
- (6) Miyaki, K.; Nishiwaki, Y.; Maekawa, K.; Ogawa, Y.; Asukai, N.; Yoshimura, K.; Etoh, N.; Matsumoto, Y.; Kikuchi, Y.; Kumagai, N.; Omae, K. Effects of Sarin on the Nervous System of Subway Workers Seven Years after the Tokyo Subway Sarin Attack. *J Occup Health* **2005**, 47 (4), 299–304. <https://doi.org/10.1539/joh.47.299>.
- (7) Okumura, T.; Hisaoka, T.; Yamada, A.; Naito, T.; Isonuma, H.; Okumura, S.; Miura, K.; Sakurada, M.; Maekawa, H.; Ishimatsu, S.; Takasu, N.; Suzuki, K. The Tokyo Subway Sarin Attack - Lessons Learned. In *Toxicology and Applied Pharmacology*; 2005. <https://doi.org/10.1016/j.taap.2005.02.032>.
- (8) Davis, E. D.; Gordon, W. O.; Wilmsmeyer, A. R.; Troya, D.; Morris, J. R. Chemical Warfare Agent Surface Adsorption: Hydrogen Bonding of Sarin and Soman to Amorphous Silica. *J Phys Chem Lett* **2014**, 5 (8), 1393–1399. <https://doi.org/10.1021/jz500375h>.
- (9) Osovsky, R.; Kaplan, D.; Nir, I.; Rotter, H.; Elisha, S.; Columbus, I. Decontamination of Adsorbed Chemical Warfare Agents on Activated Carbon Using Hydrogen Peroxide

- Solutions. *Environ Sci Technol* **2014**, *48* (18), 10912–10918. <https://doi.org/10.1021/es502981y>.
- (10) Osovsky, R.; Kaplan, D.; Rotter, H.; Nir, I.; Columbus, I. Hydrothermal Degradation of Chemical Warfare Agents on Activated Carbon: Rapid Chemical-Free Decontamination. *Ind Eng Chem Res* **2013**, *52* (28), 9705–9708. <https://doi.org/10.1021/ie401517a>.
- (11) Altmann, H. J.; Jung, M.; Richardt, A. Decontamination of Chemical Warfare Agents – What Is Thorough? In *CBRN Protection*; Wiley, 2013; pp 351–382. <https://doi.org/10.1002/9783527650163.ch13>.
- (12) Nawala, J.; Jóźwik, P.; Popiel, S. Thermal and Catalytic Methods Used for Destruction of Chemical Warfare Agents. *International Journal of Environmental Science and Technology* **2019**, *16* (7), 3899–3912. <https://doi.org/10.1007/s13762-019-02370-y>.
- (13) Tsyshevsky, R.; McEntee, M.; Durke, E. M.; Karwacki, C.; Kuklja, M. M. Degradation of Fatal Toxic Nerve Agents on Dry TiO₂. *ACS Appl Mater Interfaces* **2021**, *13* (1), 696–705. <https://doi.org/10.1021/acsami.0c19261>.
- (14) MiarAlipour, S.; Friedmann, D.; Scott, J.; Amal, R. TiO₂/Porous Adsorbents: Recent Advances and Novel Applications. *Journal of Hazardous Materials*. 2018. <https://doi.org/10.1016/j.jhazmat.2017.07.070>.
- (15) Zhu, Y.; Cheng, Z.; Xiang, Q.; Chen, X.; Xu, J. Synthesis of Functionalized Mesoporous TiO₂-SiO₂ with Organic Fluoroalcohol as High Performance DMMP Gas Sensor. *Sens Actuators B Chem* **2017**. <https://doi.org/10.1016/j.snb.2016.10.080>.
- (16) Dulub, O.; Valentin, C. Di; Selloni, A.; Diebold, U. Structure, Defects, and Impurities at the Rutile TiO₂(011)-(2×1) Surface: A Scanning Tunneling Microscopy Study. *Surf Sci* **2006**, *600* (19), 4407–4417. <https://doi.org/https://doi.org/10.1016/j.susc.2006.06.042>.
- (17) Thompson, T. L.; Yates, J. T. TiO₂-Based Photocatalysis: Surface Defects, Oxygen and Charge Transfer. *Topics in Catalysis*. 2005. <https://doi.org/10.1007/s11244-005-3825-1>.

- (18) Tan, S. J.; Wang, B. Active Sites for Adsorption and Reaction of Molecules on Rutile TiO₂(110) and Anatase TiO₂(001) Surfaces. *Chinese Journal of Chemical Physics*. 2015. <https://doi.org/10.1063/1674-0068/28/cjcp1506129>.
- (19) Sánchez-Sánchez, C.; González, C.; Jelinek, P.; Méndez, J.; De Andres, P. L.; Martín-Gago, J. A.; López, M. F. Understanding Atomic-Resolved STM Images on TiO₂(110)-(1 × 1) Surface by DFT Calculations. *Nanotechnology* **2010**. <https://doi.org/10.1088/0957-4484/21/40/405702>.
- (20) Diebold, U.; Lehman, J.; Mahmoud, T.; Kuhn, M.; Leonardelli, G.; Hebenstreit, W.; Schmid, M.; Varga, P. Intrinsic Defects on a TiO₂(110)(1 × 1) Surface and Their Reaction with Oxygen: A Scanning Tunneling Microscopy Study. *Surf Sci* **1998**. [https://doi.org/10.1016/S0039-6028\(98\)00356-2](https://doi.org/10.1016/S0039-6028(98)00356-2).
- (21) Dulub, O.; Valentin, C. Di; Selloni, A.; Diebold, U. Structure, Defects, and Impurities at the Rutile TiO₂(0 1 1)-(2 × 1) Surface: A Scanning Tunneling Microscopy Study. *Surf Sci* **2006**. <https://doi.org/10.1016/j.susc.2006.06.042>.
- (22) Yan, J.; Wu, G.; Guan, N.; Li, L.; Li, Z.; Cao, X. Understanding the Effect of Surface/Bulk Defects on the Photocatalytic Activity of TiO₂: Anatase versus Rutile. *Physical Chemistry Chemical Physics* **2013**. <https://doi.org/10.1039/c3cp50927c>.
- (23) Quintero, Y. C.; Nagarajan, R. Molecular and Dissociative Adsorption of DMMP, Sarin and Soman on Dry and Wet TiO₂(110) Using Density Functional Theory. *Surf Sci* **2018**, *675*, 26–35. <https://doi.org/https://doi.org/10.1016/j.susc.2018.04.002>.
- (24) Hirakawa, T.; Sato, K.; Komano, A.; Kishi, S.; K. Nishimoto, C.; Mera, N.; Kugishima, M.; Sano, T.; Ichinose, H.; Negishi, N.; Seto, Y.; Takeuchi, K. Experimental Study on Adsorption and Photocatalytic Decomposition of Isopropyl Methylphosphonofluoridate at Surface of TiO₂ Photocatalyst. *The Journal of Physical Chemistry C* **2010**, *114* (5), 2305–2314. <https://doi.org/10.1021/jp910911x>.

- (25) Panayotov, D. A.; Morris, J. R. Uptake of a Chemical Warfare Agent Simulant (DMMP) on TiO₂: Reactive Adsorption and Active Site Poisoning. *Langmuir* **2009**, *25* (6), 3652–3658. <https://doi.org/10.1021/la804018b>.
- (26) Panayotov, D. A.; Morris, J. R. Thermal Decomposition of a Chemical Warfare Agent Simulant (DMMP) on TiO₂: Adsorbate Reactions with Lattice Oxygen as Studied by Infrared Spectroscopy. *The Journal of Physical Chemistry C* **2009**, *113* (35), 15684–15691. <https://doi.org/10.1021/jp9036233>.
- (27) Rusu, C. N.; Yates, J. T. Adsorption and Decomposition of Dimethyl Methylphosphonate on TiO₂. *J Phys Chem B* **2000**, *104* (51), 12292–12298. <https://doi.org/10.1021/jp002560q>.
- (28) Panayotov, D. A.; Morris, J. R. Uptake of a Chemical Warfare Agent Simulant (DMMP) on TiO₂: Reactive Adsorption and Active Site Poisoning. *Langmuir* **2009**, *25* (6), 3652–3658. <https://doi.org/10.1021/la804018b>.
- (29) Panayotov, D. A.; Morris, J. R. Catalytic Degradation of a Chemical Warfare Agent Simulant: Reaction Mechanisms on TiO₂-Supported Au Nanoparticles. *The Journal of Physical Chemistry C* **2008**, *112* (19), 7496–7502. <https://doi.org/10.1021/jp7118668>.
- (30) Tesvara, C.; Walenta, C.; Sautet, P. Oxidative Decomposition of Dimethyl Methylphosphonate on Rutile TiO₂ (110): The Role of Oxygen Vacancies. *Physical Chemistry Chemical Physics* **2022**, *24* (38), 23402–23419.
- (31) Tesvara, C.; Walenta, C.; Sautet, P. Oxidative Decomposition of Dimethyl Methylphosphonate on Rutile TiO₂ (110): The Role of Oxygen Vacancies. *Physical Chemistry Chemical Physics* **2022**, *24* (38), 23402–23419.
- (32) Holdren, S.; Tsyshevsky, R.; Fears, K.; Owrutsky, J.; Wu, T.; Wang, X.; Eichhorn, B. W.; Kuklja, M. M.; Zachariah, M. R. Adsorption and Destruction of the G-Series Nerve Agent Simulant Dimethyl Methylphosphonate on Zinc Oxide. *ACS Catal* **2019**, *9* (2), 902–911. <https://doi.org/10.1021/acscatal.8b02999>.

- (33) Schweigert, I. v.; Gunlycke, D. Hydrolysis of Dimethyl Methylphosphonate by the Cyclic Tetramer of Zirconium Hydroxide. *Journal of Physical Chemistry A* **2017**, *121* (40). <https://doi.org/10.1021/acs.jpca.7b06403>.
- (34) Troya, D. Reaction Mechanism of Nerve-Agent Decomposition with Zr-Based Metal Organic Frameworks. *Journal of Physical Chemistry C* **2016**, *120* (51). <https://doi.org/10.1021/acs.jpcc.6b10530>.
- (35) Plonka, A. M.; Wang, Q.; Gordon, W. O.; Balboa, A.; Troya, D.; Guo, W.; Sharp, C. H.; Senanayake, S. D.; Morris, J. R.; Hill, C. L.; Frenkel, A. I. In Situ Probes of Capture and Decomposition of Chemical Warfare Agent Simulants by Zr-Based Metal Organic Frameworks. *J Am Chem Soc* **2017**, *139* (2), 599–602. <https://doi.org/10.1021/jacs.6b11373>.
- (36) Wang, G.; Sharp, C.; Plonka, A. M.; Wang, Q.; Frenkel, A. I.; Guo, W.; Hill, C.; Smith, C.; Kollar, J.; Troya, D.; Morris, J. R. Mechanism and Kinetics for Reaction of the Chemical Warfare Agent Simulant, DMMP(g), with Zirconium(IV) MOFs: An Ultrahigh-Vacuum and DFT Study. *The Journal of Physical Chemistry C* **2017**, *121* (21), 11261–11272. <https://doi.org/10.1021/acs.jpcc.7b00070>.
- (37) Vasudevan, A.; Senyurt, E. I.; Schoenitz, M.; Dreizin, E. L. Removal of Diisopropyl Methyl Phosphonate (DIMP) from Heated Metal Oxide Surfaces. *J Hazard Mater* **2023**, *443*, 130154. <https://doi.org/https://doi.org/10.1016/j.jhazmat.2022.130154>.
- (38) Qiao, B.; Wang, A.; Yang, X.; Allard, L. F.; Jiang, Z.; Cui, Y.; Liu, J.; Li, J.; Zhang, T. Single-Atom Catalysis of CO Oxidation Using Pt1/FeOx. *Nat Chem* **2011**. <https://doi.org/10.1038/nchem.1095>.
- (39) Zhang, H.; Liu, G.; Shi, L.; Ye, J. Single-Atom Catalysts: Emerging Multifunctional Materials in Heterogeneous Catalysis. *Adv Energy Mater* **2018**, *8* (1). <https://doi.org/10.1002/aenm.201701343>.

- (40) Flytzani-Stephanopoulos, M.; Gates, B. C. Atomically Dispersed Supported Metal Catalysts. *Annu Rev Chem Biomol Eng* **2012**, *3* (1), 545–574. <https://doi.org/10.1146/annurev-chembioeng-062011-080939>.
- (41) Cheng, N.; Zhang, L.; Doyle-Davis, K.; Sun, X. Single-Atom Catalysts: From Design to Application. *Electrochemical Energy Reviews* **2019**, *2* (4), 539–573. <https://doi.org/10.1007/s41918-019-00050-6>.
- (42) Thompson, C. B.; Liu, L.; Leshchev, D. S.; Hoffman, A. S.; Hong, J.; Bare, S. R.; Unocic, R. R.; Stavitski, E.; Xin, H.; Karim, A. M. CO Oxidation on Ir₁/TiO₂: Resolving Ligand Dynamics and Elementary Reaction Steps. *ACS Catal* **2023**, *13* (12), 7802–7811. <https://doi.org/10.1021/acscatal.3c01433>.
- (43) Li, Y.; Cheng, D.; Wei, Z.; Sautet, P. Photoelectron Storage at the WO₃/TiO₂ Interface: Modeling in Ambient Conditions from First-Principles Calculations. *ACS Catal* **2023**, *13* (15), 9979–9986. <https://doi.org/10.1021/acscatal.3c01756>.
- (44) Son, G.; Li, Y.; Shneidman, A. V.; Han, J. H.; Aizenberg, M.; Sautet, P.; Aizenberg, J. Facet-Dependence of Electron Storage in Gold-Decorated Titania Nanocrystals. *Chemistry of Materials* **2023**, *35* (22), 9505–9516. <https://doi.org/10.1021/acs.chemmater.3c01252>.
- (45) Kumari, S.; Sautet, P. Highly Dispersed Pt Atoms and Clusters on Hydroxylated Indium Tin Oxide: A View from First-Principles Calculations. *J Mater Chem A Mater* **2021**, *9* (28), 15724–15733. <https://doi.org/10.1039/D1TA03177E>.
- (46) Kumari, S.; Sautet, P. Elucidation of the Active Site for the Oxygen Evolution Reaction on a Single Pt Atom Supported on Indium Tin Oxide. *J Phys Chem Lett* **2023**, *14* (10), 2635–2643. <https://doi.org/10.1021/acs.jpcclett.3c00160>.
- (47) Kumari, S.; Sautet, P. Highly Dispersed Pt Atoms and Clusters on Hydroxylated Indium Tin Oxide: A View from First-Principles Calculations. *J Mater Chem A Mater* **2021**, *9* (28), 15724–15733.

- (48) Kumari, S.; Sautet, P. Highly Dispersed Pt Atoms and Clusters on Hydroxylated Indium Tin Oxide: A View from First-Principles Calculations. *J Mater Chem A Mater* **2021**, *9* (28), 15724–15733.
- (49) Kumari, S.; Alexandrova, A. N.; Sautet, P. Nature of Zirconia on a Copper Inverse Catalyst Under CO₂ Hydrogenation Conditions. *J Am Chem Soc* **2023**, *145* (48), 26350–26362. <https://doi.org/10.1021/jacs.3c09947>.
- (50) Sun, G.; Sautet, P. Active Site Fluxional Restructuring as a New Paradigm in Triggering Reaction Activity for Nanocluster Catalysis. *Acc Chem Res* **2021**, *54* (20), 3841–3849.
- (51) Sun, G.; Sautet, P. Active Site Fluxional Restructuring as a New Paradigm in Triggering Reaction Activity for Nanocluster Catalysis. *Acc Chem Res* **2021**, *54* (20), 3841–3849.
- (52) Tušek, D.; Ašperger, D.; Bačić, I.; Čurković, L.; Macan, J. Environmentally Acceptable Sorbents of Chemical Warfare Agent Simulants. *J Mater Sci* **2017**, *52* (5), 2591–2604.
- (53) Aliha, H. M.; Khodadadi, A. A.; Mortazavi, Y. The Sensing Behaviour of Metal Oxides (ZnO, CuO and Sm₂O₃) Doped-SnO₂ for Detection of Low Concentrations of Chlorinated Volatile Organic Compounds. *Sens Actuators B Chem* **2013**, *181*, 637–643.
- (54) Oh, S. W.; Kim, Y. H.; Yoo, D. J.; Oh, S. M.; Park, S. J. Sensing Behaviour of Semconducting Metal Oxides for the Detection of Organophosphorus Compounds. *Sens Actuators B Chem* **1993**, *13* (1–3), 400–403.
- (55) Mitchell, M. B.; Sheinker, V. N.; Mintz, E. A. Adsorption and Decomposition of Dimethyl Methylphosphonate on Metal Oxides. *J Phys Chem B* **1997**, *101* (51), 11192–11203. <https://doi.org/10.1021/jp972724b>.
- (56) Chen, D. A.; Ratliff, J. S.; Hu, X.; Gordon, W. O.; Senanayake, S. D.; Mullins, D. R. Dimethyl Methylphosphonate Decomposition on Fully Oxidized and Partially Reduced Ceria Thin Films. *Surf Sci* **2010**, *604* (5–6), 574–587. <https://doi.org/10.1016/j.susc.2009.12.028>.

- (57) Mitchell, M. B.; Sheinker, V. N.; Tesfamichael, A. B.; Gatimu, E. N.; Nunley, M. Decomposition of Dimethyl Methylphosphonate (DMMP) on Supported Cerium and Iron Co-Impregnated Oxides at Room Temperature. *J Phys Chem B* **2003**, *107* (2), 580–586.
- (58) Walenta, C.; Xu, F.; Tesvara, C.; O'Connor, C.; Sautet, P.; Friend, C. Facile Decomposition of Organophosphonates by Dual Lewis Sites on a Fe₃O₄(111) Film. *The Journal of Physical Chemistry C* *124* (23), 12432–12441. <https://doi.org/10.1021/acs.jpcc.0c01708>.
- (59) Templeton, M. K.; Weinberg, W. H. Adsorption and Decomposition of Dimethyl Methylphosphonate on an Aluminum Oxide Surface. *J Am Chem Soc* **1985**, *107* (1), 97–108.
- (60) Mitchell, M. B.; Sheinker, V. N.; Cox, W. W.; Gatimu, E. N.; Tesfamichael, A. B. The Room Temperature Decomposition Mechanism of Dimethyl Methylphosphonate (DMMP) on Alumina-Supported Cerium Oxide– Participation of Nano-Sized Cerium Oxide Domains. *J Phys Chem B* **2004**, *108* (5), 1634–1645.
- (61) Housaindokht, M. R.; Zamand, N. A DFT Study of Associative and Dissociative Chemical Adsorption of DMMP onto SnO₂ (110) Surface Nano-Cluster. *Struct Chem* **2015**, *26* (1), 87–96.
- (62) Biswas, S.; Wong, B. M. High-Temperature Decomposition of Diisopropyl Methylphosphonate on Alumina: Mechanistic Predictions from Ab Initio Molecular Dynamics. *The Journal of Physical Chemistry C* **2021**, *125* (40), 21922–21932. <https://doi.org/10.1021/acs.jpcc.1c05632>.
- (63) Zhou, J.; Varazo, K.; Reddic, J. E.; Myrick, M. L.; Chen, D. A. Decomposition of Dimethyl Methylphosphonate on TiO₂(110): Principal Component Analysis Applied to X-Ray Photoelectron Spectroscopy. *Anal Chim Acta* **2003**, *496* (1–2), 289–300. [https://doi.org/10.1016/S0003-2670\(03\)01008-0](https://doi.org/10.1016/S0003-2670(03)01008-0).

- (64) Michalkova, A.; Ilchenko, M.; Gorb, L.; Leszczynski, J. Theoretical Study of the Adsorption and Decomposition of Sarin on Magnesium Oxide. *Journal of Physical Chemistry B* **2004**, *108* (17). <https://doi.org/10.1021/jp036766d>.
- (65) Tsyshevsky, R.; Head, A. R.; Trotochaud, L.; Bluhm, H.; Kuklja, M. M. Mechanisms of Degradation of Toxic Nerve Agents: Quantum-Chemical Insight into Interactions of Sarin and Soman with Molybdenum Dioxide. *Surf Sci* **2020**, *700*. <https://doi.org/10.1016/j.susc.2020.121639>.
- (66) Tsyshevsky, R.; Holdren, S.; Eichhorn, B. W.; Zachariah, M. R.; Kuklja, M. M. Sarin Decomposition on Pristine and Hydroxylated ZnO: Quantum-Chemical Modeling. *Journal of Physical Chemistry C* **2019**, *123* (43). <https://doi.org/10.1021/acs.jpcc.9b07974>.
- (67) Kuiper, A. E. T.; van Bokhoven, J. J. G. M.; Medema, J. The Role of Heterogeneity in the Kinetics of a Surface Reaction: I. Infrared Characterization of the Adsorption Structures of Organophosphonates and Their Decomposition. *J Catal* **1976**, *43* (1), 154–167. [https://doi.org/https://doi.org/10.1016/0021-9517\(76\)90302-X](https://doi.org/https://doi.org/10.1016/0021-9517(76)90302-X).
- (68) Bermudez, V. M. Computational Study of the Adsorption of Dimethyl Methylphosphonate (DMMP) on the (010) Surface of Anatase TiO₂ with and without Faceting. *Surf Sci* **2010**, *604* (7), 706–712. <https://doi.org/https://doi.org/10.1016/j.susc.2010.01.021>.
- (69) Bermudez, V. M. First-Principles Study of Adsorption of Dimethyl Methylphosphonate on the TiO₂ Anatase (001) Surface: Formation of a Stable Titanyl (Ti=O) Site. *The Journal of Physical Chemistry C* **2011**, *115* (14), 6741–6747. <https://doi.org/10.1021/jp200009s>.
- (70) Bermudez, V. M. Ab Initio Study of the Interaction of Dimethyl Methylphosphonate with Rutile (110) and Anatase (101) TiO₂ Surfaces. *The Journal of Physical Chemistry C* **2010**, *114* (7), 3063–3074.
- (71) Zhou, J.; Ma, S.; Kang, Y. C.; Chen, D. A. Dimethyl Methylphosphonate Decomposition on Titania-Supported Ni Clusters and Films: A Comparison of Chemical Activity on Different

- Ni Surfaces. *J Phys Chem B* **2004**, *108* (31), 11633–11644. <https://doi.org/10.1021/jp040185m>.
- (72) Trubitsyn, D. A.; Vorontsov, A. v. Molecular and Reactive Adsorption of Dimethyl Methylphosphonate over (0 0 1) and (1 0 0) Anatase Clusters. *Comput Theor Chem* **2013**, *1020*, 63–71.
- (73) Kresse, G.; Furthmüller, J. Software VASP, Vienna (1999). *Phys. Rev. B* **1996**, *54* (11), 169.
- (74) Kresse, G.; Furthmüller, J. Efficiency of Ab-Initio Total Energy Calculations for Metals and Semiconductors Using a Plane-Wave Basis Set. *Comput Mater Sci* **1996**, *6* (1), 15–50. [https://doi.org/https://doi.org/10.1016/0927-0256\(96\)00008-0](https://doi.org/https://doi.org/10.1016/0927-0256(96)00008-0).
- (75) Anisimov, V. I.; Aryasetiawan, F.; Lichtenstein, A. I. First-Principles Calculations of the Electronic Structure and Spectra of Strongly Correlated Systems: The **LDA + U** Method. *Journal of Physics: Condensed Matter* **1997**, *9* (4), 767–808. <https://doi.org/10.1088/0953-8984/9/4/002>.
- (76) Dudarev, S. L.; Botton, G. A.; Savrasov, S. Y.; Humphreys, C. J.; Sutton, A. P. Electron-Energy-Loss Spectra and the Structural Stability of Nickel Oxide: An LSDA+U Study. *Phys Rev B* **1998**, *57* (3), 1505–1509. <https://doi.org/10.1103/PhysRevB.57.1505>.
- (77) Morgan, B. J.; Watson, G. W. A DFT+U Description of Oxygen Vacancies at the TiO₂ Rutile (110) Surface. *Surf Sci* **2007**, *601* (21), 5034–5041. <https://doi.org/https://doi.org/10.1016/j.susc.2007.08.025>.
- (78) Steinmann, S. N.; Corminboeuf, C. Comprehensive Benchmarking of a Density-Dependent Dispersion Correction. *J Chem Theory Comput* **2011**, *7* (11), 3567–3577. <https://doi.org/10.1021/ct200602x>.
- (79) Steinmann, S. N.; Corminboeuf, C. A Generalized-Gradient Approximation Exchange Hole Model for Dispersion Coefficients. *J Chem Phys* **2011**, *134* (4), 044117. <https://doi.org/10.1063/1.3545985>.

- (80) Perdew, J. P.; Burke, K.; Ernzerhof, M. Generalized Gradient Approximation Made Simple. *Phys Rev Lett* **1996**, *77* (18), 3865–3868. <https://doi.org/10.1103/PhysRevLett.77.3865>.
- (81) Kresse, G.; Joubert, D. From Ultrasoft Pseudopotentials to the Projector Augmented-Wave Method. *Phys Rev B* **1999**, *59* (3), 1758–1775. <https://doi.org/10.1103/PhysRevB.59.1758>.
- (82) Kresse, G.; Furthmüller, J. Efficient Iterative Schemes for Ab Initio Total-Energy Calculations Using a Plane-Wave Basis Set. *Phys Rev B* **1996**, *54* (16), 11169–11186. <https://doi.org/10.1103/PhysRevB.54.11169>.
- (83) Blöchl, P. E. Projector Augmented-Wave Method. *Phys Rev B* **1994**, *50* (24), 17953–17979. <https://doi.org/10.1103/PhysRevB.50.17953>.
- (84) Makov, G.; Payne, M. C. Periodic Boundary Conditions in Ab Initio Calculations. *Phys Rev B* **1995**, *51* (7), 4014–4022. <https://doi.org/10.1103/PhysRevB.51.4014>.
- (85) Tang, Y.; Asokan, C.; Xu, M.; Graham, G. W.; Pan, X.; Christopher, P.; Li, J.; Sautet, P. Rh Single Atoms on TiO₂ Dynamically Respond to Reaction Conditions by Adapting Their Site. *Nat Commun* **2019**, *10* (1), 1–18. <https://doi.org/10.1038/s41467-019-12461-6>.
- (86) Yu, Y.-Y.; Gong, X.-Q. CO Oxidation at Rutile TiO₂(110): Role of Oxygen Vacancies and Titanium Interstitials. *ACS Catal* **2015**, *5* (4), 2042–2050. <https://doi.org/10.1021/cs501900q>.
- (87) Deskins, N. A.; Rousseau, R.; Dupuis, M. Distribution of Ti³⁺ Surface Sites in Reduced TiO₂. *The Journal of Physical Chemistry C* **2011**, *115* (15), 7562–7572. <https://doi.org/10.1021/jp2001139>.
- (88) Li, H.; Guo, Y.; Robertson, J. Calculation of TiO₂ Surface and Subsurface Oxygen Vacancy by the Screened Exchange Functional. *The Journal of Physical Chemistry C* **2015**, *119* (32), 18160–18166. <https://doi.org/10.1021/acs.jpcc.5b02430>.
- (89) Pacchioni, G. Oxygen Vacancy: The Invisible Agent on Oxide Surfaces. *ChemPhysChem* **2003**, *4* (10), 1041–1047.

- (90) Sánchez-Sánchez, C.; González, C.; Jelinek, P.; Méndez, J.; de Andres, P. L.; Martín-Gago, J. A.; López, M. F. Understanding Atomic-Resolved STM Images on TiO_2 (110)-(1 × 1) Surface by DFT Calculations. *Nanotechnology* **2010**, *21* (40), 405702. <https://doi.org/10.1088/0957-4484/21/40/405702>.
- (91) di Valentin, C.; Pacchioni, G.; Selloni, A. Electronic Structure of Defect States in Hydroxylated and Reduced Rutile $\{\mathrm{TiO}\}_2(110)$ Surfaces. *Phys Rev Lett* **2006**, *97* (16), 166803. <https://doi.org/10.1103/PhysRevLett.97.166803>.
- (92) Schaub, R.; Wahlström, E.; Rønnau, A.; Lægsgaard, E.; Stensgaard, I.; Besenbacher, F. Oxygen-Mediated Diffusion of Oxygen Vacancies on the $\text{TiO}_2(110)$ Surface. *Science (1979)* **2003**, *299* (5605), 377–379. <https://doi.org/10.1126/science.1078962>.
- (93) Henderson, M. A.; Otero-Tapia, S.; Castro, M. E. The Chemistry of Methanol on the TiO_2 (110) Surface: The Influence of Vacancies and Coadsorbed Species. *Faraday Discuss* **1999**, *114*, 313–329.
- (94) Le, N. Q.; Bazargan, G.; Schweigert, I. v; Gunlycke, D. Vibrational Signatures of Sarin Adsorption on Anatase Surfaces. *Surf Sci* **2021**, *705*, 121765.
- (95) Wang, L.; Denchy, M.; Blando, N.; Hansen, L.; Bilik, B.; Tang, X.; Hicks, Z.; Bowen, K. H. Thermal Decomposition of Dimethyl Methylphosphonate on Size-Selected Clusters: A Comparative Study between Copper Metal and Cupric Oxide Clusters. *The Journal of Physical Chemistry C* **2021**, *125* (21), 11348–11358. <https://doi.org/10.1021/acs.jpcc.1c00952>.
- (96) Segal, S. R.; Cao, L.; Suib, S. L.; Tang, X.; Satyapal, S. Thermal Decomposition of Dimethyl Methylphosphonate over Manganese Oxide Catalysts. *J Catal* **2001**, *198* (1), 66–76.
- (97) Mukhopadhyay, S.; Schoenitz, M.; Dreizin, E. L. Vapor-Phase Decomposition of Dimethyl Methylphosphonate (DMMP), a Sarin Surrogate, in Presence of Metal Oxides. *Defence*

Technology **2021**, *17* (4), 1095–1114.
<https://doi.org/https://doi.org/10.1016/j.dt.2020.08.010>.

- (98) De, S.; Burange, A. S.; Luque, R. Conversion of Biomass-Derived Feedstocks into Value-Added Chemicals over Single-Atom Catalysts. *Green Chemistry* **2022**, *24* (6), 2267–2286. <https://doi.org/10.1039/D1GC04285H>.
- (99) Shan, J.; Li, M.; Allard, L. F.; Lee, S.; Flytzani-Stephanopoulos, M. Mild Oxidation of Methane to Methanol or Acetic Acid on Supported Isolated Rhodium Catalysts. *Nature* **2017**, *551* (7682), 605–608. <https://doi.org/10.1038/nature24640>.
- (100) Lin, L.; Yao, S.; Gao, R.; Liang, X.; Yu, Q.; Deng, Y.; Liu, J.; Peng, M.; Jiang, Z.; Li, S.; Li, Y.-W.; Wen, X.-D.; Zhou, W.; Ma, D. A Highly CO-Tolerant Atomically Dispersed Pt Catalyst for Chemoselective Hydrogenation. *Nat Nanotechnol* **2019**, *14* (4), 354–361. <https://doi.org/10.1038/s41565-019-0366-5>.
- (101) Yan, H.; Cheng, H.; Yi, H.; Lin, Y.; Yao, T.; Wang, C.; Li, J.; Wei, S.; Lu, J. Single-Atom Pd₁/Graphene Catalyst Achieved by Atomic Layer Deposition: Remarkable Performance in Selective Hydrogenation of 1,3-Butadiene. *J Am Chem Soc* **2015**, *137* (33), 10484–10487. <https://doi.org/10.1021/jacs.5b06485>.
- (102) Yan, X.; Duan, P.; Zhang, F.; Li, H.; Zhang, H.; Zhao, M.; Zhang, X.; Xu, B.; Pennycook, S. J.; Guo, J. Stable Single-Atom Platinum Catalyst Trapped in Carbon Onion Graphitic Shells for Improved Chemoselective Hydrogenation of Nitroarenes. *Carbon NY* **2019**, *143*, 378–384. <https://doi.org/10.1016/j.carbon.2018.11.021>.
- (103) Zhang, L.; Zhou, M.; Wang, A.; Zhang, T. Selective Hydrogenation over Supported Metal Catalysts: From Nanoparticles to Single Atoms. *Chem Rev* **2020**, *120* (2), 683–733. <https://doi.org/10.1021/acs.chemrev.9b00230>.
- (104) Ding, K.; Gulec, A.; Johnson, A. M.; Schweitzer, N. M.; Stucky, G. D.; Marks, L. D.; Stair, P. C. Identification of Active Sites in CO Oxidation and Water-Gas Shift over Supported Pt

- Catalysts. *Science* (1979) **2015**, 350 (6257), 189–192.
<https://doi.org/10.1126/science.aac6368>.
- (105) Therrien, A. J.; Hensley, A. J. R.; Marcinkowski, M. D.; Zhang, R.; Lucci, F. R.; Coughlin, B.; Schilling, A. C.; McEwen, J.-S.; Sykes, E. C. H. An Atomic-Scale View of Single-Site Pt Catalysis for Low-Temperature CO Oxidation. *Nat Catal* **2018**, 1 (3), 192–198.
<https://doi.org/10.1038/s41929-018-0028-2>.
- (106) Zhang, Z.; Zhu, Y.; Asakura, H.; Zhang, B.; Zhang, J.; Zhou, M.; Han, Y.; Tanaka, T.; Wang, A.; Zhang, T.; Yan, N. Thermally Stable Single Atom Pt/m-Al₂O₃ for Selective Hydrogenation and CO Oxidation. *Nat Commun* **2017**, 8.
<https://doi.org/10.1038/ncomms16100>.
- (107) Ji, S.; Chen, Y.; Wang, X.; Zhang, Z.; Wang, D.; Li, Y. Chemical Synthesis of Single Atomic Site Catalysts. *Chem Rev* **2020**, 120 (21), 11900–11955.
<https://doi.org/10.1021/acs.chemrev.9b00818>.
- (108) Lu, Y.; Zhou, S.; Kuo, C.-T.; Kunwar, D.; Thompson, C.; Hoffman, A. S.; Boubnov, A.; Lin, S.; Datye, A. K.; Guo, H.; Karim, A. M. Unraveling the Intermediate Reaction Complexes and Critical Role of Support-Derived Oxygen Atoms in CO Oxidation on Single-Atom Pt/CeO₂. *ACS Catal* **2021**, 11 (14), 8701–8715. <https://doi.org/10.1021/acscatal.1c01900>.
- (109) Kottwitz, M.; Li, Y.; Palomino, R. M.; Liu, Z.; Wang, G.; Wu, Q.; Huang, J.; Timoshenko, J.; Senanayake, S. D.; Balasubramanian, M.; Lu, D.; Nuzzo, R. G.; Frenkel, A. I. Local Structure and Electronic State of Atomically Dispersed Pt Supported on Nanosized CeO₂. *ACS Catal* **2019**, 9 (9), 8738–8748. <https://doi.org/10.1021/acscatal.9b02083>.
- (110) DeRita, L.; Resasco, J.; Dai, S.; Boubnov, A.; Thang, H. V.; Hoffman, A. S.; Ro, I.; Graham, G. W.; Bare, S. R.; Pacchioni, G.; Pan, X.; Christopher, P. Structural Evolution of Atomically Dispersed Pt Catalysts Dictates Reactivity. *Nat Mater* **2019**.
<https://doi.org/10.1038/s41563-019-0349-9>.

- (111) Dessal, C.; Len, T.; Morfin, F.; Rousset, J. L.; Aouine, M.; Afanasiev, P.; Piccolo, L. Dynamics of Single Pt Atoms on Alumina during CO Oxidation Monitored by Operando X-Ray and Infrared Spectroscopies. *ACS Catal* **2019**, *9* (6), 5752–5759. <https://doi.org/10.1021/acscatal.9b00903>.
- (112) Moses-Debusk, M.; Yoon, M.; Allard, L. F.; Mullins, D. R.; Wu, Z.; Yang, X.; Veith, G.; Stocks, G. M.; Narula, C. K. CO Oxidation on Supported Single Pt Atoms: Experimental and Ab Initio Density Functional Studies of CO Interaction with Pt Atom on θ -Al₂O₃(010) Surface. *J Am Chem Soc* **2013**, *135* (34), 12634–12645. <https://doi.org/10.1021/ja401847c>.
- (113) Diasanayake, M. A. K. L.; Senadeera, G. K. R.; Sarangika, H. N. M.; Ekanayake, P. M. P. C.; Thotawattage, C. A.; Divarathne, H. K. D. W. M. N. R.; Kumari, J. M. K. W. TiO₂ as a Low Cost, Multi Functional Material. *Mater Today Proc* **2016**, *3*, S40–S47. <https://doi.org/10.1016/j.matpr.2016.01.006>.
- (114) Cargnello, M.; Gordon, T. R.; Murray, C. B. Solution-Phase Synthesis of Titanium Dioxide Nanoparticles and Nanocrystals. *Chem Rev* **2014**, *114* (19), 9319–9345. <https://doi.org/10.1021/cr500170p>.
- (115) Banfield, J. Thermodynamic Analysis of Phase Stability of Nanocrystalline Titania. *J Mater Chem* **1998**, *8* (9), 2073–2076.
- (116) Hanaor, D. A. H.; Sorrell, C. C. Review of the Anatase to Rutile Phase Transformation. *J Mater Sci* **2011**, *46* (4), 855–874.
- (117) Periyat, P.; Naufal, B.; Ullattil, S. G. A Review on High Temperature Stable Anatase TiO₂ Photocatalysts. In *Materials Science Forum*; Trans Tech Publ, 2016; Vol. 855, pp 78–93.
- (118) Tanemura, S.; Miao, L.; Wunderlich, W.; Tanemura, M.; Mori, Y.; Toh, S.; Kaneko, K. Fabrication and Characterization of Anatase/Rutile–TiO₂ Thin Films by Magnetron Sputtering: A Review. *Sci Technol Adv Mater* **2005**, *6* (1), 11–17.
- (119) Monai, M.; Montini, T.; Fornasiero, P. Brookite: Nothing New under the Sun? *Catalysts* **2017**, *7* (10), 304.

- (120) Wang, C.; Deng, Z.-X.; Li, Y. The Synthesis of Nanocrystalline Anatase and Rutile Titania in Mixed Organic Media. *Inorg Chem* **2001**, *40* (20), 5210–5214. <https://doi.org/10.1021/ic0101679>.
- (121) Chen, L.; Unocic, R. R.; Hoffman, A. S.; Hong, J.; Braga, A. H.; Bao, Z.; Bare, S. R.; Szanyi, J. Unlocking the Catalytic Potential of TiO₂-Supported Pt Single Atoms for the Reverse Water–Gas Shift Reaction by Altering Their Chemical Environment. *JACS Au* **2021**, *1* (7), 977–986. <https://doi.org/10.1021/jacsau.1c00111>.
- (122) Thang, H. V.; Thang, H. V.; Pacchioni, G.; DeRita, L.; Christopher, P. Nature of Stable Single Atom Pt Catalysts Dispersed on Anatase TiO₂. *J Catal* **2018**, *v. 367*, 104–114–2018 v.367. <https://doi.org/10.1016/j.jcat.2018.08.025>.
- (123) Kuai, L.; Chen, Z.; Liu, S.; Kan, E.; Yu, N.; Ren, Y.; Fang, C.; Li, X.; Li, Y.; Geng, B. Titania Supported Synergistic Palladium Single Atoms and Nanoparticles for Room Temperature Ketone and Aldehydes Hydrogenation. *Nat Commun* **2020**, *11* (1), 1–9.
- (124) Tang, Y.; Asokan, C.; Xu, M.; Graham, G. W.; Pan, X.; Christopher, P.; Li, J.; Sautet, P. Rh Single Atoms on TiO₂ Dynamically Respond to Reaction Conditions by Adapting Their Site. *Nat Commun* **2019**, *10* (1), 4488. <https://doi.org/10.1038/s41467-019-12461-6>.
- (125) Zhang, J.; Alexandrova, A. N. The Golden Crown: A Single Au Atom That Boosts the CO Oxidation Catalyzed by a Palladium Cluster on Titania Surfaces. *J Phys Chem Lett* **2013**, *4* (14), 2250–2255. <https://doi.org/10.1021/jz400981a>.
- (126) Zhou, X.; Hwang, I.; Tomanec, O.; Fehn, D.; Mazare, A.; Zboril, R.; Meyer, K.; Schmuki, P. Advanced Photocatalysts: Pinning Single Atom Co-Catalysts on Titania Nanotubes. *Adv Funct Mater* **2021**, *31* (30), 2102843.
- (127) Lu, Y.; Thompson, C.; Kunwar, D.; Datye, A. K.; Karim, A. M. Origin of the High CO Oxidation Activity on CeO₂ Supported Pt Nanoparticles: Weaker Binding of CO or Facile Oxygen Transfer from the Support? *ChemCatChem* **2020**, *12* (6), 1726–1733.

- (128) Gänzler, A. M.; Casapu, M.; Doronkin, D. E.; Maurer, F.; Lott, P.; Glatzel, P.; Votsmeier, M.; Deutschmann, O.; Grunwaldt, J.-D. Unravelling the Different Reaction Pathways for Low Temperature CO Oxidation on Pt/CeO₂ and Pt/Al₂O₃ by Spatially Resolved Structure–Activity Correlations. *J Phys Chem Lett* **2019**, *10* (24), 7698–7705. <https://doi.org/10.1021/acs.jpcelett.9b02768>.
- (129) Li, T.; Tsyshevsky, R.; McEntee, M.; Durke, E. M.; Karwacki, C.; Rodriguez, E. E.; Kuklja, M. M. Titania Nanomaterials for Sarin Decomposition: Understanding Fundamentals. *ACS Appl Nano Mater* **2022**, *5* (5), 6659–6670. <https://doi.org/10.1021/acsanm.2c00693>.
- (130) Li, T.; Algrim, L.; McEntee, M.; Tsyshevsky, R.; Leonard, M.; Durke, E. M.; Karwacki, C.; Kuklja, M. M.; Zachariah, M. R.; Rodriguez, E. E. Aliovalent-Doping Effects on the Surface Activity of Mesoporous CeO₂ toward Nerve Agent Simulant DMMP Decomposition. *The Journal of Physical Chemistry C* **2022**, *126* (42), 17923–17934. <https://doi.org/10.1021/acs.jpcc.2c04853>.
- (131) Li, T.; Tsyshevsky, R.; Algrim, L.; McEntee, M.; Durke, E. M.; Eichhorn, B.; Karwacki, C.; Zachariah, M. R.; Kuklja, M. M.; Rodriguez, E. E. Understanding Dimethyl Methylphosphonate Adsorption and Decomposition on Mesoporous CeO₂. *ACS Appl Mater Interfaces* **2021**, *13* (45), 54597–54609. <https://doi.org/10.1021/acsmi.1c16668>.
- (132) Tesvara, C.; Karwacki, C.; Sautet, P. Decomposition of the Toxic Nerve Agent Sarin on Oxygen Vacancy Sites of Rutile TiO₂(110). *The Journal of Physical Chemistry C* **127** (17), 8006–8015. <https://doi.org/10.1021/acs.jpcc.2c08525>.
- (133) Walenta, C. A.; Xu, F.; Tesvara, C.; O'Connor, C. R.; Sautet, P.; Friend, C. M. Facile Decomposition of Organophosphonates by Dual Lewis Sites on a Fe₃O₄(111) Film. *The Journal of Physical Chemistry C* **2020**, *124* (23), 12432–12441. <https://doi.org/10.1021/acs.jpcc.0c01708>.
- (134) Housaindokht, M. R.; Zamand, N. A DFT Study of Associative and Dissociative Chemical Adsorption of DMMP onto SnO₂(110) Surface Nano-Cluster. *Struct Chem* **2015**. <https://doi.org/10.1007/s11224-014-0465-8>.

- (135) Bermudez, V. M. Computational Study of Environmental Effects in the Adsorption of DMMP, Sarin, and VX on γ -Al₂O₃: Photolysis and Surface Hydroxylation. *Journal of Physical Chemistry C* **2009**. <https://doi.org/10.1021/jp809053u>.
- (136) Harvey, J. A.; McEntee, M. L.; Garibay, S. J.; Durke, E. M.; DeCoste, J. B.; Greathouse, J. A.; Sava Gallis, D. F. Spectroscopically Resolved Binding Sites for the Adsorption of Sarin Gas in a Metal-Organic Framework: Insights beyond Lewis Acidity. *Journal of Physical Chemistry Letters* **2019**. <https://doi.org/10.1021/acs.jpcelett.9b01867>.
- (137) Tesvara, C.; Yousuf, M. R.; Albrahim, M.; Troya, D.; Shrotri, A.; Stavitski, E.; Karim, A. M.; Sautet, P. Unraveling the CO Oxidation Mechanism over Highly Dispersed Pt Single Atom on Anatase TiO₂ (101). *ACS Catal* **2024**, 7562–7575. <https://doi.org/10.1021/acscatal.4c01018>.
- (138) Johnson, E. M.; Boyanich, M. C.; Gibbons, B.; Sapienza, N. S.; Yang, X.; Karim, A. M.; Morris, J. R.; Troya, D.; Morris, A. J. Aqueous-Phase Destruction of Nerve-Agent Simulants at Copper Single Atoms in UiO-66. *Inorg Chem* **2022**, 61 (22), 8585–8591. <https://doi.org/10.1021/acs.inorgchem.2c01351>.
- (139) Cai, C.; Chen, Q.; Su, H.; Huang, P.; Mao, J.; Wu, F.-Y. Single Copper Sites Dispersed on Metal-Organic Frameworks Boost the Degradation of Nerve Agent Simulants. *Sci China Mater* **2023**, 66 (6), 2475–2482. <https://doi.org/10.1007/s40843-022-2378-8>.
- (140) Panayotov, D. A.; Morris, J. R. Catalytic Degradation of a Chemical Warfare Agent Simulant: Reaction Mechanisms on TiO₂-Supported Au Nanoparticles. *The Journal of Physical Chemistry C* **2008**, 112 (19), 7496–7502. <https://doi.org/10.1021/jp7118668>.
- (141) Bonney, M. J.; Tesvara, C.; Sautet, P.; White, M. G. Understanding the Decomposition of Dimethyl Methyl Phosphonate on Metal-Modified TiO₂ (110) Surfaces Using Ensembles of Product Configurations. *ACS Appl Mater Interfaces* **2024**. <https://doi.org/10.1021/acsami.4c01250>.

- (142) DeSario, P. A.; Gordon, W. O.; Balboa, A.; Pennington, A. M.; Pitman, C. L.; McEntee, M.; Pietron, J. J. Photoenhanced Degradation of Sarin at Cu/TiO₂ Composite Aerogels: Roles of Bandgap Excitation and Surface Plasmon Excitation. *ACS Appl Mater Interfaces* **2021**, *13* (10), 12550–12561. <https://doi.org/10.1021/acsami.0c21988>.
- (143) Kresse G. a Joubert, D. b. From Ultrasoft Pseudopotentials to the Projector Augmented-Wave Method. *Phys Rev B Condens Matter Mater Phys* **1999**.
- (144) Dudarev, S.; Botton, G. Electron-Energy-Loss Spectra and the Structural Stability of Nickel Oxide: An LSDA+U Study. *Phys Rev B Condens Matter Mater Phys* **1998**. <https://doi.org/10.1103/PhysRevB.57.1505>.
- (145) Anisimov, V. I.; Zaanen, J.; Andersen, O. K. Band Theory and Mott Insulators: Hubbard U Instead of Stoner I. *Phys Rev B* **1991**. <https://doi.org/10.1103/PhysRevB.44.943>.
- (146) Tian, Y.; Plonka, A. M.; Ebrahim, A. M.; Palomino, R. M.; Senanayake, S. D.; Balboa, A.; Gordon, W. O.; Troya, D.; Musaeov, D. G.; Morris, J. R.; Mitchell, M. B.; Collins-Wildman, D. L.; Hill, C. L.; Frenkel, A. I. Correlated Multimodal Approach Reveals Key Details of Nerve-Agent Decomposition by Single-Site Zr-Based Polyoxometalates. *Journal of Physical Chemistry Letters* **2019**. <https://doi.org/10.1021/acs.jpcllett.9b01002>.
- (147) Devulapalli, V. S. D.; Richard, M.; Luo, T.-Y.; De Souza, M. L.; Rosi, N. L.; Borguet, E. Tuning the Lewis Acidity of Metal–Organic Frameworks for Enhanced Catalysis. *Dalton Transactions* **2021**, *50* (9), 3116–3120. <https://doi.org/10.1039/D1DT00180A>.
- (148) Tesvara, C.; Walenta, C.; Sautet, P. Oxidative Decomposition of Dimethyl Methylphosphonate on Rutile TiO₂(110): The Role of Oxygen Vacancies. *Physical Chemistry Chemical Physics* **2022**, *24* (38), 23402–23419. <https://doi.org/10.1039/d2cp02246j>.
- (149) Panayotov, D. A.; Morris, J. R. Catalytic Degradation of a Chemical Warfare Agent Simulant: Reaction Mechanisms on TiO₂-Supported Au Nanoparticles. *The Journal of Physical Chemistry C* **2008**, *112* (19), 7496–7502. <https://doi.org/10.1021/jp7118668>.

- (150) Yoon, S.; Oh, K.; Liu, F.; Seo, J. H.; Somorjai, G. A.; Lee, J. H.; An, K. Specific Metal–Support Interactions between Nanoparticle Layers for Catalysts with Enhanced Methanol Oxidation Activity. *ACS Catal* **2018**, *8* (6), 5391–5398. <https://doi.org/10.1021/acscatal.8b00276>.
- (151) Lang, R.; Du, X.; Huang, Y.; Jiang, X.; Zhang, Q.; Guo, Y.; Liu, K.; Qiao, B.; Wang, A.; Zhang, T. Single-Atom Catalysts Based on the Metal–Oxide Interaction. *Chem Rev* **2020**, *120* (21), 11986–12043. <https://doi.org/10.1021/acs.chemrev.0c00797>.
- (152) Thang, H. V.; Pacchioni, G.; DeRita, L.; Christopher, P. Nature of Stable Single Atom Pt Catalysts Dispersed on Anatase TiO₂. *J Catal* **2018**, *367*, 104–114. <https://doi.org/10.1016/J.JCAT.2018.08.025>.
- (153) DeRita, L.; Dai, S.; Lopez-Zepeda, K.; Pham, N.; Graham, G. W.; Pan, X.; Christopher, P. Catalyst Architecture for Stable Single Atom Dispersion Enables Site-Specific Spectroscopic and Reactivity Measurements of CO Adsorbed to Pt Atoms, Oxidized Pt Clusters, and Metallic Pt Clusters on TiO₂. *J Am Chem Soc* **2017**, *139* (40), 14150–14165. <https://doi.org/10.1021/jacs.7b07093>.
- (154) Tatibouët, J. M. Methanol Oxidation as a Catalytic Surface Probe. *Appl Catal A Gen* **1997**, *148* (2), 213–252. [https://doi.org/10.1016/S0926-860X\(96\)00236-0](https://doi.org/10.1016/S0926-860X(96)00236-0).
- (155) Reece, C.; Redekop, E. A.; Karakalos, S.; Friend, C. M.; Madix, Robert. J. Crossing the Great Divide between Single-Crystal Reactivity and Actual Catalyst Selectivity with Pressure Transients. *Nat Catal* **2018**, *1* (11), 852–859. <https://doi.org/10.1038/s41929-018-0167-5>.
- (156) Sapienza, N. S.; Knight, K. N.; Albrahim, M.; Yousuf, Md. R.; Karim, A. M.; Morris, J. R. Autocatalysis through the Generation of Water during Methanol Oxidation over a Titania-Supported Platinum Catalyst. *ACS Catal* **2023**, *13* (15), 9997–10006. <https://doi.org/10.1021/acscatal.3c01740>.

- (157) Steinmann, S. N.; Corminboeuf, C. A System-Dependent Density-Based Dispersion Correction. *J Chem Theory Comput* **2010**. <https://doi.org/10.1021/ct1001494>.
- (158) Steinmann, S. N.; Corminboeuf, C. Comprehensive Benchmarking of a Density-Dependent Dispersion Correction. *J Chem Theory Comput* **2011**. <https://doi.org/10.1021/ct200602x>.
- (159) Sun, G.; Alexandrova, A. N.; Sautet, P. Structural Rearrangements of Subnanometer Cu Oxide Clusters Govern Catalytic Oxidation. *ACS Catal* **2020**, *10* (9), 5309–5317.
- (160) Geng Sun. *Github.com/GengSS/catalapp*. <https://github.com/GengSS/catalapp/tree/main>.
- (161) Motagamwala, A. H.; Dumesic, J. A. Microkinetic Modeling: A Tool for Rational Catalyst Design. *Chem Rev* **2021**, *121* (2), 1049–1076. <https://doi.org/10.1021/acs.chemrev.0c00394>.
- (162) Cohen, M.; Vlachos, D. G. Modified Energy Span Analysis Reveals Heterogeneous Catalytic Kinetics. *Ind Eng Chem Res* **2022**, *61* (15), 5117–5128. <https://doi.org/10.1021/acs.iecr.2c00390>.
- (163) Redhead, P. A. Thermal Desorption of Gases. *Vacuum* **1962**, *12* (5), 274. [https://doi.org/10.1016/0042-207x\(62\)90543-2](https://doi.org/10.1016/0042-207x(62)90543-2).
- (164) Niemantsverdriet, J. W.; Chorkendorff, I. *Concepts of Modern Catalysis and Kinetics*; Weinheim, 2003.